

NUMERICAL SIMULATIONS IN LOW DOSE
COMPUTED TOMOGRAPHY

BY
ELZBIETA J. MAZUR

A THESIS
SUBMITTED TO THE FACULTY OF GRADUATE STUDIES
IN PARTIAL FULFILLMENT OF THE REQUIREMENTS
FOR THE DEGREE OF
DOCTOR OF PHILOSOPHY

DEPARTMENT OF ELECTRICAL AND COMPUTER ENGINEERING
UNIVERSITY OF MANITOBA
WINNIPEG, MANITOBA

COPYRIGHT © 1992 by ELZBIETA J. MAZUR



National Library
of Canada

Acquisitions and
Bibliographic Services Branch

395 Wellington Street
Ottawa, Ontario
K1A 0N4

Bibliothèque nationale
du Canada

Direction des acquisitions et
des services bibliographiques

395, rue Wellington
Ottawa (Ontario)
K1A 0N4

Your file *Votre référence*

Our file *Notre référence*

The author has granted an irrevocable non-exclusive licence allowing the National Library of Canada to reproduce, loan, distribute or sell copies of his/her thesis by any means and in any form or format, making this thesis available to interested persons.

L'auteur a accordé une licence irrévocable et non exclusive permettant à la Bibliothèque nationale du Canada de reproduire, prêter, distribuer ou vendre des copies de sa thèse de quelque manière et sous quelque forme que ce soit pour mettre des exemplaires de cette thèse à la disposition des personnes intéressées.

The author retains ownership of the copyright in his/her thesis. Neither the thesis nor substantial extracts from it may be printed or otherwise reproduced without his/her permission.

L'auteur conserve la propriété du droit d'auteur qui protège sa thèse. Ni la thèse ni des extraits substantiels de celle-ci ne doivent être imprimés ou autrement reproduits sans son autorisation.

ISBN 0-315-77838-5

Canada

NUMERICAL SIMULATIONS IN LOW DOSE COMPUTED TOMOGRAPHY

BY

ELZBIETA J. MAZUR

A Thesis submitted to the Faculty of Graduate Studies of the University of Manitoba in partial fulfillment of the requirements for the degree of

DOCTOR OF PHILOSOPHY

© 1992

Permission has been granted to the LIBRARY OF THE UNIVERSITY OF MANITOBA to lend or sell copies of this thesis, to the NATIONAL LIBRARY OF CANADA to microfilm this thesis and to lend or sell copies of the film, and UNIVERSITY MICROFILMS to publish an abstract of this thesis.

The author reserves other publication rights, and neither the thesis nor extensive extracts from it may be printed or otherwise reproduced without the author's permission.

ABSTRACT

CT reconstructions are usually done using the Fourier Backprojection algorithm, which requires many equally spaced projections. When the number of projections is too small or the projections are confined to a limited angle range, the resulting image quality deteriorates very quickly.

This thesis introduces two new reconstruction methods, Interpolative Algebraic Reconstruction Techniques (IART) and Matching Reconstruction Technique (MRT), suitable for reconstruction from incomplete data and for any radiation beam geometry. The goal is to minimize the radiation dose for a given image quality. IART uses a novel approach to relate pixels (elements of a reconstruction matrix) to projections that eliminates errors due to the discretization characteristic of ART algorithms. The method complies with real conditions where projections at every direction are taken with the same number of equally spaced detectors, whether parallel or fan beam. IART is iterative and vulnerable to noise. IART with filtered projections is introduced that was tested on data that included simulated photon noise. The results obtained showed improvement in the image quality.

To filter out photon noise different approaches have been examined:

1. Using a set of projections to form a sinogram image, real space enhancement techniques have been applied. The result was negative.
2. Applying the windowing technique in Fourier space produced positive results.

MRT does not use the backprojection operation. The image is produced by random changes of intensities of constituent pixels of a reconstruction matrix with selection of changes by simulated annealing.

New ways of using a Fourier spectrum in a reconstruction process are introduced: as a measure for distinguishing a linear from nonlinear reconstruction method , as a new

criterion in estimation of the optimal number of iterations, and as a new qualitative similarity measure.

This thesis also includes a comparative study that consists of:

1. Comparison of images obtained using the same reconstruction method but from a different number of projections;
2. Comparison of images from the same number of projections but resulting from different reconstruction methods. In both cases, the IART and FBP reconstruction images were used.

The objective was the applicability of quantitative criteria and the newly introduced qualitative criterion of the subtraction of Fourier spectra of images (reconstruction from reference) as the similarity measures.

ACKNOWLEDGMENTS

I wish to express my gratitude to my supervisor, Dr. Richard Gordon, who has made it possible for this work to be done. Without him this opportunity could not have existed.

I have much to be thankful to the Dean of Graduate Studies, Dr. Kenneth Hughes, whose attitude and support sustained me.

I would also like to thank my committee members, Drs. Edward Lyons, Miroslaw Pawlak, and Ed Shwedyk for being on my committee and their insights from time to time.

I acknowledge Dr. Douglas Boyd, the best external examiner. I continue to be impressed by his professional approach and comments. I thank him very much.

My additional thanks to Dr. Edward Lyons for giving me the opportunity to use a faster Siemens LiteBox computer. It made my long hours in front of the computer a little shorter.

Finally, my special thanks go to my husband, Andrzej, who was always for me whenever I needed it.

TABLE OF CONTENTS

ABSTRACT	ii
ACKNOWLEDGMENTS.....	iv
LIST OF FIGURES	viii
LIST OF TABLES.....	xiv
I. INTRODUCTION	
1.1. Thesis Objective.....	1
1.2. Outline of the Thesis.....	3
II. RECONSTRUCTION METHODS	
2.1. Interpolative Algebraic Reconstruction Techniques (IART).....	5
2.1.1. Introduction	5
2.1.2. Relating Pixels to Projections without Beam Partitioning	7
Parallel Geometry Beam	10
Fan Geometry Beam	12
2.1.3. Reconstruction Algorithm	15
2.1.4. Results	16
2.1.5. Discussion and Conclusions.....	26
2.2. IART. The Discrepancy Convergence Criterion and Round-off Computation Errors	28
2.3. IART with Filtered Projections.....	41
2.4. Convolution Backprojection/ Fourier Backprojection. An Overview.....	41
III. NOISE IN COMPUTED TOMOGRAPHY	
3.1. Sources of Noise and Their Influence on a Reconstruction Image.....	45
3.2. Simulation of Photon Noise	53
3.3. Noisy Sinograms.....	60
3.4. Noise Removal from Noisy Projections	72

3.5. Filtering Noisy Sinograms of Different Objects.....	84
3.6. Concluding Remarks	91
IV. FOURIER SPECTRUM. NEW WAYS OF USING IT	
4.1. Introduction	93
4.2. Fourier Spectrum as a Measure for Distinguishing Linear from Nonlinear Reconstruction Methods	95
4.3. Fourier Spectrum as a Qualitative Image Evaluation Measure.....	102
4.4. Fourier Spectrum as a Criterion for Iterative Reconstruction Methods	107
4.5. Concluding Remarks	113
V. IMAGE RECONSTRUCTION FROM LIMITED NUMBER OF VIEWS USING IART AND IART WITH FILTERED PROJECTIONS	
5.1. Simulation of the CT Data Under Various Assumptions of Photon Noise.....	114
5.2. Methods of Evaluating Image Fidelity.....	116
5.3. Simulated Experiments. Results	120
5.4. Discussion and Conclusions.....	154
VI. EVALUATION OF OUTCOMES FROM IART AND FBP RECONSTRUCTION METHODS. COMPARISON	
6.1. Evaluation and Comparison of Reconstruction Images From Different Number of Projections. IART	157
6.2. Evaluation and Comparison of Reconstruction Images From Different Number of Projections. FBP.....	159
6.3. Evaluation and Comparison of Reconstruction Images From IART and FBP.....	169
6.4. Discussion and Conclusions.....	173
VII. MATCHING RECONSTRUCTION TECHNIQUE. A NEW PROPOSAL	
7.1. Introduction	176
7.2. Matching Reconstruction Technique	177
7.3. Concluding Remarks	182

VIII. CONCLUSIONS AND FUTURE WORK.....	183
BIBLIOGRAPHY.....	188
APPENDIX	
SOURCE CODE	197

LIST OF FIGURES

2.1.1.	{ δ_k } - set of rays for the projection direction at the angle θ . Centroids represent the individual optical density pixels of the reconstruction matrix { \tilde{r}_{ij} }. Every radiation ray is represented by a projection value p_k	6
2.1.2.	For a parallel geometry beam, estimation of a pixel shadow on the line of detectors using: accurate, (a), and rotation, (b), interpolation.....	9
2.1.3.	Geometry of a parallel beam scanning system. The line at the angle θ represents the line of detectors for a projection direction $\theta + 90^0$. a_x, a_y - distance between pixel centers in a row and column of the backprojection matrix, respectively; d - detector width.....	10
2.1.4.	Geometry of a fan beam scanning system. S - an x-ray source, P - center of the (i,j) 'th pixel, P_{ij} - center of the shadow cast by the (i,j) 'th pixel on the arc of detectors.....	12
2.1.5.	Fan beam scanning system. Shadow cast by the (i,j) 'th pixel onto the detectors arc	13
2.1.6.	The reference image, a superposition of 10 ellipses. At overlaps grey levels are added.....	17
2.1.7.	Parallel beam, 30 projection directions equally spaced over 180^0 . IART reconstruction of Fig. 2.1.6 after: (a), six iterations; (b), nine iterations	19
2.1.8.	Parallel beam, 30 projection directions equally spaced over 180^0 . IART reconstruction of Fig. 2.1.6 using the fixed pixel interpolation function after: (a), one iteration; (b), three iterations.....	20
2.1.9.	Parallel beam, 30 projection directions equally spaced over 180^0 . IART reconstruction of Fig. 2.1.6 using the rotated pixel interpolation function after: (a), one iteration; (b), three iterations.....	21
2.1.10.	Correlation coefficients computed for the IART reconstruction images. (Parallel geometry beam.).....	22
2.1.11.	Fan beam, 30 projection directions equally spaced over 360^0 . IART reconstruction of Fig. 2.1.6 after: (a), one iteration; (b), two iterations.....	24
2.1.12.	Fan beam, 30 projection directions equally spaced over 360^0 . IART reconstruction of Fig. 2.1.6 after: (a), three iterations; (b), four iterations.....	25
2.1.13.	Reconstruction of Fig. 2.1.6 using Fourier Backprojection method. 30 projection directions equally spaced over 360^0	26
2.2.1.	Test objects. Vertical bars represent the grow in density (100). The base density is zero	30
2.2.2.	Test object A. Iteration discrepancy: (a), integer projection data - integer pseudoprojections; (b), integer projection data - real pseudoprojections. The iterations are circled for which the projection direction discrepancy is presented in Fig. 2.2.3.....	31
2.2.2(c).	Test object A. Iteration discrepancy: real projection data - real pseudoprojections. The iteration is circled for which the projection direction discrepancy is presented in Fig. 2.2.3	32
2.2.3.	Test object A. Projection direction discrepancy: (a), integer projection data - integer pseudoprojections; (b), integer projection data - real pseudoprojections; (c), real projection data - real pseudoprojections.....	32

2.2.4.	Test object B. Iteration discrepancy: (a), integer projection data - integer pseudoprojections; (b), integer projection data - real pseudoprojections; (c), real projection data - real pseudoprojections. The iterations are circled for which the projection direction discrepancy is presented in Fig. 2.2.5	33
2.2.5.	Test object B. Projection direction discrepancy: (a), integer projection data - integer pseudoprojections; (b), integer projection data - real pseudoprojections; (c), real projection data - real pseudoprojections.....	34
2.2.6.	Test object C. Iteration discrepancy: (a), integer projection data - integer pseudoprojections; (b), integer projection data - real pseudoprojections; (c), real projection data - real pseudoprojections. The iterations are circled for which the projection direction discrepancy is presented in Fig. 2.2.7	35
2.2.7.	Test object C. Projection direction discrepancy: (a), integer projection data - integer pseudoprojections; (b), integer projection data - real pseudoprojections; (c), real projection data - real pseudoprojections.....	36
2.2.8.	Test object A. Reconstruction matrix data: (a), integer projection data - integer pseudoprojections; (b), integer projection data - real pseudoprojections; (c), real projection data - real pseudoprojections.....	37
2.2.9.	Test object B. Reconstruction matrix data: (a), integer projection data - integer pseudoprojections; (b), integer projection data - real pseudoprojections; (c), real projection data - real pseudoprojections.....	38
2.2.10.	Test object C. Reconstruction matrix data: (a), integer projection data - integer pseudoprojections; (b), integer projection data - real pseudoprojections; (c), real projection data - real pseudoprojections.....	39
2.4.1.	Illustration of the Fourier slice theorem. The Fourier transform of $f(t)$ gives the values along the dashed line in the uv -plane.....	42
3.1.1.	CT detector system. B - radiation beam, D - detector, M - attenuating material	46
3.1.2.	Transfer characteristic of typical photoelectronic detector.....	48
3.1.3.	Illustration of the partial volume effect.....	50
3.2.1.	A comparison between the exact Poisson distribution and the Gaussian approximation to it for $\langle K \rangle = 3; 5$	58
3.2.2.	A comparison between the exact Poisson distribution and the Gaussian approximation to it for $\langle K \rangle = 10; 15$	59
3.3.1(a).	The reference image "dolls".....	62
3.3.1(b).	The sinogram of the reference image "dolls". 35 parallel projections equally spaced over 180°	63
3.3.2.	(a), Noisy sinogram that was produced from the reference sinogram in Fig. 3.3.1(b); (b), Noise that was superimposed on the reference sinogram to produce Fig. 3.3.2(a).....	64
3.3.3.	The Fourier spectra of: (a), the reference sinogram in Fig. 3.3.1(b), and (b), the noisy one in Fig. 3.3.2(a).....	65
3.3.4.	Photon range $10^3 - 10^4$. (a), Noisy sinogram, and (b), its Fourier spectrum,.....	66
3.3.5.	Photon range $10^2 - 10^3$. (a), Noisy sinogram, and (b), its Fourier spectrum.....	67
3.3.6.	Photon range $10 - 10^2$. (a), Noisy sinogram, and (b), its Fourier spectrum.....	68

3.3.7.	IART reconstructions from: (a), noisy sinogram in Fig. 3.3.2(a), and (b), noisy sinogram in Fig. 3.3.4(a).....	69
3.3.7contd.	IART reconstructions from: (c), noisy sinogram in Fig. 3.3.5(a), and (d), noisy sinogram in Fig. 3.3.6(a).....	70
3.3.8.	The 6 iteration IART reconstruction from the reference sinogram in Fig. 3.3.1(b).....	71
3.3.9.	The ratio of a random computed number k of a distribution with a mean $\langle K \rangle$ to the mean of the distribution as a function of a mean. One sample at each value of the mean was taken.....	71
3.4.1.	Hamming window with a cut off frequency $f_c = 0.5$	75
3.4.2.	Method of designating a Butterworth filter.....	77
3.4.3.	IART reconstruction images from (a), noisy, and (b), filtered with Hamming window with $\alpha = 0.54$ sinograms of $10^4 - 10^5$ photon count range.....	80
3.4.4.	IART reconstruction images from (a), noisy, and (b), filtered with Hamming window with $\alpha = 0.54$ sinograms of $10^3 - 10^4$ photon count range.....	81
3.4.5.	IART reconstruction images from (a), noisy, and (b), filtered with Hamming window with $\alpha = 0.54$ sinograms of $10^2 - 10^3$ photon count range.....	82
3.4.6.	IART reconstruction images from (a), noisy, and (b), filtered with Hamming window with $\alpha = 0.54$ sinograms of $10 - 10^2$ photon count range.....	83
3.5.1(a).	The reference image "head".....	86
3.5.1(b).	The sinogram of the reference image "head". 45 parallel projections equally spaced over 180°	87
3.5.2.	(a), Noisy sinogram that was produced from the reference sinogram in Fig. 3.5.1(b); (b), Noise that was superimposed on the reference sinogram to produce Fig. 3.5.2(a).....	88
3.5.3.	The Fourier spectra of (a), the reference sinogram in Fig. 3.5.1(b), and (b), the noisy one in Fig. 3.5.2(a).....	89
3.5.4.	IART reconstructions from (a), the reference sinogram in Fig. 3.5.1(b), and (b), the noisy sinogram in Fig. 3.5.2(a).....	90
3.5.4(c).	IART reconstruction from the noise filtered sinogram with Hamming window with $a = 0.8$	91
4.2.1.	(a) Reference image "dolls", 128 x 128 pixels; (b) Fourier spectrum of "dolls".....	97
4.2.2.	Parallel beam geometry, 35 projection directions equally spaced over 180° . Reconstruction of "dolls" using: (a), Fourier Backprojection (FBP); (b), Interpolative Algebraic Reconstruction Techniques (IART) (21 iterations).....	98
4.2.3.	Fourier spectrum of: (a), Fig. 4.2.2(a), FBP reconstruction of "dolls"; (b), Fig. 4.2.2(b), IART (21 iterations) reconstruction of "dolls".....	99
4.2.4.	Sobel edge enhancement filter with a 3 x 3 pixel window used on: (a), Fourier spectrum in Fig. 4.2.3(a); (b), Fourier spectrum in Fig. 4.2.3(b).....	100
4.2.5.	Fourier phase of: (a), reference image "dolls"; (b), FBP reconstruction of "dolls".....	101
4.2.5(c).	Fourier phase of IART reconstruction of "dolls" (21 iterations).....	102

4.3.1.	Fourier spectrum as a quantitative measure in reconstruction: (a), FBP, subtraction of Fig. 4.2.3(a) from Fig. 4.2.1(b); (b), IART, subtraction of Fig. 4.2.3(b) from Fig. 4.2.1(b).....	105
4.3.2.	Subtraction of Fourier phase images: (a), FBP, Fig. 4.2.4(b) from Fig. 4.2.4(a); (b), IART, Fig. 4.2.4(c) from Fig. 4.2.4(a).....	106
4.4.1.	IART, 3 iterations, parallel geometry beam, 35 projection directions equally spaced over 180° : (a), Reconstruction image, (b), corresponding Fourier spectrum.....	108
4.4.2.	IART, 9 iterations, parallel geometry beam, 35 projection directions equally spaced over 180° : (a), Reconstruction image, (b), corresponding Fourier spectrum.....	109
4.4.3.	IART, 18 iterations, parallel geometry beam, 35 projection directions equally spaced over 180° : (a), Reconstruction image, (b), corresponding Fourier spectrum.....	110
4.4.4.	Fourier spectrum as a convergence criterion for IART. Subtraction images after: (a), 3 iterations; (b), 9 iterations.....	111
4.4.4(c).	Fourier spectrum as a convergence criterion for IART. Subtraction image after 18 iterations.....	112
5.2.1.	ROC curves for two reconstruction methods, with Method 1 yielding superior results.....	120
5.3.1.	The reference image "squares". Superposition of squares.....	123
5.3.2.	The reference image "ellipses". Superposition of ellipses.....	123
5.3.3.	Reconstruction of the reference image "squares" from 60 parallel projections with simulated photon noise equally spaced over 180° : (a), IART, and (b), IART with filtered projections. X-ray source intensity = 10^6 emitted photons per measurement, difference in attenuation coefficients = 10%.....	124
5.3.4.	Reconstruction of the reference image "squares" from 35 parallel projections with simulated photon noise equally spaced over 180° : (a), IART, and (b), IART with filtered projections. X-ray source intensity = 10^6 emitted photons per measurement, difference in attenuation coefficients = 10%.....	125
5.3.5.	Reconstruction of the reference image "squares" from 19 parallel projections with simulated photon noise equally spaced over 180° : (a), IART, and (b), IART with filtered projections. X-ray source intensity = 10^6 emitted photons per measurement, difference in attenuation coefficients = 10%.....	126
5.3.6.	Fourier spectra of the reference object: (a), "squares" with $\partial\mu = 10\%$, and (b), "ellipses" with $\partial\mu$'s as in Table 5.3.7.....	130
5.3.7.	The subtraction, from the Fourier spectrum of "squares" in Fig. 5.3.6(a), of the Fourier spectrum of the 60 projection image of: (a), IART of Fig. 5.3.3(a); (b), IART with filtered projections of Fig. 5.3.3(b).....	131
5.3.8.	The subtraction, from the Fourier spectrum of "squares" in Fig. 5.3.6(a), of the Fourier spectrum of the 35 projection image of: (a), IART of Fig. 5.3.4(a); (b), IART with filtered projections of Fig. 5.3.4(b).....	132
5.3.9.	The subtraction, from the Fourier spectrum of "squares" in Fig. 5.3.6(a), of the Fourier spectrum of the 19 projection image of: (a), IART of Fig. 5.3.5(a); (b), IART with filtered projections of Fig. 5.3.5(b).....	133
5.3.10.	Reconstruction of the reference image "squares" from 60 parallel projections with simulated photon noise equally spaced over 180° : (a), IART, and (b), IART with filtered projections. X-ray source intensity = 10^4 emitted photons per measurement, difference in attenuation coefficients = 15%.....	139

5.3.11.	Reconstruction of the reference image "squares" from 35 parallel projections with simulated photon noise equally spaced over 180^0 : (a), IART, and (b), IART with filtered projections. X-ray source intensity = 10^4 emitted photons per measurement, difference in attenuation coefficients = 15%.....	140
5.3.12.	Reconstruction of the reference image "squares" from 19 parallel projections with simulated photon noise equally spaced over 180^0 : (a), IART, and (b), IART with filtered projections. X-ray source intensity = 10^4 emitted photons per measurement, difference in attenuation coefficients = 15%.....	141
5.3.13.	The subtraction, from the Fourier spectrum of "squares" with $\partial\mu = 15\%$, of the Fourier spectrum of the 60 projection image of: (a), IART of Fig. 5.3.10(a); (b), IART with filtered projections of Fig. 5.3.10(b).....	142
5.3.14.	The subtraction, from the Fourier spectrum of "squares" with $\partial\mu = 15\%$, of the Fourier spectrum of the 35 projection image of: (a), IART of Fig. 5.3.11(a); (b), IART with filtered projections of Fig. 5.3.11(b).....	143
5.3.15.	The subtraction, from the Fourier spectrum of "squares" with $\partial\mu = 15\%$, of the Fourier spectrum of the 19 projection image of: (a), IART of Fig. 5.3.12(a); (b), IART with filtered projections of Fig. 5.3.12(b).....	144
5.3.16.	Reconstruction of the reference image "ellipses" from 60 parallel projections with simulated photon noise equally spaced over 180^0 : (a), IART, and (b), IART with filtered projections. X-ray source intensity = 10^4 emitted photons per measurement, difference in attenuation coefficients as in Table 5.3.7.....	147
5.3.17.	Reconstruction of the reference image "ellipses" from 35 parallel projections with simulated photon noise equally spaced over 180^0 : (a), IART, and (b), IART with filtered projections. X-ray source intensity = 10^4 emitted photons per measurement, difference in attenuation coefficients as in Table 5.3.7.....	148
5.3.18.	Reconstruction of the reference image "ellipses" from 19 parallel projections with simulated photon noise equally spaced over 180^0 : (a), IART, and (b), IART with filtered projections. X-ray source intensity = 10^4 emitted photons per measurement, difference in attenuation coefficients as in Table 5.3.7.....	149
5.3.19.	The subtraction, from the Fourier spectrum of "ellipses" in Fig. 5.3.6(b), of the Fourier spectrum of the 60 projection image of: (a), IART of Fig. 5.3.16(a); (b), IART with filtered projections of Fig. 5.3.16(b).....	151
5.3.20.	The subtraction, from the Fourier spectrum of "ellipses" in Fig. 5.3.6(b), of the Fourier spectrum of the 35 projection image of: (a), IART of Fig. 5.3.17(a); (b), IART with filtered projections of Fig. 5.3.17(b).....	152
5.3.21.	The subtraction, from the Fourier spectrum of "ellipses" in Fig. 5.3.6(b), of the Fourier spectrum of the 19 projection image of: (a), IART of Fig. 5.3.18(a); (b), IART with filtered projections of Fig. 5.3.18(b).....	153
6.2.1.	The FBP reconstruction of the reference image "squares" from 60 parallel projections with simulated photon noise equally spaced over 180^0 . X-ray source intensity = 10^6 emitted photons per measurement; difference in the attenuation coefficient = 10%.....	163
6.2.2.	The FBP reconstruction of the reference image "squares" from 35 parallel projections with simulated photon noise equally spaced over 180^0 . X-ray source intensity = 10^6 emitted photons; difference in the attenuation coefficient = 10%	163
6.2.3.	The FBP reconstruction of the reference image "squares" from 19 parallel projections with simulated photon noise equally spaced over 180^0 . X-ray source intensity = 10^6 emitted photons per measurement; difference in the attenuation coefficient = 10%.....	164

6.2.4.	The subtraction of the Fourier spectrum of the 60 projection FBP image from the Fourier spectrum of "squares" in Fig. 5.3.6(a)	164
6.2.5.	The subtraction of the Fourier spectrum of the 35 projection FBP image from the Fourier spectrum of "squares" in Fig. 5.3.6(a)	165
6.2.6.	The subtraction of the Fourier spectrum of the 19 projection FBP image from the Fourier spectrum of "squares" in Fig. 5.3.6(a)	165
6.2.7.	The FBP reconstruction of the reference image "ellipses" from 60 parallel projections with simulated photon noise equally spaced over 180° . X-ray source intensity = 10^4 emitted photons per measurement; difference in the attenuation coefficient as in Table 5.3.7.....	166
6.2.8.	The FBP reconstruction of the reference image "ellipses" from 35 parallel projections with simulated photon noise equally spaced over 180° . X-ray source intensity = 10^4 emitted photons; difference in the attenuation coefficient as in Table 5.3.7.....	166
6.2.9.	The FBP reconstruction of the reference image "ellipses" from 19 parallel projections with simulated photon noise equally spaced over 180° . X-ray source intensity = 10^4 emitted photons per measurement; difference in the attenuation coefficient as in Table 5.3.7.....	167
6.2.10.	The subtraction of the Fourier spectrum of the 60 projection FBP image from the Fourier spectrum of "ellipses" in Fig. 5.3.6(b).....	167
6.2.11.	The subtraction of the Fourier spectrum of the 35 projection FBP image from the Fourier spectrum of "ellipses" in Fig. 5.3.6(b).....	168
6.2.12.	The subtraction of the Fourier spectrum of the 19 projection FBP image from the Fourier spectrum of "ellipses" in Fig. 5.3.6(b).....	168
7.2.1.	(a), reference image and (b), its MRT reconstruction from 10 parallel beam projection directions equally spaced over 180°	181

LIST OF TABLES

2.1.1.	Component ellipses of the reference image in Fig. 2.1.6.....	17
3.3.1.	Reference image "dolls". Correlation coefficients for noisy sinograms of different ranges of photon counts and for the reconstruction images they produce	61
3.4.1.	Reference image "dolls". Correlation coefficient for a sinogram filtered with real space filters. Photon count range $10^4 - 10^5$	74
3.4.2.	Reference image "dolls". Correlation coefficient for a sinogram filtered with generalized Hamming window. Photon count range $10^4 - 10^5$	76
3.4.3.	Reference image "dolls". Correlation coefficients for noisy and filtered with Hamming window sinograms of different ranges of photon counts	78
3.4.4.	Reference image "dolls". Correlation coefficients for a reconstruction image from noisy sinograms and filtered with a Hamming window for different ranges of photon counts.....	79
3.5.1.	Reference image "head". Correlation coefficient for a sinogram filtered with generalized Hamming window	85
4.4.1.	Correlation coefficients for the sequence of IART reconstructions of the reference object "dolls"	112
5.3.1.	Computed quantitative similarity measures of Eq. (5.2-1) for the reconstruction images of the "squares" reference image from simulated noisy projection data. Case: $\partial\mu = 10\%$, source intensity = 10^6 emitted photons per measurement.....	127
5.3.2.	Computed quantitative similarity measures of Eq. (5.2-1) for the reconstruction images of the "squares" reference image from simulated noisy projection data. Case: $\partial\mu = 10\%$, source intensity = 10^4 emitted photons per measurement.....	128
5.3.3.	Computed quantitative similarity measures of Eq. (5.2-1) for the reconstruction images of the "squares" reference image from simulated noisy projection data. Case: $\partial\mu = 10\%$, source intensity = 10^2 emitted photons per measurement.....	129
5.3.4.	Computed quantitative similarity measures of Eq. (5.2-1) for the reconstruction images of the "squares" reference image from simulated noisy projection data. Case: $\partial\mu = 15\%$, source intensity = 10^6 emitted photons per measurement.....	136
5.3.5.	Computed quantitative similarity measures of Eq. (5.2-1) for the reconstruction images of the "squares" reference image from simulated noisy projection data. Case: $\partial\mu = 15\%$, source intensity = 10^4 emitted photons per measurement.....	137
5.3.6.	Computed quantitative similarity measures of Eq. (5.2-1) for the reconstruction images of the "squares" reference image from simulated noisy projection data. Case: $\partial\mu = 15\%$, source intensity = 10^2 emitted photons per measurement.....	138
5.3.7.	The reference image "ellipses". Attenuation coefficients of the constituent ellipses.....	145
5.3.8.	Computed quantitative similarity measures of Eq. (5.2-1) for the reconstruction images of the "ellipses" reference image from simulated noisy projection data.....	150
6.2.1.	Computed quantitative similarity measures of Eq. (5.2-1) for the reconstruction images of the "squares" reference image from simulated noisy projection data. Case: $\partial\mu = 10\%$, source intensity = 10^6 emitted photons per measurement.....	162

- 6.2.2. Computed quantitative similarity measures of Eq. (5.2-1) for the reconstruction images of the "ellipses" reference image from simulated noisy projection data. X-ray source intensity = 10^4 emitted photons per measurement..... 162
- 6.3.1. Cumulative quantitative similarity measures of Eq. (5.2.1) for reconstruction images of the "squares" reference image from simulated noisy projection data. Case: $\partial\mu = 10\%$, source intensity = 10^6 emitted photons per measurement 170
- 6.3.2. Cumulative quantitative similarity measures of Eq. (5.2.1) for reconstruction images of the "ellipses" reference image from simulated noisy projection data. Source intensity = 10^4 emitted photons per measurement..... 171

CHAPTER I

INTRODUCTION

1.1. Thesis Objective

Nowadays, imaging has grown to play an important role in medicine. X-rays are used for diagnostic as well as for screening purposes (routine chest films, mammography, routine dental films, etc.). High quality computed tomography images with high resolution are in high demand. To obtain such, a number of projections is required. The more the better. But one must remember that every projection taken means delivering a certain radiation dose to a patient. The total dose resulting from the examination is directly proportional to the number of projections taken. There are three potential hazards that can result from diagnostic x-rays [Hall, 1978]:

a) Genetic mutations may be greatly increased in future generations because approximately half of the population receives x-rays annually,

b) The risk of cancer or leukemia may be increased in the patients themselves who receive multiple x-rays,

c) Anomalies and/or malignancies may be produced in children irradiated *in utero*.

The risk of cancer produced by x-ray exposure is increased even further for human organs that are most sensitive to radiation carcinogenesis, like the thyroid or the female breast. Especially the latter is one of the body tissues known to be particularly susceptible to radiation-induced cancer [Recommendations of ICRP, 1977], [Report of NIH, 1985]. Studies of different exposed populations have yielded consistent results. As observations at low dose levels are difficult, the risk associated with low dose exposures is usually estimated from higher dose data. These included Japanese survivors of atomic bombings of

Hiroshima and Nagasaki [Tokunaga, 1979], as well as North American sanatoria patients from Massachusetts [Boice, 1977] and Canada [Howe, 1984], [MacKenzie, 1965] who underwent multiple chest fluoroscopies during treatment for pulmonary tuberculosis, and groups of patients treated with radiotherapy for postpartum mastitis in Rochester, New York [Shore, 1977] and other benign breast conditions in Sweden [Baral, 1977]. The most important resulting finding was that linearity or near-linearity, appeared to describe the dose-response relationship for breast tissue doses over a very wide range, including the lower end of scale [Land, 1980], [MacKenzie, 1965], [Boice, 1977], [Tokunaga, 1979], [Shore, 1977]. The significance of linearity for radiation protection is that excess risk from low-dose exposures can be estimated with some confidence from high-dose data. A second important finding was that the distribution over time after exposure of radiation-induced breast cancer risk conformed to age-specific population rates [Land, 1977], [Land, 1978], [McGregor, 1977], [Land, 1980]. The time of clinical appearance of both radiation-induced and other breast cancers seemed to be determined by factors related to age, and it may be well that these factors influence when and whether cancer occurs. Another major finding was that breast tissue seemed to be the most sensitive to radiation carcinogenesis during the second decade of life [Boice, 1977], [Boice, 1978], [McGregor, 1977], [Tokunaga, 1979]. The influence of age at exposure on the risk of breast cancer may be explainable in terms of hormonal levels and breast development. There is some evidence of increased sensitivity to radiation induced cancer at menarche and just before [Boice, 1977], [Boice, 1978], [McGregor, 1977], [Tokunaga, 1979] and during pregnancy [Boice, 1978].

During our lifetime we accumulate all the doses that have been delivered to us, i.e. , every time we undergo x-ray examination we add to our cumulative dose. Therefore, for the patient's sake, the amount delivered during a single examination should be as small as possible. That is in contradiction to the requirements for a high resolution image.

Finding an answer to the problem of how to obtain a satisfactory high quality image from a limited number of views would be the ideal solution to the above mentioned dilemma.

This thesis addresses the above problem by introducing a new reconstruction method for limited number of views and working on improvement of reconstruction image quality from it. A novel approach to relate pixels to projections has been used. The new algorithm adapts equations of Algebraic Reconstruction Techniques that have already been proven to work well on incomplete projection data [Oskoui-Fard, 1988], [Andersen, 1989], [Peng, 1989]. The method that is suggested has the considerable advantage of complying with real conditions. It has been shown that it works equally well for parallel and fan beam geometry. Moreover, it can be easily generalized to three dimensions.

Another new reconstruction method is also suggested, that can be used with any number of projections, including very few and from the limited sector of directions. The method, Matching Reconstruction Technique, uses totally a new approach and looks promising.

1.2. Outline of the Thesis

Chapter II covers the description of the new reconstruction algorithm, Interpolative Algebraic Reconstruction Technique, (IART), its variation that is suggested to improve image quality, and also an overview of the Fourier Backprojection algorithm, (FBP), that was used in this study as a reference method for comparison. In this chapter, also results of an analysis are included of how to best handle round-off errors on our computer. The IART algorithm was used for testing.

Chapter III discusses sources of noise in computed tomography. A procedure for the simulation of photon noise is presented along with results obtained using different method

of filtering out the noise from the projections. The filtered projections subsequently were used as input data to the IART algorithm with positive results.

New ways of using the Fourier spectrum in a reconstruction process are presented in Chapter IV.

In Chapter V, a simulation procedure for CT data collection affected by photon noise is presented. The procedure was used for experiments of this chapter: Noisy and filtered projections were entered as input data to the IART method and the resulting images were evaluated for differences. To assess the images, several similarity methods were applied, discussion of which is included in Section 5.2.

Chapter VI contains results of the comparative study. The reconstruction images from different number of projections were evaluated and compared with respect to the applicability of the quantitative and qualitative criteria as evaluation measures. This is something new, as usually, the evaluation is done on images produced from the same number of projections [Herman, 1972], [Herman, 1973a], [Heffernan, 1983], [Oskoui, 1989], [Ollinger, 1988], [Suzuki, 1988], [Cho, 1975]. The analysis includes images from IART and Fourier backprojection reconstruction methods. This study also were extended to verify the use of similarity measures to compare images from IART and FBP for the same input set of projection data.

In Chapter VII, a description of another new reconstruction method that uses the simulated annealing optimization technique is given. The algorithm is suitable for reconstruction from incomplete projection data (all cases), as well as from the full set of projections. Preliminary results are presented. The method still requires refinement and further investigation.

Concluding remarks and discussion of future work are in Chapter VIII.

CHAPTER II

RECONSTRUCTION METHODS

2.1. Interpolative Algebraic Reconstruction Techniques (IART)

2.1.1. Introduction

Algebraic Reconstruction Techniques (ART) were introduced by Gordon, Bender and Herman for solving what is now known as the computed tomography problem [Gordon, 1970]. They are based on an intuitive approach of smearing back each projection of the estimate of the object's optical density with repeated corrections until an agreement with the corresponding measured projections is reached.

All ART algorithms have the same basis, the partition of a reconstruction matrix into a set of rays $\{\delta_k\}$ through which the radiation traverses the object (Fig. 2.1.1.). Every radiation passage is represented by a projection value p_k :

$$p_k = \int_{\delta_k} f(\vec{r}) d\vec{r} \quad (2.1-1)$$

where \vec{r} represents the position vector of the centre of a pixel of the reconstruction matrix, and $f(\vec{r})$ is the unknown optical density function.

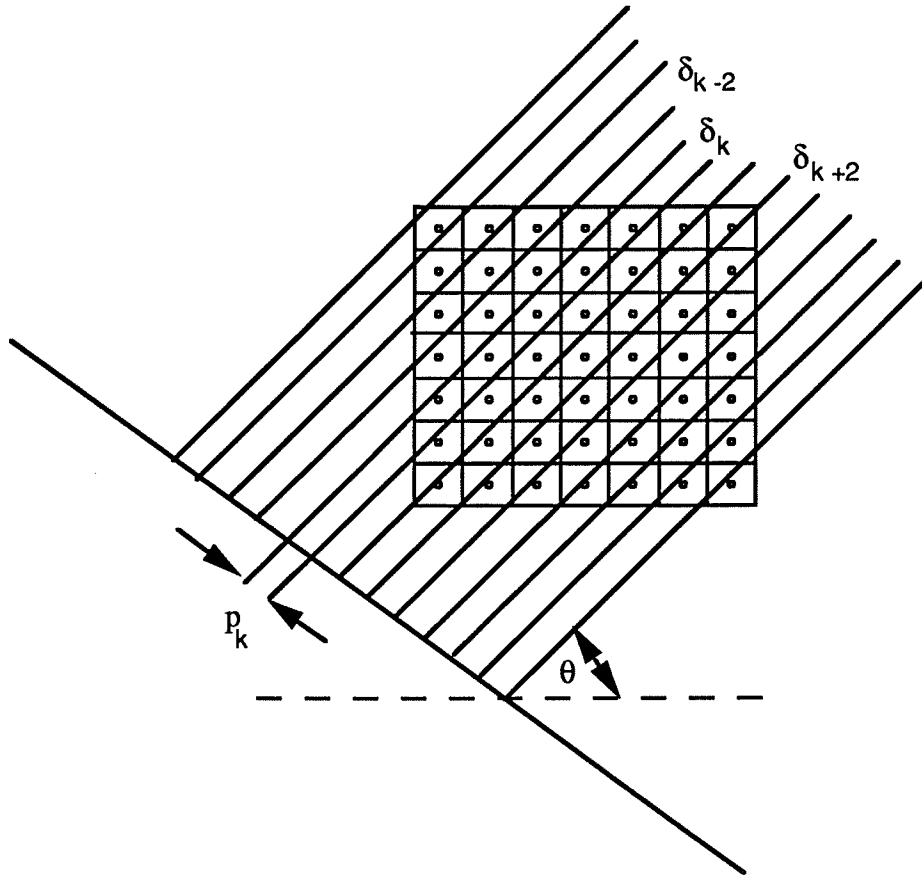


Fig. 2.1.1. $\{\delta_k\}$ - set of rays for the projection direction at the angle θ . Centroids represent the individual optical density pixels of the reconstruction matrix $\{\tilde{r}_{ij}\}$. Every radiation ray is represented by a projection value p_k .

The reconstruction is done over a set of pixels generally chosen in a regular array, to which we want to assign estimates $\tilde{f}(\tilde{r}_{ij})$ of $f(\tilde{r})$ such that:

$$p_k = \sum_{ij \in \delta_k} w_{ij} \tilde{f}(\tilde{r}_{ij}) \quad (2.1-2)$$

For every pixel, to obtain an approximation for the unknown function $f(\tilde{r})$, we estimate its value based on the fraction w_{ij} of the pixel covered by the ray and the values of the projections for that particular ray. The process is repeated many times until a convergence

criterion is met. (We are assuming uniform density of the radiation across a passage, though this could be taken into account by modifying the values of the w_{ij} 's.)

In order to make the calculations less cumbersome, in the parallel beam case for every projection direction the passage width can be chosen so that one pixel centroid per row is encountered, except for the last row [Herman, 1973], [Gordon, 1974]. The assumption that centroids can replace pixels simplifies the procedure, as for every projection direction we only need to find which centroids belong to which ray. (That is if we disregard the edge or "partial volume" effect [Gordon, 1974].) This eases a little the pain of calculating for every pixel and for every projection direction how much of the pixel is being covered, and by which of the rays. However, it requires that during the reconstruction process, for every projection direction one has to calculate the width of the ray δ_k , as well as to record or recalculate which centroids belong to which rays.

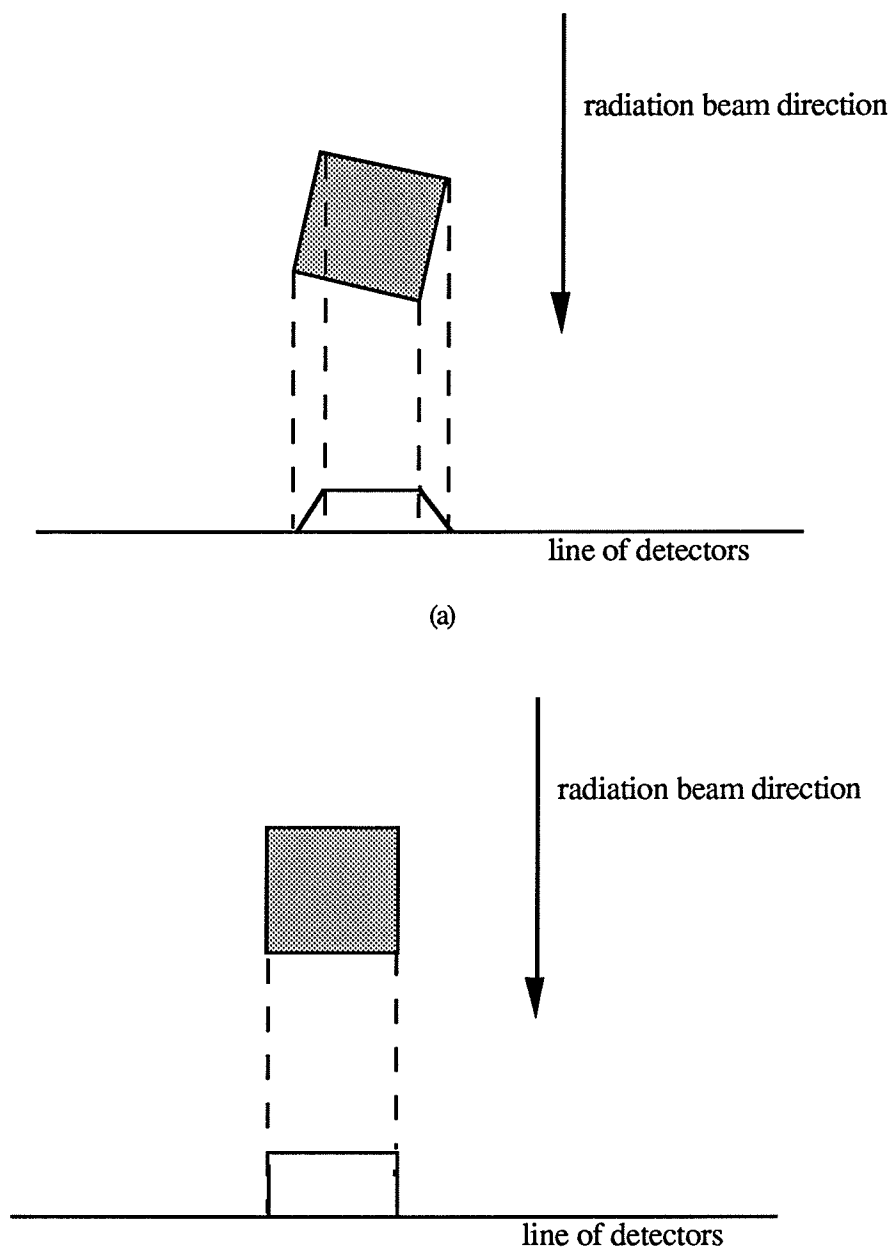
This thesis introduces a new method to relate the pixels to their projections that is more suitable for data from detectors of unchanging width, which is the practical case. Unlike the centroid approach, the new method is, moreover, readily applicable to both parallel and diverging beam geometry.

2.1.2. Relating Pixels to Projections without Beam Partitioning

In a computed tomography scanner, when the radiation beam passes through an object or patient, it produces readings on a line of detectors behind the object. In order to find out the relationship between the individual pixels of the reconstruction matrix and the line of detectors we use the shadow cast by the pixel on the line of detectors (Fig. 2.1.2.). By evaluating how much of the shadow is covered by which of the detectors, we estimate the contribution of the optical density of the element to the detectors involved. We can do the calculations either by very accurately estimating the shape of the shadow for every projection direction ("accurate" interpolation), or by making an assumption that the shadow

will be of the same rectangular shape regardless of projection direction. The latter is equivalent to rotating the pixel so that it is aligned with the projection direction, so we will call it the "rotation" interpolation. With accurate interpolation, the shadow will change its shape from rectangular through trapezoid to triangular depending on the angle of a projection direction. With the rotation interpolation, the shadow of a pixel is always the same rectangle. Since the shapes of pixels are artifacts of our digitization of images, consideration of alternative shapes for them seems reasonable.

Below, for both parallel and diverging beam, the description of the rotation interpolation is presented as this is the one that is expected to be more popular. Later in this chapter, it will be shown that results obtained using it differ only slightly from those obtained through the accurate interpolation, while the computation time is shorter.



(b)
Fig. 2.1.2. For a parallel geometry beam, estimation of a pixel shadow on the line of detectors using: accurate, (a), and rotation, (b), interpolation.

Parallel Geometry Beam

We start by projecting the center of the element onto the line of the detectors (Fig. 2.1.3).

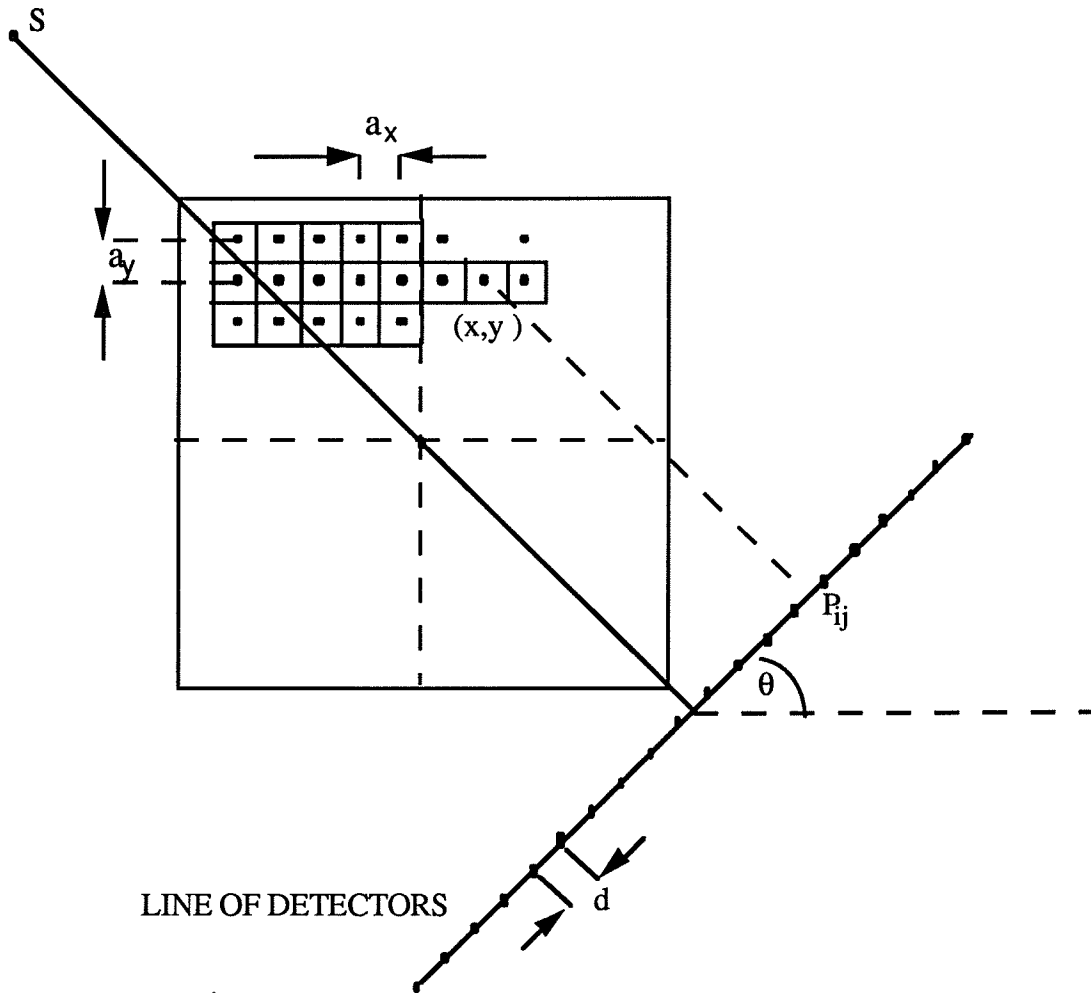


Fig. 2.1.3. Geometry of a parallel beam scanning system. The line at the angle θ represents the line of detectors for a projection direction $\theta + 90^\circ$. a_x , a_y - distance between pixel centers in a row and column of the backprojection matrix, respectively; d - detector width.

Let us assume that the (i,j) 'th pixel in the backprojection matrix is described by a pair of coordinates (x,y) such as

$$x = i a_x$$

$$y = j a_y$$

where a_x and a_y represent the horizontal and vertical distances between pixel centers in the matrix as in Fig. 2.1.3. Usually $a_x = a_y = a$. The position of the projection of the pixel center onto the projection line at angle θ is equal to

$$P_{ij} = (y \sin\theta + x \cos\theta) / d \quad (2.1-3)$$

where d is the detector width. The pixel will contribute to all detectors that are covered by its shadow. In practice, it is common and justified to set the reconstruction element size a equal to the detector width d . In that case, the pixel will contribute to a maximum of two detectors that are the closest to point P_{ij} . The portion of the element density that adds to a detector reading is calculated using the interpolation function

$$g_{ij}(u) = \left\{ \begin{array}{ll} 1 & \text{for } |u - P_{ij}| = 0 \\ d - |u - P_{ij}| & \text{for } 0 < |u - P_{ij}| \leq d \\ 0 & \text{for } |u - P_{ij}| > d \end{array} \right\} \quad (2.1-4)$$

where u represents the center of the detector, d the detector width and P_{ij} is the projection of the centroid of the (i,j) 'th pixel onto the detector line.

Fan Geometry Beam

Fan-beam scanning introduces the dependence of the pixel contribution on its distances from the radiation source and the detectors. Pixels that are closer to the source will contribute to more detector readings than those that are closer to the arc of detectors. Finding the detectors that receive radiation via the particular pixel can be achieved by calculating the shadow cast by this pixel on the line of detectors. The length and position of the shadow uniquely define detectors to which this particular pixel contributes.

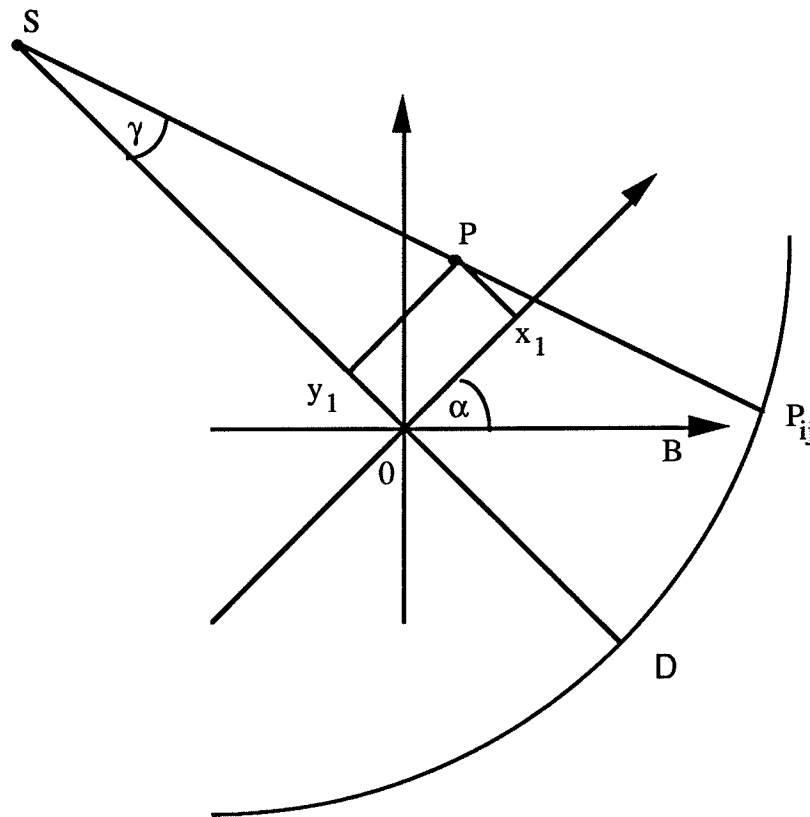


Fig. 2.1.4. Geometry of a fan beam scanning system. S - an x-ray source, P - center of the (i,j) 'th pixel, P_{ij} - center of the shadow cast by the (i,j) 'th pixel on the arc of detectors.

From the geometry of the system (Fig. 2.1.4.), we find the center of the shadow P_{ij} cast by (i,j) 'th object pixel:

$$\overline{DP}_{ij} = \overline{SD} \gamma \quad (2.1-5)$$

$$\gamma = \tan^{-1} \left(\frac{x_1}{\overline{SO} - y_1} \right)$$

$$y_1 = y \cos(\alpha) - x \sin(\alpha)$$

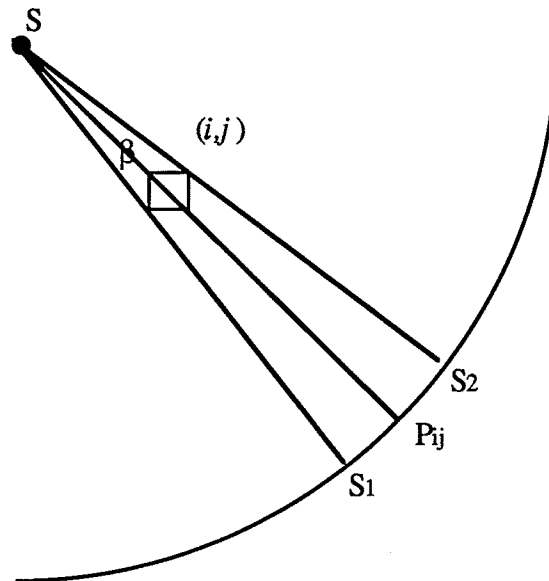


Fig. 2.1.5. Fan beam scanning system. Shadow cast by the (i,j) 'th pixel onto the detectors arc.

The length of the shadow (Fig. 2.1 5) is described by

$$\overline{s^2} = \overline{SD} \beta \quad (2.1-6)$$

$$\beta = 2 \tan^{-1}(a / (2 \overline{SP}))$$

where a is the pixel side,

$$\overline{SP} = x_1 / \sin(\gamma)$$

$$x_1 = x \cos(\alpha) + y \sin(\alpha)$$

Based on Equations (2.1-5) and (2.1-6), detectors that are affected by the (i,j) 'th pixel are found.

How much of the optical density of the pixel adds to each of the detector readings depends on the portion of the shadow that is covered by each of the detectors. We make an assumption that the pixel side a is equal to the detector width d , which is common and justified in practice, and further we express the system dimensions in units of the detector width. This allows us to use the following interpolation function $g_{ij}(u)$ to calculate the pixel contribution to the detector readings:

$$g_{ij}(u) = \begin{cases} \frac{1}{2h} & \text{for } |u - P_{ij}| \leq h - 0.5 \\ 1 - \frac{|u - P_{ij}| - (h - 0.5)}{2h} & \text{for } h - 0.5 < |u - P_{ij}| \leq h + 0.5 \\ 0 & \text{for } |u - P_{ij}| > h + 0.5 \end{cases} \quad (2.1-7)$$

where h equals one half of the shadow length $\overline{s^2}$ (Fig. 2.1.5.), u represents the position of the center of the detector, and P_{ij} is the center of the shadow.

2.1.3. Reconstruction Algorithm

Using the method in the above Section 2.1.2 to relate pixels to the projections, we can generalize that in both cases (parallel and diverging beam) projection values are calculated as

$$p_k = \sum_{i,j=1}^{\text{matrix size}} g_{ij}(u_k) f(\vec{r}_{ij}) \quad k \in \{1,2,\dots,N\} \quad (2.1-8)$$

where u_k is the position of (k)'th detector, $f(\vec{r}_{ij})$ represents the optical density of (i,j)'th pixel and N is the total number of detectors.

To compute the estimates of the unknown function $f(\vec{r})$ for an (i,j)'th object pixel, we can use basic ART equations altered to accommodate the interpolation function $g_{ij}(u)$. For example, the multiplicative ART equation:

$$\tilde{f}^{q+1}(\vec{r}_{ij}) = \frac{p_k}{p_k^q} \tilde{f}^q(\vec{r}_{ij}) \quad (2.1-9)$$

where superscripts $q+1$, q represent the ($q+1$)' and (q)'th estimates $\tilde{f}(\vec{r})$, and p_k and p_k^q are the measured and corresponding calculated projections, respectively, becomes

$$\tilde{f}^{q+1}(\vec{r}_{ij}) = \sum_{k=1}^N g_{ij}(u_k) \frac{p_k}{p_k^q} \tilde{f}^q(\vec{r}_{ij}) \quad (2.1-10)$$

where

$$\sum_{k=1}^N g_{ij}(u_k) = 1$$

and $g_{ij}(u_k)$ is the interpolation function. One increment of q means that all projections of each pixel have been considered once. The major difference between Equations (2.1-9) and (2.1-10) is that the former one is applied to every single ray of a projection while the latter refers to a whole projection.

To measure the convergence of the estimate $\tilde{f}^q(\tilde{r}_{ij})$, the discrepancy between the measured and corresponding calculated projections can be used

$$\Delta p_q = \sqrt{\frac{1}{N} \sum_{i=1}^N (p_k - p_k^q)^2} \quad (2.1-11)$$

2.1.4. Results

The new reconstruction algorithm was tested on a reference image illustrated in Fig. 2.1.6. The parameters of the constituent ellipses including grey levels are given in the Table 2.1.1. A major advantage of using an image like Fig. 2.1.6 for computer simulation is that one can write analytical expressions for the projections [Ekstrom, 1984].

Calculations were performed using Equation (2.1-9), for thirty projection directions equally spaced over the angle of 180° and 360° for parallel and diverging beam, respectively. The starting value of the estimate of the object optical density was chosen to be equal to 1, i.e. $\tilde{f}^0(\tilde{r}_{ij}) = 1$. The reference image and all reconstruction images were on 128×128 matrices.

All reconstructions were performed using a Macintosh II computer. Programs were written in the THINK Pascal language.

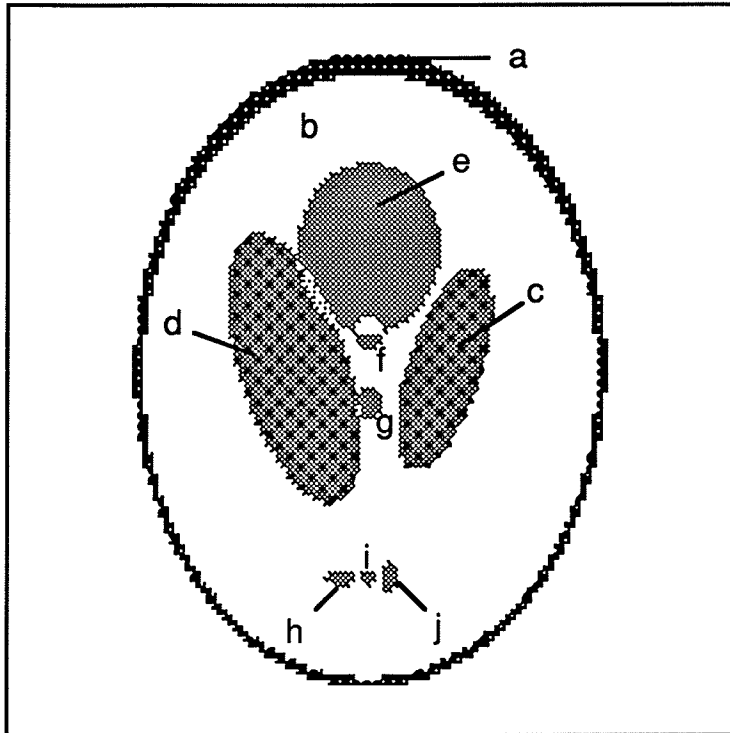


Fig. 2.1.6. The reference image, a superposition of 10 ellipses. At overlaps gray levels are added.

Table 2.1.1. Component ellipses of the reference image in Fig. 2.1.6.

Ellipse	Coordinates of the center	Major axis	Minor axis	Rotation angle	Gray level
a	0, 0	0.92	0.69	90°	300
b	0, -0.0184	0.874	0.6624	90°	2
c	0.22, 0	0.31	0.11	72°	98
d	-0.22, 0	0.41	0.16	108°	98
e	0, 0.35	0.25	0.21	90°	101
f	0, 0.1	0.046	0.046	0	101
g	0, -0.1	0.046	0.046	0	101
h	-0.08, -0.605	0.046	0.023	0	101
i	0, -0.605	0.023	0.023	0	101
j	0.06, -0.605	0.046	0.023	90°	101

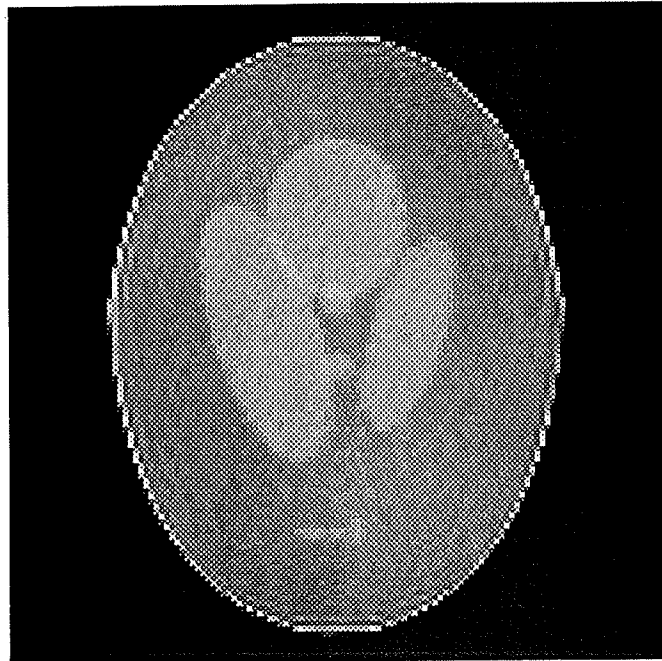
Parallel Beam Geometry

The reference image in Fig. 2.1.6 was reconstructed with at most 12 iterations, since the best quality reconstructed image was obtained after the sixth iteration. Afterwards the picture quality deteriorated (Fig. 2.1.7.).

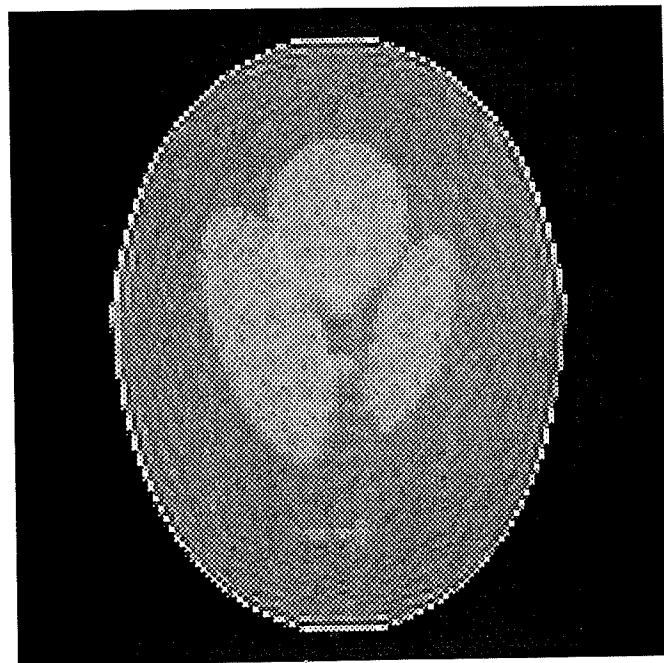
Two sets of reconstructed images were obtained using the fixed and rotated pixel interpolation functions. We used the correlation coefficient to assess how using the different versions of the interpolation function influence the resulting reconstructed picture. Visually, one can hardly see the difference (Figs. 2.1.8 - 9). For either version of the interpolation function, for different numbers of iterations, the resulting reconstructed images were evaluated against the reference image using the correlation coefficient similarity measure (see Section 5.2):

$$\varepsilon = \frac{\sum_{ij=1}^N (f_{ij} - \bar{f})(f_{ij}^* - \bar{f}^*)}{\left[\sum_{ij=1}^N (f_{ij} - \bar{f})^2 \sum_{ij=1}^N (f_{ij}^* - \bar{f}^*)^2 \right]^{1/2}} \quad (2.1-12)$$

where $N \times N$ is the size (in pixels) of either, reference and reconstruction, matrix; f_{ij} and f_{ij}^* represent the pixel intensity in the reference and the reconstruction images, respectively, and \bar{f} and \bar{f}^* is the average density of the reconstruction and reference images, respectively.

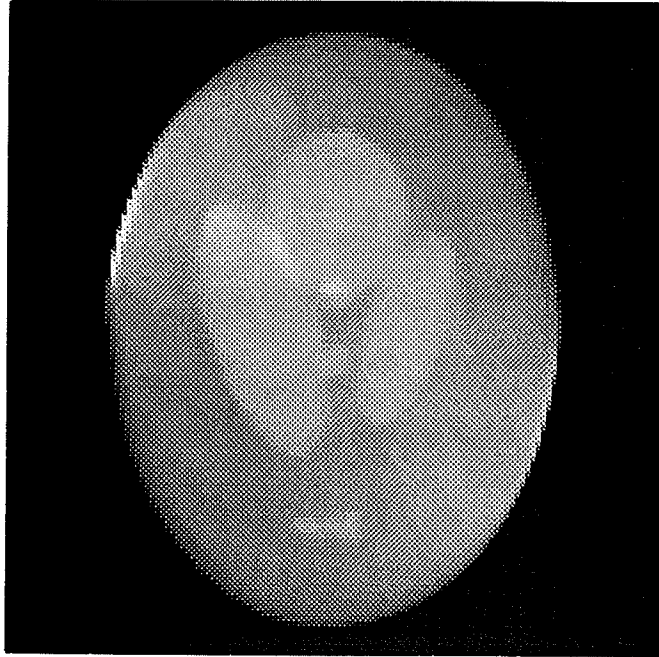


(a)

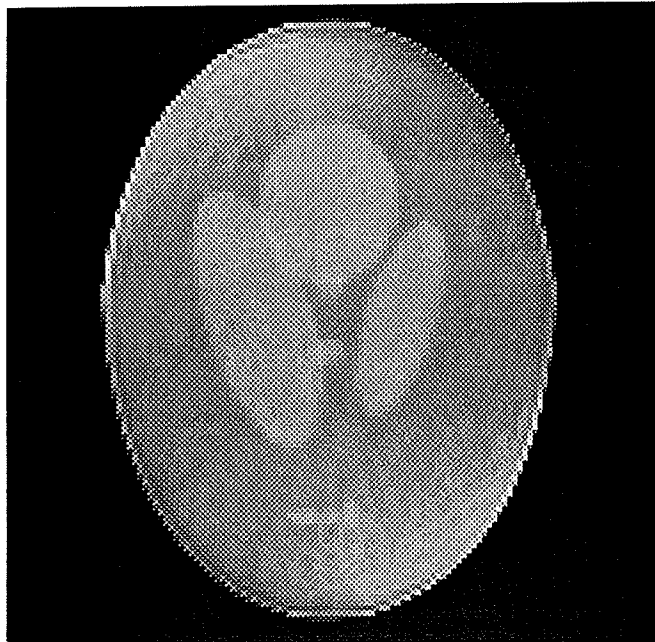


(b)

Fig. 2.1.7. Parallel beam, 30 projection directions equally spaced over 180° . IART reconstruction of Fig. 2.1.6 after: (a), six iterations; (b), nine iterations.



(a)

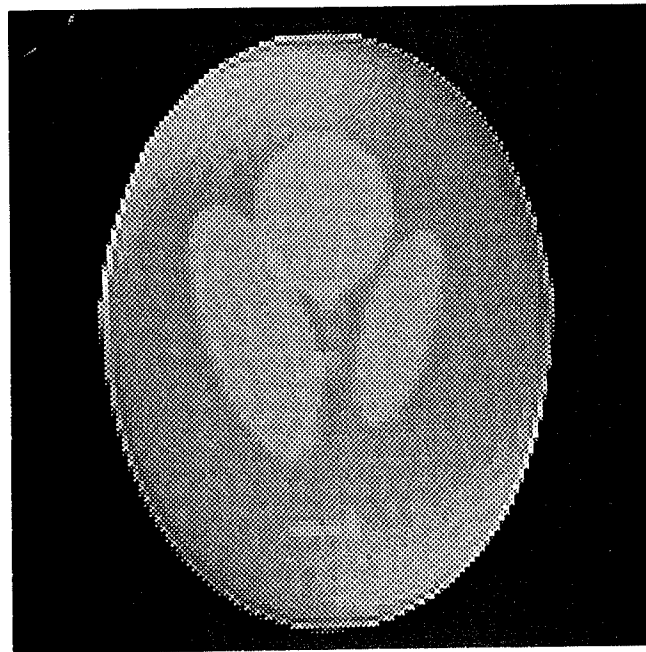


(b)

Fig. 2.1.8. Parallel beam, 30 projection directions equally spaced over 180° . IART reconstruction of Fig. 2.1.6 using the fixed pixel interpolation function after: (a), one iteration; (b), three iterations.



(a)



(b)

Fig. 2.1.9. Parallel beam, 30 projection directions equally spaced over 180° . IART reconstruction of Fig. 2.1.6 using the rotated pixel interpolation function after: (a), one iteration; (b), three iterations.

Results of the comparison are presented graphically in Fig. 2.1.10, in which it can be observed that using the fixed pixel interpolation function produces a slightly better reconstructed picture. The disadvantage of using it is longer calculation time. (Computation time for the fixed pixel interpolation function was approximately 1.5 times longer than when the rotated pixel interpolation was used.)

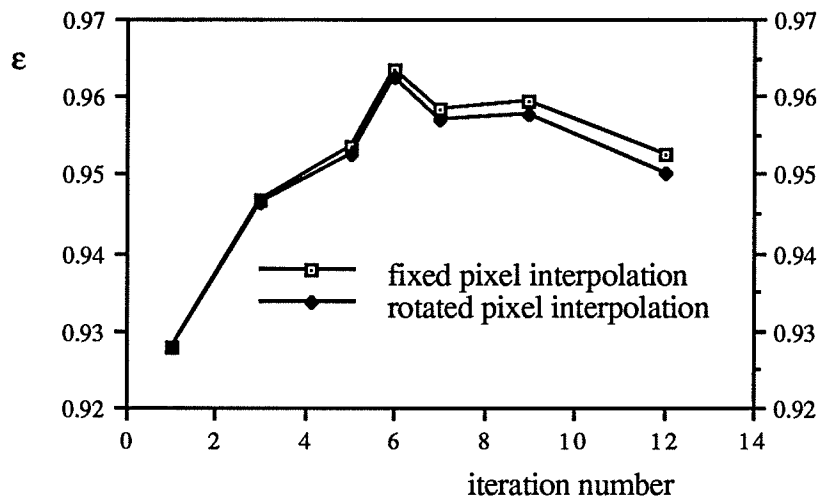


Fig. 2.1.10. Correlation coefficients computed for the IART reconstruction images. (Parallel geometry beam.)

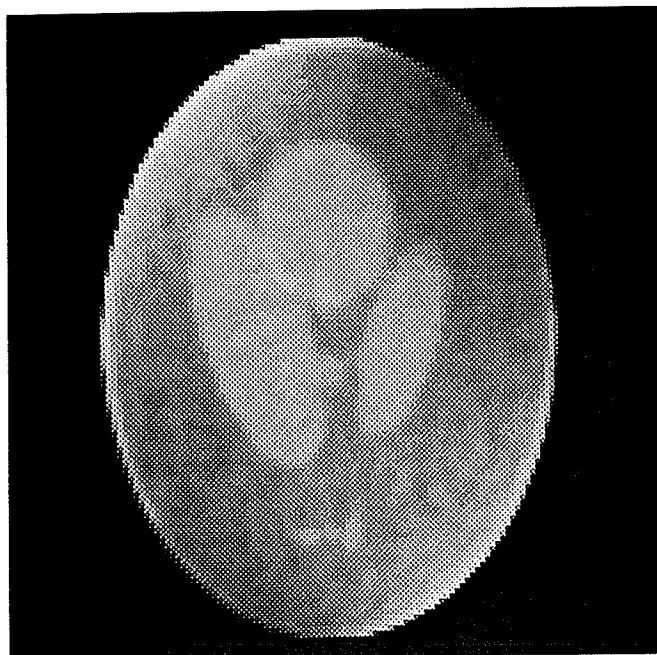
Fan Beam

The geometry system as depicted in Fig. 2.1.4 was used. The detector length was equal to one unit of length, the distances from the origin to the source \overline{SO} and the detector arc \overline{OD} were 300 and 80 units, respectively.

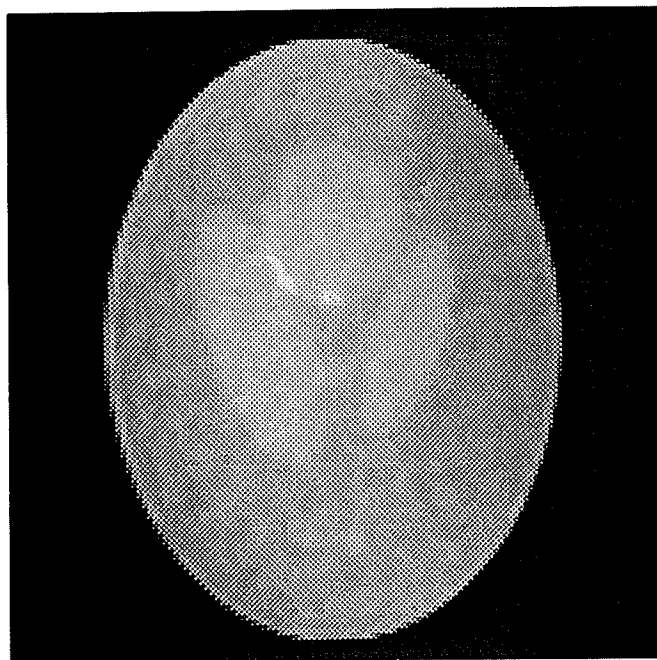
The best reconstruction was obtained after three iterations. Thus no more than four iterations are shown, since, in our experience, the error function ϵ has at most one peak. The reconstructed pictures are presented in Fig. 2.1.11 - 12.

For comparison with a standard algorithm, using the same data, the reconstruction of the reference image in Fig. 2.1.6 was computed using the fan beam Fourier Backprojection (FBP) method with a Shepp & Logan kernel [Rosenfeld, 1982] (Fig. 2.1.13.) Correlation coefficients for images computed using IART (3 iterations) and FBP methods were respectively $\epsilon = 0.995$ and 0.975 , showing that IART gave a substantial improvement as the figures visually suggest.

The computing time for the Fourier Backprojection method was comparable to a single iteration of IART.



(a)

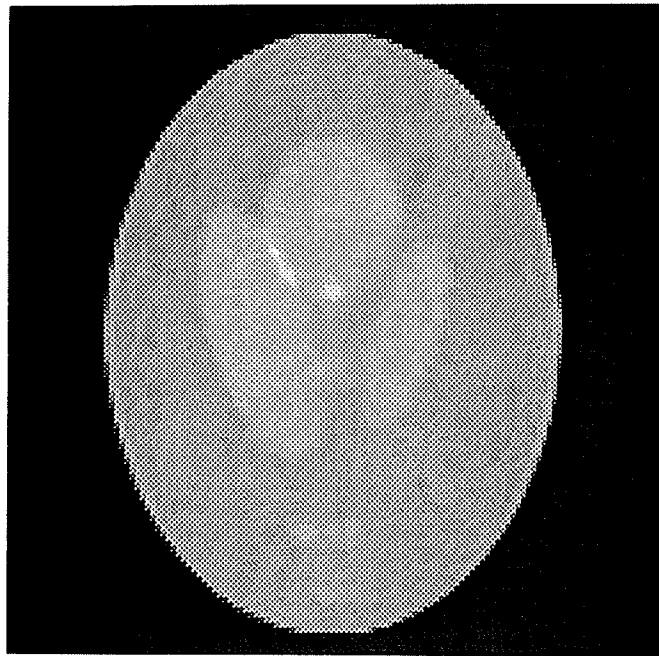


(b)

Fig. 2.1.11. Fan beam, 30 projection directions equally spaced over 360° . IART reconstruction of Fig. 2.1.6 after: (a), one iteration; (b), two iterations.



(a)



(b)

Fig. 2.1.12. Fan beam, 30 projection directions equally spaced over 360° . IART reconstruction of Fig. 2.1.6 after: (a), three iterations; (b), four iterations.

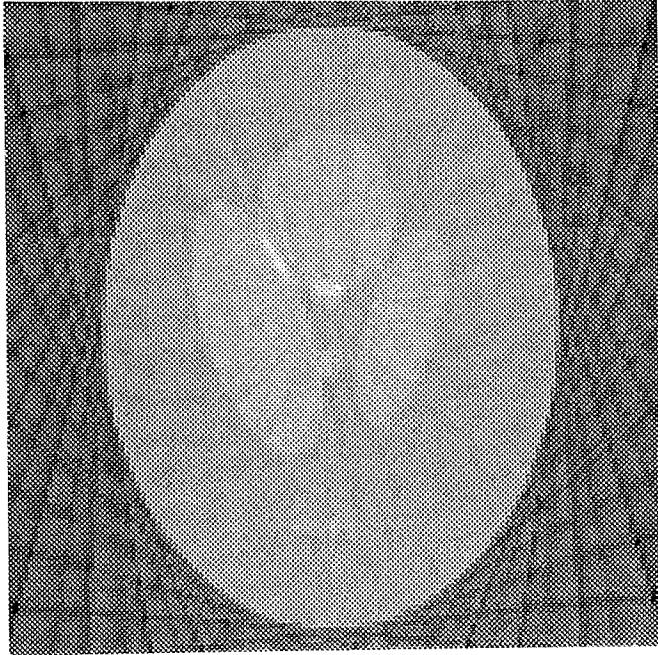


Fig. 2.1.13. Reconstruction of Fig. 2.1.6 using Fourier Backprojection method. 30 projection directions equally spaced over 360° .

2.1.5. Discussion and Conclusions

A good reconstruction method should not introduce any false detail into an image and the density values at adjacent points should vary as smoothly as possible in a manner which is consistent with the projection data. In the ART algorithm errors are introduced due to the way the estimates of the unknown function $f(\vec{r})$ for an (i,j) 'th object pixel are computed: ART formulas are applied to every single ray of a given projection at angle θ and then are used in the same manner for the next projection, and so on. This way even for the same projection, the estimate $\tilde{f}(\vec{r}_{ij})$ of the (i,j) 'th pixel that is included in more than one ray is being readjusted many times depending on the ray number the pixel is covered by. In

addition, in case of the additive ART [Gordon, 1970], [Gordon, 1974], the correction made to the single pixel estimate depends on the number of reconstruction matrix pixels included in a given ray which varies according to the angle of the projection. Assume a square $N \times N$ reconstruction matrix that is composed of small square pixels. Thus a ray of the width of the size of a single pixel will contain roughly N pixels, i.e. the number equal the size of a reconstruction matrix at $\theta = 0$. But when $\theta = \pi/4$ the ray can contain as many as $\sqrt{2}N$ pixels, or as few as one pixel, or a fraction of it depending on the position of the ray. There is a similar effect for rays of projections at angles between these two extremes. All these cause errors in ART algorithms when rays of the pixel width are used, which is the practical case, [Gilbert, 1972], [Andersen, 1974], [Andersen, 1989]. The novel feature of IART, the approach that was used, is to relate pixels to the projections in a way that eliminates these sources of error and ultimately leads to the production of a smoother image. To put it in mathematical language, this approach creates a system of equations of a smaller degree of inconsistency that results in less noisy image.

The reconstruction images obtained using the Interpolative Algebraic Reconstruction Techniques proved to be of good quality. At least for the reference image we used, IART gave a better reconstructed image than the standard Fourier Backprojection method, both visually and by quantitative comparison with the phantom.

Results from the implementation of Interpolative Algebraic Reconstruction Techniques for fan beam geometry showed the suitability of the method for real data.

Results of the IART implementation for the two variations of the method indicate that using rotated pixel interpolation produces results similar to fixed pixel interpolation function. In addition, it shortens the computation time.

The new Interpolative Algebraic Reconstruction Techniques have the considerable advantage of complying with real conditions where projections at every direction are taken with the same number of equally spaced detectors. Furthermore, compared to ART, the calculation algorithm is simpler and faster and there is no need to rescale the input data for

each projection, nor do any edge effects exist [Gordon, 1974]. They can be easily implemented for a fan beam geometry with no limitations regarding the geometry of the system. Generalization into three dimensions is also straightforward.

2.2. IART. The Discrepancy Convergence Criterion and Round-off Computation Errors

A computer is usually equipped with two types of arithmetic operations, calculation with fixed point and, with more accurately, floating point. "Point" means the decimal point if the base is 10, or the binary point if the base is 2, etc. Computation with floating point means that one works with a constant number of digits (decimal point) or bits (binary point); computation with fixed decimal point means that one works with a constant number of digits/bits after the decimal point. If the computer which one is using cannot handle numbers which have more than, say, s -digits/bits then the exact product of two s -digits/bits numbers (which contains $2s$ or $2s-1$ digits/bits) cannot be used in subsequent calculations; the product must be rounded-off. In practice, rounding affects all conversions and arithmetic operations except comparison and remainder [Dahlquist, 1974], [Apple, 1985], [Think, 1986]. The effect of such roundings can be quite noticeable in an extensive calculation, or in an algorithm which is numerically unstable (badly chosen recursion formula).

To observe the influence of the round-off errors on the IART algorithm run on a Macintosh II computer that was used to produce reconstruction images, three very simple test objects (Fig. 2.2.1.) were taken and reconstructed, each one of them three times; every time handling calculations differently. The first and second time the projection data was entered as integer values and the pseudoprojections (projections of an intermediate image) were calculated as integers and reals respectively. The third time, the projection data was entered as reals and the pseudoprojections were calculated as reals. In all three cases, the

arithmetic operations were performed in floating point. The resulting reconstruction images were compared against the corresponding reference objects in Fig. 2.2.1. We used the discrepancy between the projection values of the reconstructed image and the corresponding reference object as a similarity measure. For a given projection direction, the discrepancy was computed using the equation:

$$D^q = \sqrt{\frac{1}{m} \sum_{j=1}^m (p_j - p_j^q)^2} \quad (2.2-1)$$

where a superscript q represents the iteration number, m is the number of sampling points of the projection, p_j and p_j^q are the projection and pseudoprojection values at the (j)'th sampling point, respectively.

From the above equation, it would seem that when approaching the optimal solution, the discrepancy values should converge to and ultimately achieve zero. In practice, however, the discrepancy value rarely achieves zero value although it does approach it very closely. This is due to round-off errors.

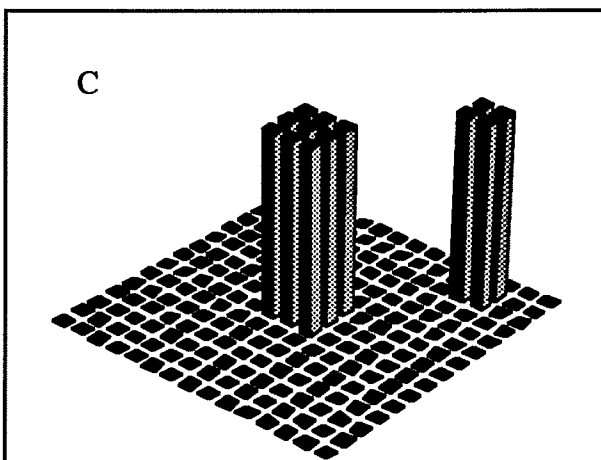
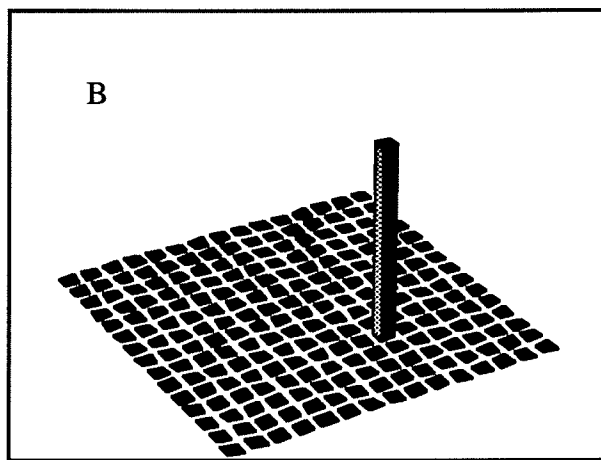
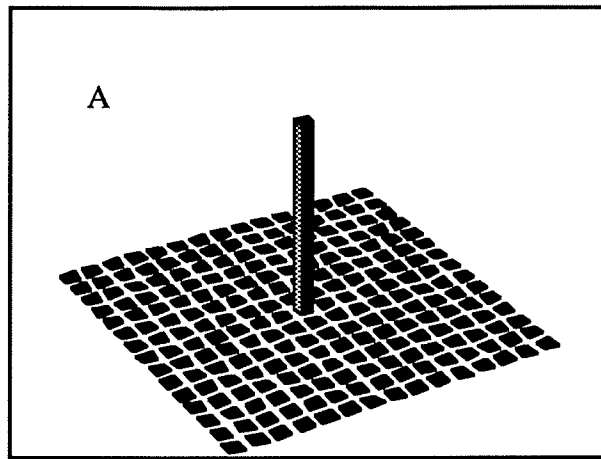


Fig. 2.2.1. Test objects. Vertical bars represent the grow in density (100). The base density is zero.

Also, the discrepancy D^q for a given q 'th iteration was computed as the average of all projection direction discrepancies:

$$\overline{D}^q = \sum_{i=1}^N \frac{D_i^q}{N} \quad (2.2-2)$$

where N , the number of projections, was taken to be 30 for every test object. The projections were equally spaced over the 180° angle. The obtained results are shown below.

Test object A

In all three (integer-integer, integer-real, real-real) cases the discrepancy values converged to zero as soon as the second iteration (Figs. 2.2.2 - 2.2.3).

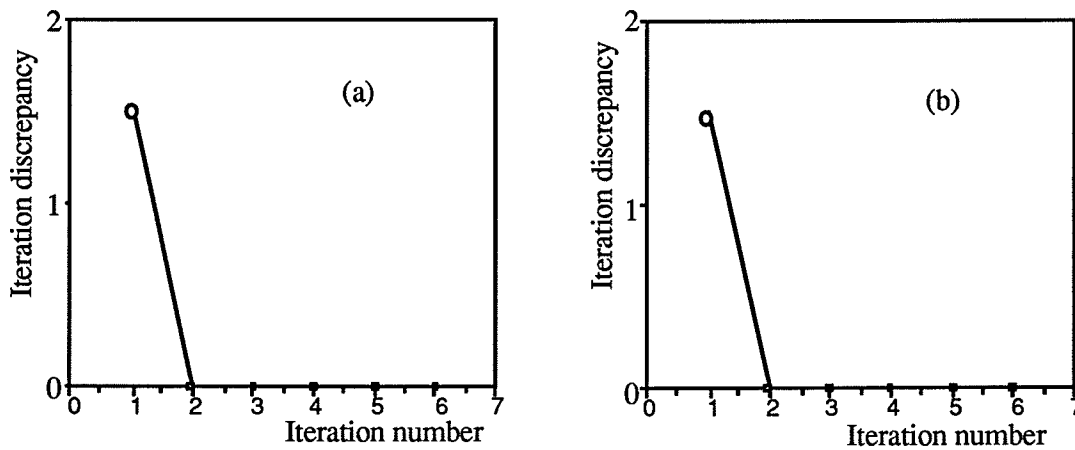


Fig. 2.2.2. Test object A. Iteration discrepancy: (a), integer projection data - integer pseudoprojections; (b), integer projection data - real pseudoprojections. The iterations are circled for which the projection direction discrepancy is presented in Fig. 2.2.3.

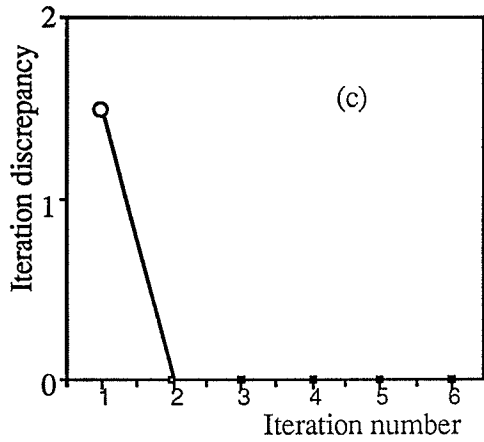


Fig. 2.2.2(c). Test object A. Iteration discrepancy: real projection data - real pseudoprojections. The iteration is circled for which the projection direction discrepancy is presented in Fig. 2.2.3.

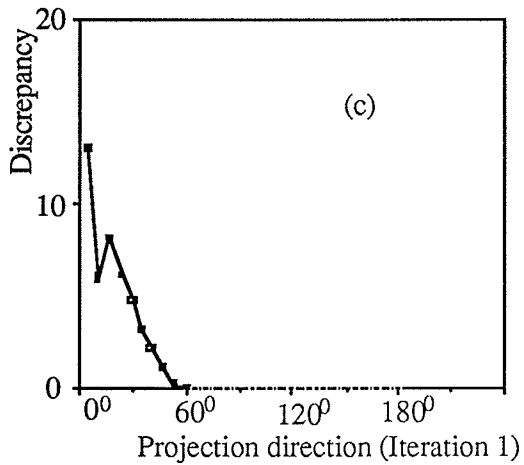
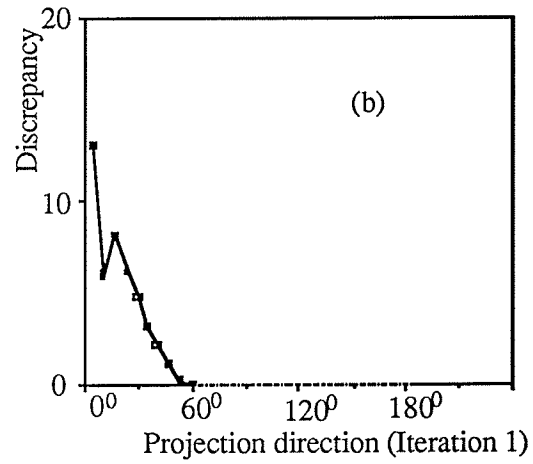
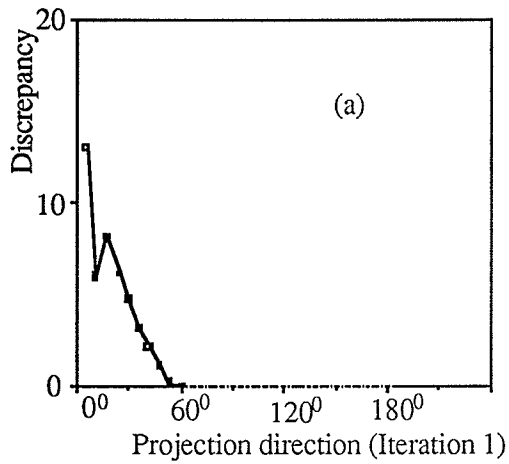


Fig. 2.2.3. Test object A. Projection direction discrepancy: (a), integer projection data - integer pseudoprojections; (b), integer projection data - real pseudoprojections; (c), real projection data - real pseudoprojections.

Test object B

The discrepancy values converged to zero only for the integer-integer case (for the 8-th iteration). For the other two (integer-real and real-real) cases, the discrepancy approached very closely to zero but did not achieve it, remaining at the same level that it reached during the second iteration (Fig. 2.2.4.). Fig. 2.2.5 displays the discrepancy as a function of a projection direction. As it can be seen, for the integer - real and real - real cases the fluctuations although close to zero but remain.

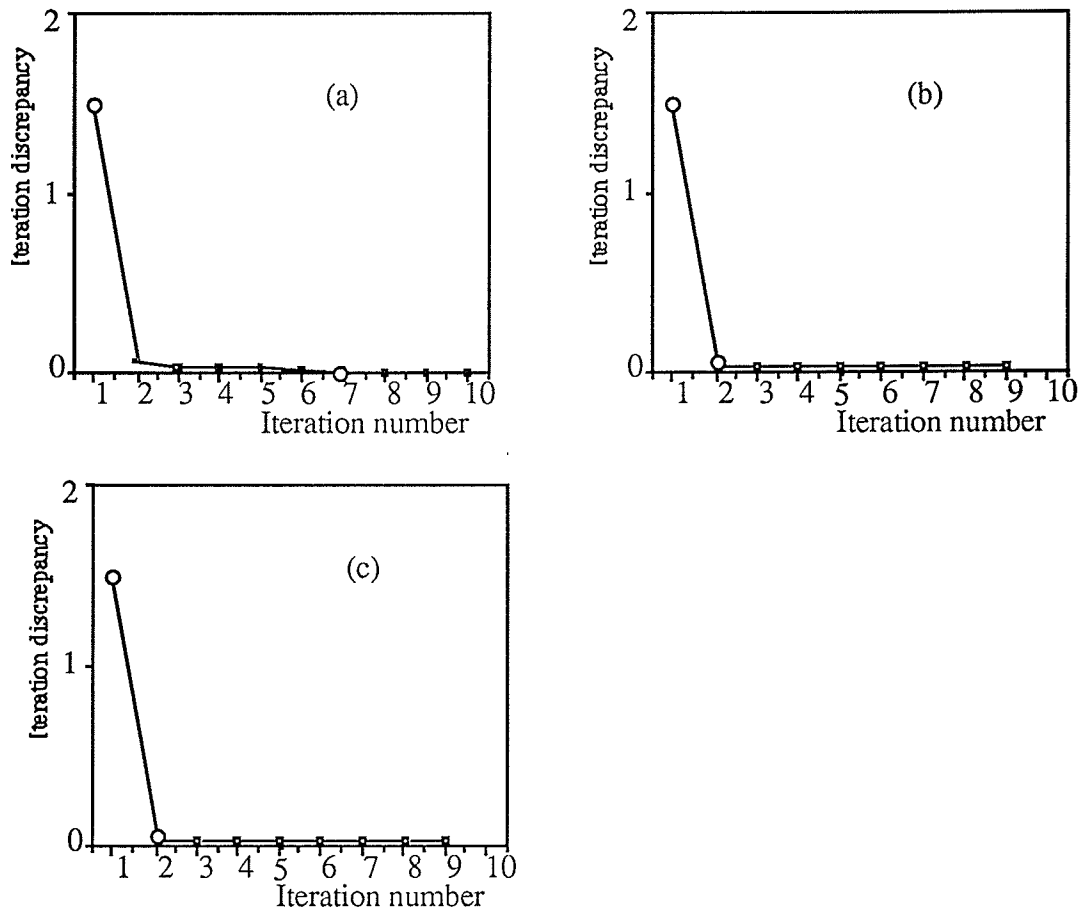


Fig. 2.2.4. Test object B. Iteration discrepancy: (a), integer projection data - integer pseudoprojections; (b), integer projection data - real pseudoprojections; (c), real projection data - real pseudoprojections. The iterations are circled for which the projection direction discrepancy is presented in Fig. 2.2.5.

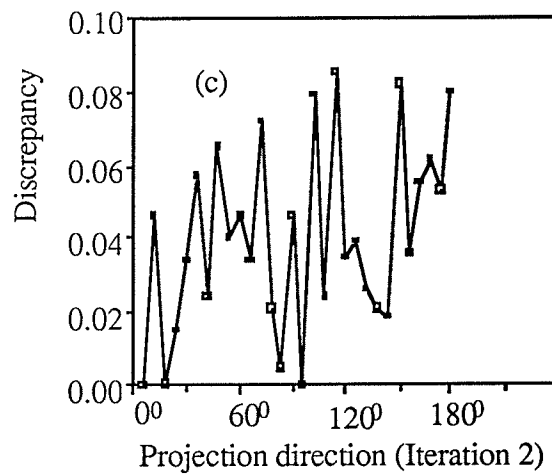
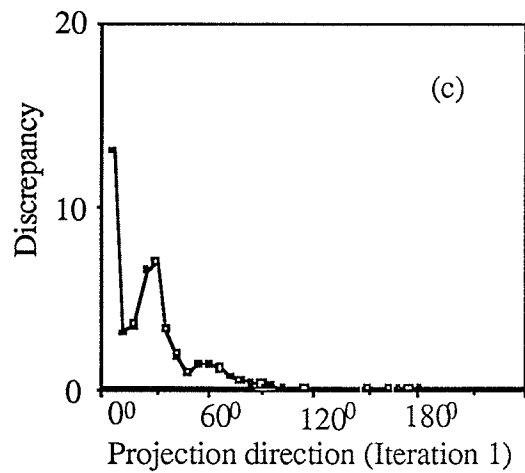
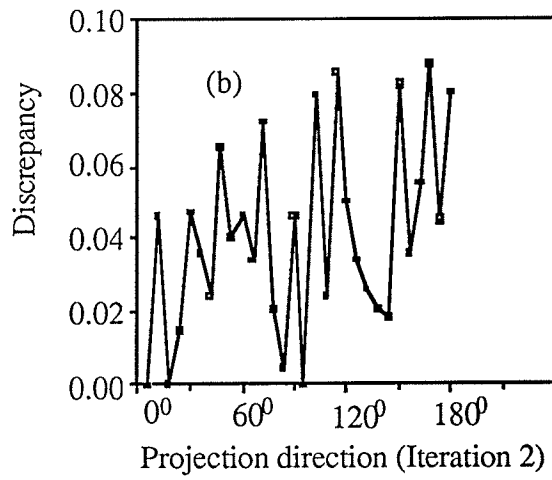
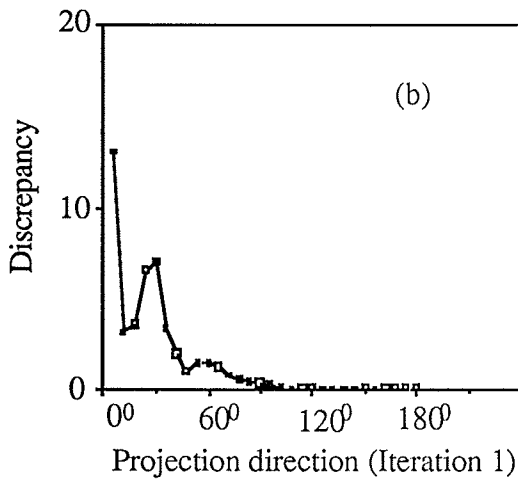
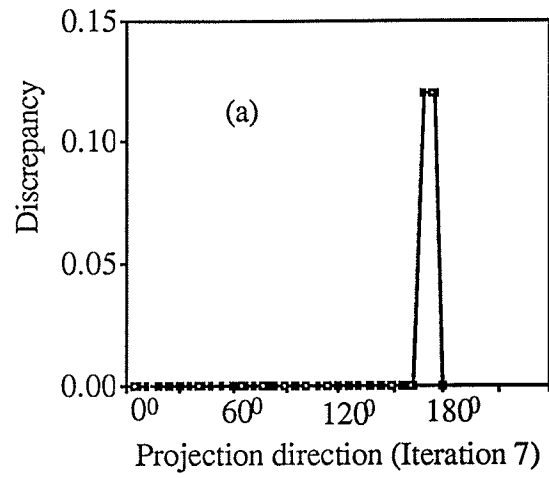
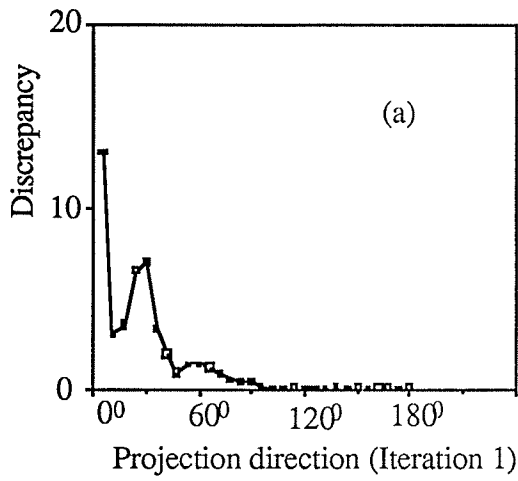


Fig. 2.2.5. Test object B. Projection direction discrepancy: (a), integer projection data - integer pseudoprojections; (b), integer projection data - real pseudoprojections; (c), real projection data - real pseudoprojections.

Test object C

The discrepancy values did not converge to zero in any one of the cases, although they approached it very close (Figs. 2.2.6 - 2.2.7).

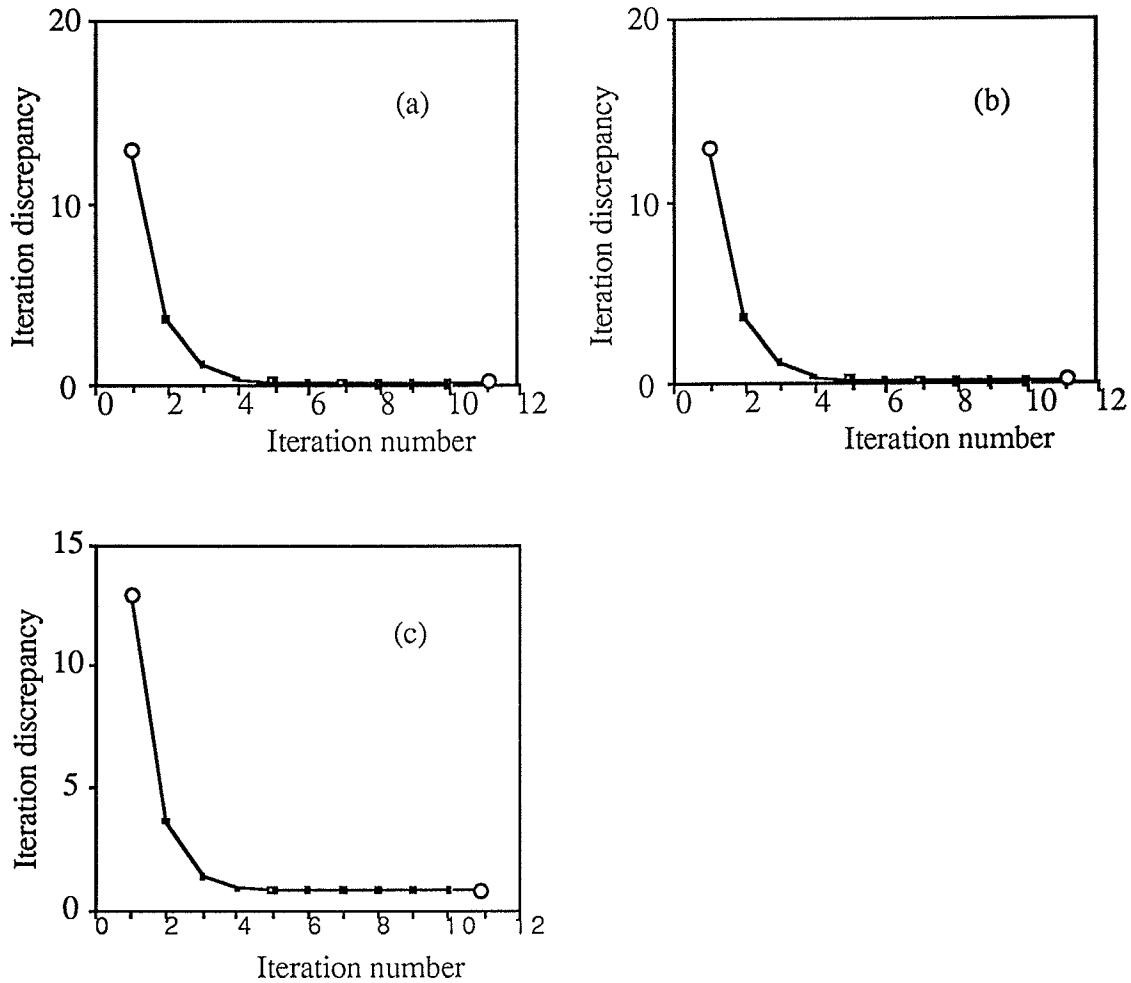


Fig. 2.2.6. Test object C. Iteration discrepancy: (a), integer projection data - integer pseudoprojections; (b), integer projection data - real pseudoprojections; (c), real projection data - real pseudoprojections. The iterations are circled for which the projection direction discrepancy is presented in Fig. 2.2.7.

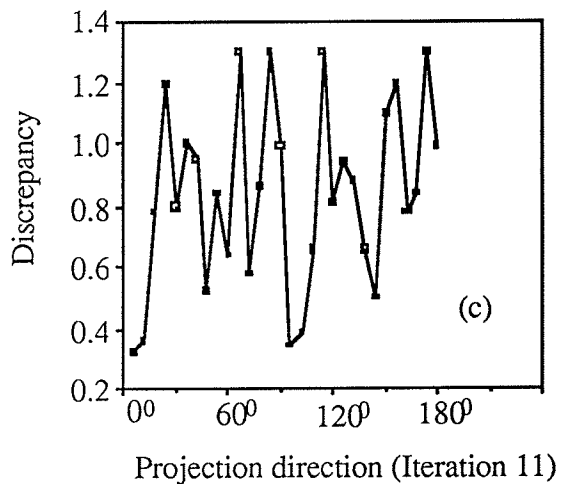
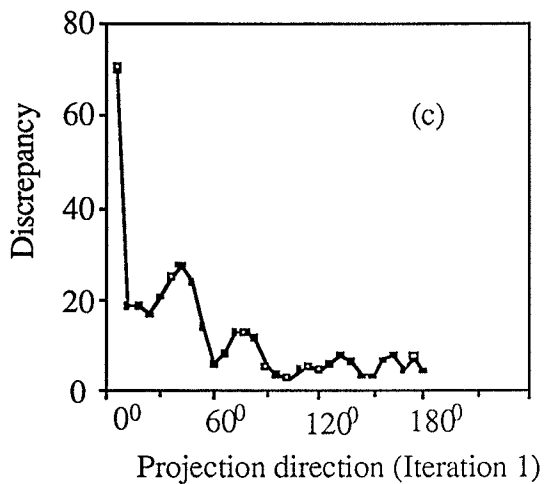
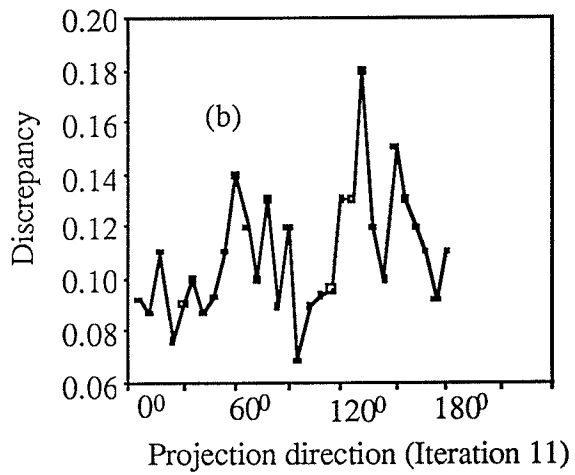
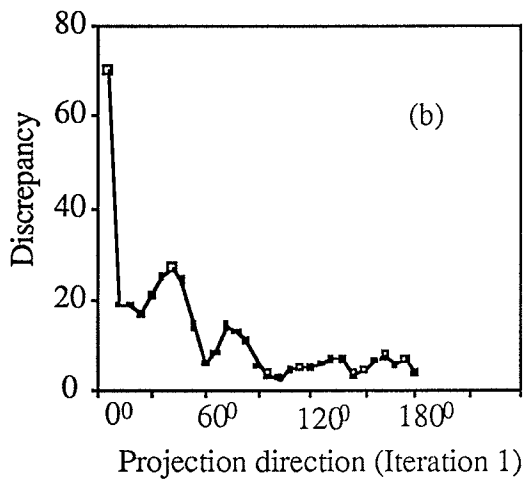
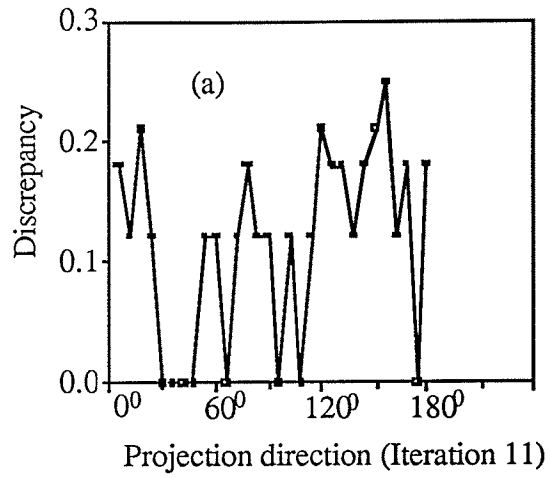
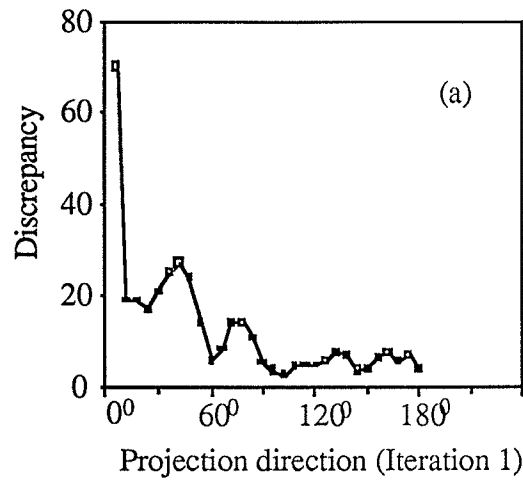


Fig. 2.2.7. Test object C. Projection direction discrepancy: (a), integer projection data - integer pseudoprojections; (b), integer projection data - real pseudoprojections; (c), real projection data - real pseudoprojections.

0.0	0.0	0.0	0.0	0.0	0.0	0.0	0.0	0.0	0.0	0.0	0.0	0.0	0.0	0.0
0.0	0.0	0.0	0.0	0.0	0.0	0.0	0.0	0.0	0.0	0.0	99.6	100.2	0.0	0.0
0.0	0.0	0.0	0.0	0.0	0.0	0.0	0.0	0.0	0.0	0.0	99.7	100.1	0.0	0.0
0.0	0.0	0.0	0.0	0.0	0.0	0.0	0.0	0.0	0.0	0.0	0.0	0.0	0.0	0.0
0.0	0.0	0.0	0.0	0.0	0.0	0.0	0.0	0.0	0.0	0.0	0.0	0.0	0.0	0.0
0.0	0.0	0.0	0.0	0.0	0.0	99.9	100.1	100.1	0.0	0.0	0.0	0.0	0.0	0.0
0.0	0.0	0.0	0.0	0.0	0.0	100.0	99.9	99.6	0.0	0.0	0.0	0.0	0.0	0.0
0.0	0.0	0.0	0.0	0.0	0.0	99.9	99.5	99.8	0.0	0.0	0.0	0.0	0.0	0.0
0.0	0.0	0.0	0.0	0.0	0.0	0.0	0.0	0.0	0.0	0.0	0.0	0.0	0.0	0.0
0.0	0.0	0.0	0.0	0.0	0.0	0.0	0.0	0.0	0.0	0.0	0.0	0.0	0.0	0.0
0.0	0.0	0.0	0.0	0.0	0.0	0.0	0.0	0.0	0.0	0.0	0.0	0.0	0.0	0.0
0.0	0.0	0.0	0.0	0.0	0.0	0.0	0.0	0.0	0.0	0.0	0.0	0.0	0.0	0.0
0.0	0.0	0.0	0.0	0.0	0.0	0.0	0.0	0.0	0.0	0.0	0.0	0.0	0.0	0.0
0.0	0.0	0.0	0.0	0.0	0.0	0.0	0.0	0.0	0.0	0.0	0.0	0.0	0.0	0.0
0.0	0.0	0.0	0.0	0.0	0.0	0.0	0.0	0.0	0.0	0.0	0.0	0.0	0.0	0.0
0.0	0.0	0.0	0.0	0.0	0.0	0.0	0.0	0.0	0.0	0.0	0.0	0.0	0.0	0.0

(a)

0.0	0.0	0.0	0.0	0.0	0.0	0.0	0.0	0.0	0.0	0.0	0.0	0.0	0.0	0.0
0.0	0.0	0.0	0.0	0.0	0.0	0.0	0.0	0.0	0.0	0.0	99.7	100.4	0.0	0.0
0.0	0.0	0.0	0.0	0.0	0.0	0.0	0.0	0.0	0.0	0.0	99.9	100.0	0.0	0.0
0.0	0.0	0.0	0.0	0.0	0.0	0.0	0.0	0.0	0.0	0.0	0.0	0.0	0.0	0.0
0.0	0.0	0.0	0.0	0.0	0.0	0.0	0.0	0.0	0.0	0.0	0.0	0.0	0.0	0.0
0.0	0.0	0.0	0.0	0.0	0.0	0.0	0.0	0.0	0.0	0.0	0.0	0.0	0.0	0.0
0.0	0.0	0.0	0.0	0.0	0.0	100.1	99.8	100.5	0.0	0.0	0.0	0.0	0.0	0.0
0.0	0.0	0.0	0.0	0.0	0.0	99.6	100.3	99.6	0.0	0.0	0.0	0.0	0.0	0.0
0.0	0.0	0.0	0.0	0.0	0.0	100.4	99.7	100.1	0.0	0.0	0.0	0.0	0.0	0.0
0.0	0.0	0.0	0.0	0.0	0.0	0.0	0.0	0.0	0.0	0.0	0.0	0.0	0.0	0.0
0.0	0.0	0.0	0.0	0.0	0.0	0.0	0.0	0.0	100.0	0.0	0.0	0.0	0.0	0.0
0.0	0.0	0.0	0.0	0.0	0.0	0.0	0.0	0.0	0.0	0.0	0.0	0.0	0.0	0.0
0.0	0.0	0.0	0.0	0.0	0.0	0.0	0.0	0.0	0.0	0.0	0.0	0.0	0.0	0.0
0.0	0.0	0.0	0.0	0.0	0.0	0.0	0.0	0.0	0.0	0.0	0.0	0.0	0.0	0.0
0.0	0.0	0.0	0.0	0.0	0.0	0.0	0.0	0.0	0.0	0.0	0.0	0.0	0.0	0.0

(b)

0.0	0.0	0.0	0.0	0.0	0.0	0.0	0.0	0.0	0.0	0.0	0.0	0.0	0.0	0.0
0.0	0.0	0.0	0.0	0.0	0.0	0.0	0.0	0.0	0.0	0.0	99.3	100.4	0.0	0.0
0.0	0.0	0.0	0.0	0.0	0.0	0.0	0.0	0.0	0.0	0.0	99.5	99.7	0.0	0.0
0.0	0.0	0.0	0.0	0.0	0.0	0.0	0.0	0.0	0.0	0.0	0.0	0.0	0.0	0.0
0.0	0.0	0.0	0.0	0.0	0.0	0.0	0.0	0.0	0.0	0.0	0.0	0.0	0.0	0.0
0.0	0.0	0.0	0.0	0.0	0.0	99.9	99.6	100.6	0.0	0.0	0.0	0.0	0.0	0.0
0.0	0.0	0.0	0.0	0.0	0.0	100.2	100.4	100.4	0.0	0.0	0.0	0.0	0.0	0.0
0.0	0.0	0.0	0.0	0.0	0.0	100.7	99.9	99.9	0.0	0.0	0.0	0.0	0.0	0.0
0.0	0.0	0.0	0.0	0.0	0.0	0.0	0.0	0.0	0.0	0.0	0.0	0.0	0.0	0.0
0.0	0.0	0.0	0.0	0.0	0.0	0.0	0.0	0.0	0.0	0.0	0.0	0.0	0.0	0.0
0.0	0.0	0.0	0.0	0.0	0.0	0.0	0.0	0.0	0.0	0.0	0.0	0.0	0.0	0.0
0.0	0.0	0.0	0.0	0.0	0.0	0.0	0.0	0.0	0.0	0.0	0.0	0.0	0.0	0.0
0.0	0.0	0.0	0.0	0.0	0.0	0.0	0.0	0.0	0.0	0.0	0.0	0.0	0.0	0.0
0.0	0.0	0.0	0.0	0.0	0.0	0.0	0.0	0.0	0.0	0.0	0.0	0.0	0.0	0.0
0.0	0.0	0.0	0.0	0.0	0.0	0.0	0.0	0.0	0.0	0.0	0.0	0.0	0.0	0.0

(c)

Fig. 2.2.10. Test object C. Reconstruction matrix data: (a), integer projection data - integer pseudoprojections; (b), integer projection data - real pseudoprojections; (c), real projection data - real pseudoprojections.

Figs. 2.2.8 - 10 display the resulting reconstruction matrices.

All three test objects in Fig. 2.2.1. were chosen to increase the complexity of calculations. Starting from the simplest one A through B to C, the discrepancy values converged to and achieved zero (test object A, Fig. 2.2.2.), or converged to a very close to zero minimum (B, C test objects, Figs. 2.2.4 and 2.2.6). In the latter, the minimum was approximately of one order less in value for the test object B (Fig. 2.2.5) compare to the test object C (Fig. 2.2.7). This confirmed that with increasing complexity of calculations the effect of round-off errors amplifies. As for the best way to handle the calculations, judging from the above results, one may say that there is not much difference in how the calculations are handled. The reconstruction results are very much alike. One possible explanation to it that we can give is that in the Standard Apple Numeric Environment (SANE) of a Macintosh computer all arithmetic is done internally using extended-precision arithmetic, i.e. with the highest precision. The floating point storage formats, that we have used, provide binary encodings of a sign (+ or -), an *exponent*, and *significand*. A represented number has the value

$$\pm \text{significand} 2^{\text{exponent}}$$

where the significand has a single bit to the left of the binary point (that is , $0 \leq \text{significand} < 2$) [Think, 1986]. An extended type of a variable has a binary exponent range (-163838 - 16384) compared to (-126 - 127) of the real or integer type variable. The significand of the extended is represented by 19 - 20 decimal digits compared to 7 - 8 for the real or integer.

2.3. IART with Filtered Projections

The Interpolative Algebraic Reconstruction Techniques algorithm described in Section 2.1.3 is vulnerable to noise. This feature is inherent to all iterative methods. To alleviate the problem, we suggest using preprocessed projection data. We propose that the raw data undergo the noise filtering operation prior to being used by an iterative reconstruction algorithm, IART. From our preliminary results presented in Chapters III and V, we have found that using window functions helps to obtain smoother, less noisy images.

2.4. Convolution Backprojection/ Fourier Backprojection. An Overview

Fourier Backprojection (FBP) is the reconstruction method most commonly used in CT scanners. It is based on the Fourier slice theorem that relates the one-dimensional Fourier transform of a projection of an object function $g(x,y)$ to its two-dimensional Fourier transform: The Fourier transform of a projection function for a projection direction at angle θ gives the values of the Fourier transform of the object along the straight line at angle θ (Fig. 2.4.1) [Rosenfeld, 1982], [Ekstrom, 1984], [Rowland, 1979].

The FBP algorithm consists of the following sequence of operations:

- Fourier transformation of the projection data vector;
- Multiplication of the complex values by a filter (the choice of filter is dependent on the data collection method and the type of object which is to be reconstructed);
- Taking the inverse Fourier transformation of the modified (filtered) frequencies;
- Back projection of the modified projection data.

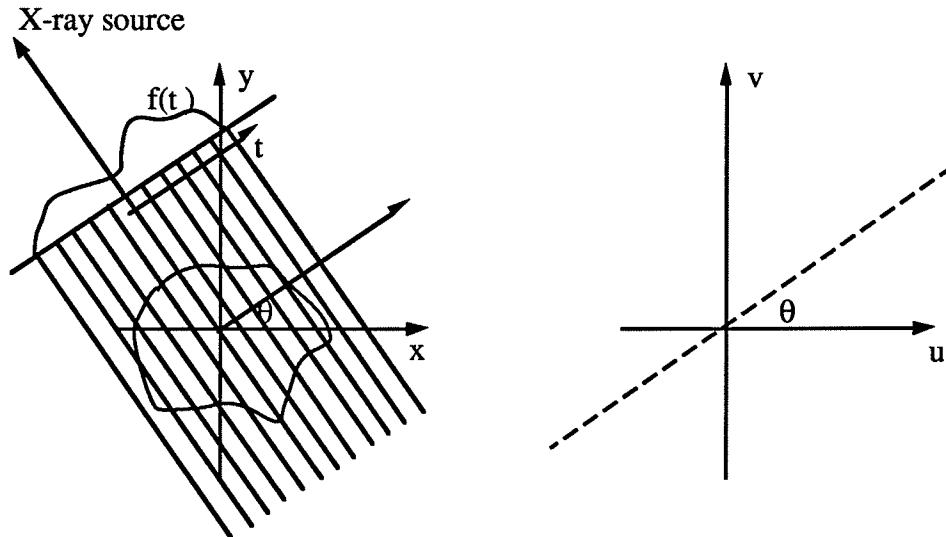


Fig. 2.4.1. Illustration of the Fourier slice theorem. The Fourier transform of $f(t)$ gives the values along the dashed line in the uv -plane.

The discrete reconstruction formula of the algorithm is:

$$\rho(x,y) = \left[\overline{P \mathcal{B}_s^N} \left\{ \mathcal{I}_d^f \left[\overline{M \mathcal{F}^{-1}} \left[\overline{AM} \times \overline{M \mathcal{F}} g_n \right] \right] \right\} \right] (x,y) \quad (2.4-1)$$

where $\rho(x,y)$ is the estimate of the optical density function of an object matrix, g_n stands for the n -th projection function and \overline{AM} is the M -point discrete filter function. \mathcal{I}_d^f is the interpolation operator; $\overline{M \mathcal{F}}$, $\overline{M \mathcal{F}^{-1}}$, $\overline{P \mathcal{B}_s^N}$ are the operators of the M -point discrete Fourier transform, the inverse M -point discrete Fourier transform and the discrete backprojection on a regularly spaced grid of P^2 points centered about the origin with a grid spacing of s , respectively:

$$\left[\mathcal{F}_d^f g \right] (x) = \sum_{m=M_{LO}}^{M_{HI}} g(m) f\left(\frac{x}{d} - m\right) \quad (2.4-2)$$

where d is the distance between the sampled points and f is the interpolating function;

$$\left[\overline{M \mathcal{F} g} \right] (m) = \sum_{n=M_{LO}}^{M_{HI}} g(n) \exp\left(-2\pi i \frac{nm}{M}\right) \quad (2.4-3)$$

and

$$\left[\overline{M \mathcal{F}^{-1} g} \right] (m) = \frac{1}{M} \sum_{n=M_{LO}}^{M_{HI}} g(n) \exp\left(2\pi i \frac{nm}{M}\right) \quad (2.4-4)$$

where

$$M_{LO} = \begin{cases} -(M-1)/2 & \text{if } M \text{ is odd} \\ -(M-2)/2 & \text{if } M \text{ is even} \end{cases}$$

$$M_{HI} = \begin{cases} (M-1)/2 & \text{if } M \text{ is odd} \\ M/2 & \text{if } M \text{ is even} \end{cases}$$

$$\left[\overline{P \mathcal{B}_S^N \{g_n\}} \right] (x,y) = \Delta \sum_{n=0}^{N-1} w_n(x,y) g_n\left(sx \cos n \Delta + sy \sin n \Delta\right) \quad (2.4-5)$$

where N is the number of projections, $\Delta = \frac{\pi}{N}$ and $w_n(x,y)$ is the weighting factor. For parallel beam geometry $w_n(x,y)$ is constant and equals 1.

The operation of multiplying the Fourier transform of a projection function by a filter function is equivalent to the operation of convolving the projection function with a convolution function which is the inverse Fourier transform of the filter function. When we replace the operation of filtering in the Fourier space by the convolution operation in the

real space, the discrete reconstruction formula becomes:

$$\rho(x,y) = \left[\overline{P \mathcal{B}_s^N} \left\{ \mathcal{F}_d \left[(\overline{M \mathcal{F}^{-1} A}) \overline{M} * g_n \right] \right\} \right] (x,y) \quad (2.4-6)$$

and we talk about the convolution back projection reconstruction method.

CHAPTER III

NOISE IN COMPUTED TOMOGRAPHY

3.1. Sources of Noise and Their Influence on a Reconstruction Image

Noise in a reconstruction process is introduced during the acquisition of data and by a reconstruction procedure itself [Barrett, 1981], [Evans, 1981], [Herman, 1980], [Andrews, 1977].

Limitations to the accuracy of CT measurements (projection data) are due to:

1. Statistical nature of the processes of x-ray photon production, photon interaction with matter, and photon detection;
2. Detector efficiency including dark current and dead time;
3. Others, that include beam hardening, partial volume effect, scattered photons, motion artifacts, etc..

As for the first mentioned factor, the properties of the introduced error are considered as a random variable following the Poisson probability law [Barrett, 1981], [Herman, 1980]. Suppose that a photon leaves the source in the direction of the detector. Then there is a fixed probability (transmittance) that the photon will get as far as the detector without being absorbed or scattered. This probability depends on the energy of the photon and the material intersected between the source and the detector. A photon which reaches the detector is not necessarily counted. For each energy, there is a fixed probability, called the efficiency of the detector at that particular energy, that a photon which reaches the detector is counted by the detector. Assume some average number of photons at a given energy emitted in one unit of time by a stable x-ray source towards the detector, then the number of photons at given energy that:

- reach the detector without having been absorbed or scattered,
- are counted by the detector in one unit of time,

is a sample of a Poisson random variable with parameter equal to a product of the transmittance, detector efficiency and the average of the photon number.

Fig. 3.1.1 delineates a typical CT detector system [GE, 1987], [GE, 1988].

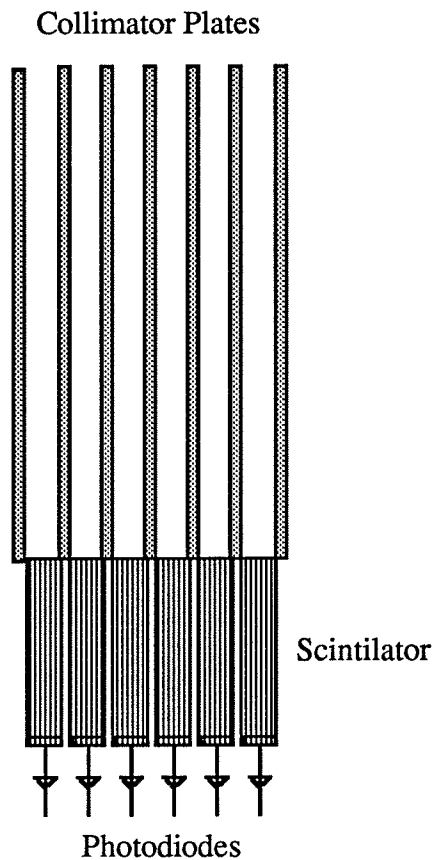


Fig. 3.1.1. CT detector system.

Parameters that influence the detector system efficiency are:

Geometric efficiency, that is an indication of how well the detecting system is designed. It refers to the percentage of x-ray energy exiting the patient that is incident on

the cells (individual detectors) of the system. It is primarily determined by the amount of post-patient collimation, particularly the plates separating the individual system cells ;

Absorption efficiency, defined as the percentage of x-ray energy absorbed in the scintillator material relative to the total energy incident on the material. Once the x-ray energy has been absorbed into the material within each cell, the goal is to convert as much as possible into the emission of visible light and to minimize energy dissipation in other forms;

Scintillation efficiency of the detector system, that is the ratio of emitted light energy to the absorbed x-ray energy;

To complete the task of x-ray detection, the visible *light must be collected and channeled to a photodiode for conversion to an electrical signal*. Maximizing collection is a formidable challenge because scintillations are emitted equally in all directions, and some of the light will be absorbed by the scintillator;

Afterglow, refers to residual light emitted from the scintillator after termination of x-rays, due to an intrinsic delayed reaction of the scintillation process. It can contribute to image degradation. As the entire detector rotates for data acquisition during a scan, lengthy afterglow can blur the acquired data, and consequently, the final image;

Stability of the detector. Scintillator detectors are known to exhibit performance degradation in response to external factors such as prolonged x-ray exposure, temperature and humidity. The degradation are usually manifested as a CT number shift and/or a visual artifact such as a ring;

Cell spacing, that is a major factor affecting spatial resolution of a CT system. In general, spatial resolution improves as the cell spacing decreases. However, as the cell spacing decreases so does the number of incident x-ray quanta per cell. This, in turn, increases the image noise at a given scan. Typically, patient radiation exposure is increased to maintain a desirable signal-to-noise ratio.

The photodiodes of a CT detector are usually tuned for maximum signal output at the scintillation light frequency. Fig. 3.1.2 below, displays a typical plot of input and output for a photoelectronic detector [Andrews, 1977].

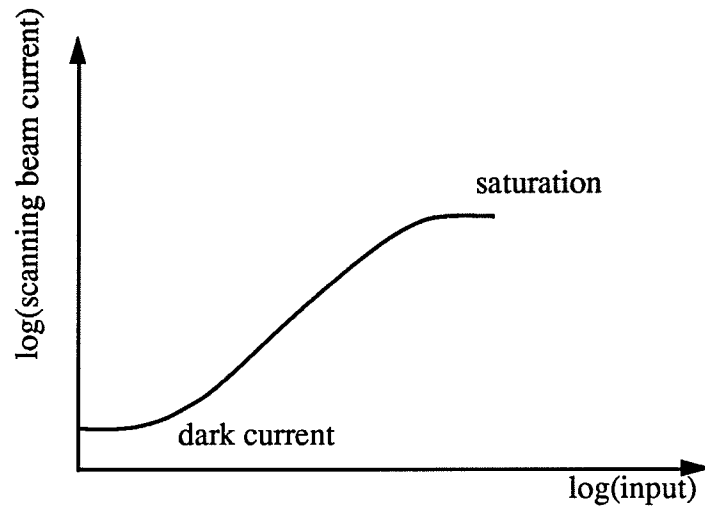


Fig. 3.1.2. Transfer characteristic of typical photoelectronic detector.

The characteristic curve shows that there is a saturation response at high intensities and a limit response at low intensities, usually referred to as the dark current. There also exists a linear region in which the log of response is proportional to the log of stimulus and it is conventional practice to refer to the slope of the portion of the curve as the "gamma" of the detector. In this region the scanning beam current i_b is represented by the equation

$$\log i_b = \gamma \log i_o + C \quad (3.1-1)$$

where i_o is the incident illumination intensity, γ is the linear slope, and C is the offset (the linear portion does not pass through the origin). Thus, we have the relation

$$i_b = C_1 (i_0)^{\gamma} \quad (3.1-2)$$

which governs the transfer. Photoelectronic detector efficiency is assumed to be independent of the number of photons the single detector has to count. This may be difficult to achieve in practice, since detectors can be saturated by too many photons getting to them. One way of combating this is by insertion of a compensator which ensures that even along lines which either miss or hardly touch the object to be reconstructed, the total attenuation is significant enough for the detector not to get saturated. Also, the detector's threshold value plays an important role, i.e., the point when the dark current transforms into the linear region.

"Beam hardening" is an expression to describe changes in energy distribution of an x-ray beam as it passes through the object. (The x-ray beam used in CT is polychromatic, i.e. consists of photons of different energies.) X-ray beams reaching a particular point inside the body from different directions are likely to have different spectra (having passed through different materials before reaching the point in question) and thus will be attenuated differently at that point. This makes it difficult to assign a single value for the attenuation coefficient at a point in the body. A possible solution to this difficulty is to assign to the point the attenuation coefficient of photons at a particular energy. (If we used monochromatic x-ray beams, i.e. consisting of photons only at the single energy, beams from different directions would be attenuated in the same way at a fixed point.) In practice, to correct for beam hardening specially shaped filters or wedges are used and beam-hardening corrections are performed mathematically [Macovski, 1976], [Herman, 1979], [Greening 1979]. All the methods of correction for beam hardening aim, in effect, to produce the distribution of attenuation values which would have been obtained if a monochromatic x-ray source had been used in the scanner.

The partial volume effect is a consequence of the non negligible size of the focal spot and detector, and thus the photons that are counted do not travel along the same line, but rather they travel along one of a bundle of lines forming a rather complicated shape. For the situation when the beam is only partially blocked by attenuating material (Fig. 3.1.3), the estimation of the average of the line integral of the relative linear attenuation between the source and the points on the detector introduces errors.

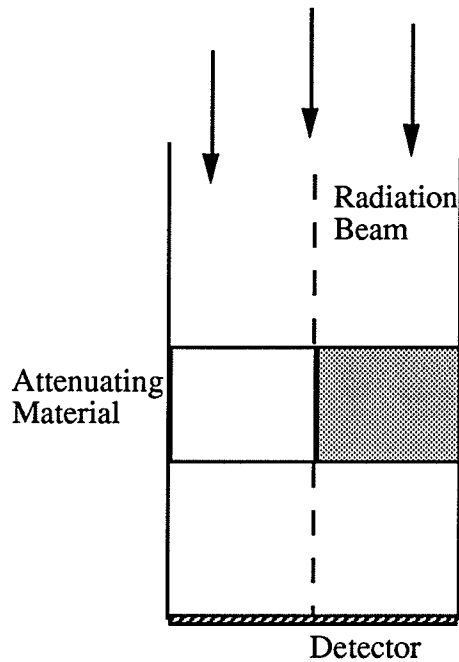


Fig. 3.1.3. Illustration of the partial volume effect.

Suppose, we have a ray of a monochromatic x-ray beam B that strikes a detector D . Let M be the attenuating material volume of interest. Suppose that a linear attenuation coefficient μ is everywhere zero except in that half of the volume M which is filled with the pattern, where its value is two. It is assumed that the length of intersection with M of any line from the beam is unity. Suppose that during a reference measurement, we use a reference material of a linear attenuation coefficient equal zero (vacuum) and that the

number of photons registered N is equal to the number of photons which leave the source in the direction of the detector N_0 and is 1000. Breaking the x-ray beam into two equal halves as shown in Fig. 3.1.3, we see that 500 photons on average will enter both halves of M . During the actual measurement, in the left half of the volume where the transmittance is one ($e^{-0} = 1$), all 500 photons will reach the detector. In the right half, where the linear attenuation μ is two, and hence the transmittance is $e^{-2} \approx 0.135$, the number of photons that reach the detector is about 68. Hence the total number of detected photons is about 568. Using the equation

$$\mu = -\ln\left(\frac{N}{N_0}\right) \quad (3.1-3)$$

we calculate that the average attenuation coefficient of the volume under consideration is about 0.566. However, it is easy to see that the true value of it is 1. The reason for this rather large error (43.4%) resulting from the calculations is due to the processes of taking exponentials and logarithms that give unproportionately great importance to the unblocked portion of the beam.

In practice, lead shielding with long narrow pinholes in front of the source and the detector are being used to reduce the size of both of them.

Scattered photons produce a problem when we have an array of detectors: a photon scattered out of its path towards one detector may very well reach another detector and be counted by it. In CT detector systems, scatter is the major factor that influences the geometric efficiency of the system. Since the ratio of scattered photons to unscattered ones which reach a detector is dependent on the object to be reconstructed, the error introduced by scatter cannot be totally removed from the measurements prior to reconstruction. However, scattered radiation may be minimized by:

- limiting the area of the incident beam;
- using an air gap between the scattering medium (the object) and the detector;

- using a collimating grid between the scattering medium and the detector;
- optimizing the spectrum of the incident beam;
- energy discrimination in the detector.

The beam area should be large enough to encompass everything of medical interest in the region being imaged. But making it larger than necessary increases the scatter fraction as well as the patient's dose. Each volume element in the patient's body acts as a source of scattered radiation. Hence, as the detected scatter intensity falls off as the inverse square of the distance from the scatter source to the detector, using an air gap between the patient and the detector increases the distance and helps. Collimation absorbs photons coming towards a detector from directions other than the x-ray source. In its simplest form, the collimating grid is a series of parallel slats made of tungsten or other high-atomic-number material, and perhaps spaced apart with fiber-board or some other material with low-x-ray absorption [Johns, 1983], [Hendee, 1970], [Herman 1980], [GE, 1987]. For an x-ray source a long distance away from the detector, the incident beam is essentially collimated. If the distance between x-ray absorbing slats is much larger than the width of an individual slat, very few of the unscattered photons strike the slats and the primary image is largely unaffected by the grid. The only degradation of the primary image is a set of very fine lines, the shadows of the slats. This problem can be eliminated by moving the grid uniformly parallel to the detector during exposure. Scattered radiation, on the other hand, is no longer collimated, and most of it is blocked by the grid. As for the optimization of the x-ray spectrum; high-energy photons interact with soft tissue predominantly by Compton scattering in the direction of the detector [Johns, 1983], [Hendee, 1979], [Hobbie, 1988]. As the result, it might be expected that scattering problems would be particularly bad at these energies. However, higher energy photons suffer fewer interactions in the body for a given number of transmitted photons. This effect reduces the scattered flux but also reduces the contrast in the primary image. Low energy photons give a high -contrast primary image but are strongly absorbed in the

body. The primary absorption process is photoelectric at very low energies ($\leq 40 \text{ keV}$). Scattered radiation could therefore be greatly diminished just by keeping the photon energy below about 40 keV , but this would not be acceptable in terms of patient dose for imaging of thick body parts. The choice of an optimum photon energy or spectrum is thus a complicated trade-off involving noise, dose, detector characteristic, scatter, image contrast, and the specific diagnostic information needed.

The underlying assumption in CT is that the projection values are integrals along different lines of the same function. For a moving organ, such as the lung or the heart, this assumption is violated if the actual measurements are taken at different times for different projections. One way of combating this is to use multiple arrays of detectors and possibly even multiple sources. But this results in increase of error due to detection of scattered photons.

3.2. Simulation of Photon Noise

Noise that is introduced into a detector array is likely to be a contribution of two separate processes: (1) random fluctuations in the number of photons and photoelectrons in the photoactive surface of detectors; (2) random thermal noise sources in the circuits that sense, acquire, and process the signal from the photoactive surface of the detectors. The second process has a behavior that is well known; random thermal noise is usually described by a zero-mean Gaussian process with a uniform ("white") power spectrum [Andrews, 1977]. The first process is more complex to describe. Electromagnetic radiation is of a discrete, quantum nature. Therefore a detector absorbs radiation energy in increments of $h\nu$, where ν is the frequency of the radiation and h is Planck's constant. As a result, the output of the detector is not smooth but exhibits fluctuations known variously as quantum noise, photon noise, or Poisson noise [Barrett, 1981]. This type of

noise plays a crucial role in radiographic imaging systems, primarily because the energy is so large for x-rays.

The arrival of photons at the detector can be described as a random process defined by the Poisson distribution or Poisson probability law:

$$\Pr(K \text{ in } T) = (a^K T^K / K!) \exp(-aT) \quad (3.2-1)$$

where K represents the number of photons that are detected in an observation time T and a is a constant as described by Equation (3.2-2), below.

Equation (3.2-1) was derived for a stationary process and under the three physically reasonable assumptions:

(a) The number of photons detected in the interval $(0, T)$ is statistically independent of the number detected in any other overlapping interval.

(b) The probability of detecting one photon in a vanishingly small time interval ΔT is directly proportional to ΔT , i. e.

$$\lim_{\Delta T \rightarrow 0} \Pr(1 \text{ in } \Delta T) = a \Delta T \quad (3.2-2)$$

(c) The probability of more than one photon being detected in ΔT is zero. Since the probability of more than one photon being detected vanishes as ΔT approaches zero, the quantity $a \Delta T$ may also be interpreted as the mean number of photons detected in ΔT . Under the assumption of stationary statistics, the mean number per unit time must be a constant and aT must be the mean number detected in T , i. e.

$$\bar{K} = aT \quad (3.2-3)$$

This important result can also be verified by directly calculating \bar{K} from $\Pr(K \text{ in } T)$. As a result, we can write the simplified notation for $\Pr(K \text{ in } T)$

$$\Pr(K) = \exp(-\bar{K}) \bar{K}^K / K! \quad (3.2-4)$$

For stationary statistics, the mean number of detected photons per unit time was assumed to be independent of time, the probability density for the arrival times was assumed to be constant, and the auto correlation function for a sum of Poisson impulses was shown to depend only on the time difference and not on the actual time. In real physical problems, stationary statistics are not exactly correct: Radioactive decay, variations in source- detector geometry, etc. all cause deviations from strict temporal stationarity. Nonstationarity is even more important in terms of the image, as it is the deviations from uniformity in a radiographic image that convey useful diagnostic information. Fortunately, it is possible to generalize Equation (3.2-3) to describe a nonstationary version of the Poisson distribution: If we represent the mean number of photons detected in time T as

$$\bar{K} = \int_0^T a(t) dt \quad (3.2-5)$$

where $a(t)$ is as described by Equation (3.2.6)

$$\lim_{\Delta T \rightarrow 0} \Pr(1 \text{ in } \Delta T) = a(T) \Delta T \quad (3.2-6)$$

Equation (3.2-1) is still valid.

The main distinguishing feature of Poisson random variables is that the variance σ^2 always equals the mean

$$\sigma^2 = \bar{K} \quad (3.2-7)$$

In many physical problems, the observed random variable is really the sum of a large number N of other independent random variables. Photon noise is not an exception. (see Section 3.1). The central limit theorem states that the probability density of the observed random variable approaches a normal distribution (Gaussian) [Tsokos, 1972], [Thomas, 1971], [Barrett, 1981]

$$\text{pr}(x) = \frac{1}{\sqrt{2\pi\sigma^2}} \exp(-(x - \bar{x})^2 / 2\sigma^2) \quad (3.2-8)$$

(where $\text{pr}(x)$ is a probability density function of a random variable x and σ^2 is the variance) as N tends to infinity, regardless of the densities of the constituent random variables. From the above theorem, we can anticipate that the Poisson distribution will approach a Gaussian for large \bar{K} , i. e., Eq. (3.2-4) is equivalent to

$$\text{Pr}(K) = (2\pi\bar{K})^{-1/2} \exp[-(K - \bar{K})^2 / 2\bar{K}] \quad (3.2-9)$$

Equation (3.2-9) is a Gaussian with the variance σ^2 equal \bar{K} . Proof of it can be found in [Barrett, 1981]. This Gaussian form is an excellent approximation of the Poisson distribution for $\bar{K} \geq 10$. A graphical comparison between the exact Poisson distribution and the Gaussian approximation is given in Figs. 3.2.1 - 3.2.2.

To simulate noisy CT projections due to photon noise one can either introduce noise into a reference image and then take projections from it , or introduce noise directly into the detector readings i.e., take projections from a clean (not noisy) reference image and make them noisy. In this thesis the second approach has been chosen as it better simulates real situation when CT data gets affected by photon noise. The procedure used to introduce noise to the detector readings takes the advantage of the fact that photons arriving at every single detector are Poisson distributed.

Having assuming that the number of photons counted by a single i -th detector \overline{K}_i was the mean of the Poisson distribution as in (3.2-4), we computed a Poisson distributed random number with the given mean and used it to replace \overline{K}_i . The procedure was repeated for every single detector. Depending on the \overline{K}_i value, we have used different equations to render new photon counts. If \overline{K}_i was less than 10 we used Equation (3.2-4), otherwise Equation (3.2-9) was used. The advantage of using the Gauss approximation of the Poisson distribution is considerably reduced computation time.

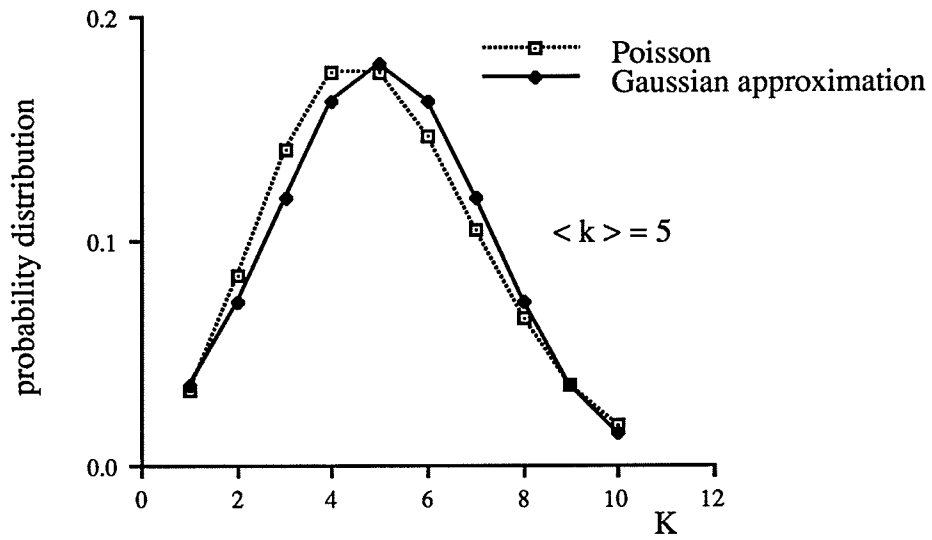
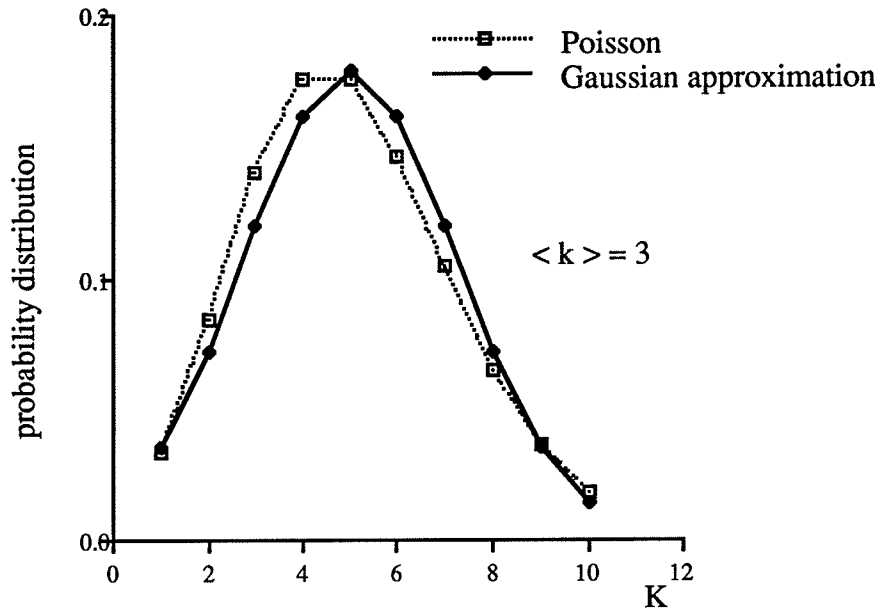


Fig. 3.2.1. A comparison between the exact Poisson distribution and the Gaussian approximation to it for $\langle K \rangle = 3; 5$.

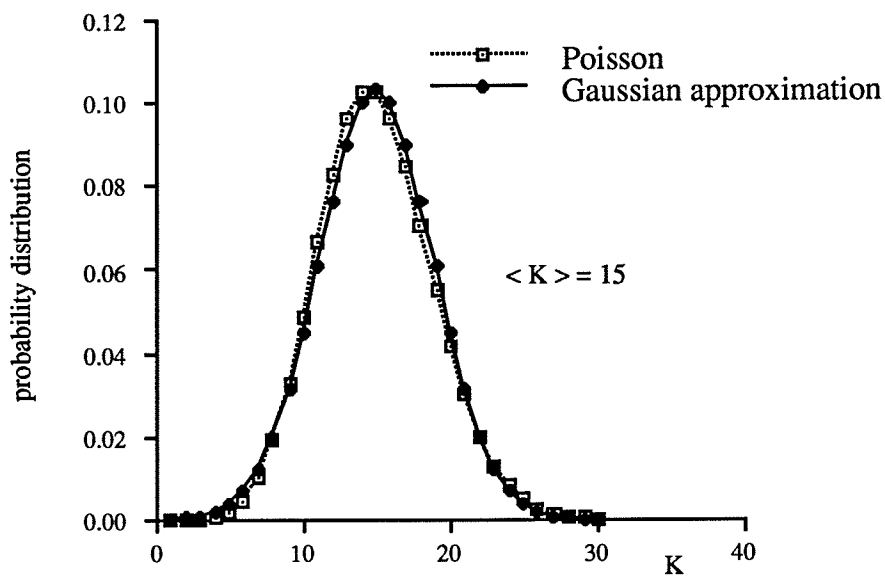
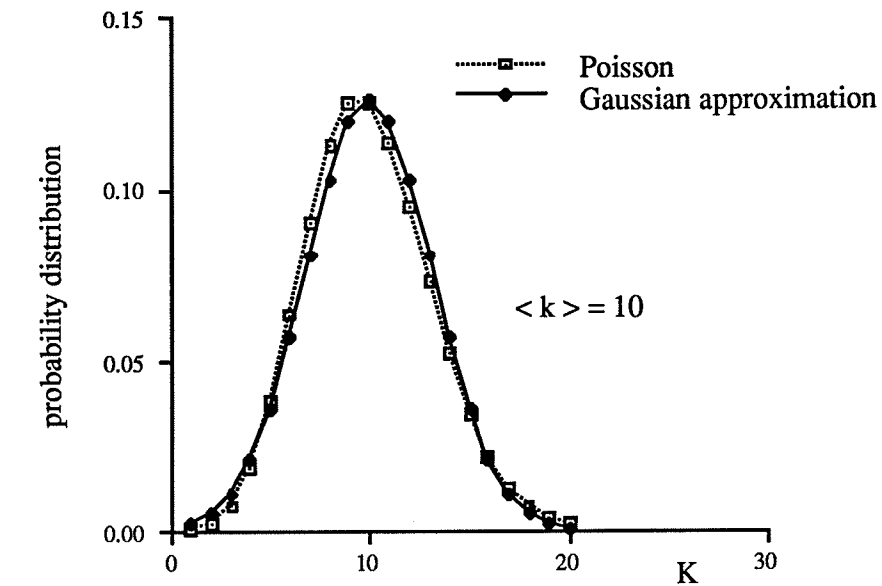


Fig. 3.2..2. A comparison between the exact Poisson distribution and the Gaussian approximation to it for $\langle K \rangle = 10; 15$.

3.3. Noisy Sinograms

This section is closely related to the next one. Here, photon noise will be superimposed on projections which subsequently will be used to produce noisy images. The results obtained will be used for the purpose of the next section that deals with the removal of noise from projections.

A sinogram consists of a set of projections taken from a volume under investigation and displayed as an image by organizing the projections in a matrix of the size $(n \times m)$, where n represents the number of projection taken and m is the number of detectors used. It is important that the order of projections be preserved, i.e., all projections in the same order in which they were taken should be placed as a consecutive rows of the matrix starting from the first projection placed as the first row of the matrix. Figs. 3.3.1(a) and (b) show the reference image "dolls" and its sinogram, respectively. The sinogram consists of 35 parallel geometry beam projections equally spaced over 180° . The length of an individual projection is 256. We used this sinogram as a reference, and by applying the simulation procedure described in Section 3.2 of this chapter we produced the noisy sinogram in Fig. 3.3.2(a). The noise that was superimposed on a reference sinogram to produce the sinogram in Fig. 3.3.2(a) is shown in Fig. 3.3.2(b). Fig. 3.3.3 represents Fourier spectra of both the reference, (a), and the noisy, (b), sinograms.

The reference sinogram in Fig. 3.3.1(b) had values in a range $10^4 - 10^5$ photon counts (detector readings). In order to analyze the influence of noise on reconstruction image quality from a data taken at different ranges of photon counts registered by a detector, the necessary sinograms were produced from the reference one (Fig. 3.3.1(b)) by adjusting its values into the required range. We have chosen to analyze three additional ranges of photon counts: $10^3 - 10^4$; $10^2 - 10^3$; $10 - 10^2$. Accordingly, noisy sinograms were produced using the same noise simulation procedure that was used to produce the

sinogram in Fig. 3.3.2(a). Figs. 3.3.4 - 3.3.6 show the resultant noisy sinograms, (a), and their Fourier spectra, (b), for the photon count ranges of $10^3 - 10^4$, $10^2 - 10^3$ and $10 - 10^2$, respectively. To evaluate changes in the sinograms due to the superposition of photon noise, all noisy sinograms were compared against their reference ones. A correlation coefficient was used as a similarity measure. Table 3.3.1 summarizes the results. It also includes the correlation coefficients for IART reconstruction images from noisy sinograms of different ranges of photon counts computed against the reference image "dolls". It is worth noting that the number of iterations to produce the best image from IART decreases with the increasing amount of noise in a sinogram.

Table 3.3.1. Reference image "dolls". Correlation coefficients for noisy sinograms of different ranges of photon counts and for the reconstruction images they produce.

Range of photon counts in reference sinogram	Correlation coefficient for noisy sinogram	Correlation coefficient for IART reconstruction image from noisy sinogram against "dolls"*	Iteration number for the best IART reconstruction image
$10^4 - 10^5$	0.99992	0.987845	6
$10^3 - 10^4$	0.99940	0.944483	6
$10^2 - 10^3$	0.99409	0.693206	5
$10 - 10^2$	0.94589	0.443530	1

* Correlation coefficient for the 6 iteration IART reconstruction image from the reference sinogram of Fig. 3.3.1 was 0.99311.

Fig. 3.3.7 includes the IART reconstruction images from noisy sinograms for the photon count ranges: $10^4 - 10^5$; $10^3 - 10^4$; $10^2 - 10^3$; $10 - 10^2$. For comparison, Fig. 3.3.8 shows the 6 iteration IART from the reference sinogram of Fig. 3.3.1(b).

From Table 3.3.1, the sinogram similarity to the reference worsens when the range of photon counts goes down. To explain this fact, we go back to the noise simulation procedure that we have used. According to the procedure a random number to replace the original one in a reference sinogram was computed from the Poisson distribution/Gaussian with a mean equal to the value from the reference sinogram (see Section 3.2). When we plot the ratio of a computed random number to the distribution mean as a function of the mean as in Fig. 3.3.9, the plot tapers towards the higher mean values. This indicates that for distributions with larger mean values, there is a greater probability that the computed random number is similar in value to the mean. In consequence, sinograms of a higher range of photon counts ($10^4 - 10^5$) will bear more resemblance to the reference than sinograms of the lower range of photon counts ($10 - 10^2$).

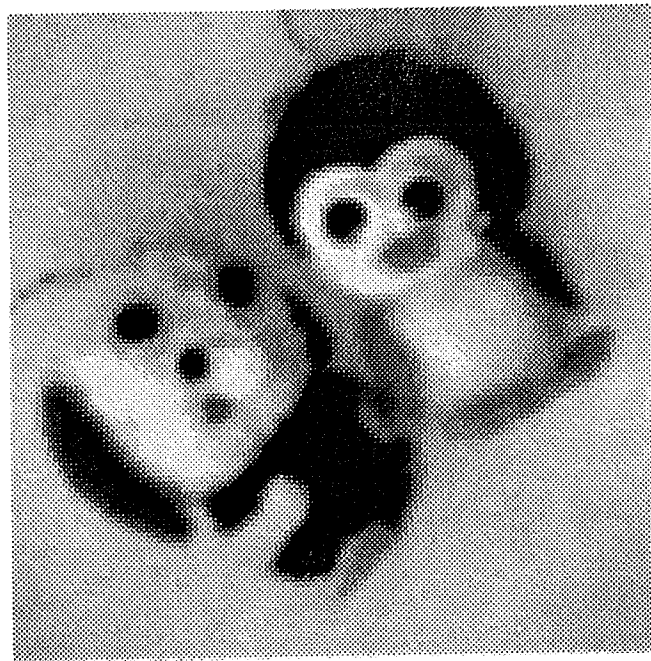


Fig. 3.3.1(a). The reference image "dolls".

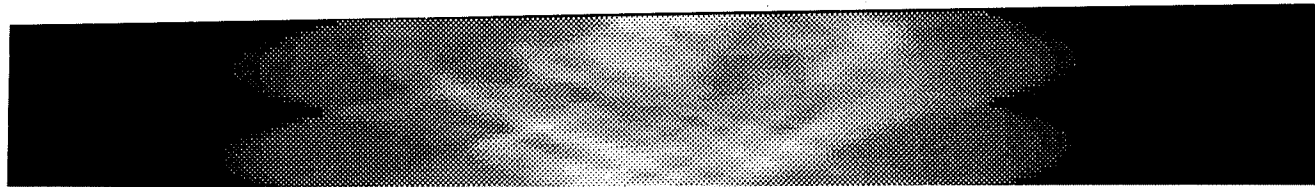
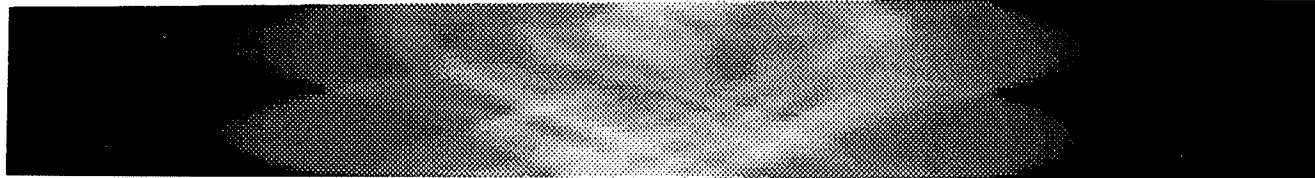
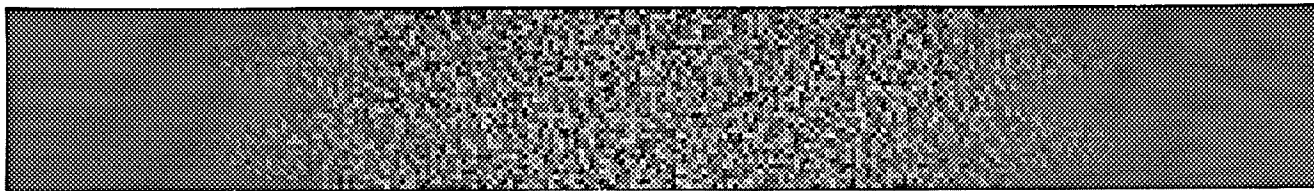


Fig. 3.3.1(b). The sinogram of the reference image "dolls". 35 parallel projections equally spaced over 180° .

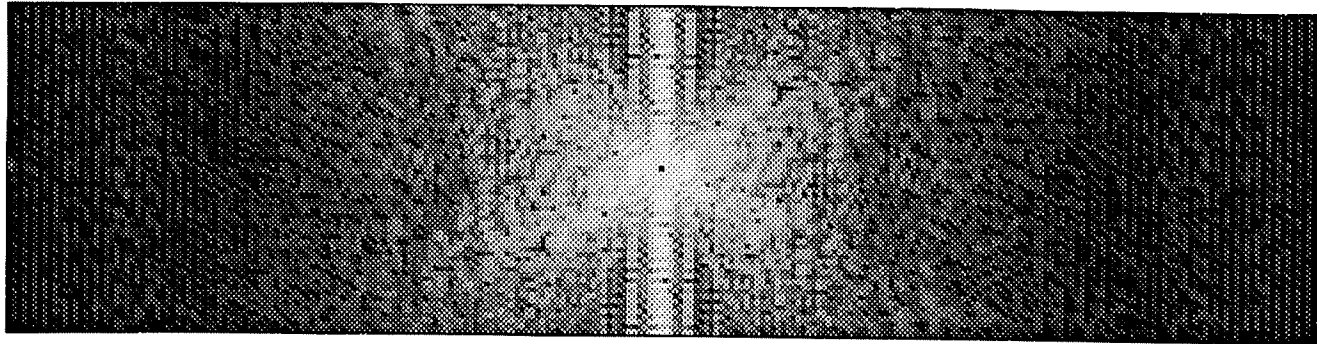


(a)

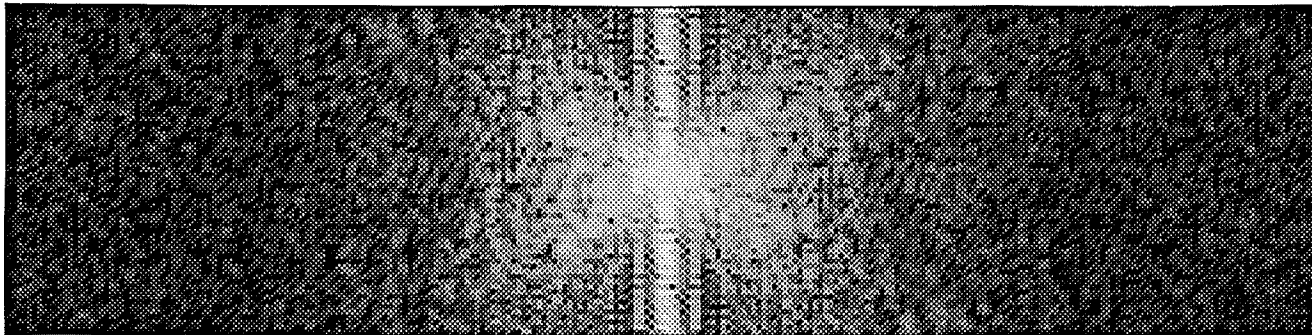


(b)

Fig. 3.3.2. (a), Noisy sinogram that was produced from the reference sinogram in Fig. 3.3.1(b); (b), Noise that was superimposed on the reference sinogram to produce Fig. 3.3.2(a).

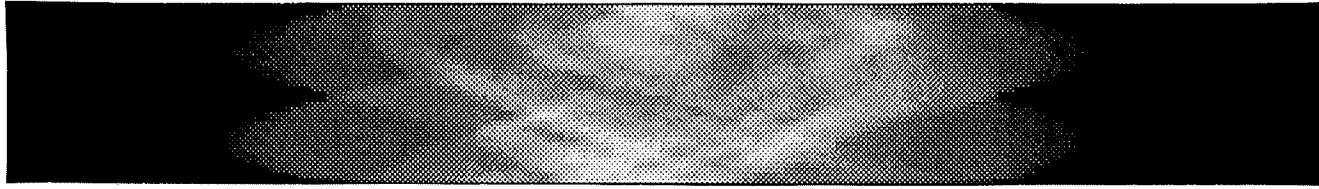


(a)

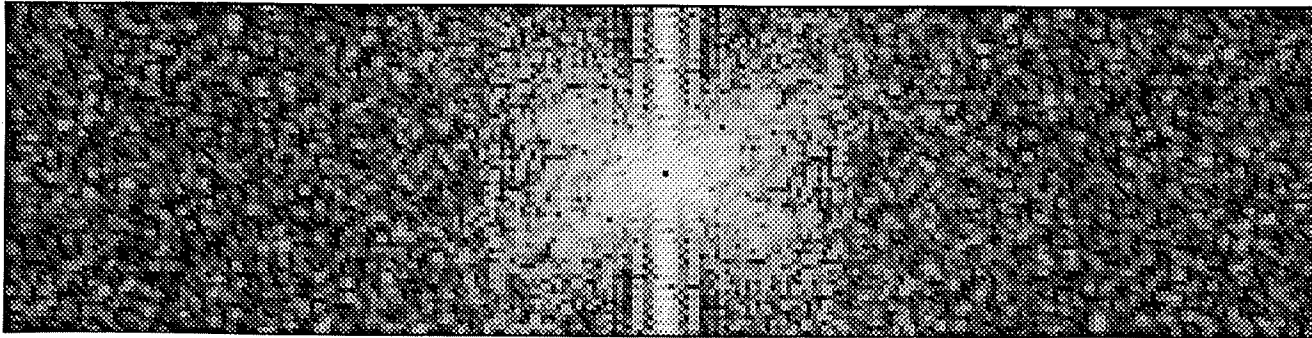


(b)

Fig. 3.3.3. The Fourier spectra of: (a), the reference sinogram in Fig. 3.3.1(b), and (b), the noisy one in Fig. 3.3.2(a).

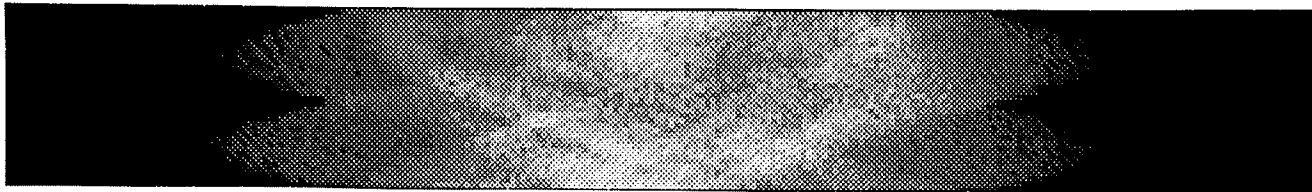


(a)

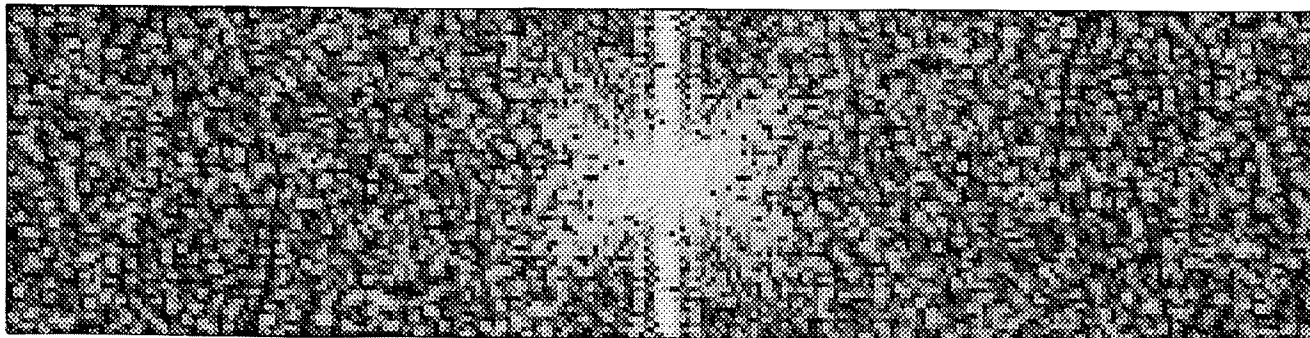


(b)

Fig. 3.3.4. Photon range $10^3 - 10^4$. (a), Noisy sinogram, and (b), its Fourier spectrum,.

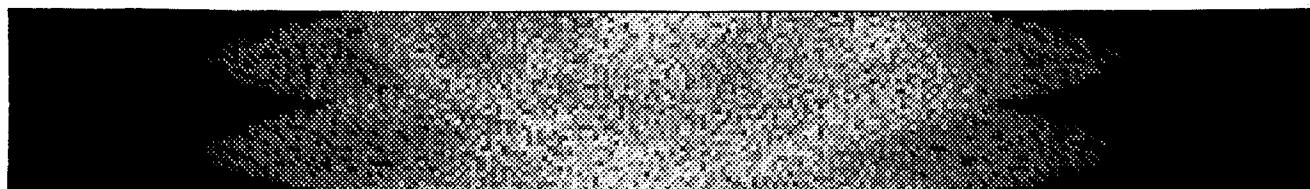


(a)

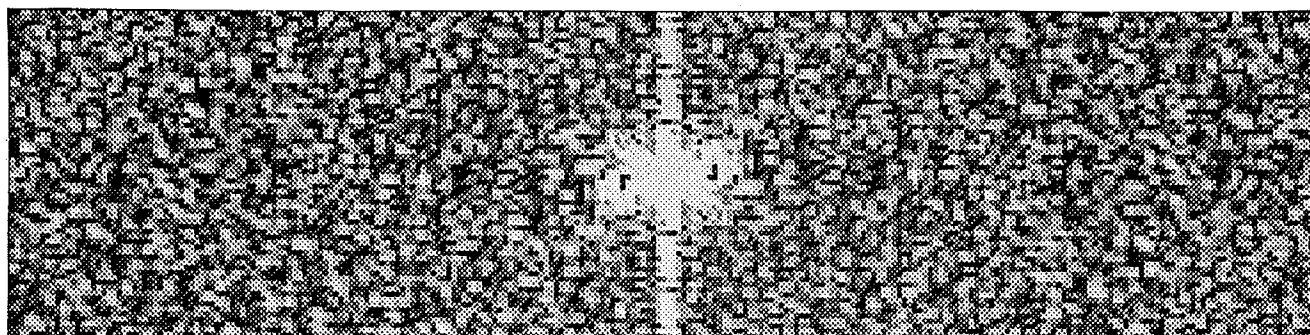


(b)

Fig. 3.3.5. Photon range $10^2 - 10^3$. (a), Noisy sinogram, and (b), its Fourier spectrum.

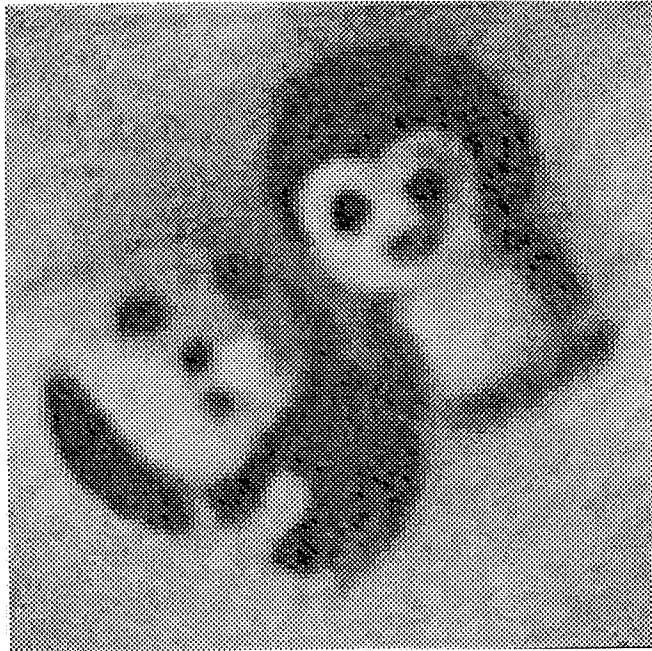


(a)

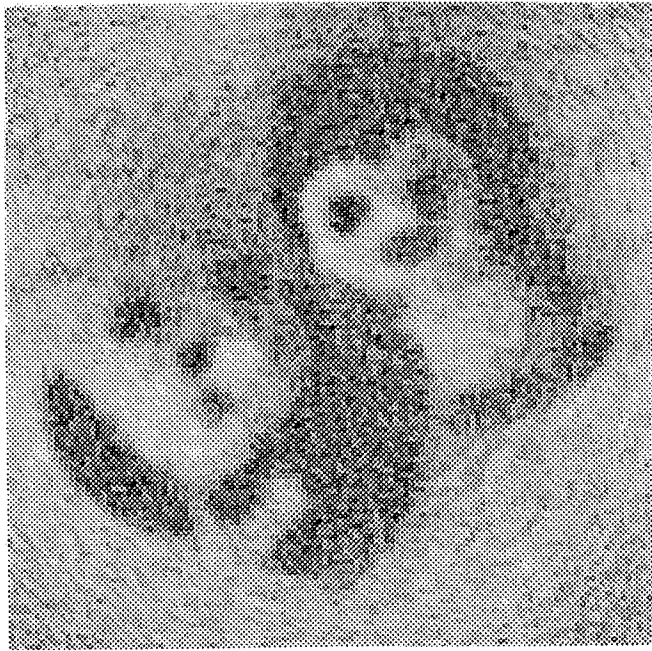


(b)

Fig. 3.3.6. Photon range $10 - 10^2$. (a), Noisy sinogram, and (b), its Fourier spectrum.

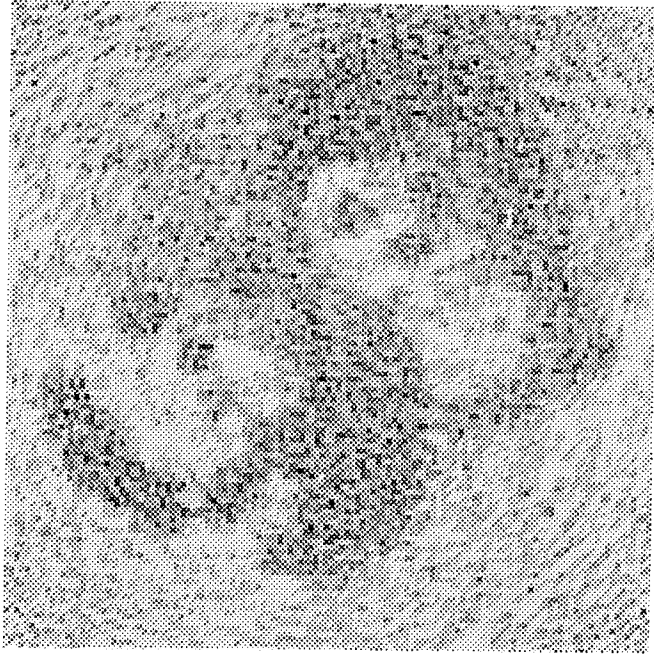


(a)

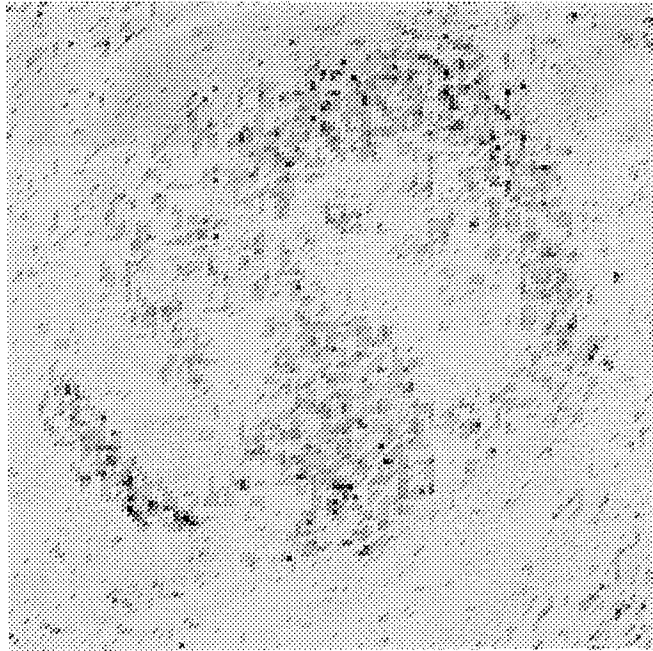


(b)

Fig. 3.3.7. IART reconstructions from: (a), noisy sinogram in Fig. 3.3.2(a), and (b), noisy sinogram in Fig. 3.3.4(a).



(c)



(d)

Fig. 3.3.7 contd. IART reconstructions from: (c), noisy sinogram in Fig. 3.3.5(a), and (d), noisy sinogram in Fig. 3.3.6(a).

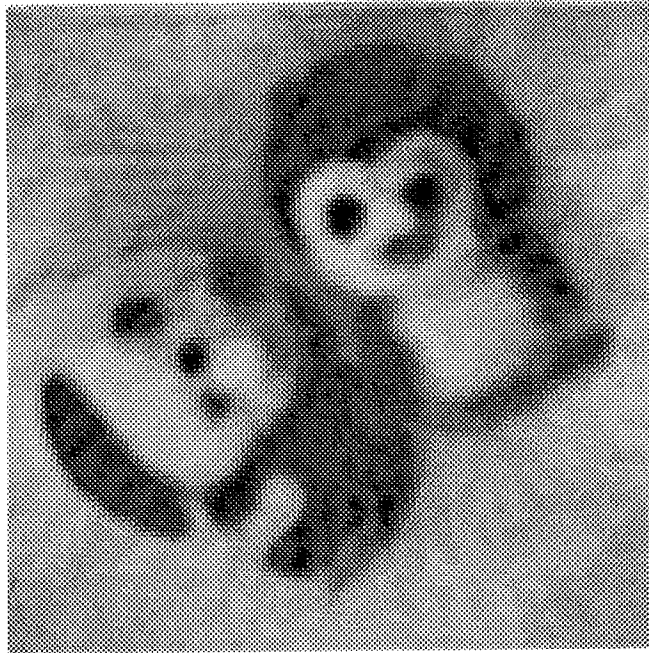


Fig. 3.3.8. The 6 iteration IART reconstruction from the reference sinogram in Fig. 3.3.1(b).

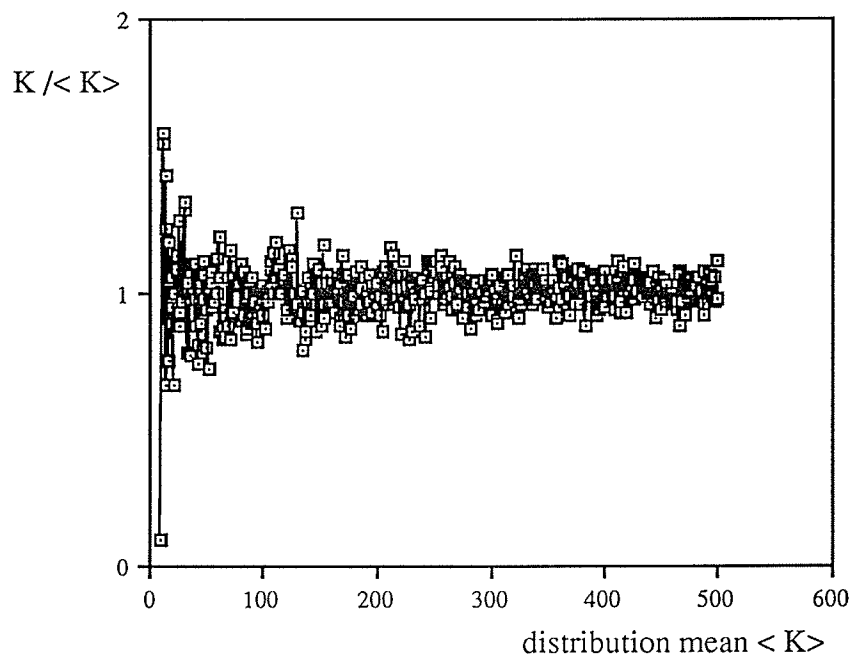


Fig. 3.3.9. The ratio of a random computed number k of a distribution with a mean $\langle K \rangle$ to the mean of the distribution as a function of a mean. One sample at each value of the mean was taken.

3.4. Noise Removal from Noisy Projections

When looking for a way to remove noise from noisy projections, we considered viewing the sinogram as an image: therefore our task became to 'clean' this noisy image. We started with using different real space filters on the noisy sinogram in Fig. 3.3.2(a) [Pavlidis, 1982], [Gonzalez, 1983], [Rosenfeld, 1982]. The efficacy of the noise removal operation was evaluated by computing the correlation coefficient for a filtered sinogram against the reference in Fig. 3.3.1(b). A smoothing low pass filter (LPF) was the first one that we used. With this filter, the value of each pixel in the filtered sinogram was the average of the weighted values of the pixels in the neighborhood around that pixel. The size of neighborhood was 3 by 3 pixels and the weighting of the pixels was one. The resultant filtered sinogram appeared to be even worse for reconstruction than the noisy one. (The correlation coefficient was 0.9465 against 0.9999 for the noisy sinogram.) Similarly, when we used a Sobel edge enhancement filter on the noisy sinogram, the correlation coefficient was 0.6184. In this technique, we used a 3 x 3 window. If the values in the window were as follows:

$$\begin{array}{ccc} v_1 & v_2 & v_3 \\ v_4 & x & v_6 \\ v_7 & v_8 & v_9 \end{array}$$

then the value of the pixel in the filtered sinogram corresponding to x was calculated as the square root of $(A^2 + B^2)$, where

$$A = (v_3 + 2v_6 + v_9) - (v_1 + 2v_4 + v_7)$$

$$B = (v_1 + 2v_2 + v_3) - (v_7 + 2v_8 + v_9)$$

The third filter that we used was a directional filter. It belongs to a group of nonlinear filters as opposed to the above described linear, space-invariant filters. The difference between these two groups of filters is that nonlinear ones do not smear edges, but only remove the noise from the interior of regions. Such filters attempt to detect edges before they apply a smoothing function. The filter procedure we used, at each pixel estimated the direction of an edge, if any, by computing the values of

$$V(\phi) = [f(x, y) - f(x + c(\phi), y + s(\phi))]^2 + [f(x, y) - f(x - c(\phi), y - s(\phi))]^2$$

for $\phi = 0, 45^\circ, 90^\circ, 135^\circ$.

Then the filter function $h(i, j, \phi)$ defined as

$$h(0, 0, \phi) = 0.5, \quad h(c(\phi), s(\phi), \phi) = h(-c(\phi), -s(\phi), \phi) = 0.25,$$

where

ϕ	0°	45°	90°	135°
$c(\phi)$	1	1	0	-1
$s(\phi)$	0	1	1	1

and zero for all other arguments i, j , was applied for that value of ϕ for which $V(\phi)$ was minimum.

The output from this filter was better than from linear filters but the correlation coefficient was still less compared to the one calculated for the noisy sinogram (0.9995 against 0.9999).

Summarized in Table 3.4.1 are the results from using real space filters, confirming that a sinogram is a very specific image that cannot be regarded as a smooth one, and real space processing techniques do not apply to it.

Table 3.4.1. Reference image "dolls". Correlation coefficient for a sinogram filtered with real space filters. Photon count range 10^4 - 10^5 .

Filter used	Correlation coefficient for a filtered sinogram*
LPF	0.946518
Sobel	0.618381
directional filter	0.999546
no filter (noisy sinogram)	0.999920

Correlation coefficient was computed against the reference sinogram in Fig. 3.3.1(b).

In another approach to removing noise from noisy projections, a windowing technique in Fourier space was used [Rowland, 1979], [Budinger, 1979], [Hamming, 1977], [Pratt, 1978], [Castleman, 1979]. In this technique, a window function $w(f)$ is superimposed on a Fourier representation of a projection and the product is transferred back into the real space to produce the noise filtered projection. Symbolically we can illustrate it as

$$\text{noise filtered projection} = \mathcal{F}^{-1}[w(f) \mathcal{F}(\text{projection data})] \quad (3.4-1)$$

where \mathcal{F} stands for a Fourier transform. The window function that we used had the effect of attenuating the contribution of frequencies near the highest frequency component of the Fourier transform of a projection while allowing the frequencies near zero to be passed almost unmodified. When choosing this shape of the window function, we took advantage of the property that the discrete Fourier transform of a function of compact support will tend to have low values at the high frequencies while the most valuable

information required to reconstruct the function in real space is centered around the zero frequency in Fourier domain. Therefore, the attenuation of high frequencies for a noisy function (projection), while slightly affecting the resolution, has the benefit of noise suppression. Depending on the shape of the window function, we can get different levels of noise suppression. In the analysis, Butterworth and generalized Hamming windows were used. The latter one is defined by the equation

$$w(f) = \begin{cases} \alpha + (1 - \alpha) \cos(\pi f / f_c) & \text{if } |f| \leq f_c \\ 0 & \text{if } |f| > f_c \end{cases} \quad (3.4-2)$$

where f_c is the highest frequency component (cutoff frequency) and α is a constant. Fig. 3.4.1 shows how the shape of a Hamming window changes for different values of the constant α .

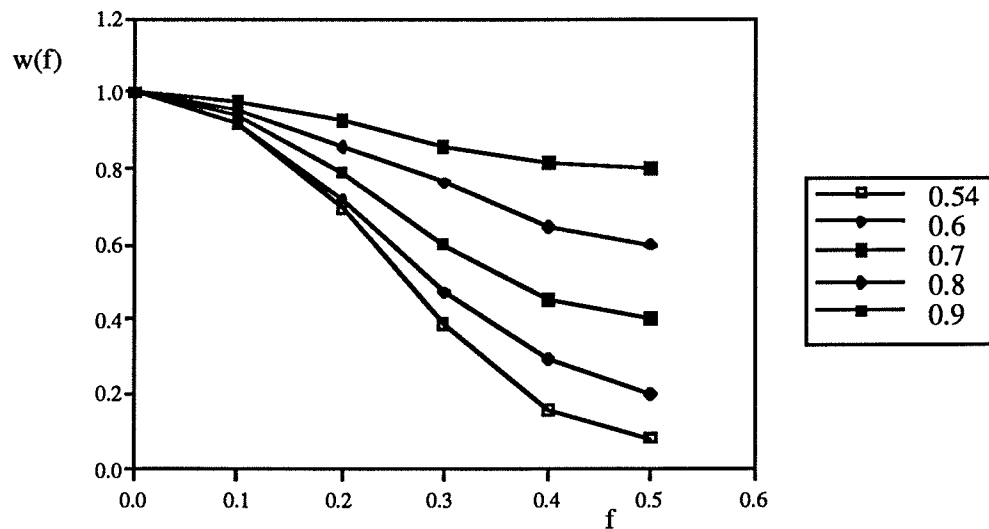


Fig. 3.4.1. Hamming window with a cut off frequency $f_c = 0.5$.

This analysis included using the Hamming window with $\alpha = 0.4; 0.54; 0.6; 0.8; 0.9$. Results on a noisy sinogram are summed up in Table 3.4.2 below.

Table 3.4.2. Reference image "dolls". Correlation coefficient for a sinogram filtered with generalized Hamming window. Photon count range $10^4 - 10^5$.

Hamming window with α equal	Correlation coefficient for a filtered sinogram*
0.4	0.999938
0.54	0.999949
0.6	0.999935
0.8	0.999940
0.9	0.999928
no filter (noisy sinogram)	0.999920

Correlation coefficient was computed against the reference sinogram in Fig. 3.3.1(b).

As it can be seen, in every case the filtered sinogram had better correlation coefficient than the noisy one. The best result was obtained with the constant $\alpha = 0.54$. A similar outcome was also obtained from using the Butterworth window:

$$w(f) = \frac{1}{1+(f/f_c)^{2n}} \quad (3.4-3)$$

where n is the order of the filter. This filter can be designed by calculating the appropriate window width between zero and the pass-band frequency f_p and the

corresponding transition bands between the pass-band frequency f_p and the stop-band frequency f_s , as illustrated in Fig. 3.4.2.

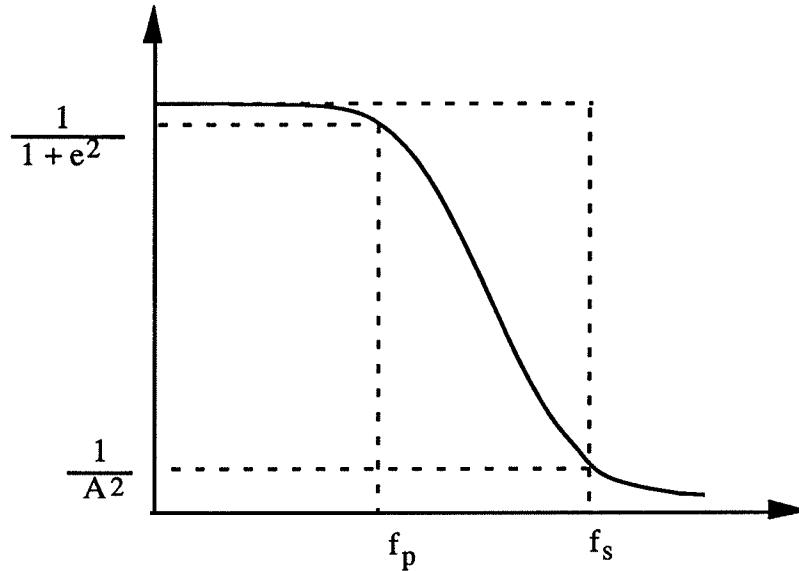


Fig. 3.4.2. Method of designating a Butterworth filter.

Knowing the values of e , A , f_p , f_s , we calculate the parameters n and f_c of the Butterworth filter using the equations

$$n = \frac{\log(e / \sqrt{A^2 - 1})}{\log(f_p / f_s)}$$

$$f_c = \frac{f_p}{e^{1/n}} \quad (3.4-3)$$

The Butterworth window that we used was designed to approach the Hamming window with $\alpha = 0.5$ as this was the case that produced the best results filtering the noisy sinogram. Parameters calculated for the Butterworth window were $n = 3.475$ and

$f_c = 0.238$. The correlation coefficient obtained for a filtered sinogram was 0.999943, i.e. was slightly less than when the Hamming window was used (0.999949).

The above results refer to a noisy sinogram in Fig. 3.3.2(a) that consists of detector readings of the photon range $10^4 - 10^5$. At this range the noisy sinogram does not differ much from the original one (see Section 3.3). Therefore using a windowing technique in Fourier space to remove noise produced only a slightly better reconstruction image compared to the one from noisy projections. This situation improved when we used this technique on sinograms with photon readings of lower ranges. The effect of noise removal was more efficient. Table 3.4.3 shows the effect of using a Hamming window with $\alpha = 0.54$ on noisy sinograms of different photon count ranges while Table 3.4.4 displays the improvement in an IART reconstruction image due to the use of a filtered sinogram.

Table 3.4.3. Reference image "dolls". Correlation coefficients for noisy and filtered with Hamming window sinograms of different ranges of photon counts.

Range of photon counts in reference sinogram	Correlation coefficient for a noisy sinogram	Correlation coefficient for a filtered sinogram*
$10^4 - 10^5$	0.99992	0.99995
$10^3 - 10^4$	0.99940	0.99974
$10^2 - 10^3$	0.99409	0.99611
$10 - 10^2$	0.94589	0.97802

*Filtered sinogram was obtained by using the Hamming window with $\alpha = 0.54$ (Equation 3.4-2).

Table 3.4.4. Reference image "dolls". Correlation coefficients for a reconstruction image from noisy sinograms and filtered with a Hamming window for different ranges of photon counts.

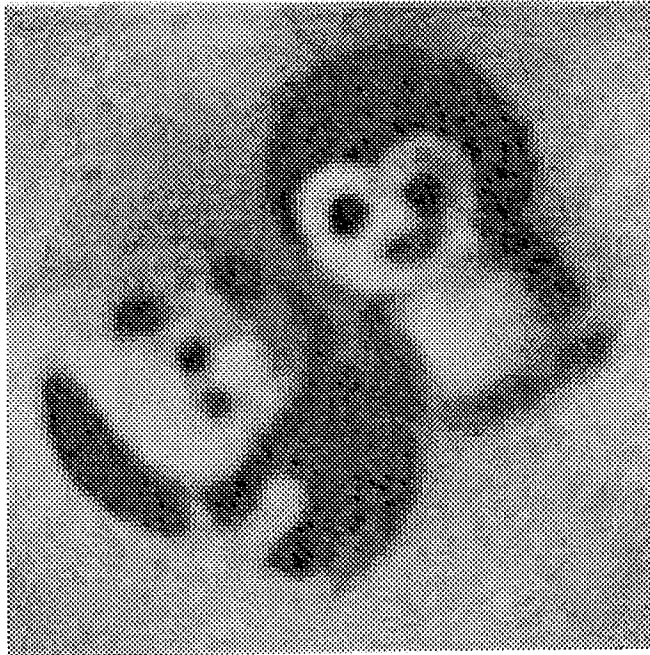
Range of photon counts in reference sinogram	Correlation coefficient* for an IART image from noisy sinogram	Correlation coefficient* for an IART image from filtered sinogram**
$10^4 - 10^5$	0.987845	0.989396
$10^3 - 10^4$	0.944483	0.964948
$10^2 - 10^3$	0.693206	0.790550
$10 - 10^2$	0.443530	0.531808

*Correlation coefficient was computed against the reference image "dolls".

**Filtered sinogram was obtained by using the Hamming window with $\alpha = 0.54$ (Equation 3.4-2).

Figs. 3.4.3 - 6, for different photon count ranges, present IART reconstruction images from (a), noisy sinograms, and (b), from filtered ones using the Hamming window with $\alpha = 0.54$.

In summary, using window functions in the frequency domain to suppress projection noise improves quality of a reconstruction image in comparison to the image obtained from noisy projections. The efficacy of the procedure in terms of the correlation coefficient value increases when the range of photon counts registered by a detector array goes down. Visually, the most gratifying effect from using the windowing procedure seems to be for a sinogram of $10^3 - 10^4$ range of photon counts.



(a)

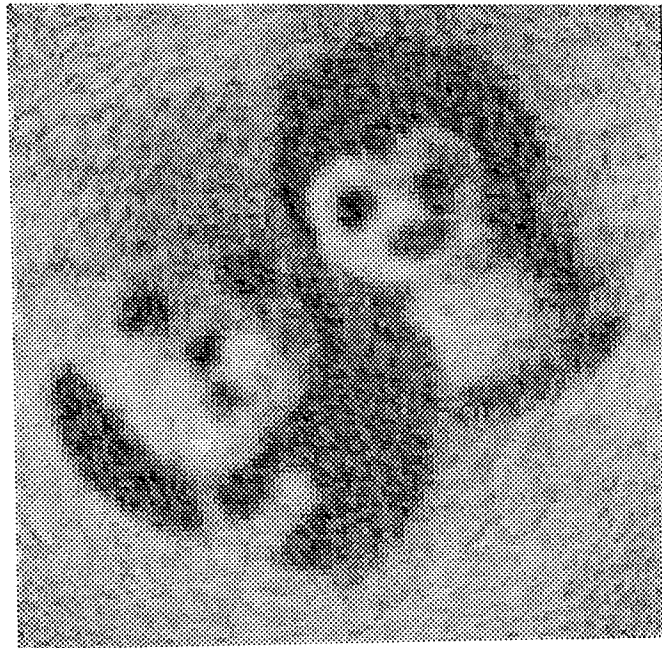


(b)

Fig. 3.4.3. IART reconstruction images from (a), noisy, and (b), filtered with Hamming window with $\alpha = 0.54$ sinograms of $10^4 - 10^5$ photon count range.

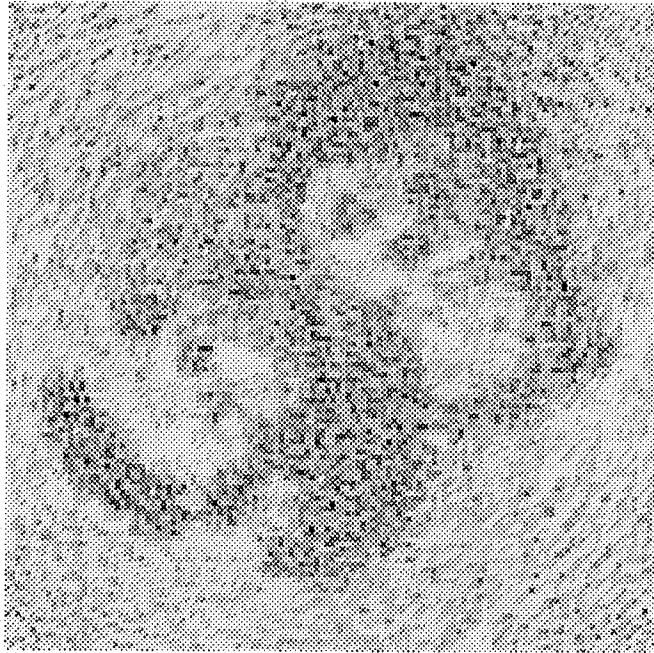


(a)

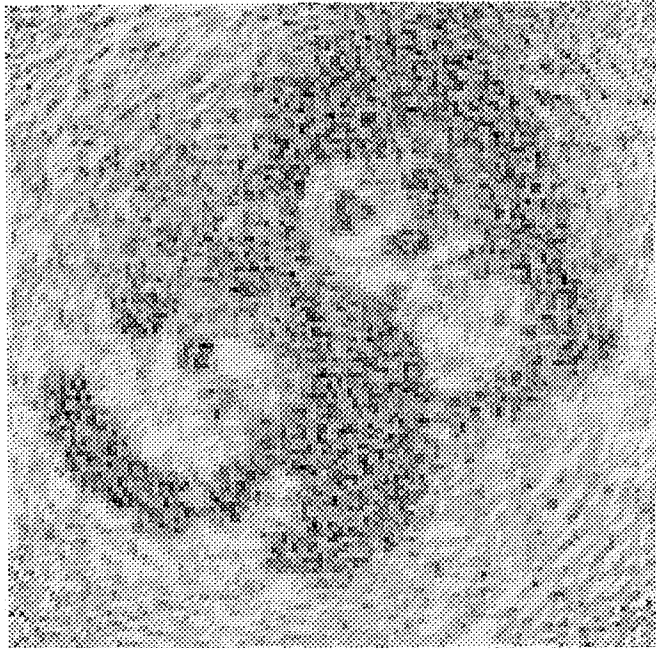


(b)

Fig. 3.4.4. IART reconstruction images from (a), noisy, and (b), filtered with Hamming window with $\alpha = 0.54$ sinograms of $10^3 - 10^4$ photon count range.

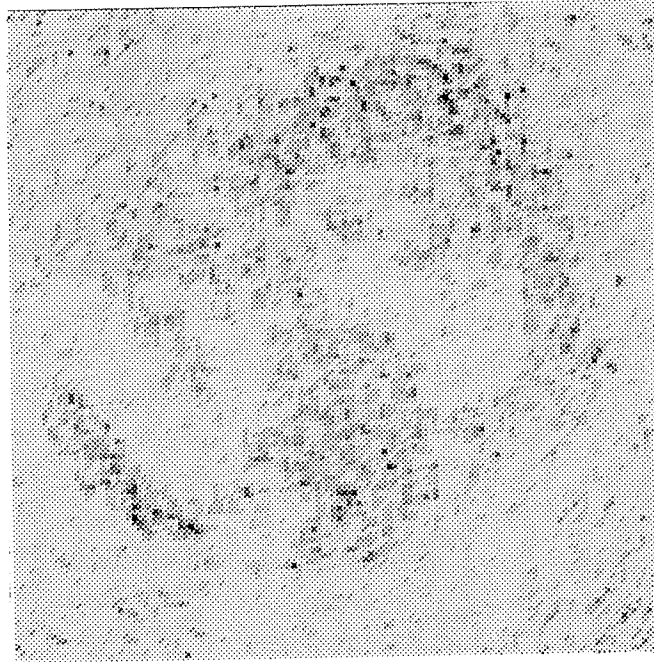


(a)

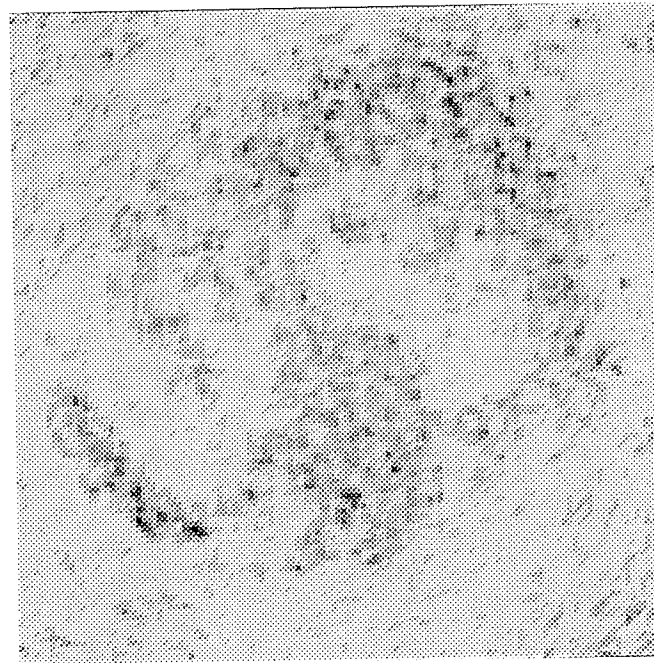


(b)

Fig. 3.4.5. IART reconstruction images from (a), noisy, and (b), filtered with Hamming window with $\alpha = 0.54$ sinograms of $10^2 - 10^3$ photon count range.



(a)



(b)

Fig. 3.4.6. IART reconstruction images from (a), noisy, and (b), filtered with Hamming window with $\alpha = 0.54$ sinograms of $10 - 10^2$ photon count range.

3.5. Filtering Noisy Sinograms of Different Objects

Medical images form a very specific group of images. Fig. 3.5.1 displays (a), an example medical image, and (b), its sinogram. The sinogram consists of 45 projections equally spaced over 180° and was produced using a parallel geometry beam. Photon count values are from the $10^4 - 10^5$ range. We used this sinogram as a reference and by applying the noise simulation procedure from Section 3.2, we produced a noisy sinogram in Fig. 3.5.2(a). Noise that was superimposed on a reference sinogram (Fig. 3.5.1(b)) is shown in Fig. 3.5.2(b). Fig. 3.5.3 represents Fourier spectra of both the reference, (a), and the noisy, (b), sinograms.

To remove noise, we began with an implementation of a real space filter on the noisy sinogram. We did it deliberately as we wanted to confirm results from Section 3.4. The filter of our choice was the directional one as this was the one that gave the best results on the noisy sinogram in Fig. 3.4.2(a) of the previous section (see Table 3.4.1). (For detailed description see Section 3.4.) The correlation coefficient calculated for a filtered sinogram was 0.999733 against 0.999925 for the noisy one. Thus the result obtained confirmed conclusions drawn in the previous section that real space processing techniques do not work well on sinograms. When using the windowing technique in the Fourier space, similarly as in the previous section, we applied the generalized Hamming window to the noisy sinogram. We started with the Hamming window with $\alpha = 0.54$. The result was a less noisy sinogram. The correlation coefficient of the filtered sinogram was 0.999938 against 0.999925 for the noisy one. As the improvement in the correlation coefficient due to the Hamming window use was less compared when it was used on the noisy sinogram of the previous section (see Table 3.4.2), we extended our analysis to include using the Hamming window with $\alpha = 0.7; 0.8; 0.9$. The results obtained, in form of correlation coefficient values are summarized in Table 3.5.1 below.

Table 3.5.1. Reference image "head". Correlation coefficient for a sinogram filtered with generalized Hamming window.

Hamming window with α equal	Correlation coefficient for a filtered sinogram*
0.54	0.999938
0.7	0.999941
0.8	0.999942
0.9	0.999941
noisy sinogram	0.999925

Correlation coefficient was computed against the reference sinogram in Fig. 3.5.1(b).

As in the previous section, for every case the correlation coefficient showed improved similarity of the filtered sinogram to the reference one, though the best result was achieved with the constant $\alpha = 0.8$. This is unlike the results for the sinogram in Fig. 3.3.2(a) of the previous section and is due to different contents of the reference sinogram used. The main dissimilarity between Figs. 3.3.2(a) and 3.5.2(a) is that the latter is characterized by relatively small variations of the intensity function values throughout the image contents in comparison to the former. This feature is characteristic for the major portion of medical images.

Fig. 3.5.4 displays the 9 iteration IART reconstruction images computed from (a), the reference projections, (b), noisy projections, and (c), filtered ones through the use of a Hamming window with $\alpha = 0.8$. The correlation coefficients are 0.975543 for the reconstruction from the reference projections, 0.962315 and 0.964103 for the reconstructions from the noisy and filtered projections, respectively.

Results of this and the previous sections indicate that a sinogram is a nonsmooth image. Therefore using real space processing techniques for noise suppression is not applicable. The windowing in the Fourier space technique can be used with positive results. Although to benefit most from this technique, the choice of an appropriate window function is required. The selection of a window function, however, can be predetermined as it depends on the contents of a reference image/object. Therefore through classification of reference images, the choice of the best window function can be made automatic.

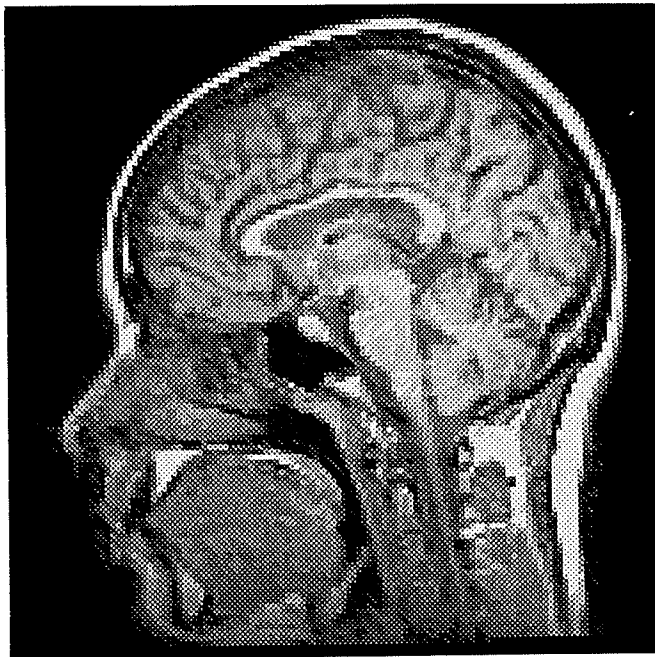


Fig. 3.5.1(a). The reference image "head".

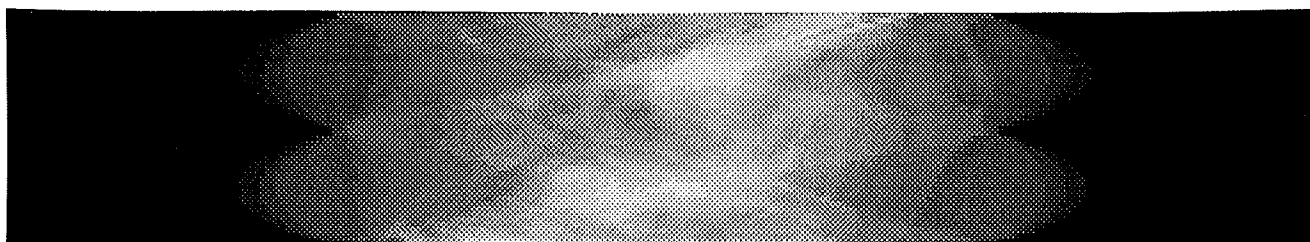
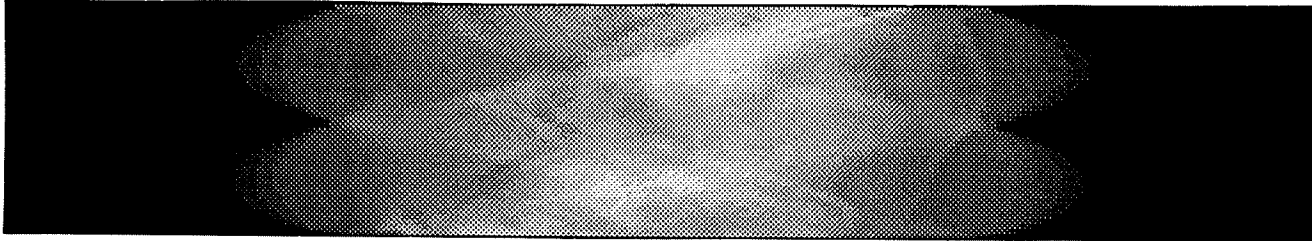
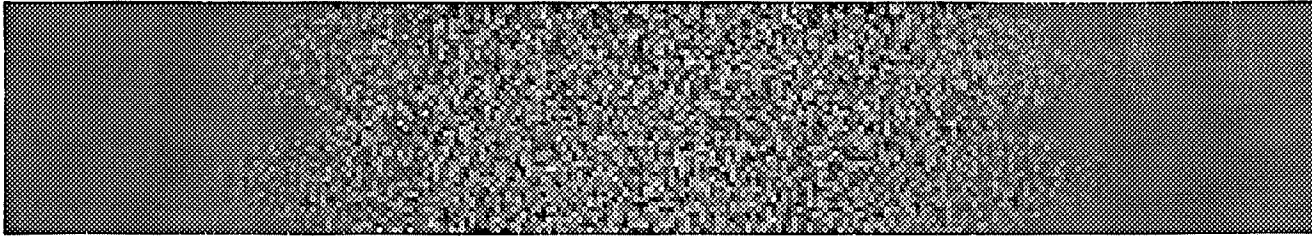


Fig. 3.5.1(b). The sinogram of the reference image "head". 45 parallel projections equally spaced over 180° .

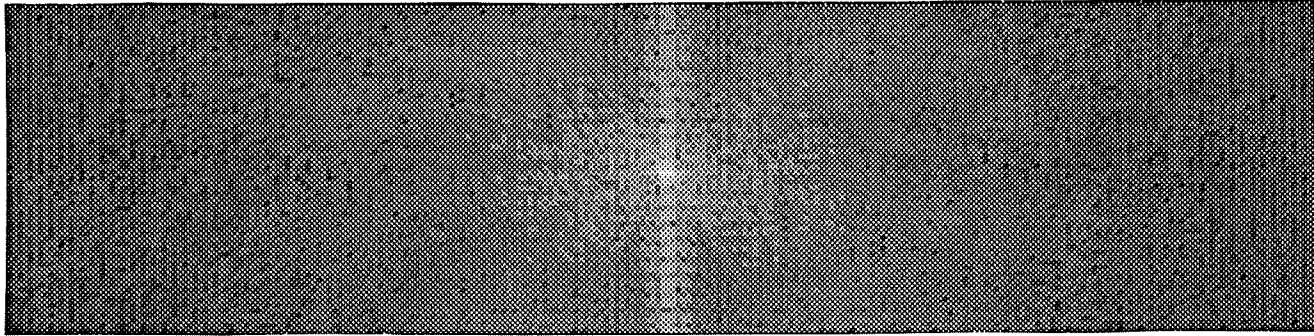


(a)

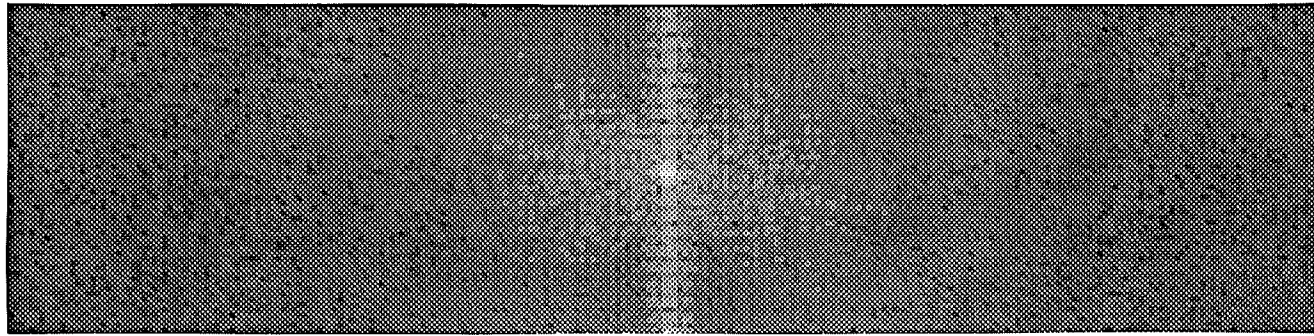


(b)

Fig. 3.5.2. (a), Noisy sinogram that was produced from the reference sinogram in Fig. 3.5.1(b); (b), Noise that was superimposed on the reference sinogram to produce Fig. 3.5.2(a).



(a)



(b)

Fig. 3.5.3. The Fourier spectra of (a), the reference sinogram in Fig. 3.5.1(b), and (b), the noisy one in Fig. 3.5.2(a).



(a)



(b)

Fig. 3.5.4. IART reconstructions from (a), the reference sinogram in Fig. 3.5.1(b), and (b), the noisy sinogram in Fig. 3.5.2(a).



Fig. 3.5.4(c). IART reconstruction from the noise filtered sinogram with Hamming window with $\alpha = 0.8$.

3.6. Concluding Remarks

Photon noise is the dominating one that affects data acquisition x-ray computed tomography. Iterative methods are sensitive to any distortion of the projection data, yet they use projections that are noisy.

In this chapter, different ways to remove noise from the projection data have been examined. The correlation similarity measure have been used to evaluate the results, i.e. the filtered projection sinogram was evaluated against the reference sinogram that was not affected by any noise at all. Also, the improvement in the reconstruction image quality was checked.

We started from using a set of projections to form a sinogram, an image, to apply enhancement techniques to it to suppress noise. The results obtained were negative,

indicating that as a sinogram is not a smooth image; the real space processing techniques do not work.

In the other approach, the windowing technique in Fourier space was used. The window functions that were used suppress high frequencies, taking advantage of the fact that the discrete Fourier transform of a function of compact support has low values at the high frequencies. Consequently, removing the high frequency components should not affect significantly image fidelity, while there is a good chance for improvement due to the fact of removing the high frequency noise components. Basically, the Hamming general window was used as a window function, for by changing the value of its constant, we could have controlled the threshold. The results obtained were positive for both reference images encouraging use of this technique for the purpose of noise suppression in the projection data.

CHAPTER IV

FOURIER SPECTRUM. NEW WAYS OF USING IT

4.1. Introduction

In image processing problems, the Fourier transform has a wide range of applications. The central slice theorem [Barrett, 1981], [Rosenfeld, 1982], [Ekstrom, 1984] has become basic to the Fourier backprojection reconstruction method, the most widely used algorithm in computed tomography. (The theorem relates a one dimensional Fourier transform of a reference image function projection to its two dimensional Fourier transform.) Two dimensional Fourier transforms are used for image enhancement, restoration, encoding, description, etc.[Gonzalez, 1987], [Castleman, 1979].

A Fourier transform $F(u,v)$ of a real function $f(x,y)$ is generally complex; that is

$$F(u,v) = R(u,v) + jI(u,v) \quad (4.1-1)$$

where $R(u,v)$ and $I(u,v)$ are, respectively, the real and imaginary components of $F(u,v)$. Equation (4.1-1) is often expressed in the exponential form:

$$F(u,v) = |F(u,v)| e^{j\Phi(u,v)} \quad (4.1-2)$$

where

$$|F(u, v)| = [R^2(u, v) + I^2(u, v)]^{1/2}$$

$$\Phi(u, v) = \tan^{-1} \left[\frac{I(u, v)}{R(u, v)} \right]$$

The magnitude function $|F(u, v)|$ is called a Fourier spectrum of $f(x, y)$, and $\Phi(u, v)$ its phase angle.

For a two-dimensional function, such as an image, its Fourier spectrum can be displayed as an intensity function. This representation is helpful for interpretation purposes. The following sections will show new ways in which the Fourier spectrum can be used:

- 1) To identify a reconstruction image computed by a linear or nonlinear reconstruction method;
- 2) To estimate the optimal number of iterations for iterative reconstruction methods;
- 3) As a qualitative evaluation measure in reconstruction.

In the experiments, the Fourier backprojection, FBP, (linear) and Interpolative Algebraic Reconstruction Techniques, IART, (nonlinear) reconstruction algorithms were used. In all experiments where IART was used, to compute the estimate $\tilde{f}(\vec{r})$ of the image density function $f(\vec{r})$, the following equation was applied

$$\tilde{f}^{q+1}(\vec{r}_{ij}) = \sum_{k=1}^N g_{ij}(u_k) \frac{p_k}{p_k^q} \tilde{f}^q(\vec{r}_{ij}) \quad (4.1-3)$$

where

$$\sum_{k=1}^N g_{ij}(u_k) = 1$$

and superscripts $q+1, q$ represent the $(q+1)$ ' and (q) 'th estimates $\tilde{f}(\vec{r})$, and p_k and p_k^q are the measured and corresponding calculated projections, respectively, $g(u_k)$ is the

interpolation function and N represents the number of detectors in a detector array. One increment of q means that all projections of each pixel have been considered once. The starting value of the estimate of the object optical density was chosen to be equal to 1, i.e. $\tilde{f}^0(\vec{r}_{ij}) = 1$. The reference image and all reconstruction images were on 128 x 128 matrices.

4.2. Fourier Spectrum as a Measure for Distinguishing Linear from Nonlinear Reconstruction Methods

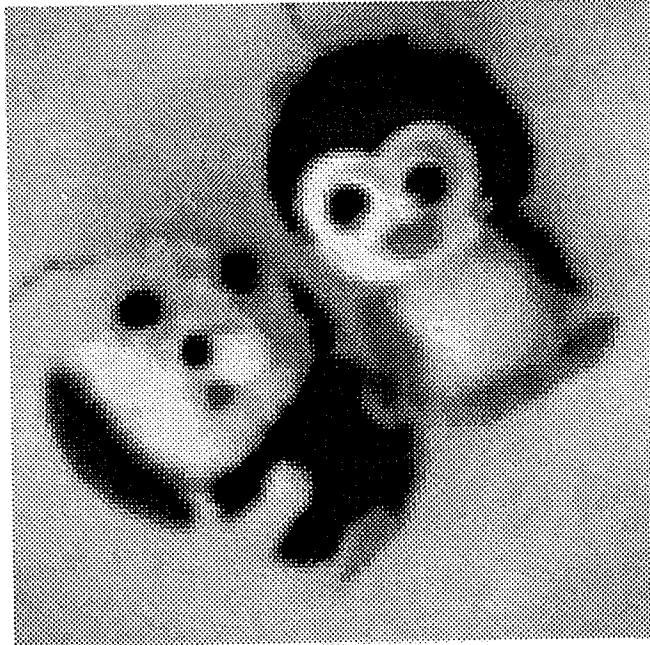
One of the new applications of a Fourier spectrum this thesis introduces is to use it as a determinant in the recognition of linear from nonlinear reconstruction methods. A reconstruction method is a mapping \mathcal{L} which maps an input array $f(n,m)$ into an output array $g(n,m) = \mathcal{L}\{f(n,m)\}$ where n and m range over the positive and negative integers. If $g_1 = \mathcal{L}\{f_1\}$ and $g_2 = \mathcal{L}\{f_2\}$ and $ag_1 + bg_2 = \mathcal{L}\{af_1 + bf_2\}$ for arbitrary constants a and b , and all f_1 and f_2 then the method is linear. Otherwise, the method is a nonlinear one.

The Fourier backprojection (FBP) is a linear reconstruction method while Interpolative Algebraic Reconstruction Techniques (IART) belong to the group of nonlinear reconstruction methods. In our experiments we used them as representatives of these two different groups of reconstruction methods.

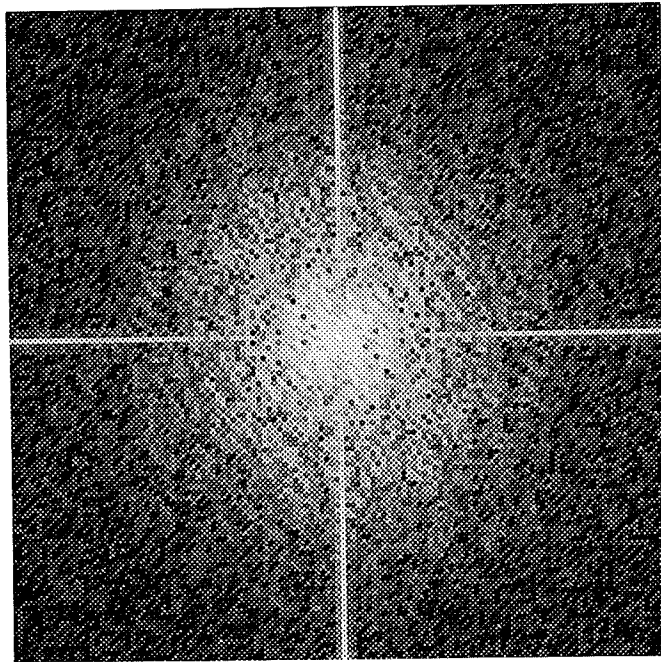
For the same set of an input data, reconstructed images were computed using FBP and IART reconstruction methods and their Fourier spectra were compared. Fig. 4.2.1 represents the (a), reference test object "dolls" that we used, and (b), its Fourier spectrum. We used 35 projection directions equally spaced over 180° and parallel beam geometry. Resulting reconstructions from Fourier backprojection (FBP) and Interpolative Algebraic Reconstruction Techniques (IART) for 21 iterations (the best quality reconstruction image) are presented in Figs. 4.2.2(a) and (b), respectively. Figs. 4.2.3(a) and (b) display Fourier spectra of the reconstruction images of Figs. 4.2.2(a) and (b), respectively. One look at the

spectra and one can see how different they are. The spectrum resulting from the use of IART bears better resemblance to the spectrum of the reference image (Fig. 4.2.1(b)). It also looks smoother and somehow interpolated, as opposed to the spectrum from the use of FBP. The latter looks sharper and the intensity function has its points allocated mainly along the projection directions (streaks). This can be explained as follows: FBP, as a representative of a linear reconstruction method, is based on the central slice theorem and an interpolation function is used only once during the final backprojection. IART, being a representative of a nonlinear reconstruction method, just by the nature of the method performs interpolation numerous times and that shows in its Fourier spectrum. In Figs. 4.2.4(a) and (b) a Sobel edge enhancement filter was used with a 3×3 pixel window, or mask, on Fourier spectra of FBP and IART reconstruction images, respectively. The interpolation achieved by IART compared to FBP becomes obvious.

For comparison, in Fig. 4.2.5 are displayed, as an intensity function, Fourier phases of (a), the test object "dolls", and its reconstructions by (b), FBP and (c), IART reconstruction methods. Although both of them are very noisy, one can see that still the phase image of IART bears more resemblance to the original than the one computed from the FBP. (Correlation coefficients of Figs. 4.2.5(b) and (c) computed with regard to the image of the Fourier phase of the reference object (Fig. 4.2.5(a)) are $\epsilon = 0.20265$ and 0.31763 respectively. For computation of ϵ , Equation 4.3-1 of the following section was used.)

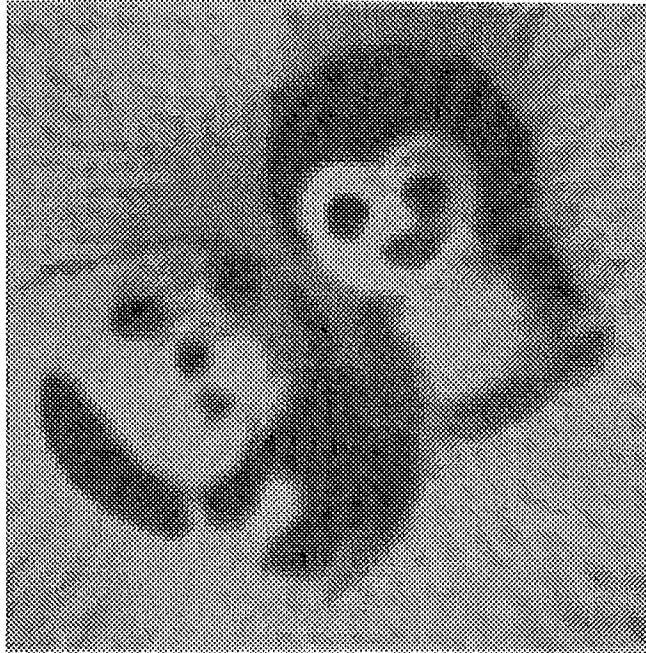


(a)

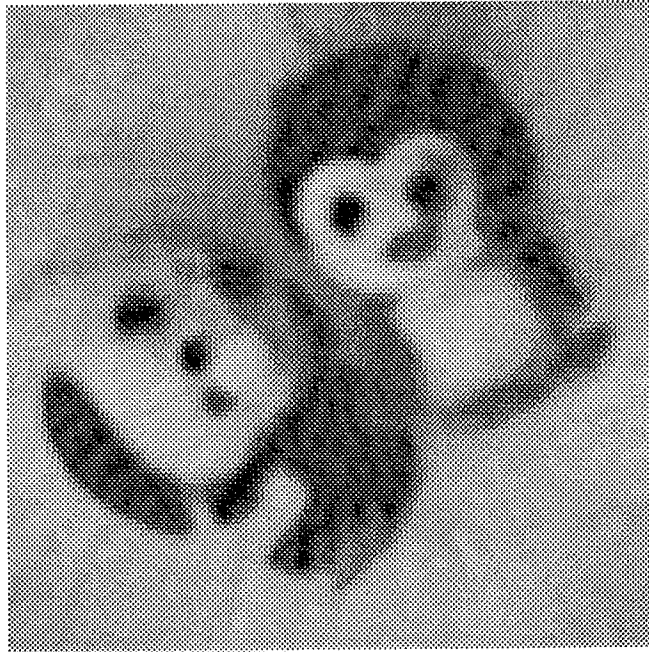


(b)

Fig. 4.2.1. (a) Reference image "dolls", 128 x 128 pixels; (b) Fourier spectrum of "dolls".

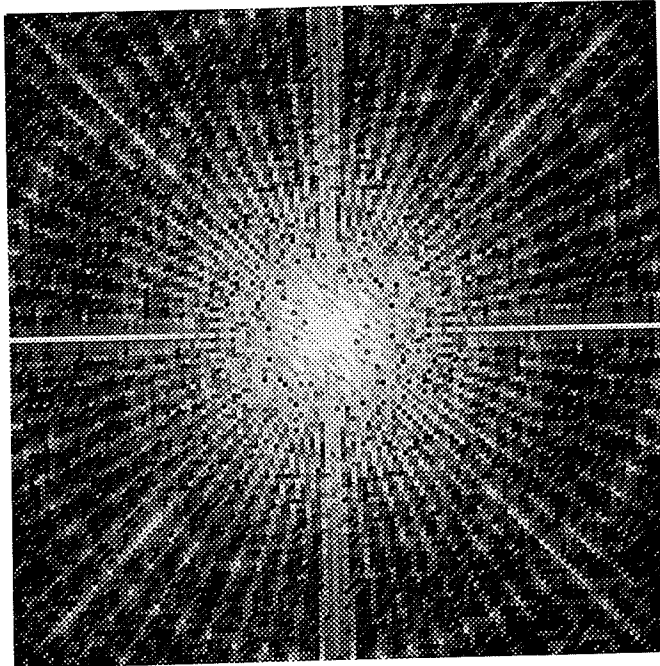


(a)

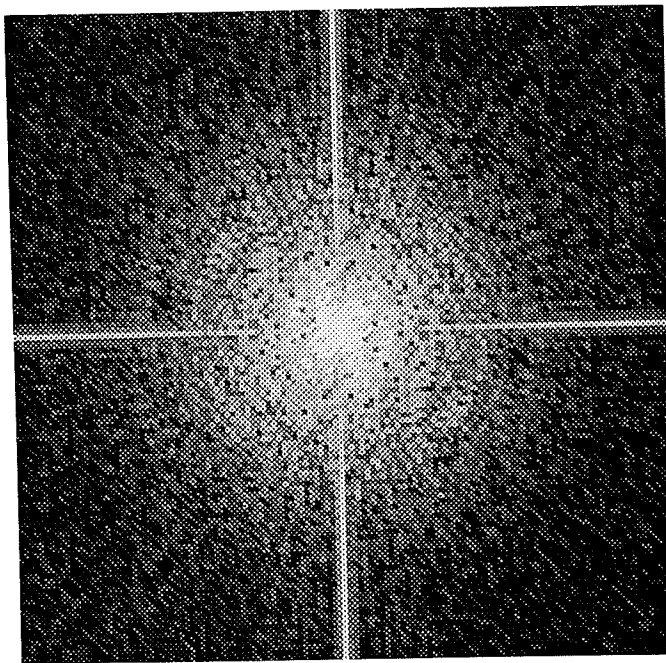


(b)

Fig. 4.2.2. Parallel beam geometry, 35 projection directions equally spaced over 180° . Reconstruction of "dolls" using: (a), Fourier Backprojection (FBP); (b), Interpolative Algebraic Reconstruction Techniques (IART) (21 iterations).

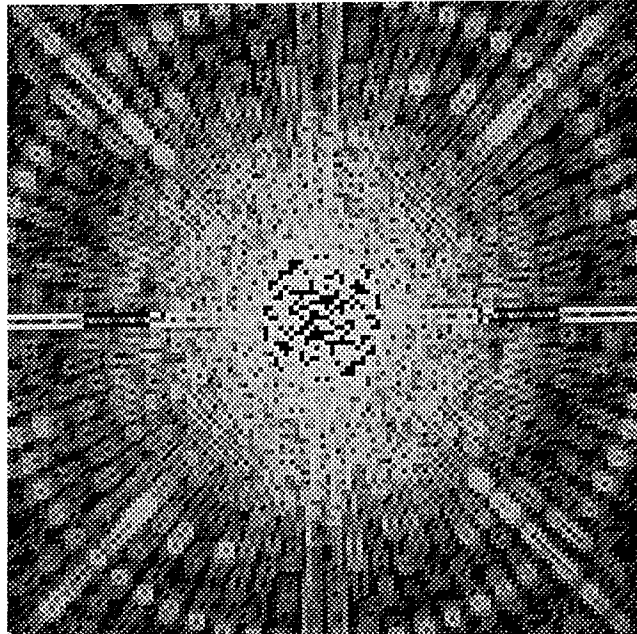


(a)

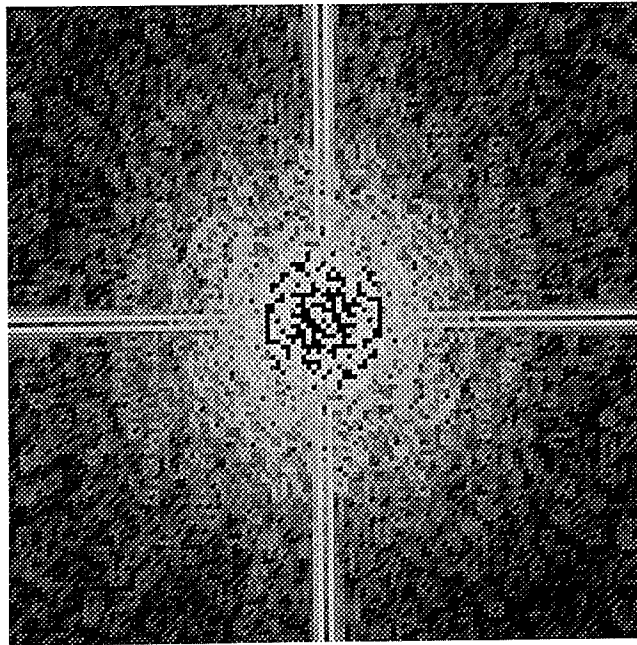


(b)

Fig. 4.2.3. Fourier spectrum of: (a), Fig. 4.2.2(a), FBP reconstruction of "dolls"; (b), Fig. 4.2.2(b), IART (21 iterations) reconstruction of "dolls".

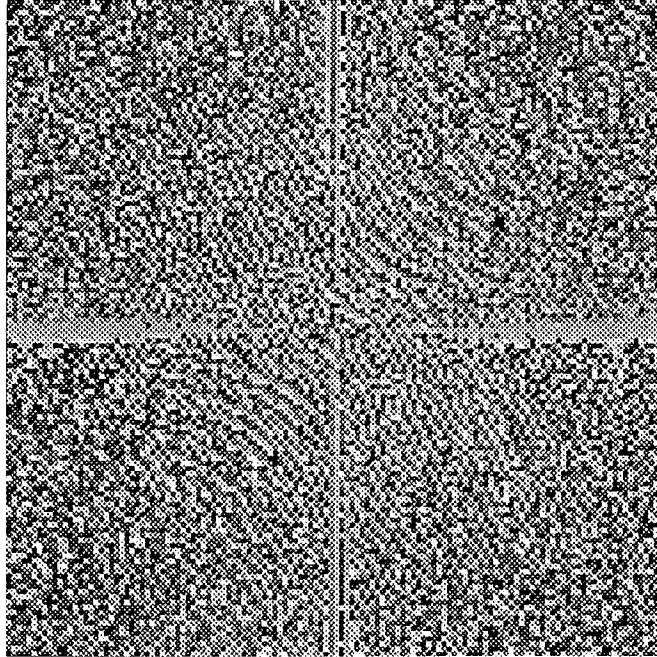


(a)

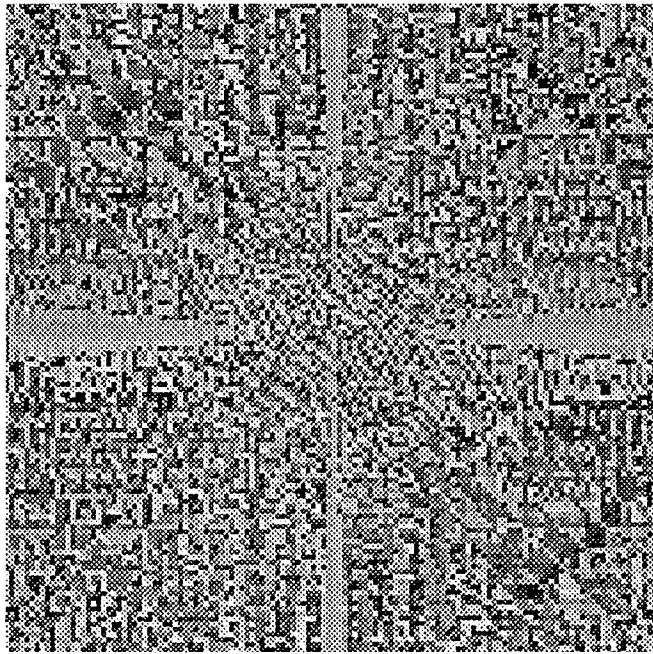


(b)

Fig. 4.2.4. Sobel edge enhancement filter with a 3 x 3 pixel window used on: (a), Fourier spectrum in Fig. 4.2.3(a); (b), Fourier spectrum in Fig. 4.2.3(b).



(a)



(b)

Fig. 4.2.5. Fourier phase of: (a), reference image "dolls"; (b), FBP reconstruction of "dolls".

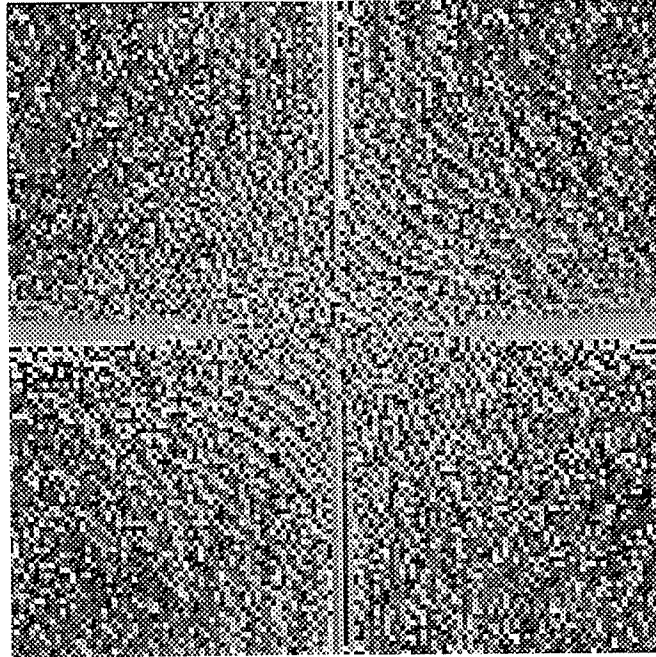


Fig. 4.2.5(c). Fourier phase of IART reconstruction of "dolls" (21 iterations).

4.3. Fourier Spectrum as a Qualitative Image Evaluation Measure

The best way to compare reconstruction algorithms is to do an experimental comparative study, rather than a theoretical one. The reason for this is that different methods perform differently relative to each other in different situations. Their relative efficiency is also affected by the input data: how many projection directions and at what range, noise level, etc.. Every algorithm appears to have its own best set of objects and conditions.

There are many comparison criteria which can be used. (Section 5.2 discusses this subject in more detail.) Quantitative evaluation measures like the similarity (correlation coefficient), overall nearness of the reference and the reconstructed images, and resolution

of fine detail are the most commonly used in practice. Visual evaluation, though subjective, cannot be ignored. In view of the way the reconstructions are used in practice, there is hardly a better way for judging which reconstruction is better under given circumstances.

This thesis introduces a new evaluation measure of qualitative nature that is based on an approach similar to the way a human eye makes the assessment. It relates to the Fourier space.

When we make a visual evaluation we are looking, in fact, for the difference in fluctuations of an intensity function of an image against the reference object. Simple subtraction of the reconstruction image from the reference object will show exactly what we have been looking for, i.e. if and how the relative intensity function has been changed throughout the image as the result of the reconstruction process.

The evaluation criterion that is being introduced is a subtraction of Fourier spectra of images (reconstruction from reference). It will be shown that by using it one can clearly recognize the type of noise, characterized by its frequency, that has been introduced during the reconstruction process. In other words one will be able to see how the reconstruction method performed on different elements of the reference image. This information can be helpful when making a choice on a reconstruction method or deciding on use of one of the image enhancement techniques.

This measure was used to compare the FBP and IART reconstruction images of the reference image "dolls" in Fig. 4.2.1(a) of the previous section. Just as a reminder, both the FBP and IART reconstruction images were computed from the same set of 35 parallel projections equally spaced over 180° and are displayed in Figs. 4.2.2(a) and (b), respectively. Corresponding spectra are displayed in Fig. 4.2.3. Subtraction results are displayed in Figs. 4.3.1: Images (a) and (b) represent the subtraction of Fourier spectra of the reconstructed images of "dolls" computed using FBP (Fig. 4.2.3(a)) and IART (Fig. 4.2.3(b)), respectively, from the spectrum of the reference image (Fig. 4.2.1(b)). It is clearly seen that FBP performed much worse by introducing greater amounts of both

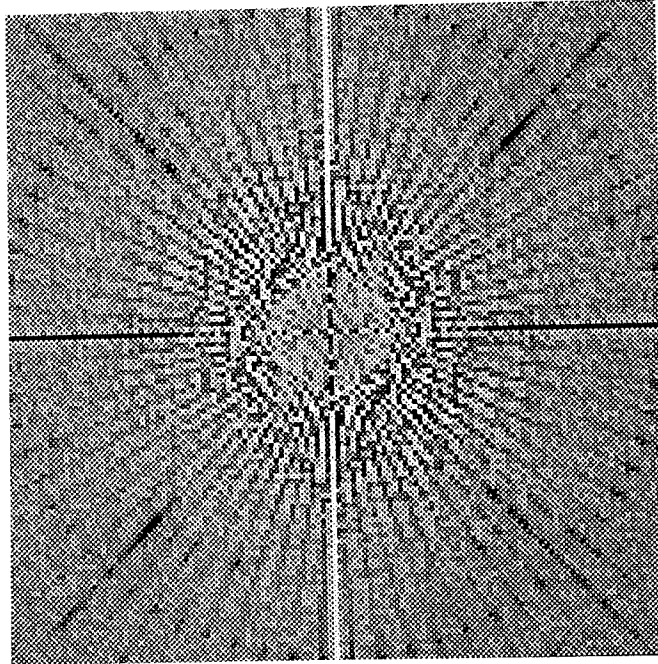
high and low frequency noise compared to IART. The latter performed well for low frequencies introducing only a small amount of a high frequency noise that causes edge unsharpness.

For comparison, Fig. 4.3.2 displays results of a similar operation of subtraction on the images of the Fourier phase for both reconstruction methods (FBP and IART). The only difference that one can notice is that IART produces phase values that are in agreement with the reference object for a larger number of elements than FBP.

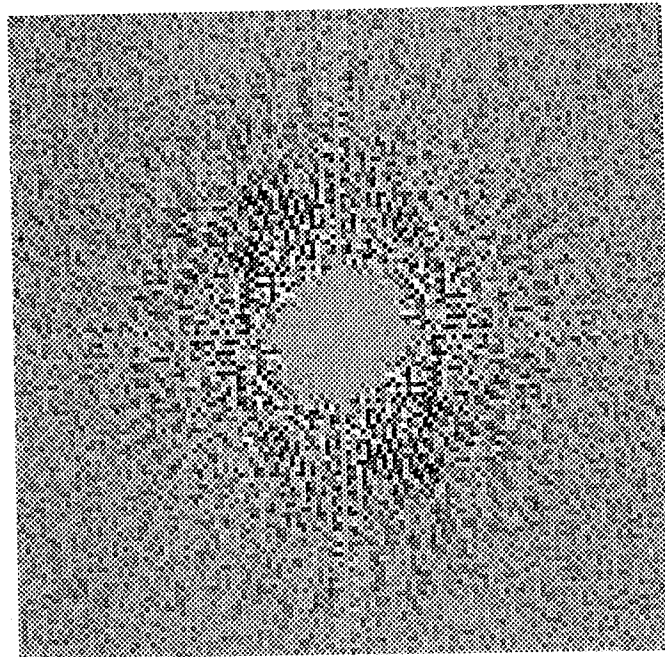
For verification, a popular reconstruction similarity measure was used, the correlation coefficient ϵ :

$$\epsilon = \frac{\sum_{ij=1}^N (f_{ij} - \bar{f})(f_{ij}^* - \bar{f}^*)}{\left[\sum_{ij=1}^N (f_{ij} - \bar{f})^2 \sum_{ij=1}^N (f_{ij}^* - \bar{f}^*)^2 \right]^{1/2}} \quad (4.3-1)$$

where $N \times N$ is the size (in pixels) of either, reference and reconstruction, matrix; f_{ij} and f_{ij}^* represent the pixel intensity in the reference and the reconstruction images, respectively, and \bar{f} and \bar{f}^* are the average densities of the reconstruction and reference images, respectively. Calculated values were $\epsilon = 0.9854$ and 0.9960 for FBP and IART reconstruction images and $\epsilon = 0.9934$ and 0.9950 for Fourier spectra of FBP and IART reconstructed images, respectively, in agreement with the results of the above qualitative measures.

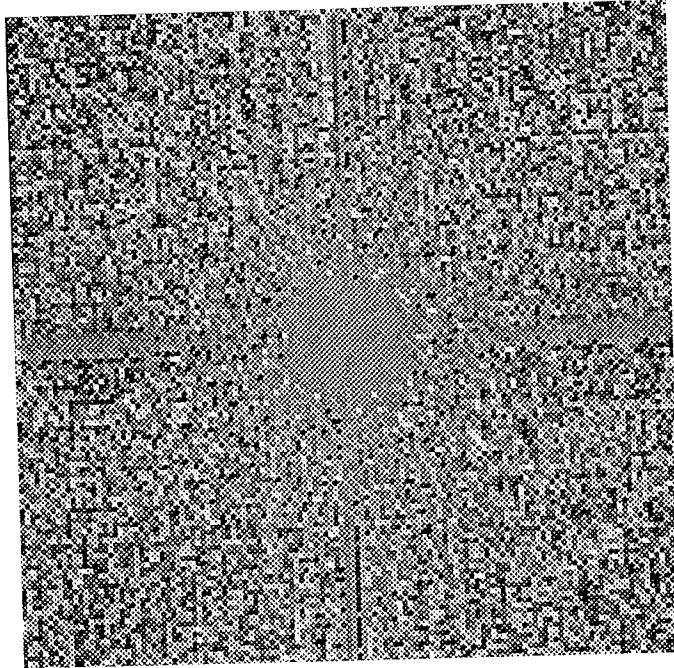


(a)

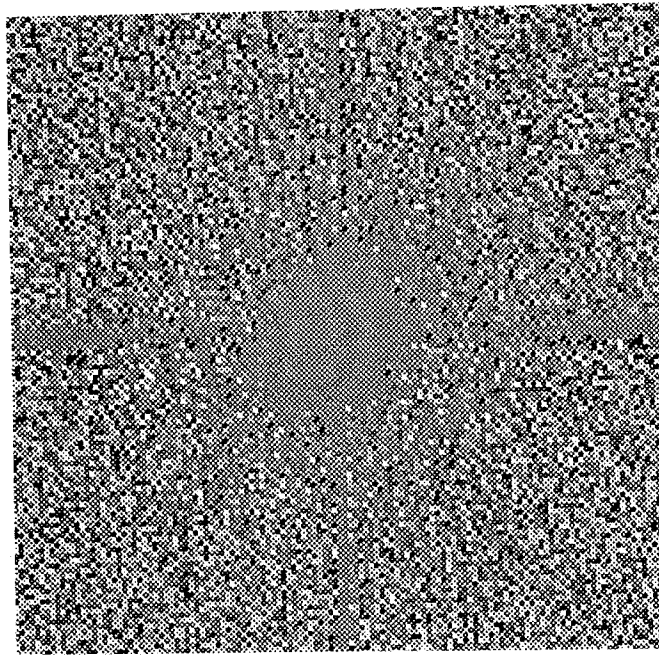


(b)

Fig. 4.3.1. Fourier spectrum as a quantitative measure in reconstruction: (a), FBP, subtraction of Fig. 4.2.3(a) from Fig. 4.2.1(b); (b), IART, subtraction of Fig. 4.2.3(b) from Fig. 4.2.1(b).



(a)

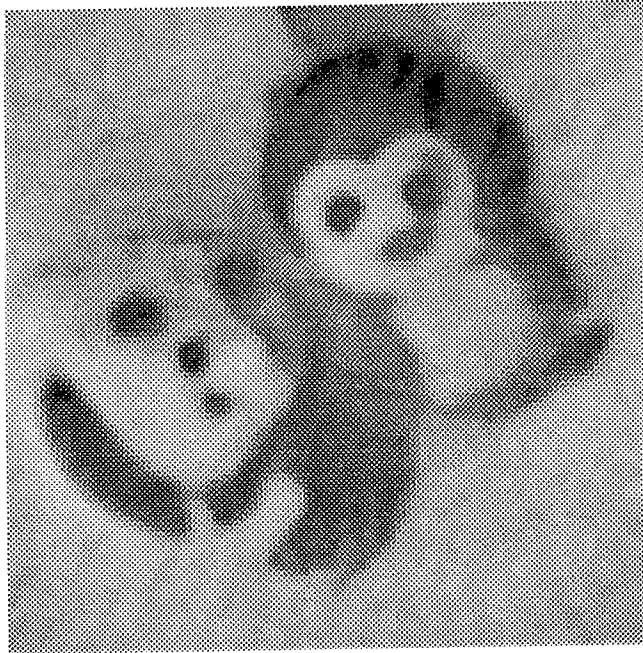


(b)

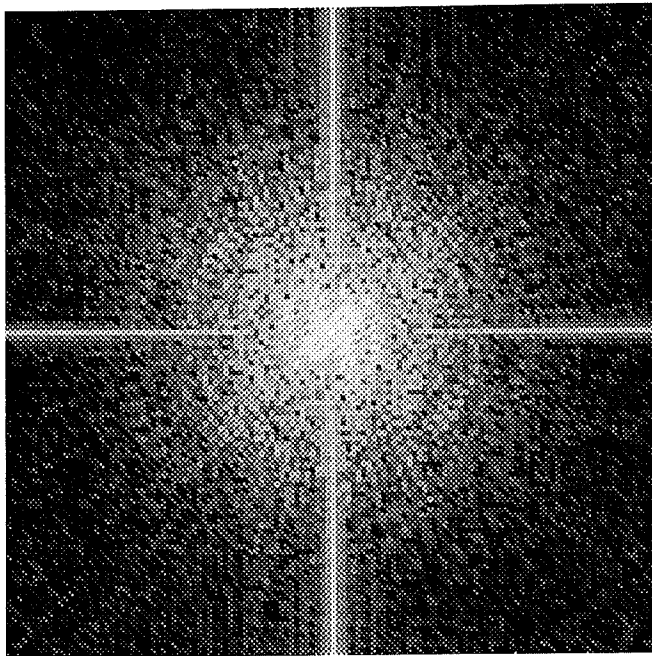
Fig. 4.3.2. Subtraction of Fourier phase images: (a), FBP, Fig. 4.2.4(b) from Fig. 4.2.4(a); (b), IART, Fig. 4.2.4(c) from Fig. 4.2.4(a).

4.4. Fourier Spectrum as a Criterion for Iterative Reconstruction Methods

Subtraction of the Fourier spectrum of a reconstructed image from that of a reference image has also proven to be useful in evaluation of the optimal number of iterations for an iterative reconstruction method like IART. Figs. 4.4.1 - 3 show how (a), the reconstructed image and (b), its Fourier spectrum change with an increasing number of iterations (starting from 3 throughout 18). Fig. 4.4.4 represents the results of subtraction of Fourier spectra of images (reconstruction from the reference) for the sequence of IART reconstruction images. One can observe how with increasing number of iterations (starting from 3) fluctuations of an intensity function decrease and disappear (for 18 iterations). The computed correlation coefficients for the sequence of images are shown in Table 4.4.1. One can notice that only when the values of correlation coefficients are the same up to the fifth decimal digit (18 and 21 iterations) the images representing the subtraction of Fourier spectra (reconstruction from the reference) show no visible difference (Figs. 4.4.4(c) and 4.3.2(b)). This suggests that the optimal number of iterations has been reached, i.e., the best quality reconstructed image obtained, and there is no use in further continuing the iteration process. When we compare the correlation coefficients of the reconstruction images (Table 4.4.1) to their respective Fourier spectrum images, we notice how sensitive an evaluation measure the Fourier spectrum is compared to the commonly used correlation coefficient.

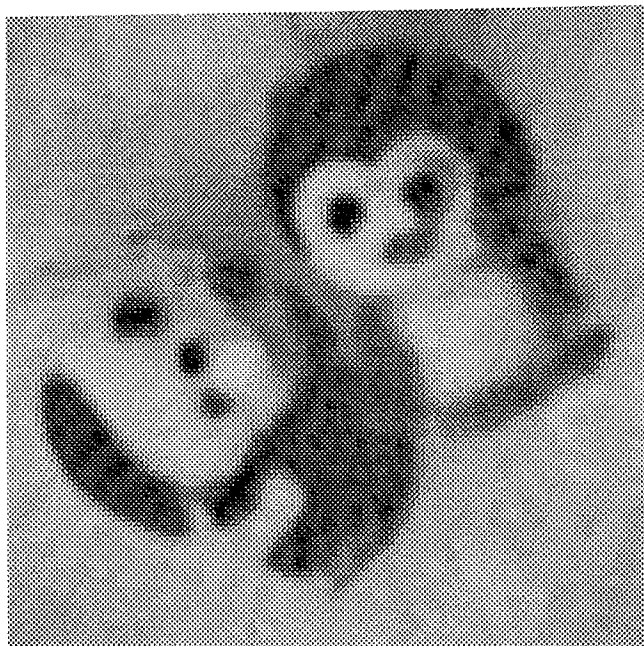


(a)

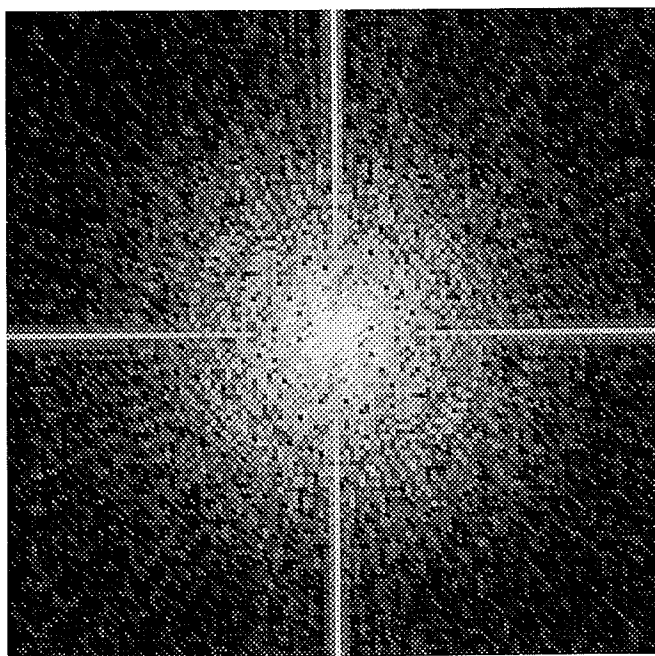


(b)

Fig. 4.4.1. IART, 3 iterations, parallel geometry beam, 35 projection directions equally spaced over 180° : (a), Reconstruction image, (b), corresponding Fourier spectrum.

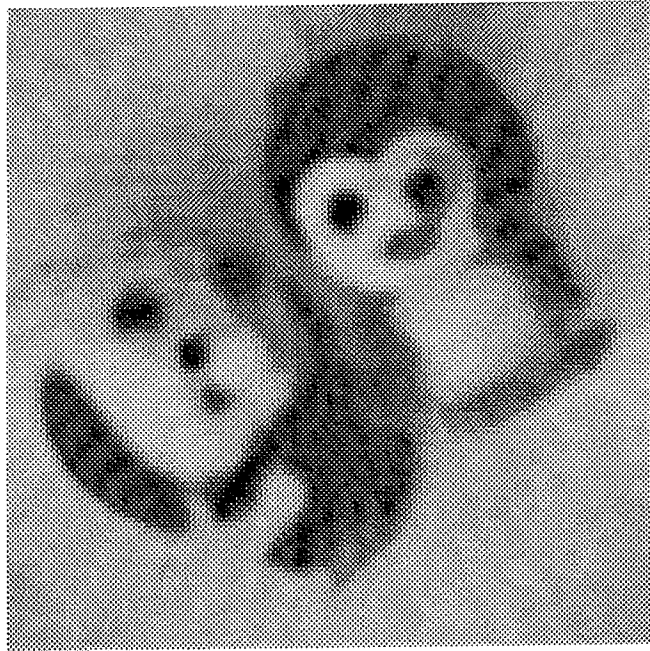


(a)

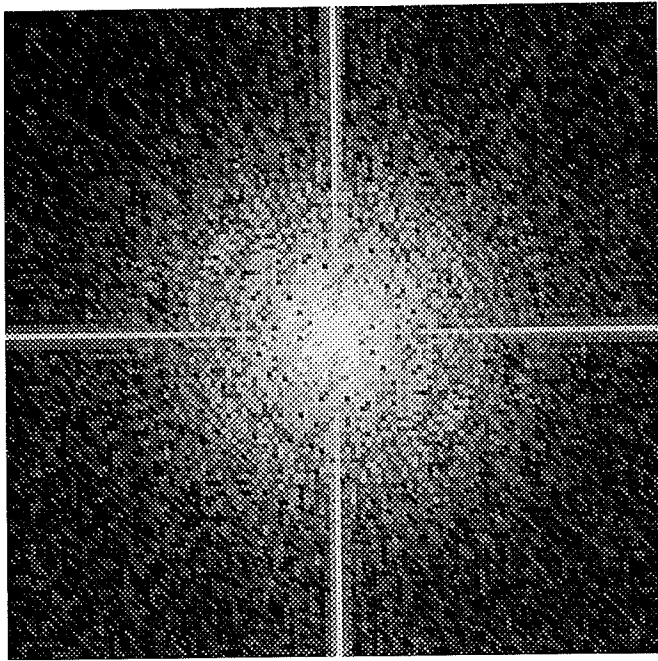


(b)

Fig. 4.4.2. IART, 9 iterations, parallel geometry beam, 35 projection directions equally spaced over 180° : (a), Reconstruction image, (b), corresponding Fourier spectrum.

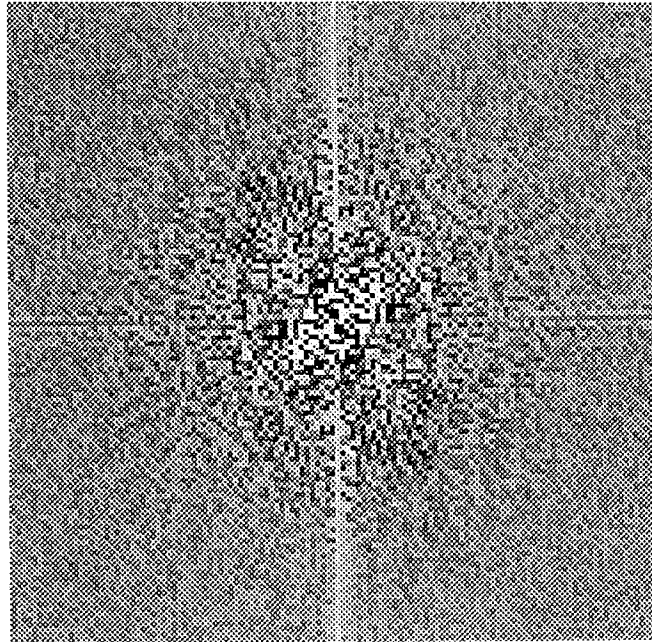


(a)

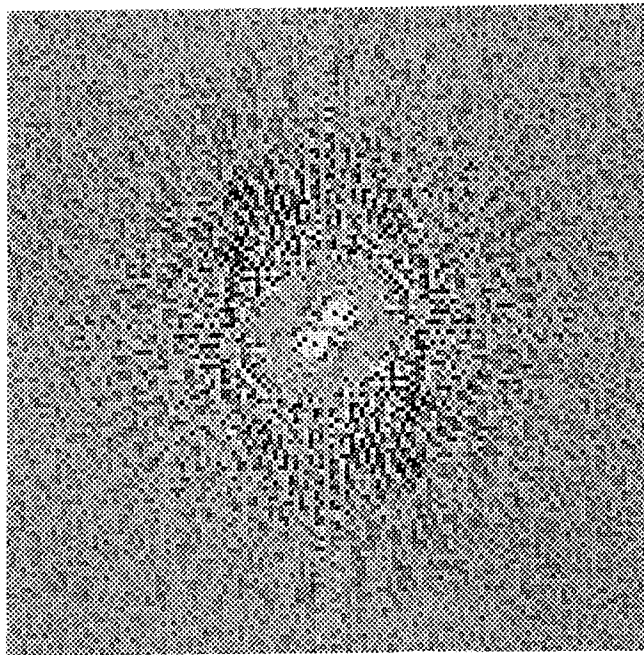


(b)

Fig. 4.4.3. IART, 18 iterations, parallel geometry beam, 35 projection directions equally spaced over 180° : (a), Reconstruction image, (b), corresponding Fourier spectrum.



(a)



(b)

Fig. 4.4.4. Fourier spectrum as a convergence criterion for IART. Subtraction images after: (a), 3 iterations; (b), 9 iterations.

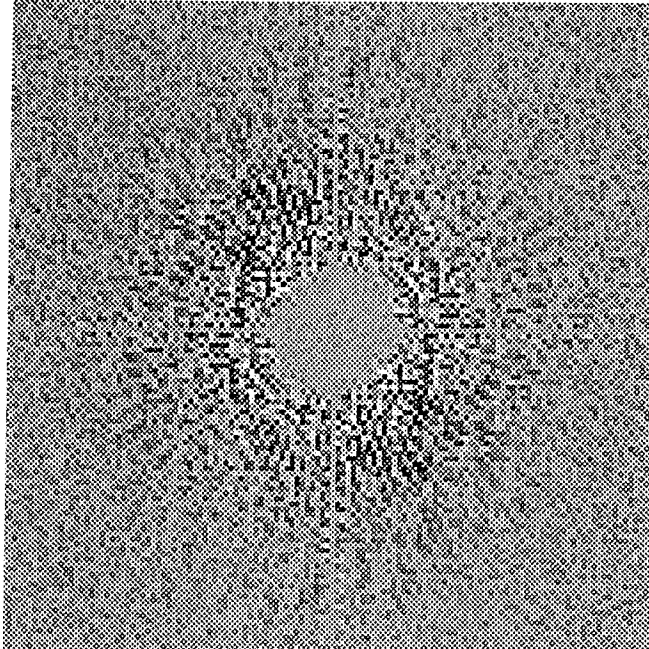


Fig. 4.4.4(c). Fourier spectrum as a convergence criterion for IART. Subtraction image after 18 iterations.

Table 4.4.1. Correlation coefficients for the sequence of IART reconstructions of the reference object "dolls".

Iteration number	Correlation coefficient
3	0.972433
6	0.994390
9	0.995842
12	0.996019
15	0.996051
18	0.996065
21	0.996066

4.5. Concluding Remarks

This chapter presented new ways of using the Fourier spectrum in the process of testing and evaluation the performance of a reconstruction algorithm:

1) To distinguish the quality of a reconstructed image computed by linear and nonlinear methods;

2) As a new convergency criterion for iterative reconstruction methods;

3) As a qualitative evaluation measure, by a subtraction of images in Fourier space.

We have considered images from FBP and IART, representatives of linear and nonlinear reconstruction methods, respectively. All images were computed using the same input data of 35 parallel projections equally spaced over 180° .

The appearance of a Fourier spectrum of a reconstructed image is characteristic for the type of reconstruction method that was used. Applying different algorithms (linear, nonlinear) produces reconstructed images having easily distinguishable spectra. Reconstructions computed with nonlinear methods (like IART) show better interpolation in Fourier space, their spectra bear more resemblance to the reference object spectrum, and are more detailed.

The subtraction of Fourier spectra proved to be a very sensitive evaluation measure compared to the widely used correlation coefficient. It shows differences in Fourier spectra up to the fifth decimal digit of the value of a correlation coefficient of a reconstructed image. The subtraction of Fourier spectra also has the advantage of displaying the frequency spectrum of noise that has been introduced by the reconstruction.

Also, it has been found that using subtraction of Fourier spectra of the images can yield a new convergence criterion to halt the iteration process for nonlinear iterative methods. IART was used as a representative.

CHAPTER V

IMAGE RECONSTRUCTION FROM LIMITED NUMBER OF VIEWS USING IART AND IART WITH FILTERED PROJECTIONS

5.1. Simulation of the CT Data Under Various Assumptions of Photon Noise

X-rays passing through the human body produce readings on a detector array that associate with attenuation properties of the tissue from the x-rayed cross section of the body. In vacuum all x-ray photons which leave the source in the direction of a detector will reach it. When a material is placed between the source and the detector some of the photons are removed from the oriented beam (i.e., they are absorbed or scattered). The probability that a photon gets removed depends on the energy of the photon and on the material between the source and the detectors. Some of the scattered x-ray photons will reach the detector, usually with reduced energy [Johns, 1983], [Hendee, 1970]. This "background" is reduced by collimators and/or energy discriminators whenever possible (see Section 3.1).

The linear attenuation coefficient μ_e^l of a tissue l at energy e is defined as:

$$\mu_e^l = -\ln \rho \quad (5.1-1)$$

where ρ is the probability that a photon of energy e which enters a uniform slab of tissue l

of unit thickness, on a direction perpendicular to the face of the slab, will not be absorbed or scattered in the slab.

A single detector reading p_e^l for a monochromatic radiation beam can be defined as

$$p_e^l = \int_0^D \mu_e^l(x, y) dz \quad (5.1-2)$$

where z is the distance of the point (x, y) with attenuation $\mu_e^l(x, y)$ on the straight line which is the path of all the x-ray photons for a particular source-detector pair. D is the length of the path segment through the scanned body. The number of photons counted by the detector is a sample of a Poisson random variable with parameter \bar{N}

$$\bar{N} = \bar{N}_0 \exp(-p_e^l) \quad (5.1-3)$$

\bar{N}_0 refers to the photons emitted by the x-ray source.

A typical method by which CT data is collected consists of two physical measurements [Herman, 1980]: a *calibration* measurement and an *actual* one. The difference between them is that during the calibration measurement, there is no object in the path of the x-ray beam from the source to the detector. (The calibration measurement serves the purpose of determining how many out of the fixed number of photons that leave the x-ray source get to the detector.) A set of CT numbers for an object under investigation is produced from the ratio of the actual and the calibration measurements:

$$p_e^l = -\ln \frac{\text{actual measurement}}{\text{calibration measurement}} \quad (5.1-4)$$

To simulate collection of data affected by photon noise, we have assumed a monochromatic

x-ray beam and no scatter. For any source-detector pair the simulated data was calculated based on the following equation:

$$p_e^l = -\ln \frac{N_a / N_{ar}}{N_c / N_{cr}} \quad (5.1-5)$$

where N_a , N_c , N_{ar} and N_{cr} represent the number of photons counted by the detector under consideration during the actual and the calibration measurement, and the number of photons counted by a reference detector during the actual and the calibration measurement, respectively. All are samples of the corresponding Poisson random variables. (The reference detector serves the purpose of compensating for fluctuations in the strength of the x-ray source.) In the experiments, we have assumed $\bar{N}_{ar} = \bar{N}_0$ and $\bar{N}_{cr} = \text{number of projections} \times \bar{N}_0$. The assumed intensity of an x-ray source was $\bar{N}_0 = 10^2, 10^4, \text{ or } 10^6$ photons emitted. The meaning of this can be explained as follows: If there is no object placed between the source and the detector then all the emitted photons ($10^2, 10^4, 10^6$, respectively) reach the detector. The energy of x-ray photons was assumed to be 60 keV. To sample the Poisson random variables, N and N_0 , the simulation procedure described in Chapter III was used.

5.2. Methods of Evaluating Image Fidelity

A reconstruction is a digitized picture. When the reconstruction is based on simulated projection data of a reference object, we can evaluate the quality of the reconstruction by comparing it to the digitized reference object. There are several ways to do it. We can use visual evaluation, similarity / dissimilarity measures, or receiver operating characteristic (ROC) curves [Gonzalez, 1983], [Pratt, 1978], [Hall, 1979], [Barrett, 1981], [Herman, 1980], [Xiaobo, 1986], [Herman, 1972], [Gordon, 1974a], [Basseville, 1989],

[Bookstein, 1990], [Evans, 1981]. We can also select a column / row of pixels that goes through the number of interesting features in the reference image and compare its pixel densities in the reference and the reconstruction images [Herman, 1980], or we can compare Fourier spectra of the reference and the reconstruction images [Mazur, 1992], (see Chapter IV). Visual evaluation is the most straightforward way. A difficulty with it is its subjectivity. It should be emphasized that the results of subjective testing are influenced by the types of images presented to the viewer and the experimental conditions. If the images are familiar to the observer, the observer is apt to be more critical of impairments because of preconceived notions of the image structure. On the other hand, impairments may go unnoticed in unfamiliar imagery unless actually brought to the attention of the observer. Also, care must be taken in the application of subjective ratings from one set of viewing conditions to another. For example, an image displayed on a computer monitor might be judged to be of "good" quality with "just perceptible" impairment. But, if the same image were viewed as a photograph recorded by a high-quality recorder / printer, impairments that were masked by nonlinearities or low resolution in the computer monitor display might suddenly become quite apparent. Clearly, it is desirable to have objective quantitative criteria as a basis for the image fidelity evaluation.

Much effort has been made towards the development and the assessment of quantitative measures. However, those measures that have been developed are not perfect; counterexample images can often be generated that have a high quality rating, but are subjectively poor in quality and vice versa. The key to the formulation of good quality measures is a better understanding of the human visual system which has peculiar characteristics: An important characteristic of the human visual system is its logarithmic sensitivity to light intensity so that errors in dark areas of an image are much more noticeable than errors in light areas. The human visual system is also sensitive to abrupt spatial changes in gray level so that errors on or near the edges are more bothersome than

errors in background texture [Bosman, 1982], [Gonzalez, 1983], [Pratt, 1978], [Hall, 1979], [Rosenfeld, 1972], [Cornsweet, 1970].

In this study, the following quantitative similarity measures were used:

$$\begin{aligned}
 \text{correlation coefficient} \quad \epsilon_1 &= \frac{\sum_{i,j=1}^N (f_{ij} - \bar{f})(f_{ij}^* - \bar{f}^*)}{\left[\sum_{i,j=1}^N (f_{ij} - \bar{f})^2 \sum_{i,j=1}^N (f_{ij}^* - \bar{f}^*)^2 \right]^{1/2}} \\
 \text{root mean square error (rms)} \quad \epsilon_2 &= \left[\frac{1}{N^2} \sum_{i,j=1}^N (f_{ij} - f_{ij}^*)^2 \right]^{1/2} \\
 \text{average absolute difference} \quad \epsilon_3 &= \frac{1}{N^2} \sum_{i,j=1}^N |f_{ij} - f_{ij}^*| \quad (5.2-1) \\
 \text{worst case difference} \quad \epsilon_4 &= \max_{1 \leq k, l \leq N/2} |F_{kl} - F_{kl}^*| \\
 \text{entropy based difference} \quad \epsilon_5 &= \sum_{i,j=1}^N \tilde{f}_{ij} \ln \frac{\tilde{f}_{ij}}{\tilde{f}_{ij}^*}
 \end{aligned}$$

where

$$\begin{aligned}
 F_{kl} &= \frac{1}{4}(f_{2k-1,2l-1} + f_{2k,2l-1} + f_{2k-1,2l} + f_{2k,2l}) \\
 F_{kl}^* &= \frac{1}{4}(f_{2k-1,2l-1}^* + f_{2k,2l-1}^* + f_{2k-1,2l}^* + f_{2k,2l}^*)
 \end{aligned}$$

$$\tilde{f}_{ij} = \frac{f_{ij}}{\sum_{k,l=1}^N f_{kl}}$$

$$\tilde{f}_{ij}^* = \frac{f_{ij}^*}{\sum_{k,l=1}^N f_{kl}^*}$$

and $N \times N$ is the size (in pixels) of either, reference and reconstruction, matrix; f_{ij} and f_{ij}^* represent the pixel intensity in the reference and the reconstruction images,

respectively, and \bar{f} and \bar{f}^* are the average densities of the reconstruction and reference images, respectively.

Note that above measures report on different aspects of image quality. The *correlation coefficient*, ϵ_1 , measures the extent to which two images are similar to each other. The *root mean square error (rms)*, ϵ_2 , is a very reasonable measure for the overall performance of a reconstruction method. A large difference in a few places causes the value of ϵ_2 to be large. The measure ϵ_3 yields the *largest difference* between the reference and the reconstruction images. As opposed to ϵ_2 , it emphasizes the importance of a many small errors rather than of a few large errors. ϵ_4 represents the *worst case difference* measure and is the largest absolute density difference between the $[N/2] \times [N/2]$ digitizations of the reference and the reconstruction images. In this measure, I used a rougher digitization than what was used for the reconstruction since the size of the smallest feature in the reference image that I have used was several pixels, and therefore, to estimate the relative attenuation coefficient of this feature, I would use the average density of all pixels involved. The measure ϵ_5 uses the statistical concept of *entropy* [Frieden, 1972], [Hershel, 1971]. Picture elements can be considered as symbols produced by a discrete information source with the grey levels as the states, and one can measure the entropy or average information per level of an element by the average, or expected value of the information contained in each possible level [Hall, 1979], [Basseville, 1989], [Gordon, 1983].

When two images match closely, the correlation coefficient approaches a value of one while the other measures tend toward zero.

Another approach that can be used to measure the fidelity of a reconstruction image is to use *receiver operating characteristic (ROC) curves* [Barrett, 1981], [Hendee, 1970], [Evans, 1981]. In this method, a series of reconstruction images is shown to a group of viewers. Each of the images may or may not contain an abnormality. If a viewer detects the abnormality, the result is scored as a "true positive". If a viewer detects the abnormality when it is not present in an image, the result is scored as a "false positive". A plot of true

positives versus false positives (Fig. 5.2.1) reveals the relative performance of the reconstruction method in the clinical diagnostic situation.

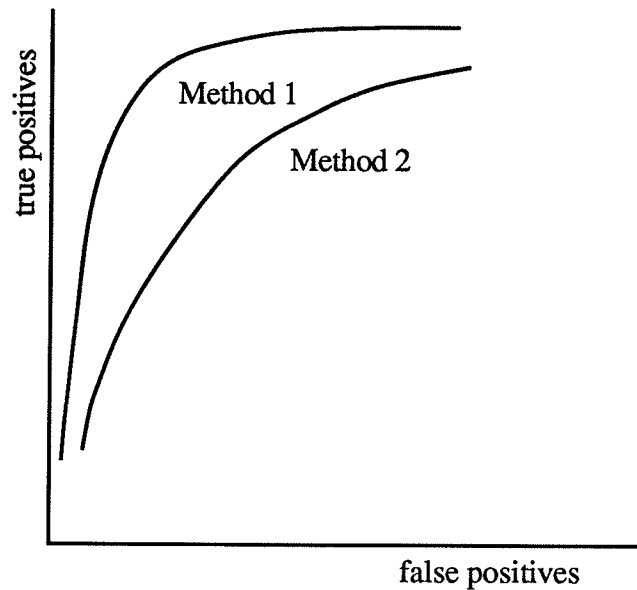


Fig. 5.2.1. ROC curves for two reconstruction methods, with Method 1 yielding superior results.

5.3. Simulated Experiments. Results

The purpose of conducting the following experiments was to compare reconstruction results from Interpolative Algebraic Reconstruction Techniques (IART). Two cases were considered: In one case, raw simulated noisy data was used, while in the other case, a filtering operation was used on the projection data to suppress noise before it was processed by the reconstruction method. The data was simulated to include photon noise. The conditions included a monochromatic x-ray beam of energy 60 keV and a set of three different settings of an x-ray source intensity (10^2 , 10^4 , 10^6 emitted photons per measurement). (The simulation procedure is described in Section 5.1.) A reference image for the first two sets of experiments consisted of two squares (Fig. 5.3.1): The large one,

of the attenuation coefficient of water at 60 keV, that formed a background and a small one positioned off the center. The latter had the attenuation coefficient larger from that of the background square by 10% and 15% in the first and the second sets of experiments, respectively. The third set of experiments was performed for a more complicated reference object (Fig. 5.3.2.). For every reference image, three sets of parallel projections were taken: 19, 35, and 60. In every set, the projections were equally spaced over 180° . The first two sets of experiments included the reconstruction of a reference image, from all three sets of projections, for all three values of the assumed intensity of an x-ray source (10^2 , 10^4 , 10^6 emitted photons per measurement), while the third set of experiments was performed for only one source intensity, 10^4 emitted photons.

Set of experiments No. 1

Conditions:

- the "squares" reference image, Fig. 5.3.1;
- the difference in the attenuation, $\partial\mu = 10\%$ (the large square attenuation coefficient is 20 m^{-1} and the small square attenuation coefficient is 22 m^{-1});
- three sets of projections: 19, 35, 60;
- three assumed x-ray source intensity values: 10^2 , 10^4 , 10^6 emitted photons.

For all three values of the assumed x-ray source intensity, the reconstruction of the "squares" reference image of Fig. 5.3.1 was performed. The input data included simulated photon noise and consisted of three sets of parallel projections (19, 35, and 60) equally spaced over 180° . For the case of IART with filtered projections, the projections were filtered prior to being used by the reconstruction method. The windowing technique was used (for the description, see Section 3.4): A generalized Hamming window with $\alpha = 0.8, 0.8, 0.54$ was used to filter the noisy projections when the x-ray source intensity was, respectively, 10^2 , 10^4 , 10^6 emitted photons per measurement. The resulting reconstruction images, from 60, 35, and 19 projections, for the assumed x-ray source

intensity of 10^6 emitted photons are presented in Figs. 5.3.3 - 5.3.5, respectively. Each of these figures displays two reconstruction images from two cases: (a), IART, and (b), IART with filtered projections. This way, a viewer is given an opportunity to make his / her own visual evaluation and judge the improvement resulting from using IART with filtered projections. Reconstruction images for the other two levels of the x-ray source intensity are not included as the high noise level makes it difficult for details to be seen.

All reconstruction images were evaluated using the equations of quantitative similarity measures (5.2-1). Tables 5.3.1 - 5.3.3. display the outcome for the x-ray source intensity of 10^2 , 10^4 , 10^6 emitted photons, respectively. Analyzing the numbers in the tables, we can conclude that filtering noisy projections improves the reconstruction image: Correlation coefficients calculated for IART with filtered projections are greater than those for IART and all the other measures (rms, average absolute value, worst case difference, entropy based difference) mostly are decreased in value compared to their IART counterparts. The above findings are also in agreement with the visual assessment of the presented images, Figs. 5.3.3 - 5.3.5.

Figs. 5.3.7 - 5.3.9 present the results of applying, to the reference and reconstruction images, a quantitative measure of the subtraction of their Fourier spectra (see Section 4.3). Fourier spectra of the reconstruction images of Figs. 5.3.3 - 5.3.5 were subtracted from the Fourier spectrum of the reference image "squares" in Fig. 5.3.6 (a). When comparing the resulting subtraction images for IART and for IART with filtered projections, it requires a brief moment of adjustment for the eye to spot the difference as the images are not smooth. In addition, the change in them, although noticeable, is relatively small. The subtraction images for IART with filtered projections are slightly better than the ones for IART: The grey level they contain is more uniform and they have a less noisy appearance. (The grey color represents the zero difference between the Fourier spectra of the reconstruction and the reference images.)

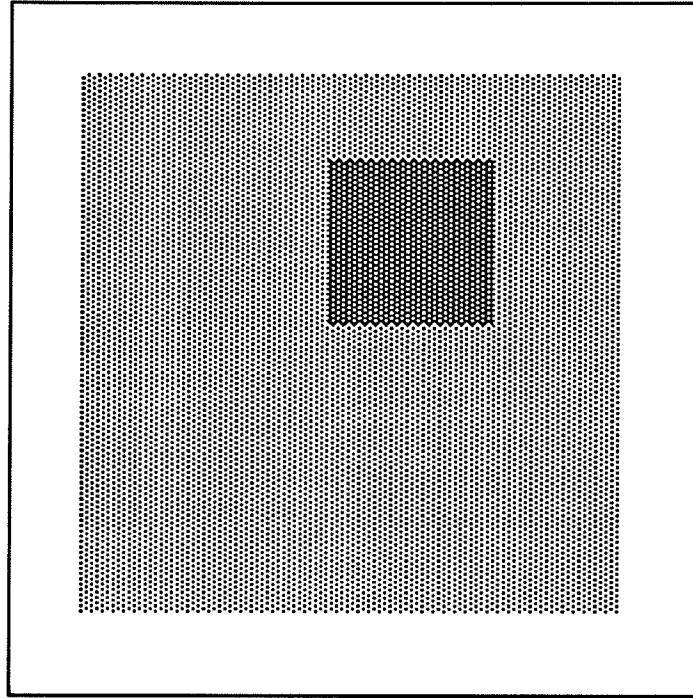


Fig. 5.3.1. The reference image "squares". Superposition of squares.

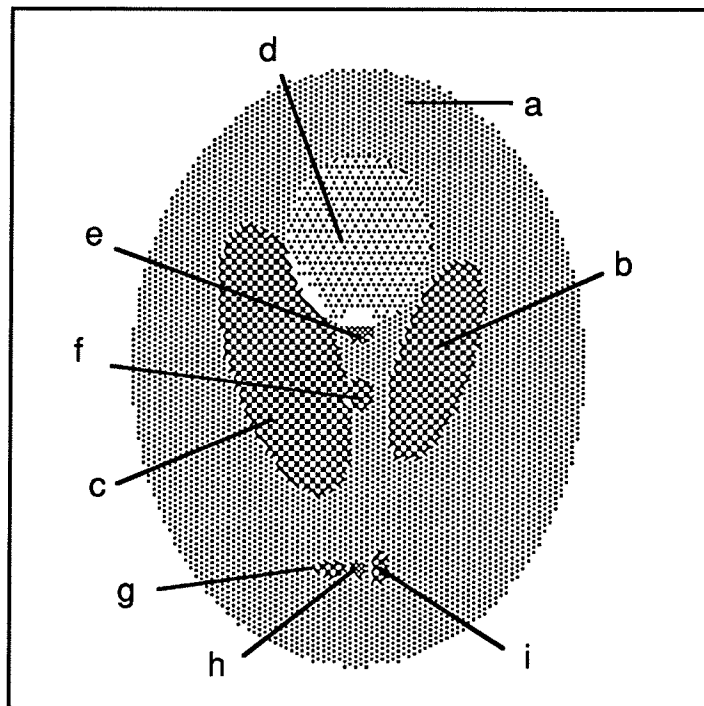
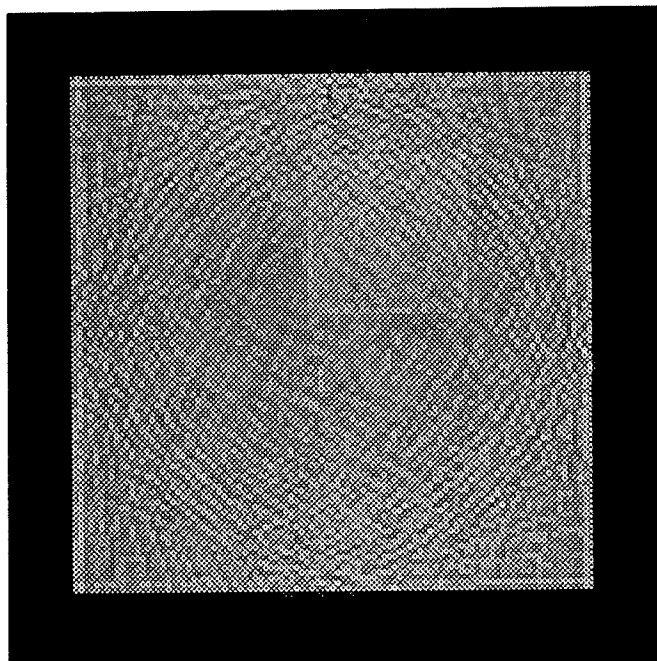
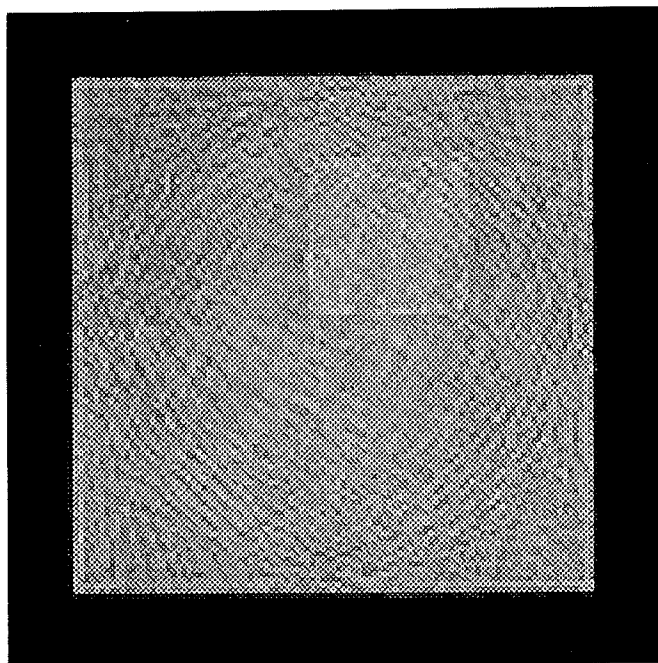


Fig. 5.3.2. The reference image "ellipses". Superposition of ellipses.

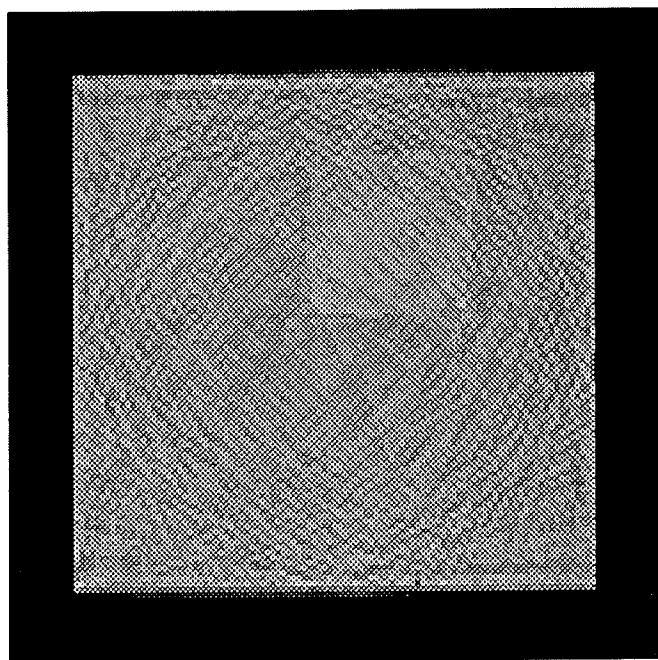


(a)

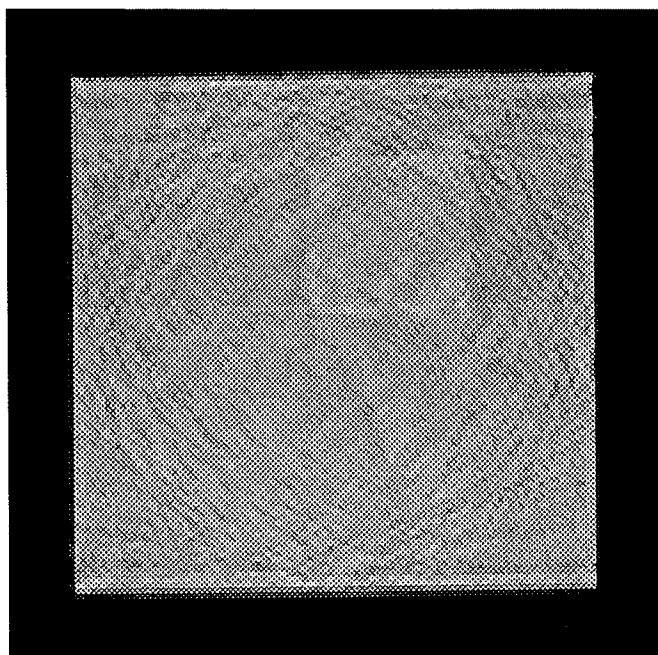


(b)

Fig. 5.3.3. Reconstruction of the reference image "squares" from 60 parallel projections with simulated photon noise equally spaced over 180° : (a), IART, and (b), IART with filtered projections. X-ray source intensity = 10^6 emitted photons per measurement, difference in attenuation coefficients = 10%.

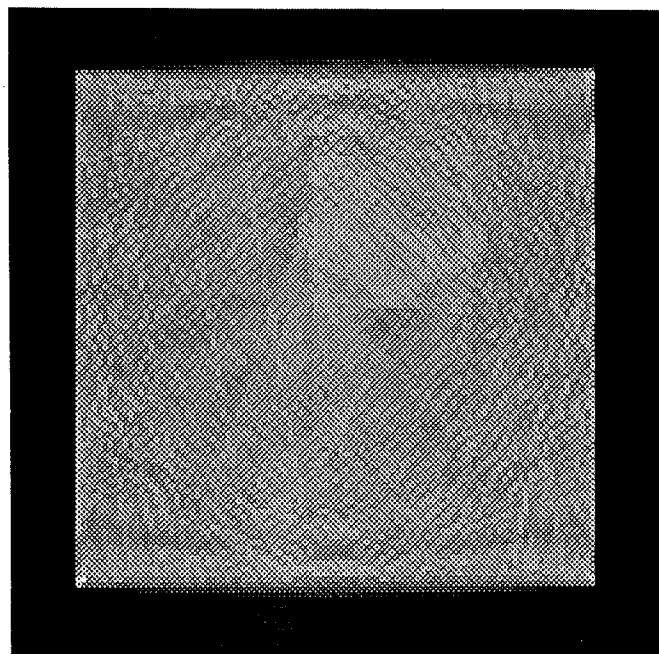


(a)

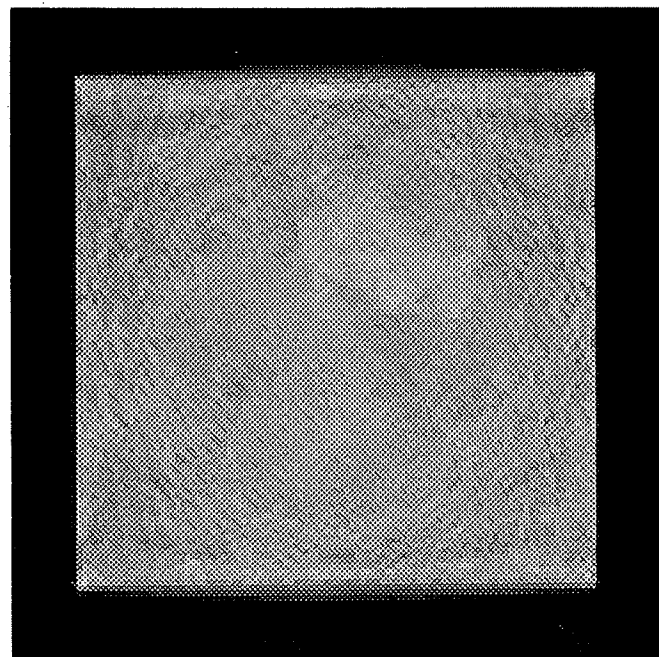


(b)

Fig. 5.3.4. Reconstruction of the reference image "squares" from 35 parallel projections with simulated photon noise equally spaced over 180° : (a), IART, and (b), IART with filtered projections. X-ray source intensity = 10^6 emitted photons per measurement, difference in attenuation coefficients = 10%.



(a)



(b)

Fig. 5.3.5. Reconstruction of the reference image "squares" from 19 parallel projections with simulated photon noise equally spaced over 1800: (a), IART, and (b), IART with filtered projections. X-ray source intensity = 106 emitted photons per measurement, difference in attenuation coefficients = 10%.

Table 5.3.1. Computed quantitative similarity measures of Eq. (5.2-1) for the reconstruction images of the "squares" reference image from simulated noisy projection data. Case: $\partial\mu = 10\%$, source intensity = 10^6 emitted photons per measurement.

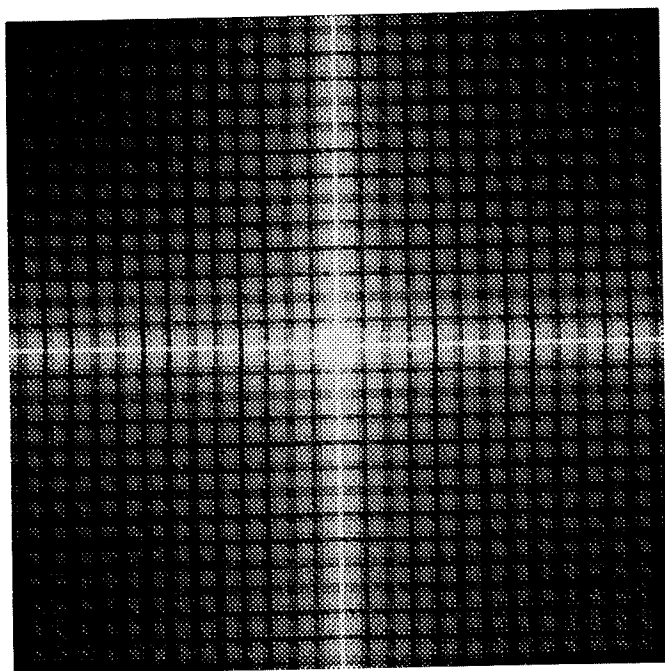
Quantitative error measures	IART			IART with filtered projections		
	Number of projections			Number of projections		
	19	35	60	19	35	60
correlation coefficient	0.984	0.984	0.975	0.987	0.990	0.987
rms	1.737	1.749	2.194	1.556	1.400	1.573
average absolute difference	1.005	1.076	1.374	0.868	0.061	1.008
worst case difference	6.792	5.355	5.975	6.615	4.305	3.470
entropy based difference	0.011	0.008	0.011	0.011	0.008	0.009

Table '5.3.2. Computed quantitative similarity measures of Eq. (5.2-1) for the reconstruction images of the "squares" reference image from simulated noisy projection data. Case: $\partial\mu = 10\%$, source intensity = 10^4 emitted photons per measurement.

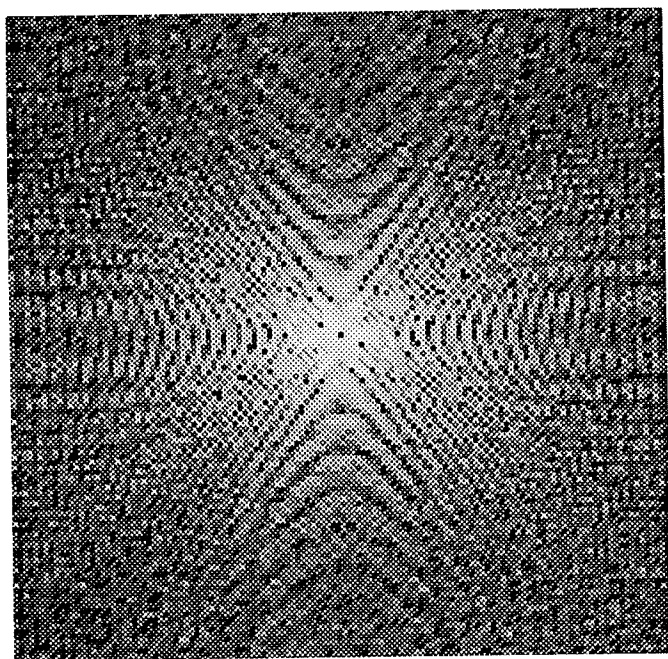
Quantitative error measures	IART			IART with filtered projections		
	Number of projections			Number of projections		
	19	35	60	19	35	60
correlation coefficient	0.970	0.963	0.941	0.978	0.977	0.967
rms	2.397	2.697	3.460	2.030	2.100	2.530
average absolute difference	1.466	1.712	2.222	1.225	1.346	1.650
worst case difference	8.858	9.127	8.802	8.550	8.078	6.698
entropy based difference	0.023	0.022	0.031	0.021	0.019	0.021

Table 5.3.3. Computed quantitative similarity measures of Eq. (5.2-1) for the reconstruction images of the "squares" reference image from simulated noisy projection data. Case: $\partial\mu = 10\%$, source intensity = 10^2 emitted photons per measurement.

Quantitative error measures	IART			IART with filtered projections		
	Number of projections			Number of projections		
	19	35	60	19	35	60
correlation coefficient	0.592	0.562	0.501	0.642	0.630	0.580
rms	12.224	13.304	16.152	10.682	11.098	13.127
average absolute difference	6.746	7.749	9.206	6.033	6.743	7.862
worst case difference	136.62	117.72	81.952	123.74	94.275	68.363
entropy based difference	0.282	0.382	0.520	0.234	0.299	0.390

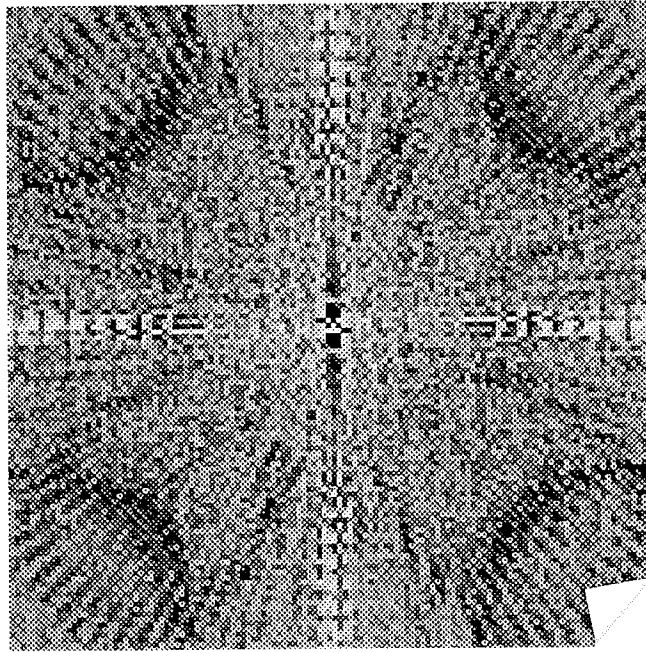


(a)

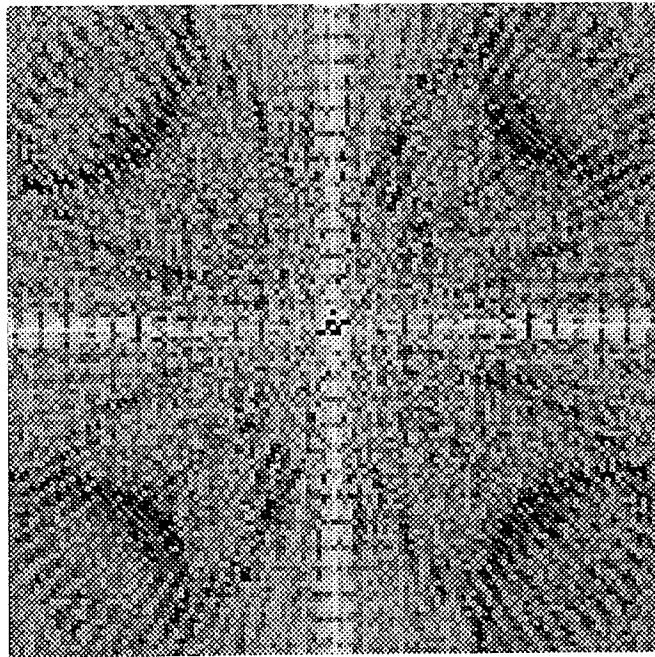


(b)

Fig. 5.3.6. Fourier spectra of the reference object: (a), "squares" with $\partial\mu = 10\%$, and (b), "ellipses" with $\partial\mu$'s as in Table 5.3.7.

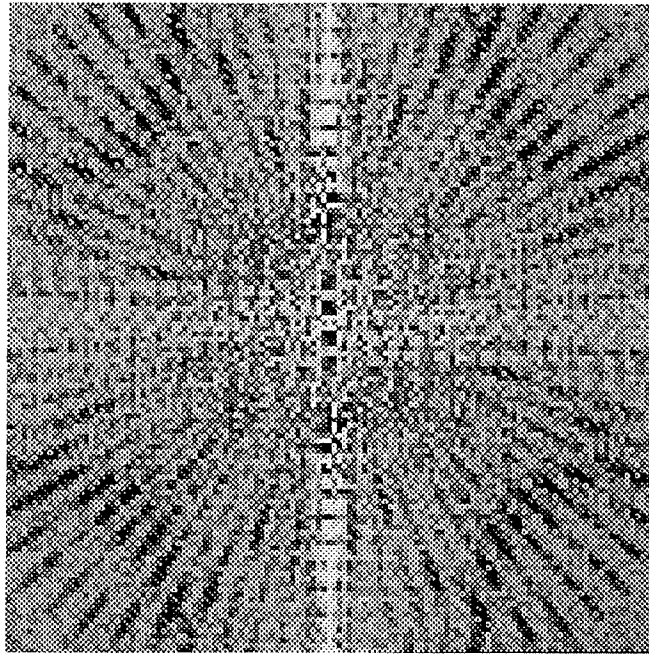


(a)

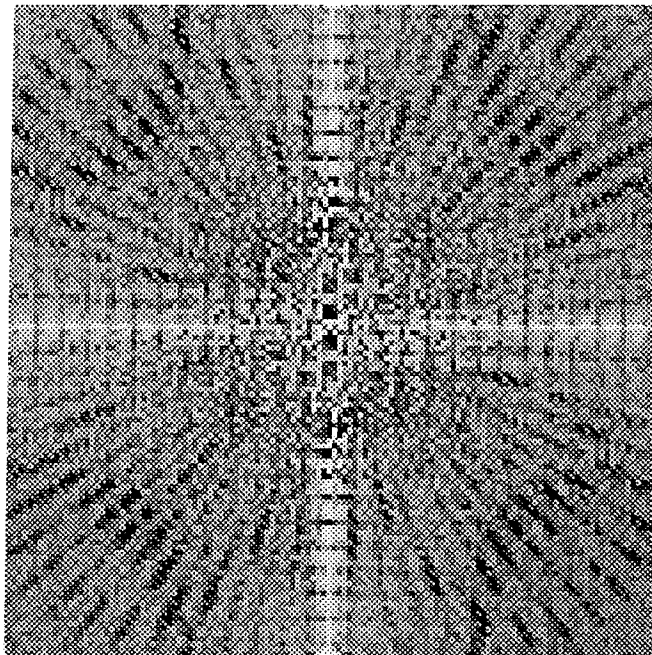


(b)

Fig. 5.3.7. The subtraction, from the Fourier spectrum of "squares" in Fig. 5.3.6(a), of the Fourier spectrum of the 60 projection image of: (a), IART of Fig. 5.3.3(a); (b), IART with filtered projections of Fig. 5.3.3(b).

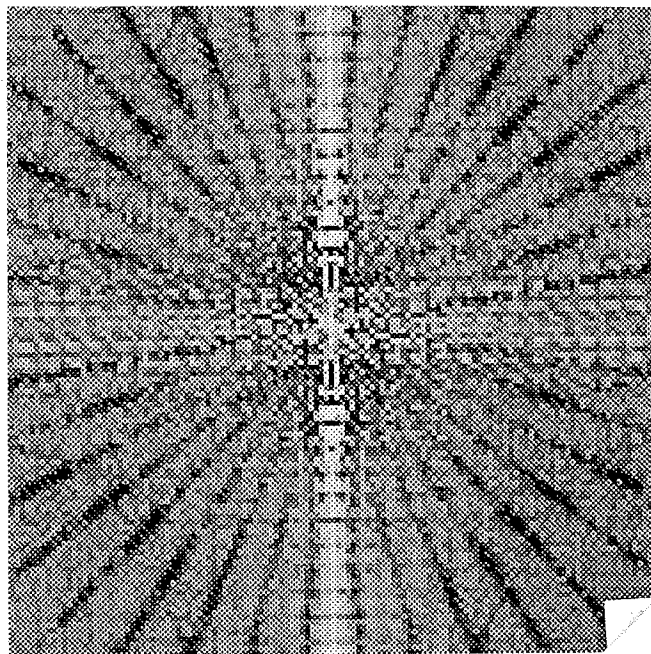


(a)

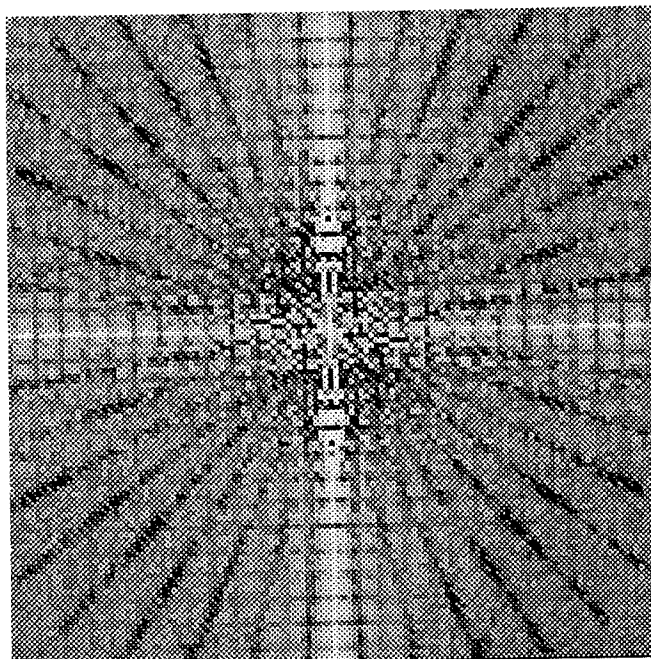


(b)

Fig. 5.3.8. The subtraction, from the Fourier spectrum of "squares" in Fig. 5.3.6(a), of the Fourier spectrum of the 35 projection image of: (a), IART of Fig. 5.3.4(a); (b), IART with filtered projections of Fig. 5.3.4(b).



(a)



(b)

Fig. 5.3.9. The subtraction, from the Fourier spectrum of "squares" in Fig. 5.3.6(a), of the Fourier spectrum of the 19 projection image of: (a), IART of Fig. 5.3.5(a); (b), IART with filtered projections of Fig. 5.3.5(b).

Set of experiments No. 2

Conditions:

- the "squares" reference image, Fig. 5.3.1;
- the difference in the attenuation, $\partial\mu = 15\%$ (the large square attenuation coefficient is 20 m^{-1} and the small square attenuation coefficient is 23 m^{-1});
- three sets of projections: 19, 35, 60;
- three assumed x-ray source intensity values: 10^2 , 10^4 , 10^6 emitted photons.

For all three values of the assumed x-ray source intensity, the reconstruction of the "squares" reference image of Fig. 5.3.1. was performed. The input data included simulated photon noise and consisted of three sets of parallel projections (19, 35, and 60) equally spaced over 180° . For the case of IART with filtered projections, the projections were filtered prior to being used by the reconstruction method via the windowing technique: A generalized Hamming window with $\alpha = 0.8, 0.65, 0.54$ was used to filter the noisy projections when the x-ray source intensity was, respectively, $10^2, 10^4, 10^6$ emitted photons per measurement. All reconstruction images were evaluated using the quantitative similarity measures of Eq.(5.2-1). Tables 5.3.4 - 5.3.6 display the reconstruction outcomes for the x-ray source intensity of $10^2, 10^4, 10^6$ emitted photons per measurement, respectively. As one can notice, for the assumed x-ray source intensity of 10^6 emitted photons per measurement, the resulting reconstruction images from IART with filtered projections were only slightly better from those produced by IART. This degree of improvement can hardly be noticed by a human eye when comparing two reconstruction outputs. Therefore, there are no reconstruction images included. For 10^2 emitted photons per measurement intensity levels of the x-ray source, too high a noise level was obtained. Figs. 5.3.10 - 5.3.12 display the reconstruction images for the x-ray source intensity of 10^4 emitted photons pr measurement for 60, 35, and 19 projections, respectively. As in the

previous case, for comparison, each of these figures displays two reconstruction images from two cases: (a), IART, and (b), IART with filtered projections.

After studying the numbers presented in the tables and the reconstruction images, we can again conclude that filtering noisy projections improves the reconstruction image: Correlation coefficient values calculated for IART with filtered projections are increased compared to those calculated for IART and all the other measures (rms, average absolute value, worst case difference, entropy based difference) are less in value than their IART counterparts; Although it is difficult to see the enhancement in the 60 projection IART image with filtered projections, the improvement in the appearance of the 35 and 19 projection reconstruction images is noticeable.

Figs. 5.3.13 - 5.3.15 display the subtraction images for (a), IART, and (b), for IART with filtered projections, outputs from the subtraction of Fourier spectra similarity measure. Again, while it is difficult to judge on the improvement for the 60 projection image of IART with filtered projections, for the 35 and 19 projections, the subtraction images for IART with filtered projections clearly look better; i.e., the grey level is more uniform, indicating better closeness to the reference image spectrum.

Table 5.3.4. Computed quantitative similarity measures of Eq. (5.2-1) for the reconstruction images of the "squares" reference image from simulated noisy projection data. Case: $\partial\mu = 15\%$, source intensity = 10^6 emitted photons per measurement.

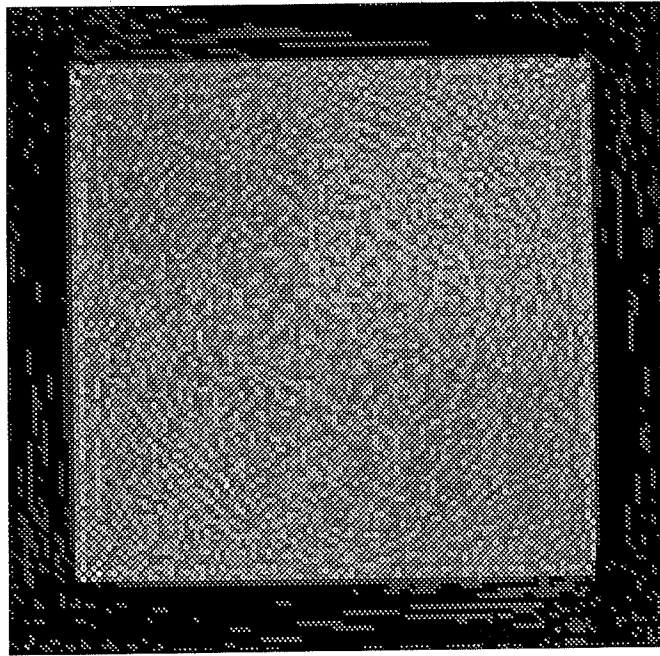
Quantitative error measures	IART			IART with filtered projections		
	Number of projections			Number of projections		
	19	35	60	19	35	60
correlation coefficient	0.984	0.982	0.975	0.985	0.983	0.977
rms	1.752	1.846	2.192	1.736	1.810	2.142
average absolute difference	1.031	1.150	1.403	1.004	1.112	1.344
worst case difference	7.050	6.118	4.515	7.000	5.933	4.425
entropy based difference	0.014	0.012	0.014	0.011	0.009	0.010

Table 5.3.5. Computed quantitative similarity measures of Eq. (5.2-1) for the reconstruction images of the "squares" reference image from simulated noisy projection data. Case: $\partial\mu = 15\%$, source intensity = 10^4 emitted photons per measurement.

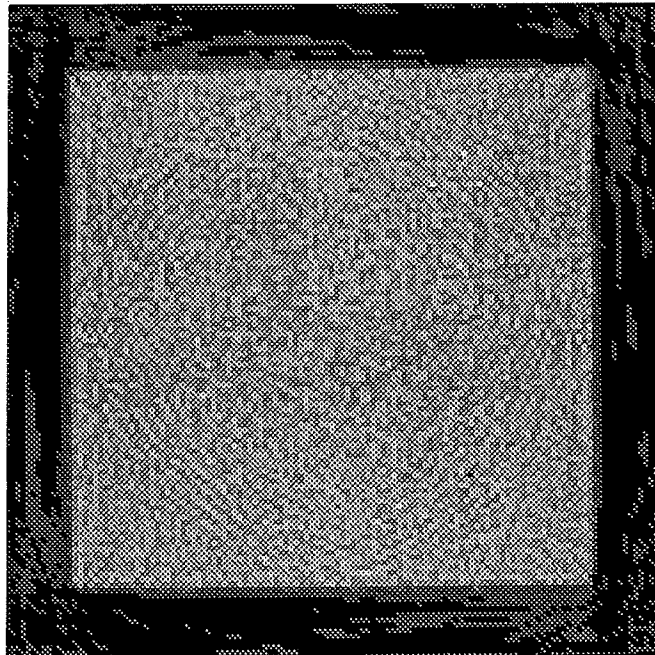
Quantitative error measures	IART			IART with filtered projections		
	Number of projections			Number of projections		
	19	35	60	19	35	60
correlation coefficient	0.969	0.960	0.941	0.974	0.968	0.955
rms	2.439	2.808	3.492	2.242	2.483	2.979
average absolute difference	1.503	1.784	2.232	1.411	1.617	1.958
worst case difference	9.118	9.970	8.530	9.667	9.748	7.952
entropy based difference	0.023	0.023	0.031	0.023	0.024	0.028

Table 5.3.6. Computed quantitative similarity measures of Eq. (5.2-1) for the reconstruction images of the "squares" reference image from simulated noisy projection data. Case: $\partial\mu = 15\%$, source intensity = 10^2 emitted photons per measurement.

Quantitative error measures	IART			IART with filtered projections		
	Number of projections			Number of projections		
	19	35	60	19	35	60
correlation coefficient	0.594	0.570	0.493	0.645	0.635	0.566
rms	12.411	13.290	16.442	10.843	11.176	13.532
average absolute difference	6.837	7.797	9.107	6.118	6.782	7.805
worst case difference	136.68	86.243	147.32	123.76	77.387	139.52
entropy based difference	0.281	0.372	0.512	0.234	0.290	0.383

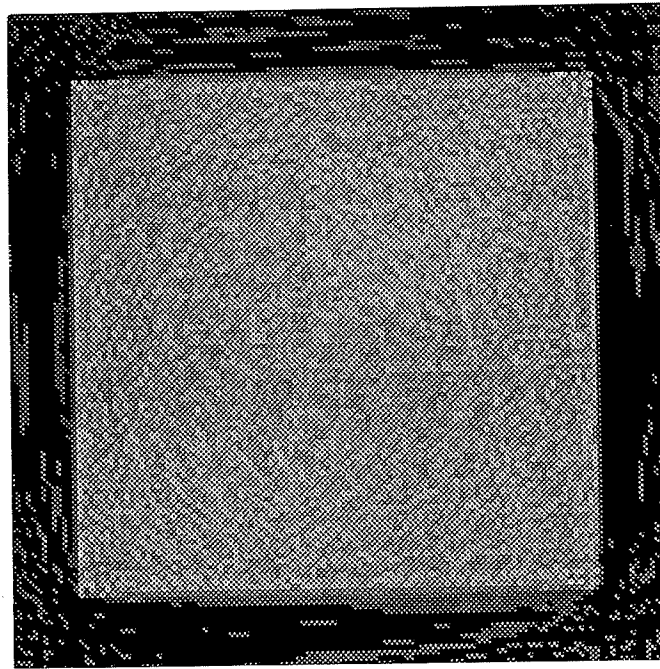


(a)

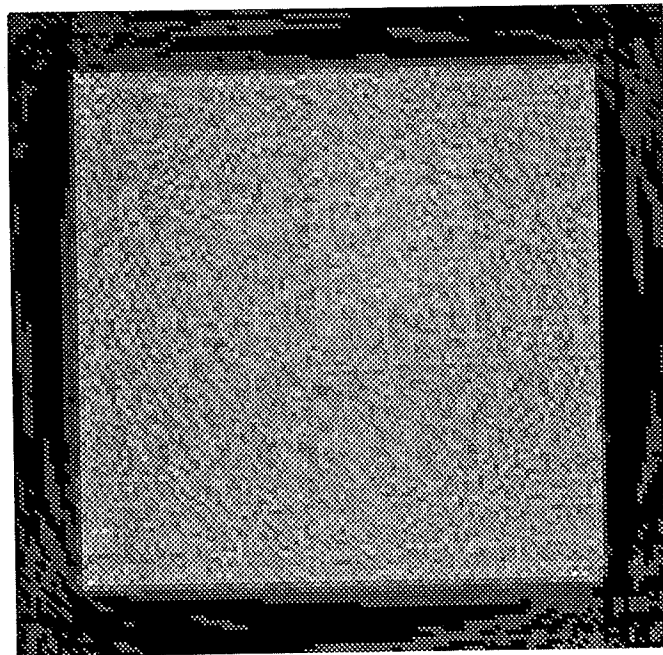


(b)

Fig. 5.3.10. Reconstruction of the reference image "squares" from 60 parallel projections with simulated photon noise equally spaced over 180° : (a), IART, and (b), IART with filtered projections. X-ray source intensity = 10^4 emitted photons per measurement, difference in attenuation coefficients = 15%.

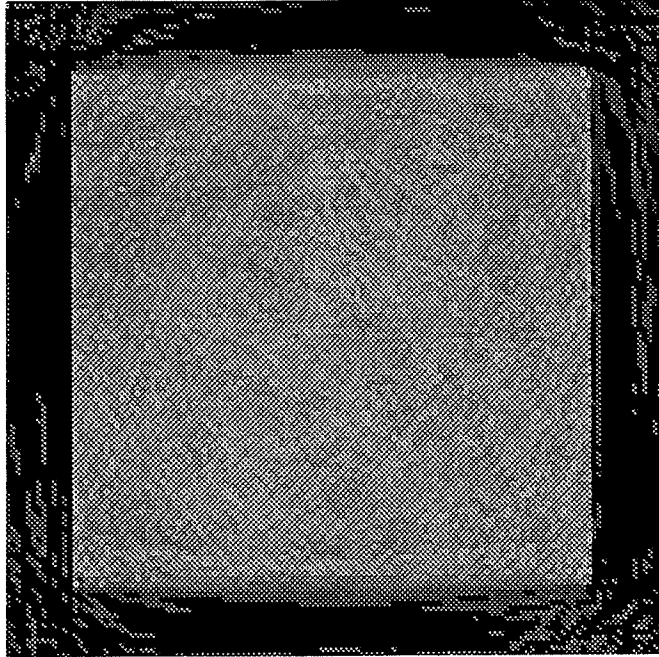


(a)

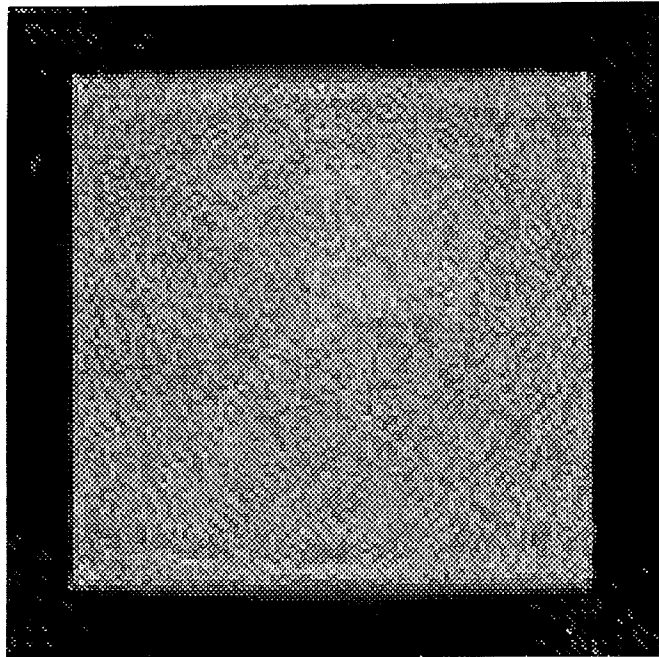


(b)

Fig. 5.3.11. Reconstruction of the reference image "squares" from 35 parallel projections with simulated photon noise equally spaced over 180° : (a), IART, and (b), IART with filtered projections. X-ray source intensity = 10^4 emitted photons per measurement, difference in attenuation coefficients = 15%.

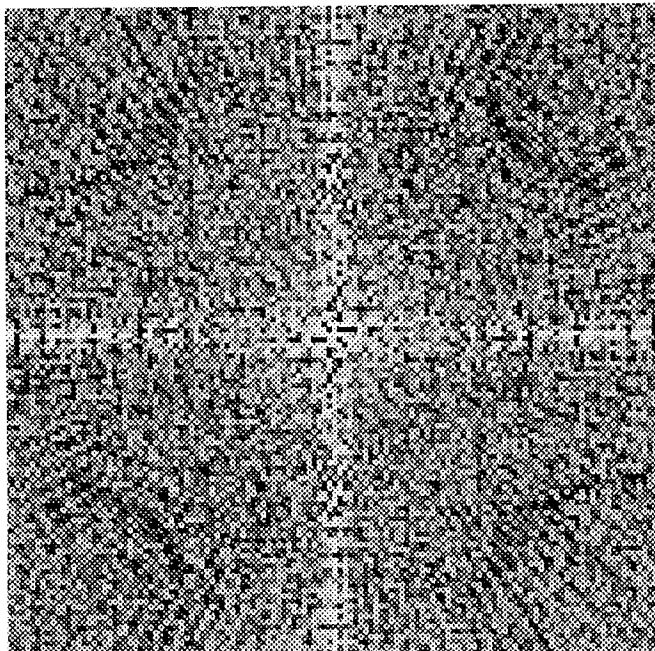


(a)

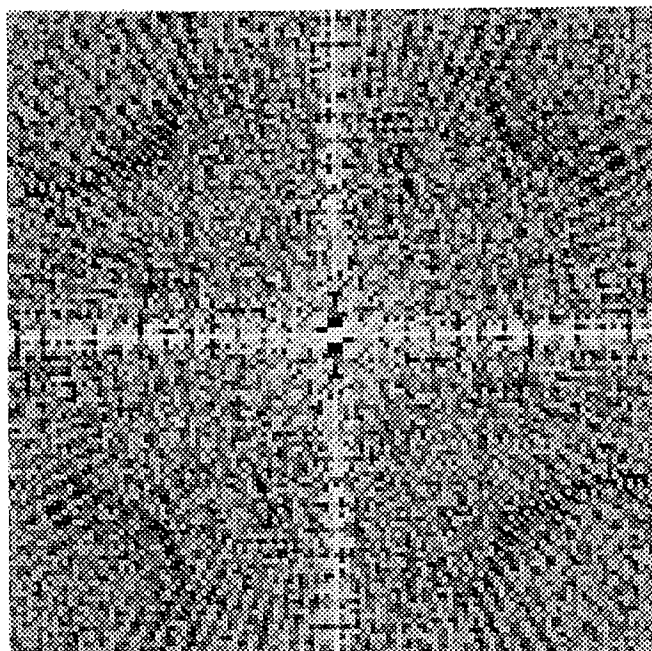


(b)

Fig. 5.3.12. Reconstruction of the reference image "squares" from 19 parallel projections with simulated photon noise equally spaced over 180° : (a), IART, and (b), IART with filtered projections. X-ray source intensity = 10^4 emitted photons per measurement, difference in attenuation coefficients = 15%.

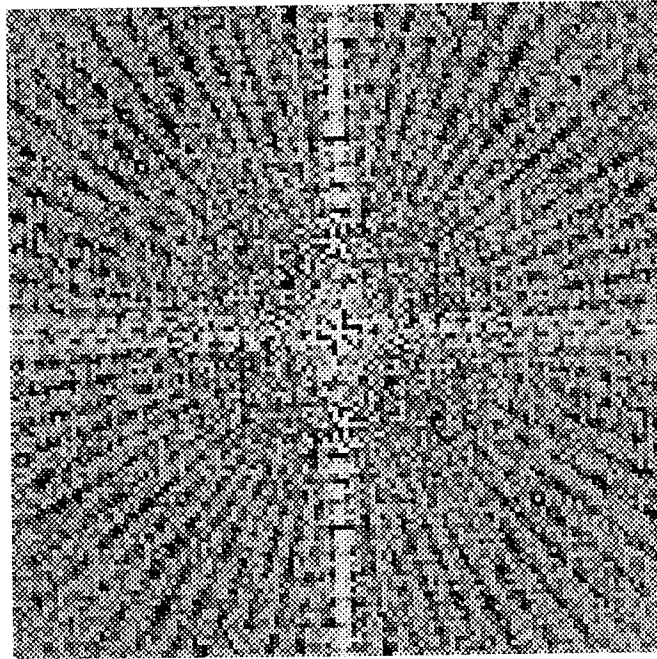


(a)

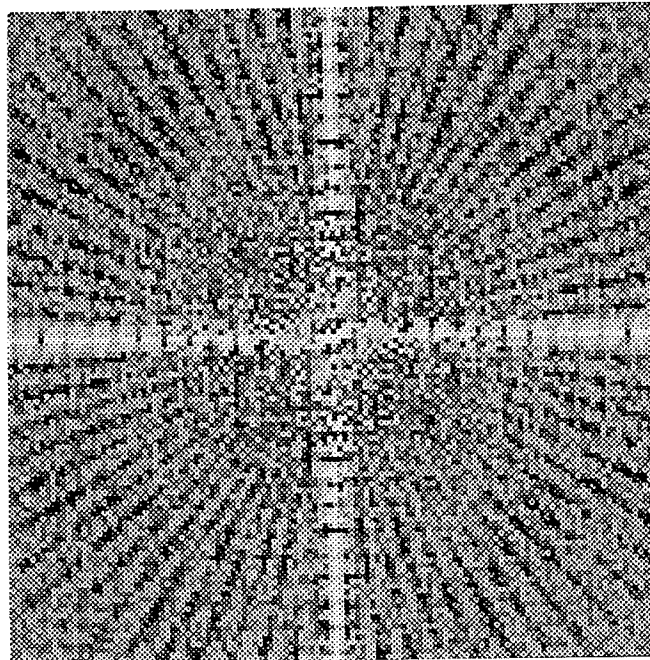


(b)

Fig. 5.3.13. The subtraction, from the Fourier spectrum of "squares" with $\partial\mu = 15\%$, of the Fourier spectrum of the 60 projection image of: (a), IART of Fig. 5.3.10(a); (b), IART with filtered projections of Fig. 5.3.10(b).

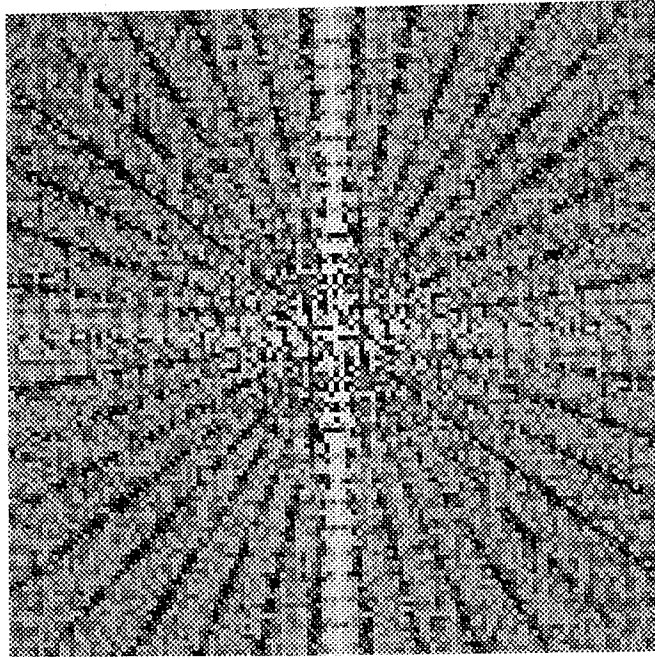


(a)

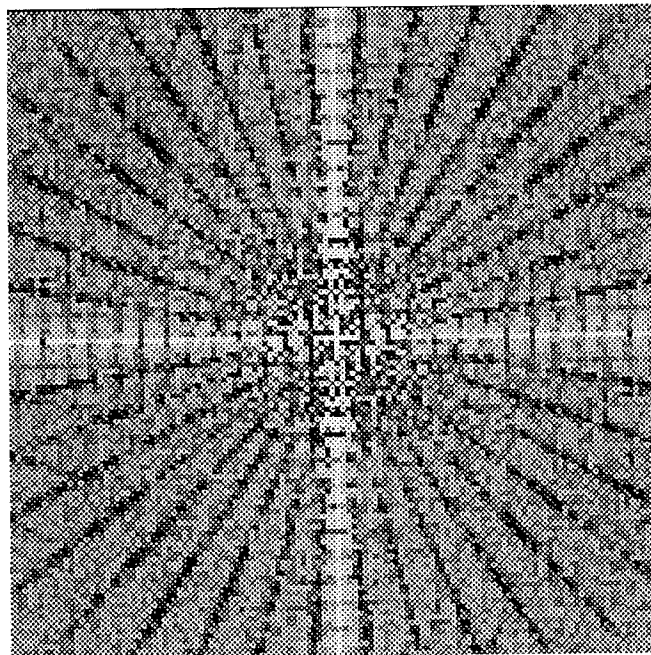


(b)

Fig. 5.3.14. The subtraction, from the Fourier spectrum of "squares" with $\partial\mu = 15\%$, of the Fourier spectrum of the 35 projection image of: (a), IART of Fig. 5.3.11(a); (b), IART with filtered projections of Fig. 5.3.11(b).



(a)



(b)

Fig. 5.3.15. The subtraction, from the Fourier spectrum of "squares" with $\partial\mu = 15\%$, of the Fourier spectrum of the 19 projection image of: (a), IART of Fig. 5.3.12(a); (b), IART with filtered projections of Fig. 5.3.12(b).

Set of experiments No. 3

Conditions:

- the "ellipses" reference image, Fig. 5.3.2;
- the difference in the attenuation, $\partial\mu$, is listed in Table 5.3.7;
- three sets of projections: 19, 35, 60;
- the assumed x-ray source intensity is 10^4 emitted photons per measurement.

Table 5.3.7. The reference image "ellipses". Attenuation coefficients of the constituent ellipses.

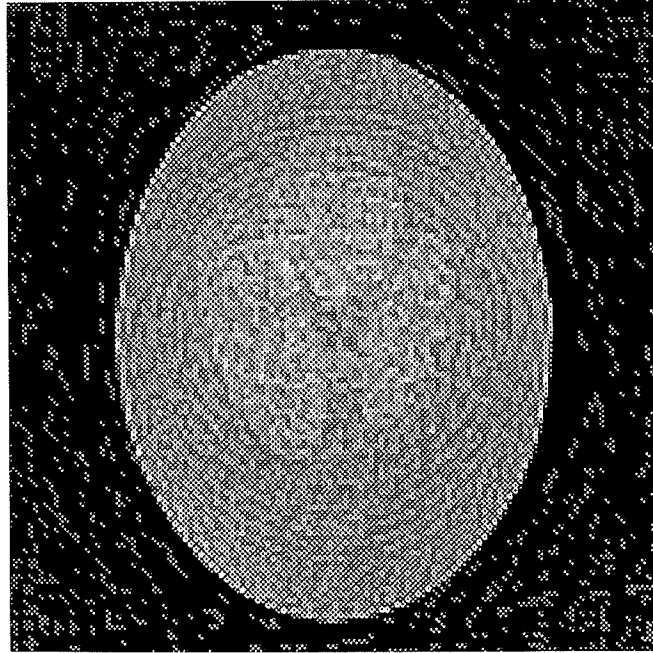
Ellipses	Attenuation coefficient μ [m^{-1}]	Difference in attenuation coefficient $\partial\mu$ [%]*
a	20	-
b	26	30
c	26	30
d	26.4	32
e	27	35
f	26	30
g	26	30
h	27	35
i	26	30
$d \cap e$	33.4	67
$d \cap c$	32.4	62
$f \cap c$	32	60

The difference in the attenuation coefficient was calculated with regard to the basis ellipse "a" that has the attenuation coefficient of water at 60 keV.

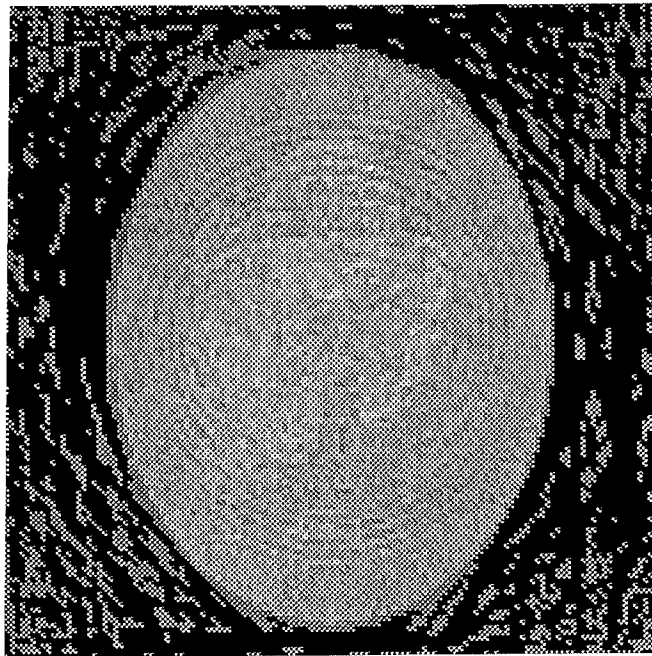
For the assumed x-ray source intensity of 10^4 emitted photons per measurement, the reconstruction of the "ellipses" reference image of Fig. 5.3.2. was performed. The input data included simulated photon noise and consisted of three sets of parallel projections (19, 35, and 60) equally spaced over 180° . For the case of IART with filtered projections, the projections were filtered prior to being used by the reconstruction method. The windowing technique with the generalized Hamming window ($\alpha = 0.65$) was used. Reconstruction images from 60, 35, and 19 projections are displayed in Figs. 5.3.16 - 5.3.18, respectively. As before, every figure displays two reconstruction images from two cases: (a), IART, and (b), IART with filtered projections.

All reconstruction images were evaluated using the quantitative similarity measures of Eq.(5.2-1). Results are presented in Table 5.3.8. Analysis of the results indicates that, as in the two previous cases, there is an improvement due to the use of the noise filtering operation on the projection data: The correlation coefficient values calculated for IART with filtered projections are greater than those of IART, and the other measures (rms, average absolute value, worst case difference, entropy based difference) are less than their IART counterparts. The reconstruction images from IART with filtered projections although still noisy in appearance, show improvement compared to the ones using IART alone.

All the reconstruction images were also evaluated using the qualitative measure of the subtraction of Fourier spectra: The spectra of the reconstruction images of Figs. 5.3.16 - 5.3.18 were subtracted from the spectrum of the reference image "ellipses" in Fig. 5.3.6 (b). Results are displayed in Figs. 5.3.19 - 5.3.21: All the subtraction images for IART with filtered projections have a less noisy appearance than the ones for IART which is suggestive of better similarity to the reference image. The most dramatic improvement can be noticed for the 35 projection case. Here, the subtraction image for IART with filtered projections shows even the beginning of the clearance of the center region, which is indicative of a good fidelity reconstruction (see Chapter IV).

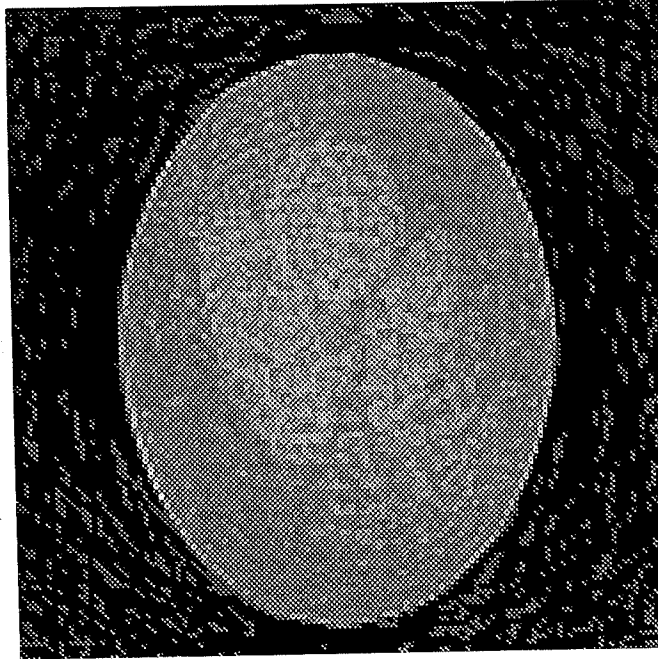


(a)

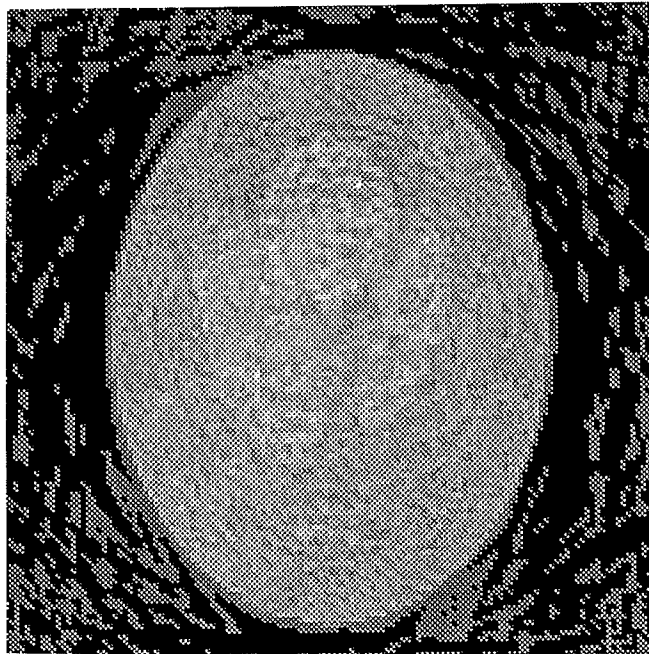


(b)

Fig. 5.3.16. Reconstruction of the reference image "ellipses" from 60 parallel projections with simulated photon noise equally spaced over 180° : (a), IART, and (b), IART with filtered projections. X-ray source intensity = 10^4 emitted photons per measurement, difference in attenuation coefficients as in Table 5.3.7.

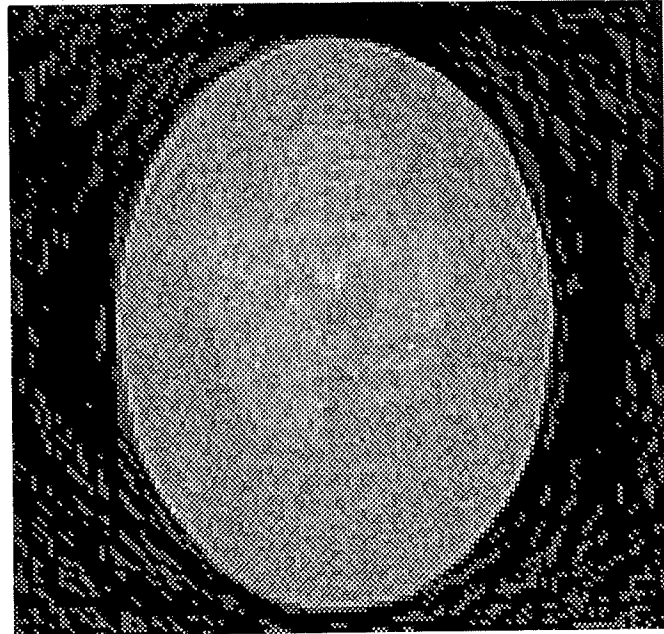


(a)

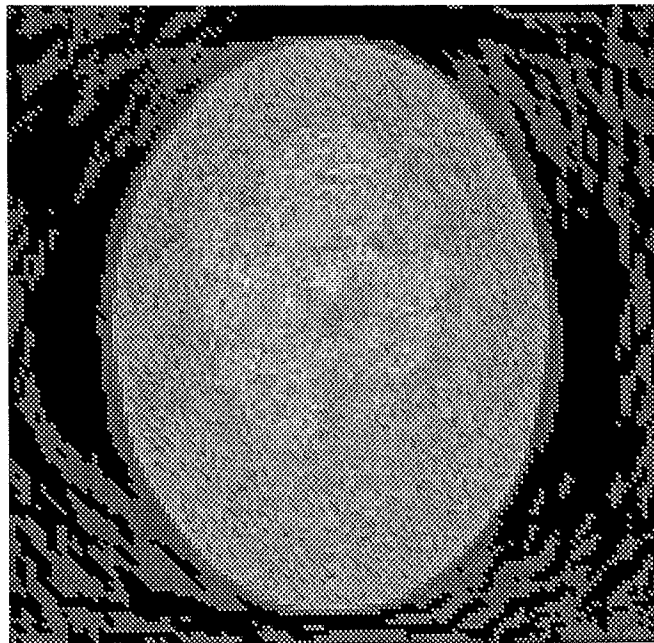


(b)

Fig. 5.3.17. Reconstruction of the reference image "ellipses" from 35 parallel projections with simulated photon noise equally spaced over 180° : (a), IART, and (b), IART with filtered projections. X-ray source intensity = 10^4 emitted photons per measurement, difference in attenuation coefficients as in Table 5.3.7.



(a)

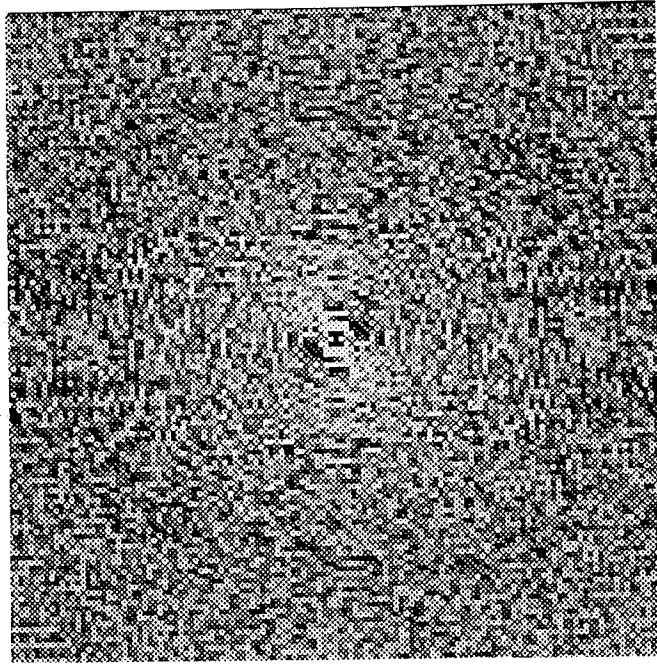


(b)

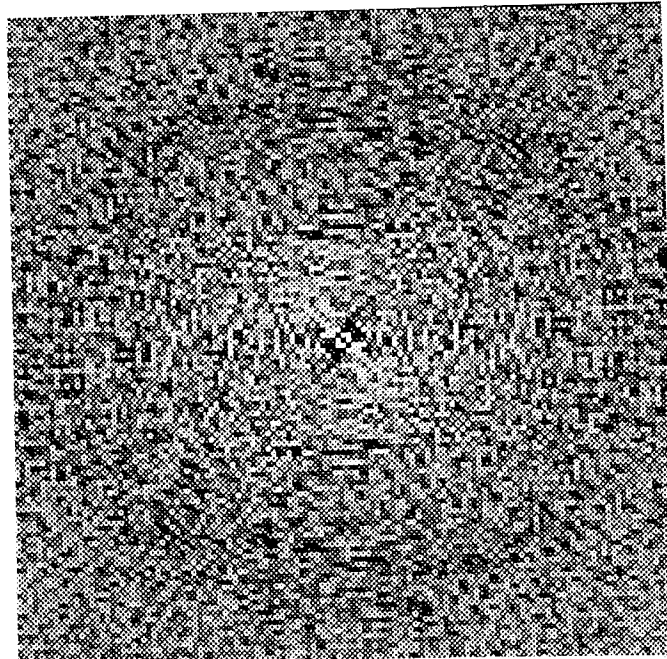
Fig. 5.3.18. Reconstruction of the reference image "ellipses" from 19 parallel projections with simulated photon noise equally spaced over 180° : (a), IART, and (b), IART with filtered projections. X-ray source intensity = 10^4 emitted photons per measurement, difference in attenuation coefficients as in Table 5.3.7.

Table 5.3.8. Computed quantitative similarity measures of Eq. (5.2-1) for the reconstruction images of the "ellipses" reference image from simulated noisy projection data.

Quantitative error measures	IART			IART with filtered projections		
	Number of projections			Number of projections		
	19	35	60	19	35	60
correlation coefficient	0.976	0.954	0.934	0.982	0.975	0.959
rms	2.426	3.440	4.245	2.083	2.476	3.175
average absolute difference	1.255	1.797	2.205	1.136	1.387	1.776
worst case difference	10.800	10.715	13.150	9.000	7.695	8.167
entropy based difference	0.029	0.053	0.074	0.026	0.027	0.036

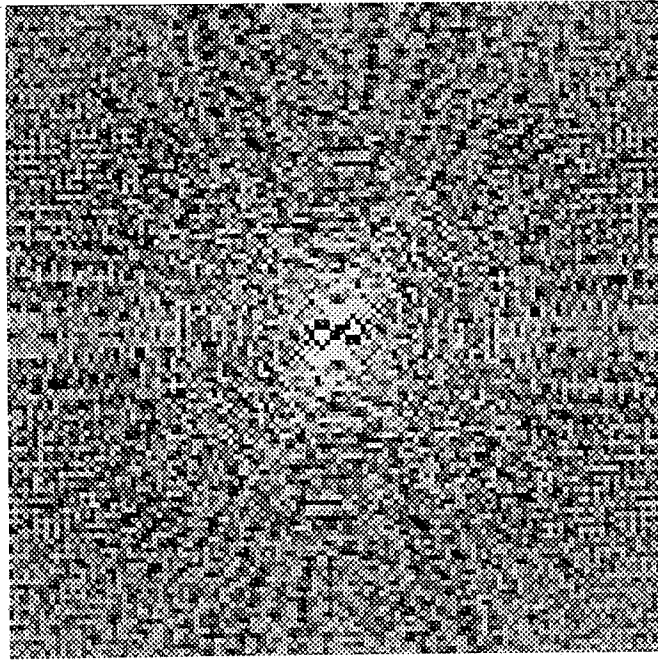


(a)

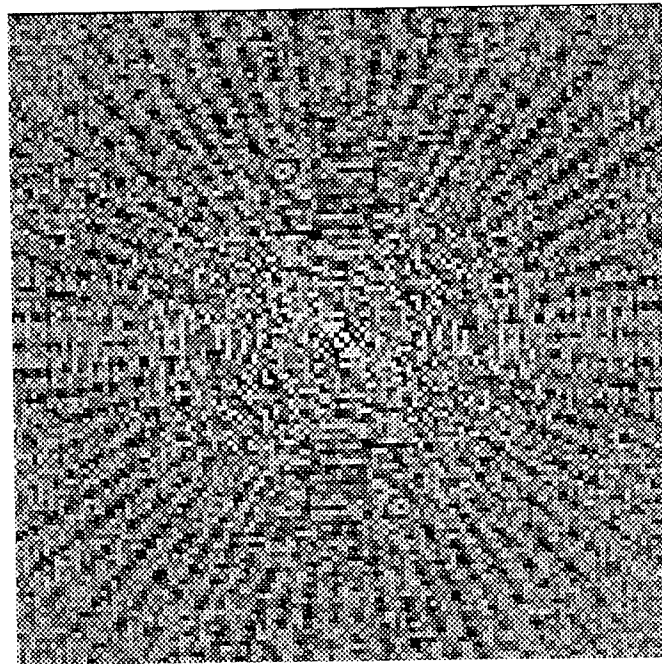


(b)

Fig. 5.3.19. The subtraction, from the Fourier spectrum of "ellipses" in Fig. 5.3.6(b), of the Fourier spectrum of the 60 projection image of: (a), IART of Fig. 5.3.16(a); (b), IART with filtered projections of Fig. 5.3.16(b).

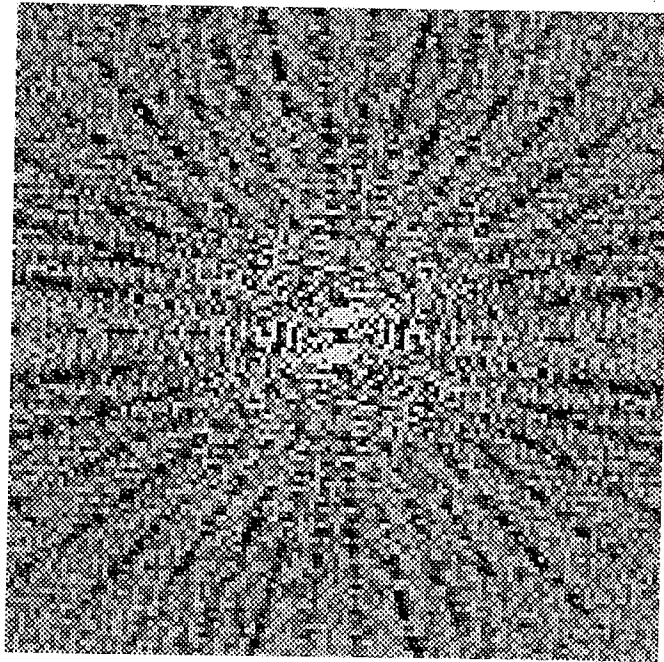


(a)

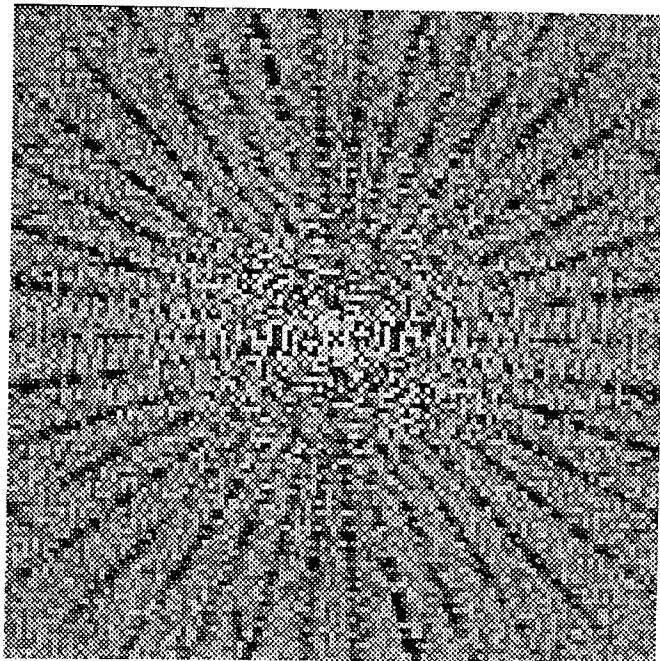


(b)

Fig. 5.3.20. The subtraction, from the Fourier spectrum of "ellipses" in Fig. 5.3.6(b), of the Fourier spectrum of the 35 projection image of: (a), IART of Fig. 5.3.17(a); (b), IART with filtered projections of Fig. 5.3.17(b).



(a)



(b)

Fig. 5.3.21. The subtraction, from the Fourier spectrum of "ellipses" in Fig. 5.3.6(b), of the Fourier spectrum of the 19 projection image of: (a), IART of Fig. 5.3.18(a); (b), IART with filtered projections of Fig. 5.3.18(b).

5.4. Discussion and Conclusions

In this chapter, the preliminary study has been conducted on the applicability of filtering the projection data prior to using it in an iterative reconstruction procedure. Interpolative Algebraic Reconstruction Methods were used as a representative of an iterative method. Two reference objects with simulated attenuation coefficient values were considered: a simple one that consisted of two different size superpositioned squares, and a more complicated one consisting of a number of ellipses. Projections were calculated to simulate the collection of data affected by photon noise. The number of projections was limited to at most 60. Projections were of parallel geometry and equally spaced over 180° .

The results obtained were consistent and confirm the advantage of using filtered projections as the input data in an iterative method (IART). Generally, all calculated quantitative similarity measures showed improvement in quality for the reconstruction images from IART with filtered projections compared to from IART on raw (noisy) data (Tables 5.3.1 - 5.3.6, 5.3.8): All, but correlation coefficients, were less in value for IART with filtered projections, which indicated that the reconstruction images more closely matched the reference image (see Section 5.2). The correlation coefficients were greater than those of IART, which also was symptomatic of the better quality reconstruction image.

As for visual evaluation, in general, all reconstruction images from IART with filtered projections were brighter and looked smoother. Images with a small difference in the attenuation coefficient of the constituent objects (Figs. 5.3.3 - 5.3.5) showed visible improvement in quality for the x-ray source intensity of 10^6 emitted photons per measurement. Images with a difference in the attenuation coefficient of 15% and greater showed minimal (not noticeable by eye) improvement in quality for this level of x-ray source intensity. For the x-ray source intensity of 10^4 emitted photons per measurement, reconstruction images from both IART and IART with filtered projections were very noisy,

and for the differences in the attenuation of 10%, hardly recognizable. When the difference was 15% and greater, the improvement was observable in reconstruction images from 35 and 19 projections (Figs. 5.3.11 - 5.3.12) of the reference object "squares", and in all images of the reference "ellipses" (Figs. 5.3.16 - 5.3.18).

Results from using the qualitative measure, the subtraction of Fourier spectra, were also in favor of the images produced by IART with filtered projections. On the whole, they appeared less noisy, displaying a more uniform grey level indicative of a close match to the reference image.

The Fourier subtraction images are not smooth ones and to detect small differences in them is not always easy. In fact, the rougher they are the tougher it is to pick out small differences when comparing them. The 60 projection case produced the least smooth subtraction images and, indeed, the images were the most difficult to judge on improvement. The most impressive enhancement was observed for the 35 projection case for the reference image "ellipses". The subtraction images are quite illustrative as far as the presence of the different level noise is concerned. When comparing the subtraction images for the intensity of an x - ray source of 10^6 and 10^4 emitted photons per measurement, it is evident how much more noise is present in the latter (compare Figs. 5.3.7 - 5.3.9 and 5.3.13 - 5.3.15).

Iterative methods converge to a solution through repeated backprojection: at first, of the input data, next, of the projections calculated from an intermediate image. Therefore, if the input projections are noisy, the intermediate image they produce will be affected by noise. This in turn, gives rise to the distorted projections calculated from the intermediate image. The following backprojection to produce an updated intermediate image will carry on and may amplify further the distortion due to the noise. As this sequence is repeated many times by an iterative procedure, the resulting reconstruction image may be more affected the more iterations are required to produce it. The amount of noise present in the reconstruction image also will magnify with the increased number of projections, since each is

contributing more noise. (Compare images from 60 and 35 projections: Figs. 5.3.16 and 5.3.17; also Figs. 5.3.3 and 5.3.4.)

Real data contains noise. To make iterative methods successful in reconstruction of real data, we need to suppress the noise to increase the fidelity of a reconstruction image. The simulation study of this chapter, although limited in the number of experiments, shows that results from an iterative reconstruction method can be improved by filtering the projection input data before processing it by the reconstruction method.

CHAPTER VI

EVALUATION OF OUTCOMES FROM IART AND FBP RECONSTRUCTION METHODS. COMPARISON

6.1. Evaluation and Comparison of Reconstruction Images From Different Number of Projections. IART

Let us take a closer look at Tables 5.3.1 and 5.3.8 of the previous Chapter V and compare the numbers with the corresponding reconstruction images. We will also analyze the results obtained from using the qualitative measure of the subtraction of Fourier spectra. Our objective is to verify that the results of calculated similarity measures are illustrative of visual impression. We are interested in comparing IART images from different numbers of projections. We will consider images produced from three different sets of projections: 19, 35 and 60, as indicated in the tables.

From Table 5.3.1:

IART: Results of the rms and the average absolute difference suggest that the reconstruction image from 19 projections is the best. This is not in agreement with the worst case difference and the entropy based difference measures that single out the image from 35 projections as the one that is the best. The correlation coefficient points out at images from 19 and 35 projections as the best ones bearing the same degree of resemblance to the reference image.

IART with filtered projections: All measures, except the worst case difference, single out the image from 35 projections as the best one.

From visual evaluation of corresponding reconstruction images from Figs. 5.3.3 - 5.3.5:

IART: The inferiority of the 19 projection image is obvious; The image apart from containing noise is blurred. The 60 projection image seems to be the best one: Although noise in it is more apparent than in the 35 projection image, it looks sharper with more distinct outlines.

IART with filtered projections: As in the *IART* case, the 19 projection image is the worst: Although noise is visibly suppressed, compared to its *IART* counterpart, blur is still present. As for the best image, the one from 60 projections seems to be the choice: It has a sharp appearance, noise is suppressed and contrast is the best.

Results of the analysis of the Fourier subtraction images (Figs. 5.3.7 - 5.3.9) show:

IART and IART with filtered projections: The 60 projection reconstruction image is the best one: The clearance around the center is of the greatest radius which is indicative of the best match; i.e., the largest percent of the energy spectrum of the reconstruction image agrees with the corresponding one of the reference image.

When analyzing results from Table 5.3.8:

IART: The majority of similarity measures (correlation coefficient, rms, average absolute difference and entropy based difference) point out at the 19 projection image as being the best.

IART with filtered projections: As in the *IART* case, the 19 projection image is suggested as the best by all but the worst case difference similarity measures.

From visual evaluation of corresponding images from Figs. 5.3.16 - 5.3.18:

IART: The 19 projection reconstruction image is the worst one; the 35 projection image shows very low contrast. The 60 projection reconstruction image looks most clear and seems to be the best, although it is very noisy.

IART with filtered projections: Here, the 35 projection reconstruction image looks superior to the others. The 19 projection image is again the worst one.

Examination of the subtraction images (Figs. 5.3.19 - 5.3.21) suggests:

IART: The 60 projection reconstruction image is the best one: The corresponding subtraction image (Fig. 5.3.19 (a)) displays the center region of the largest radius.

IART with filtered projections: The subtraction image for 35 projections shows the beginning of the clearance around the center. It also displays a more uniform grey level in the image as a whole. These suggest that the corresponding reconstruction image is the best match with the reference image.

To summarize the above: In both cases, visual evaluation of the reconstruction images was in disagreement with the results of the quantitative similarity measures.

From the above results, we can make tentative conclusions that the use of quantitative similarity measures to images of an iterative reconstruction method from the different number of projections fails.

In contrast, using the qualitative similarity measure of the subtraction of Fourier spectra, produced results that were always in agreement with the visual evaluation of the reconstruction images.

6.2. Evaluation and Comparison of Reconstruction Images From Different Number of Projections. FBP

As a "standard" for the simulation experiments from the previous chapter, the Fourier Backprojection (FBP) reconstruction method with the Shepp-Logan kernel, was used. Tables 6.2.1 and 6.2.2 display the results of the evaluation of FBP reconstruction images of the reference images "squares" and "ellipses", respectively. Figs. 6.2.1 - 6.2.6 show the corresponding reconstruction images. The reconstruction images of "squares" were produced for the difference in the attenuation coefficient of 10% and for the assumed x-ray source intensity of 10^6 emitted photons per measurement. The reconstruction images of "ellipses" were produced for the x-ray source intensity of 10^4 emitted photons per

measurement. In both cases, the images were produced for three sets of 19, 35 and 60 parallel projections equally spaced over 180° .

Let us compare the numbers, representative of the quantitative similarity measures, in the tables with visual impression from the corresponding reconstruction images to verify if they match. We will also use the qualitative measure, the subtraction of Fourier spectra. As in the previous section, we are interested in the comparison of images from different number of projections.

From Table 6.2.1, all similarity measures indicate that the 60 projection image as the best. This is in agreement with the visual evaluation of corresponding images (Figs. 6.2.1 - 6.2.3). Figs. 6.2.4 - 6.2.6 display the subtraction images for the reconstruction images of Figs. 6.2.1 - 6.2.3, respectively, obtained by subtracting the Fourier spectra of the reconstruction images from the Fourier spectrum of the reference image "squares" in Fig. 5.3.6(a). From their examination, we can conclude that the 60 projection reconstruction image is the best one: It has the largest radius of the central region suggesting the best resemblance to the reference image.

When analyzing Table 6.2.2, the results suggest the 60 projection image as being the best, and this is also confirmed by the results from the visual evaluation (Figs. 6.2.7 - 6.2.9). The results of the subtraction of Fourier spectra similarity measure are presented in Figs. 6.2.10 - 6.2.12. The images were obtained by subtracting the Fourier spectra of the reconstruction images of Figs. 6.2.7 - 6.2.9 from the Fourier spectrum of the reference image in Fig. 5.3.6(b). The subtraction image for the 60 projection case displays the largest central clearance region indicative of the best reconstruction image. This is in agreement with the above results from the quantitative measures and the visual evaluation.

To sum up the above results, we can conclude that using both, quantitative and qualitative, similarity measures to compare reconstruction images from different number of projections performs well for the Fourier Backprojection method. The subtraction images

of the qualitative measure look similar for the reconstruction images from the different number of projections. However, with the increased number of projections, the central clearance region widens which is suggestive of the improvement in the reconstruction.

Table 6.2.1. Computed quantitative similarity measures of Eq. (5.2-1) for the reconstruction images of the "squares" reference image from simulated noisy projection data. Case: $\partial\mu = 10\%$, source intensity = 10^6 emitted photons per measurement.

FBP			
Quantitative error measures	Number of projections		
	19	35	60
correlation coefficient	0.893	0.964	0.981
rms	5.332	3.193	2.600
average absolute difference	3.416	2.408	2.120
worst case difference	23.257	12.525	7.170

Table 6.2.2. Computed quantitative similarity measures of Eq. (5.2-1) for the reconstruction images of the "ellipses" reference image from simulated noisy projection data. X-ray source intensity = 10^4 emitted photons per measurement.

FBP			
Quantitative error measures	Number of projections		
	19	35	60
correlation coefficient	0.916	0.956	0.975
rms	4.932	3.598	2.864
average absolute difference	3.878	2.842	2.250
worst case difference	11.823	10.680	7.745

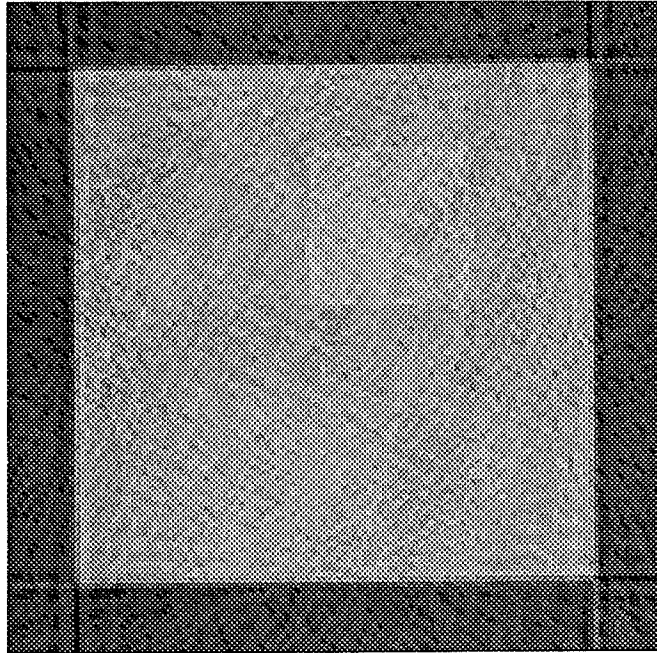


Fig. 6.2.1. The FBP reconstruction of the reference image "squares" from 60 parallel projections with simulated photon noise equally spaced over 180° . X-ray source intensity = 10^6 emitted photons per measurement; difference in the attenuation coefficient = 10%.

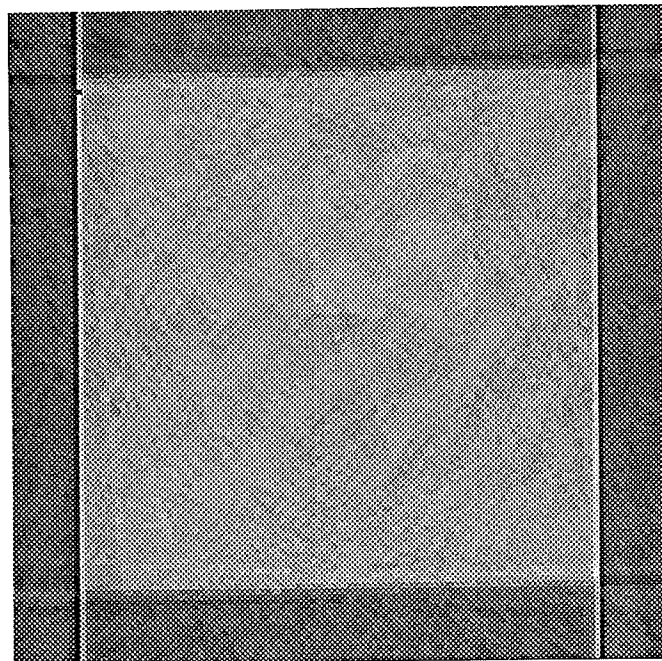


Fig. 6.2.2. The FBP reconstruction of the reference image "squares" from 35 parallel projections with simulated photon noise equally spaced over 180° . X-ray source intensity = 10^6 emitted photons per measurement; difference in the attenuation coefficient = 10%.

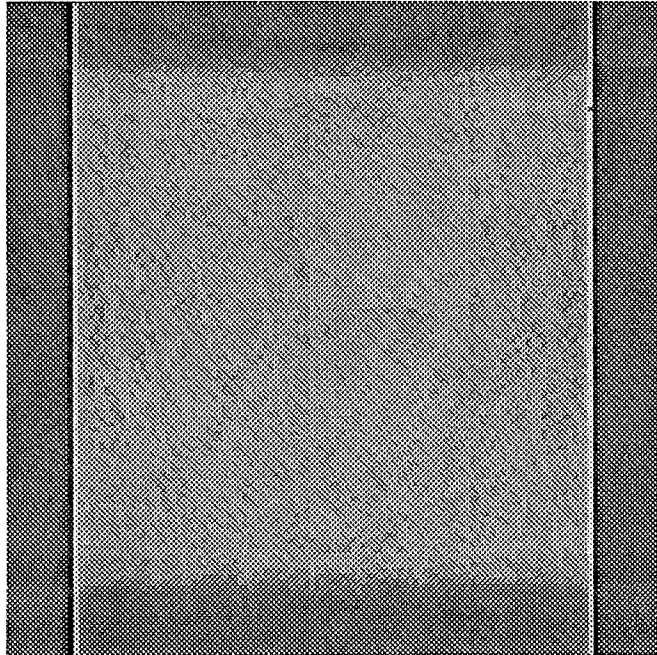


Fig. 6.2.3. The FBP reconstruction of the reference image "squares" from 19 parallel projections with simulated photon noise equally spaced over 180° . X-ray source intensity = 10^6 emitted photons per measurement; difference in the attenuation coefficient = 10%.

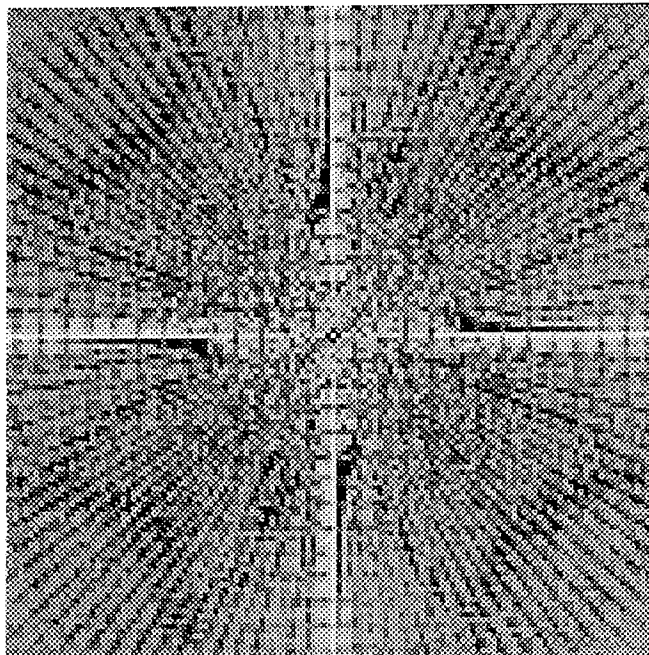


Fig. 6.2.4. The subtraction of the Fourier spectrum of the 60 projection FBP image from the Fourier spectrum of "squares" in Fig. 5.3.6(a).

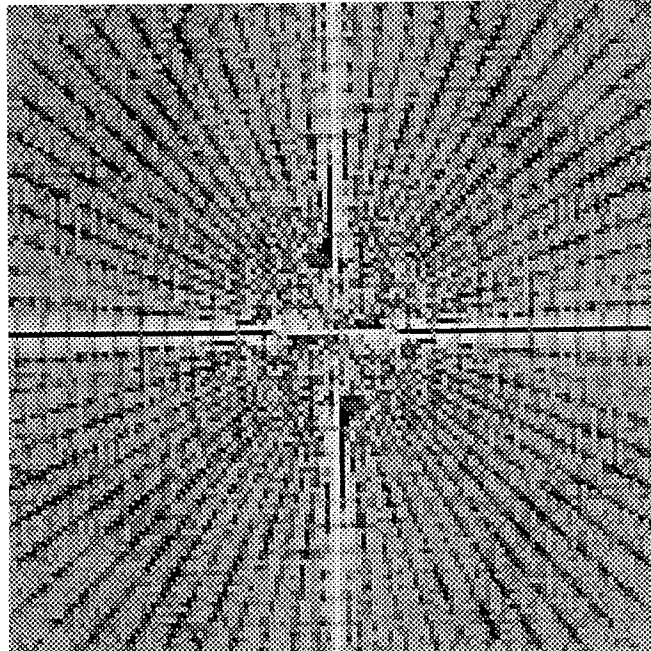


Fig. 6.2.5. The subtraction of the Fourier spectrum of the 35 projection FBP image from the Fourier spectrum of "squares" in Fig. 5.3.6(a).

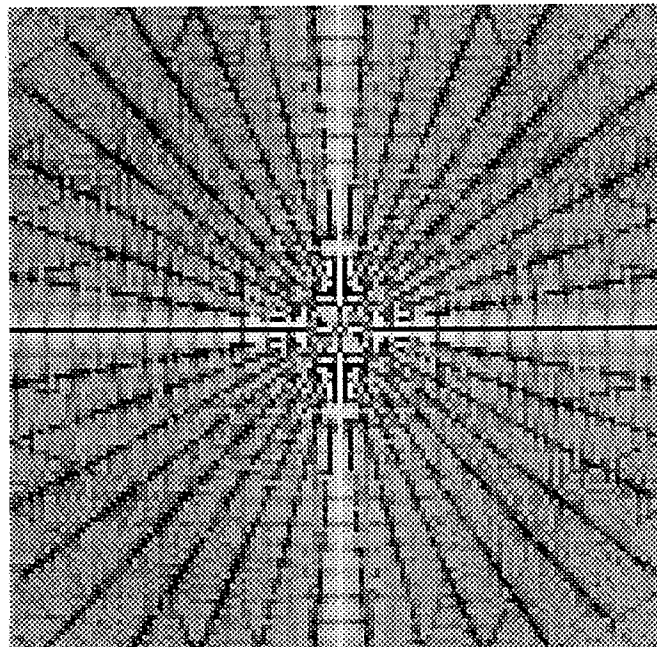


Fig. 6.2.6. The subtraction of the Fourier spectrum of the 19 projection FBP image from the Fourier spectrum of "squares" in Fig. 5.3.6(a).

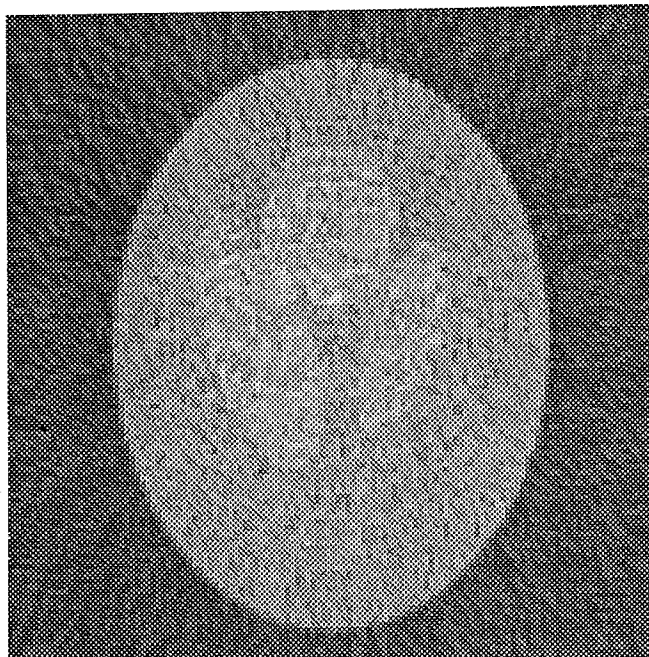


Fig. 6.2.7. The FBP reconstruction of the reference image "ellipses" from 60 parallel projections with simulated photon noise equally spaced over 180° . X-ray source intensity = 10^4 emitted photons per measurement; difference in the attenuation coefficient as in Table 5.3.7.

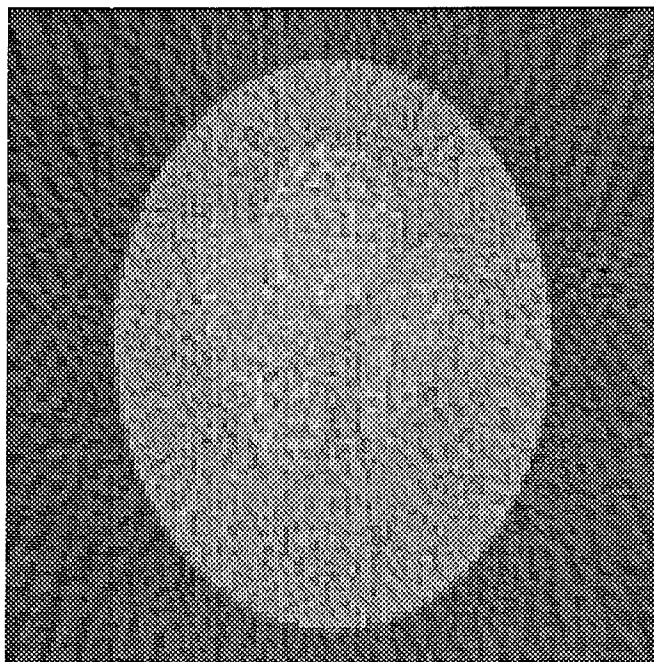


Fig. 6.2.8. The FBP reconstruction of the reference image "ellipses" from 35 parallel projections with simulated photon noise equally spaced over 180° . X-ray source intensity = 10^4 emitted photons per measurement; difference in the attenuation coefficient as in Table 5.3.7.

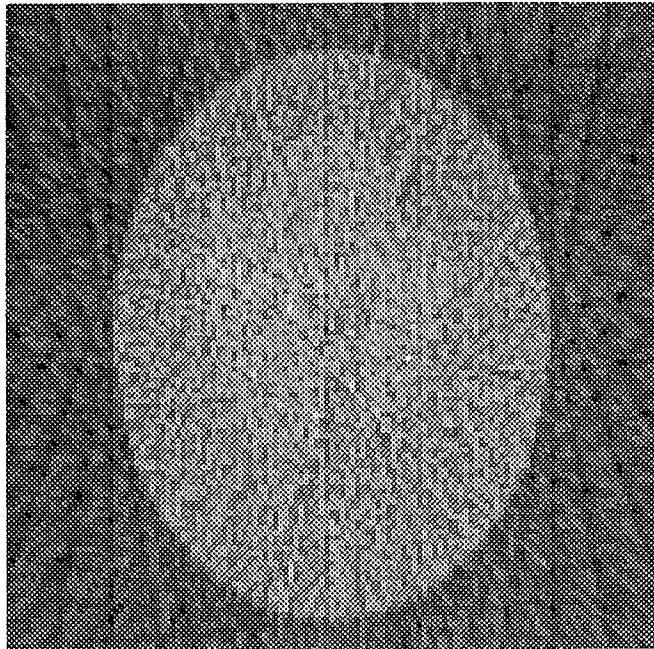


Fig. 6.2.9. The FBP reconstruction of the reference image "ellipses" from 19 parallel projections with simulated photon noise equally spaced over 180° . X-ray source intensity = 10^4 emitted photons per measurement; difference in the attenuation coefficient as in Table 5.3.7.

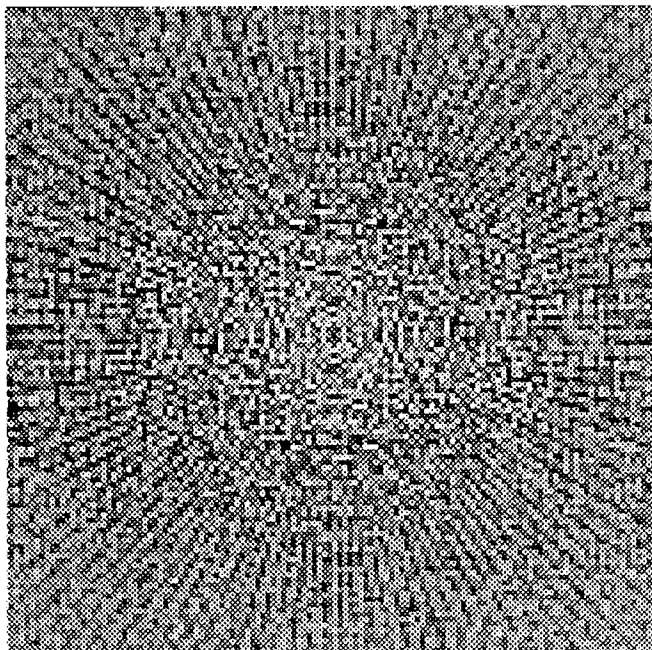


Fig. 6.2.10. The subtraction of the Fourier spectrum of the 60 projection FBP image from the Fourier spectrum of "ellipses" in Fig. 5.3.6(b).

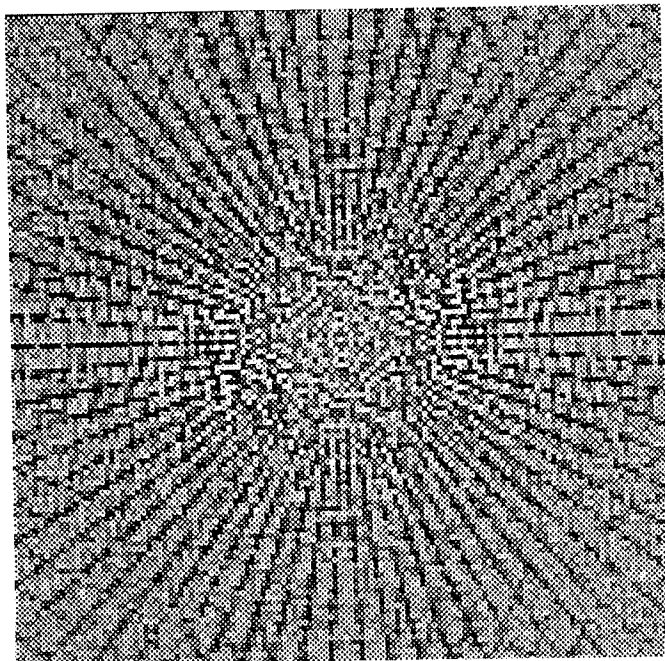


Fig. 6.2.11. The subtraction of the Fourier spectrum of the 35 projection FBP image from the Fourier spectrum of "ellipses" in Fig. 5.3.6(b).

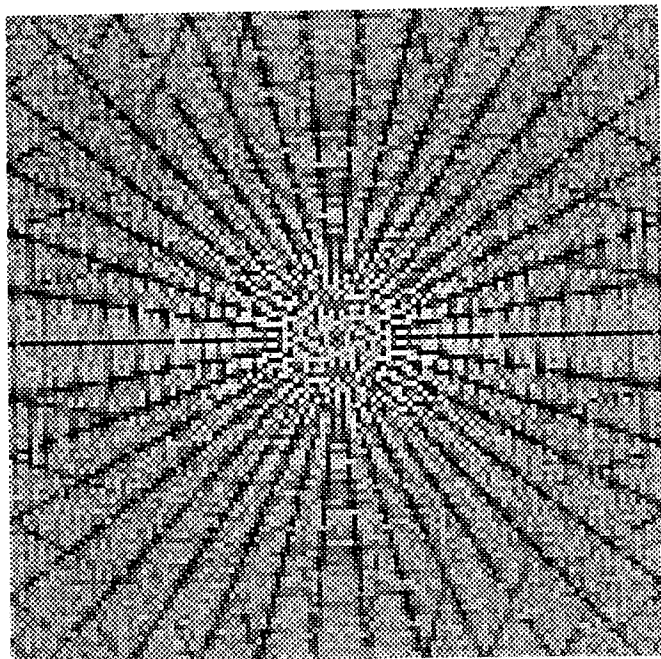


Fig. 6.2.12. The subtraction of the Fourier spectrum of the 19 projection FBP image from the Fourier spectrum of "ellipses" in Fig. 5.3.6(b).

6.3. Evaluation and Comparison of Reconstruction Images From IART and FBP

In this section, we will examine if using the quantitative and qualitative similarity measures is applicable when comparing outputs from different reconstruction methods. We will compare reconstruction images from two different kinds of algorithms: IART, an iterative and nonlinear method; and Fourier Backprojection (FBP), a single step linear method that utilizes the Fourier transformation. Absolute values of the reconstruction images resulting from these methods are different in a sense that IART produces an image of only positive values, while an FBP image contains both positive and negative values. This property makes it impossible for the entropy based difference (see Eq.(5.2-1)) to be used as a quantitative comparative measure as it requires for an image to be composed of only positive values, and therefore, we cannot use it for the FBP image.

Tables 6.3.1 - 6.3.2 display the cumulative results (IART, IART with filtered projections and FBP) from using the quantitative similarity measures on the reconstruction images of the reference images "squares" and "ellipses", respectively.

Examination of Table 6.3.1 suggest, for all three sets of projections, the choice of the images from IART with filtered projections as the best ones. Correlation coefficients calculated for IART with filtered projections images have the greatest values while all the other measures (rms, average absolute value, worst case difference) have the least values compare to their IART and FBP counterparts. Visual evaluation of the corresponding reconstructions (Figs. 5.3.3 - 5 and 6.2.1 - 6.2.3) confirms the results: IART with filtered projections images produced from the 19 and 35 projections (Figs. 5.3.4(b), 5.3.5(b)) are sharper with better delineated contours and better contrast compared to their FBP counterparts (Figs. 6.2.2 - 6.2.3). For 60 projections, the FBP reconstruction image (Fig. 6.2.1) is slightly worse than the one from IART with filtered projections (Fig. 5.3.3(b)). But it also looks smoother and the noise is less apparent.

Table 6.3.1. Cumulative quantitative similarity measures of Eq. (5.2.1) for reconstruction images of the "squares" reference image from simulated noisy projection data. Case: $\partial\mu = 10\%$, source intensity = 10^6 emitted photons per measurement.

Quantitative error measures	IART			IART with filtered projections			FBP		
	number of projections			number of projections			number of projections		
	19	35	60	19	35	60	19	35	60
correlation coefficient	0.984	0.984	0.975	0.987	0.990	0.987	0.893	0.964	0.981
rms	1.737	1.749	2.194	1.556	1.400	1.573	5.332	3.193	2.600
average absolute difference	1.005	1.076	1.374	0.868	0.061	1.008	3.416	2.408	2.120
worst case difference	6.792	5.355	5.975	6.615	4.305	3.470	23.257	12.525	7.170
entropy based difference	0.011	0.008	0.011	0.011	0.008	0.009	-	-	-

Table 6.3.2. Cumulative quantitative similarity measures of Eq. (5.2.1) for reconstruction images of the "ellipses" reference image from simulated noisy projection data. Source intensity = 10^4 emitted photons per measurement.

Quantitative error measures	IART			IART with filtered projections			FBP		
	number of projections			number of projections			number of projections		
	19	35	60	19	35	60	19	35	60
correlation coefficient	0.976	0.954	0.934	0.982	0.975	0.959	0.916	0.956	0.975
rms	2.426	3.440	4.245	2.083	2.476	3.175	4.932	3.598	2.864
average absolute difference	1.255	1.797	2.205	1.136	1.387	1.776	3.878	2.842	2.250
worst case difference	10.800	10.715	13.150	9.000	7.695	8.167	11.823	10.680	7.745
entropy based difference	0.029	0.053	0.074	0.026	0.027	0.036	-	-	-

The analysis of the corresponding subtraction images (Figs. 5.3.7 - 5.3.9 and Figs. 6.2.4 - 6.2.6) confirms the results of Table 6.3.1: The subtraction images for the IART with filtered projections have the center region more uniform. The differences from the reference spectrum are more in the form of salt and pepper rather than of whole regions of different contrast. This is especially observable for the 19 and 35 projection images as the subtraction image for the 60 projection FBP image is very close in the appearance to the one for IART with filtered projections.

Analysis of Table 6.3.2 indicates that while for 19 and 35 projections, reconstruction images from IART with filtered projections are the best, for 60 projections, the FBP reconstruction image is the finest. For 60 projections, the correlation coefficient of the FBP image is the highest, while for the other two sets of projections, 19 and 35, the correlation coefficients of the images of IART with filtered projections have the greatest values. Other measures, except for the worst case difference for the 60 projections, confirm results of the correlation coefficients. Visual impression from looking at the corresponding reconstruction images (Figs. 5.3.16 - 18 and 6.2.7 - 9) is in agreement with the results of Table 6.3.2: Figs. 6.2.7, 5.3.17(b), and 5.3.18(b) are the best reconstructions of the reference image "ellipses" from the 60, 35, and 19 projections, respectively. From the analysis of the corresponding subtraction images (Figs. 5.3.19 - 5.3.21 and 6.2.10 - 6.2.12), the subtraction image for the IART with filtered projections for the 19 projections shows the increased radius of the center region with less prominent streaks along the projection directions compared to its counterpart for FBP. The same comment applies to the subtraction images for the 35 projections. For 60 projections, the subtraction images look very much different and while the one for IART with filtered projections is in the form of a cloud, brighter in the center and darker towards the border, the corresponding one for FBP displays the clearance around the center. To sum up, the above qualitative results are not obvious in a choice of the better image.

In review, quantitative similarity measures that can be used when comparing results from linear and nonlinear reconstruction methods. The applicability of using them was confirmed on the reconstruction images of the two reference images: "squares" and "ellipses". The reconstruction images were produced by an iterative, nonlinear method, IART, and by a linear method, FBP.

The results from using the subtraction of Fourier spectra similarity measure were positive for the reconstruction images of the reference image "squares", while for the "ellipses" reference image were inconclusive.

6.4. Discussion and Conclusions

Evaluation of reconstruction images has always been a problem. There is no standard way of doing it. Quantitative criteria are convenient to use as they express the closeness of two images in the form of a number. By comparing numbers, we can determine the superiority in quality of one reconstruction image to another. The problem with the quantitative criteria is that the majority of them concentrate on the evaluation of one specific feature of an image. Therefore, it is common practice to use several of them when making a choice on a better reconstruction image.

In this chapter, we have analyzed the applicability of quantitative criteria as evaluation measures for the comparison of reconstruction images from the different number of projections. This is something new, as usually, the evaluation is done on images produced from the same number of projections [Herman, 1972], [Herman, 1973a], [Heffernan, 1983], [Oskoui, 1989], [Ollinger, 1988], [Suzuki, 1988], [Cho, 1975]. In our study, we have used images from an iterative method, IART, and Fourier backprojection. The results obtained suggest that it is possible to evaluate FBP reconstruction images using the quantitative similarity measures. Unfortunately, we cannot use them to successfully evaluate images from the IART reconstruction method. Although results from only one

iterative method are insufficient to reach any final conclusions, tentative conclusions can be made based on the analysis of the results. Our finding implies that using quantitative similarity measures for images from an iterative reconstruction method would fail when we would compare reconstruction results from the different number of projections.

The study was complemented by verifying the use of the quantitative measures when making a choice between two different reconstruction methods (linear and nonlinear). IART was used as a representative of the nonlinear methods, and FBP as a representative of the linear reconstruction methods. The analysis included the comparison of the reconstruction images for the three sets of projections (19, 35, and 60). Our findings were consistent, and confirmed the applicability of using the quantitative measures to compare images of linear and nonlinear reconstruction methods.

In addition, throughout our study, another similarity measure of the qualitative nature was used, the subtraction of the Fourier spectra. Results from it are displayed in the form of subtraction images that are basically nonsmooth and represent the disagreement between the reconstruction and the reference energy spectra. Comparison of the reconstruction images from the different number of projections in both cases, IART and FBP, gave results that were positive, i.e. in agreement with the visual evaluation of the corresponding reconstruction images. Since IART and FBP were used as the representatives of different groups of reconstruction methods (nonlinear and linear, respectively), therefore, we can expect that the above results possibly can be extended to all methods of these groups. But this requires confirmation.

When the subtraction images were used to look for the best reconstruction from IART and FBP reconstruction images from the same number of projections, the results were not consistent: The results obtained were positive for one reference image, "squares", while in the case of the "ellipses" reference image, the subtraction images were not conclusive.

The interpretation of subtraction images is not always straightforward. It is much easier to compare the subtraction images for the methods that belong to the same group because

the spectra they produce have similar appearance. When we deal with images from different reconstruction methods that have different spectra, the interpretation of subtraction images requires some experience.

CHAPTER VII

MATCHING RECONSTRUCTION TECHNIQUE. A NEW PROPOSAL

7.1. Introduction

Recently, a new method, Image Correlation Technique (ICT), has been introduced [Mazur, 1992b], [Mazur, 1992c]. The method, by matching two images of the same object, taken before and after the deformation, recovers the deformation that the object has undergone. The method treats the images as a whole and uses only the intensity pattern distribution and the geometrical relationship between the images to find the transformation of the body coordinates that uniquely connects different stages of the deformed object. The ICT method is essentially an iteration method equipped with the Boltzmann decision apparatus [Kirkpatrick, 1983], [Aarts, 1989]. It starts from an undeformed configuration of pixels (the reference image) and through a series of deformations arrives at the deformation that is close or the same as the deformation represented by the pixels of the second image (the deformation image). By doing this, the method emulates the real deformation through a sequence of simulated deformations. Each intermediate deformation is generated at random, tested how far it falls from the destination deformation, and accepted or rejected based on the Boltzmann decision apparatus. The process terminates if the correlation function no longer increases and fluctuates with a certain amplitude.

This thesis would like to introduce a new reconstruction algorithm, Matching Reconstruction Technique (MRT), that is based on the similar optimization simulated annealing technique. In the following section the formulation of the method is given.

7.2. Matching Reconstruction Technique

List of Important Symbols

Symbol	Meaning
D	number of detectors of a projection
F	optimization constant
$I(k,l)$	intensity of the (k,l) 'th element of a reconstruction matrix
I_{\max}	maximum intensity of a reconstruction matrix
M	size of a square reconstruction matrix (M x M)
N	number of projections
P_{ij}^*	for the intermediate image, calculated reading of the j 'th detector of the i 'th projection direction
P_{ij}	reading of the j 'th detector of the i 'th projection direction
T	temperature-like parameter to control the optimization process

To explain how the method works, let us place the image in three-dimensional space, where the image pixel coordinates are stored in the xy plane, and the third dimension represents the grey scale intensities of the image. The image itself can be viewed as a surface in this space. Let us assume that change in the intensity of an arbitrarily chosen pixel (let us call it a seed pixel) always induces intensity changes of all surrounding pixels. The pattern of the changes as well as the amplitudes are weighed by the distance from the

seed pixel. We can make an analogy to a canopy: When one of the supporting poles is raised (or lowered) the whole canopy is effected. However, the change is different for different parts.

In the next step the result of the intensity modification in the reconstruction image is checked against the set of projections taken from the reference image/object. If the change satisfies the acceptance criterion, a new image is retained. The reconstruction process is complete when a similarity measure computed for the latest reconstruction images fluctuates with a certain amplitude and shows no improvement of the reconstruction fidelity.

In the remaining part of this section, we will expand this general idea of MRT to include more details.

The following three steps are repeated until a system arrives at the solution.

- Step 1:* At random we select:
- a pixel $I(i, j)$, called the seed pixel;
 - a direction of intensity change d_i such that $\Delta I(i, j) \in \{-1, 1\}$;
 - two numbers, R, P , from the open interval $(0, 1)$;
 - R_f from the open interval $(0, M)$

Then, we change the intensity of every pixel of a reconstruction matrix from its actual value $I(m, n)$ to a new value $I^*(m, n)$ from the interval $(I_{\max}, 0)$:

$$I^*(m, n) = I(m, n) + \Delta I(m, n) \quad (7.2-1)$$

where:

$$\Delta I(m, n) = \begin{cases} \frac{I_{\max} - I(m, n)}{\exp(Z)} R & \text{if } d_i > 0 \\ \frac{-I(m, n)}{\exp(Z)} R & \text{if } d_i < 0 \end{cases} \quad (7.2-2)$$

and

$$Z = \frac{(m - i)^2 + (n - j)^2}{(F + R_f)^2} \quad (7.2-3)$$

Step 2: Following the random change in intensity from step 1, we evaluate the cost function C (our measure of similarity that involves temporary and original projections) and make a decision

$$C = \frac{\sum_{i=1}^N \sum_{j=1}^D p_{ij} p_{ij}^*}{\ln \left(1 + \sum_{i=1}^N \sum_{j=1}^D |p_{ij} - p_{ij}^*| \right) \sqrt{\sum_{i=1}^N \sum_{j=1}^D (p_{ij}^*)^2} \sqrt{\sum_{i=1}^N \sum_{j=1}^D (p_{ij})^2}} \quad (7.2-4)$$

We accept the change if C increases. If C decreases we may accept it only if the probability $P(C)$ is greater than the random number P chosen in step 1. This conditional decision is essential as it provides a means for escaping from local minima throughout the process of simulated annealing optimization.

$$\begin{array}{lll} \text{if } \Delta C > 0 & & \text{step is accepted} \\ \text{if } \Delta C \leq 0 & \text{and } P(C) > P & \text{step is accepted} \\ \text{if } \Delta C \leq 0 & \text{and } P(C) \leq P & \text{step is not accepted} \end{array} \quad (7.2-5)$$

where

$$P(C) = \exp \left[-\frac{|\Delta C|}{T} \right] \quad (7.2-6)$$

Step 3: The optimization terminates if C no longer increases and fluctuates with a certain small amplitude. This criterion helps to determine if we have obtained the best possible fidelity of the reconstruction.

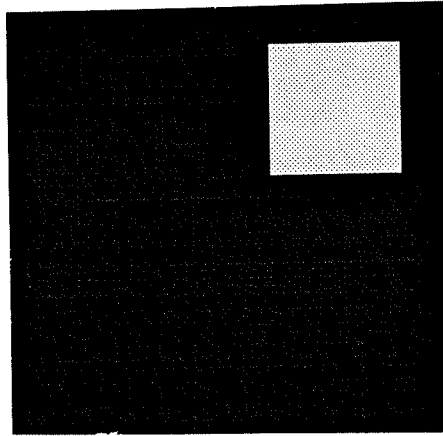
For a single value of the temperature-like parameter, T , all three steps are repeated many times. The temperature-like parameter assures the control of the process and itself is a subject to the change according to a cooling scheme, Eq. (7.2-7). As T decreases along the optimization process, the decision algorithm, Eqs.(7.2-4)-(7.2-5), accept fewer intensity changes that lead to the refinement of the solution. Traditionally the total number of trials at each temperature-like parameter level, k , is kept constant.

The cooling schedule can take many different forms. Below, we present the simplest form [Aarts, 1989]:

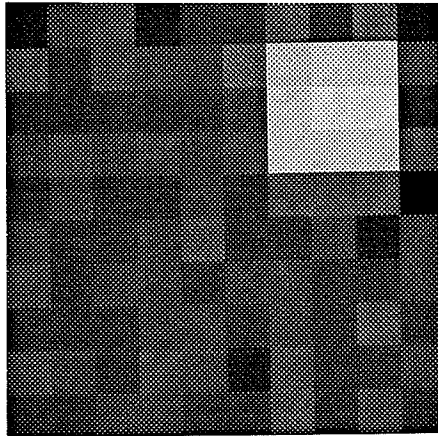
$$T_k = \alpha T_{k-1} \quad (7.2-7)$$

where the value of α is from the interval (0.8 - 1).

The method was implemented on a Macintosh computer. Preliminary, successful results consist of a reconstruction of a simple reference object (Figs. 7.2.1(b) and 7.2.1(a), respectively). The object matrix was 10 x 10 pixels in size. Input data included 10 parallel beam geometry projections equally spaced over 180°.



(a)



(b)

Fig. 7.2.1 (a), reference image and (b), its MRT reconstruction from 10 parallel beam projection directions equally spaced over 180° .

7.3. Concluding Remarks

Presented reconstruction method uses the simulated annealing technique that is totally different from the commonly used approaches to reconstruct an object. The reconstruction process is based on random changes of intensities/grey levels of the reconstruction matrix elements/pixels. Every accepted modification of the reconstruction matrix forms an intermediate image that is like a term in a sequence converging to the solution.

The change in the intensity at a particular pixel location is always accompanied by intensity changes of all surrounding pixels that make up the reconstruction image. The magnitude of changes is weighted by the distance, choice of the optimization constant F , as well as by the random selection (parameter R_f). Such an approach presents the advantage of influencing and controlling the smoothness of a reconstruction image. The lowest value of $R_f + F$ corresponds to the highest contrast that can be assigned to adjacent pixels. When R_f is zero, the optimization constant F alone sets this value.

It is probably true that in order to get the same quality of the reconstruction image, the proposed method requires fewer projections than other reconstruction methods. Moreover, this method should be readily applicable to the difficult cases of reconstructing from projections from limited angles. This is because there is no dependency of the cost function on the projection angle nor on the number of projections.

Coordinated adjustment of all pixels introduces smoothness into the reconstruction that is not necessarily accompanied by loss of contrast (blurring). In fact, the opposite might be true for the smoothness of the reconstruction and a broad range of the algorithm flexibility may result in considerable reduction of the reconstruction noise.

To its disadvantage, the proposed method requires much computer time. In addition it still requires refinement and further investigation of its capability.

CHAPTER VIII

CONCLUSIONS AND FUTURE WORK

Incomplete data is an annoying problem in computed tomography. Generally, it refers to the loss of some detector readings (truncated projections), a whole sector of missing projections, or when we deal with a limited number of projections. In industry the incomplete data problem arises mainly due to, say, an obstruction [Gordon, 1985]. In clinical CT, Medoff has shown that the problem originates when opacities are present in the object being examined [Medoff, 1987]. Looking for the reconstruction method that would produce the best fidelity image has been a subject of extensive studies [Chu, 1988], [Gore, 1980], [Grunbaum, 1980], [Hanson, 1982], [Hanson, 1983], [Inouye, 1979], [Inouye, 1982], [Lewitt, 1979], [Medoff, 1983], [Nassi, 1982], [Ogawa, 1984], [Ollinger, 1990], [Oppenheim, 1977], [Peng, 1989], [Peres, 1979], [Reeds, 1987], [Sankar, 1982], [Sezan, 1984], [Tam, 1981], [Tam, 1981a], [Tato, 1981], [Tuy, 1984], [Wagner, 1979], [Wood, 1979].

ART has been proven to work well with the incomplete projection data and authors use its approach in different implementations or use the algorithm as a reference method to evaluate the reconstruction results [Oskoui-Fard, 1988], [Andersen, 1989], [Peng, 1989]. As a main disadvantage of using ART techniques, it has been pointed out the computational effort in the calculation of the weighting coefficients required in the ray-sum calculation of the projection process. IART, which this thesis introduced, is an answer to the solution of this problem. It solves this problem not only for the parallel beam geometry but more importantly, for the radiation beam of any shape including a fan and a 3-dimensional cone beam, i.e., beams that are more likely to be used in practice. In addition, the reconstruction

images obtained are less noisy. The examples of the reconstructions in Section 2.1.4 demonstrated the applicability of the method for any shape of the radiation beam.

IART, as all iterative methods, is sensitive to noise. To make the method work successfully on real data that always contains noise, we have worked on noise removal from projection data before using it by the method. The improvement in the image quality was obtained when the projections were filtered using a windowing technique. Even better improvement is expected to be obtained when this technique is used to filter not only the projection data prior to use it by the reconstruction method, but also during the reconstruction process itself. Namely, we suggest that the projections calculated from an intermediate image should be filtered as well. The intermediate image that is produced at every iteration cycle is contaminated with noise from the noisy projections that produce it. Consequently, the projections taken from it are going to be distorted and produce even more noise in the following intermediate image. The situation worsens with every iteration step. We think that additional filtering at every iteration cycle should alleviate the noise problem and improve the quality of the reconstruction image.

The approach that has been used to relate pixels to the projections, makes the calculations less burden for the computer memory and also, as it has been shown in Section 2.1.4, makes it realistic for the iterative methods to be used on real data that, at present, is mostly produced by a fan beam. Furthermore, for IART, it eliminates errors due to the discretization characteristic for ART algorithms (see Section 2.1.5), [Andersen, 1974], [Andersen, 1989]. This novel method, that was used to relate pixels to the projections, can be used with any iterative method. Simultaneous Iterative Reconstruction Technique (SIRT) [Gilbert, 1972], [Oppenheim, 1977], is an example of another algorithm, that was formulated to overcome ART's weakness. It makes changes to the pixel estimate by using data from all projections simultaneously, and therefore exhibits more uniform convergence. Its disadvantage though, is a slow rate of convergence. Gilbert [Gilbert, 1972] reported on SIRT's better performance compared to ART in the presence of errors in the projection

data. Andersen [Andersen, 1989] tested the usefulness of the method in a study where a sequence of four iterations of an ART based method (SART) was followed by several iterations of the SIRT. He saw no further convergence being achieved this way. For the purpose of further studies, it would be advisable to use the IART approach of relating pixels to the projections and include the SIRT method in further studies. Similarly, all operations of noise removal from the projection data, including the filtering operation during the reconstruction process itself, should be applicable as well.

Two-dimensional detector arrays call for a cone beam geometry. The novel approach presented by this thesis to relate pixels to the projections is readily applicable to this geometry.

Another new reconstruction method suitable for all the cases of the incomplete data problem is presented in Chapter VII. The method uses the simulated annealing technique and is totally different from the commonly used approaches to reconstruct an object. The reconstruction process consists of random changes of grey levels of the reconstruction matrix elements/pixels. Every change produces a new image that is checked against the input set of projections for fidelity to the reference object. The reconstruction process is complete when there is no longer any improvement in the image quality. This method has a good chance to be successful for all the difficult cases of incomplete data including the one of the very limited number of projections, because of the reconstruction process itself and the similarity measure that we suggest (cost function). As it has been pointed out in Section 7.3, the cost function was formulated as to be not dependent on the projection directions nor on the number of projections. It produces a sharp peak when a match, of the original and computed projections occurs. The method has been verified by preliminary experiments. Further study should concentrate on the refinement of the method based on results from its implementation to the various cases of incomplete data. The proposed method requires extensive computations. Therefore, it should be implemented on fast computers.

In Chapter VI, a comparative study on reconstruction images was performed. The objective was the applicability of quantitative criteria and the qualitative criterion of the subtraction of Fourier spectra of images (reconstruction from reference) as similarity measures. In the study, a new approach was used, as compared images were obtained using the same reconstruction method but from different number of projections. The images used were from a nonlinear, iterative method, IART, and from a linear one, Fourier backprojection. The results obtained suggest that it is possible to compare FBP reconstruction images using the quantitative similarity measures. Unfortunately, we cannot use them to successfully evaluate and compare images from the IART reconstruction method. The outcome from using the qualitative measure of the subtraction of Fourier spectra, though, in both was positive, i.e., in agreement with the visual evaluation of the corresponding reconstruction images. As the study included only two reconstruction methods, it would be desirable to repeat the analysis on images from a few more methods to confirm the results.

The same chapter also covers the comparison of reconstruction images from the same number of projections but resulting from different reconstruction methods. Again, IART and FBP reconstruction methods were used. This study showed positive results from using the quantitative similarity measures, while the results produced by the subtraction of Fourier spectra were inconsistent, i.e. for the series of reconstruction images of the "squares" reference object, the outcome was in agreement with the visual evaluation, while for the series of images of the another reference image, "ellipses", the Fourier subtraction images were inconclusive. Further study including more diverse reference objects are recommended.

This thesis work adds to the incomplete data problem studies. Reconstructions from the limited number of projections and improvement of their quality was the major objective of this study. The recommendations given above to continue future work are based on the

results obtained and the experience gained. One more suggestion to make before concluding would be to continue research into this subject.

BIBLIOGRAPHY

1. Aarts, E., Korst, J. Simulated Annealing and Boltzmann Machines. A Stochastic Approach to Combinatorial Optimization and Neural Computing. Great Britain: John Wiley & Sons; 1989.
2. Andersen, A. H. Algebraic Reconstruction in CT from Limited Views. IEEE Trans. Med. Imaging. 1989; 8(1): 50-55.
3. Andersen, A. H., Kak, A. C. Simultaneous algebraic reconstruction technique (SART): A new implementation of the ART algorithm. Ultrason. Imaging. 1984; 6(January): 81-99.
4. Andrews, H. C., Hunt, B. R. Digital Image Restoration. USA: Prentice-Hall, Inc.; 1977. (Oppenheim, Alan V. Prentice-Hall Signal Processing Series). ISBN: 0-13-214213-9.
5. Apple Computer, I. Inside Macintosh. USA: Addison- Wesley Publishing Company; 1985.
6. Bachor, H. A., Manson, P. J. Practical implications of quantum noise. J. Modern Opt.. 1990; 37(11): 1727-1740.
7. Baral, E., Larrson, L. E., Matson, B. Breast cancer following irradiation of the breast. Cancer. 1977; 40: 2905-2910.
8. Barrett, H., Swindell, W. Radiological Imaging. The Theory of Image Formation, Detection and Processing. USA: Academic Press, Inc.; 1981; ISBN: 0-12-079601-5.
9. Basseville, M. Distance measures for signal processing and pattern recognition. Signal Processing. 1989; 18: 349-369.
10. Boice, J. D., Stone, B. J. Interaction between radiation and other breast cancer risk factors. Late Biological Effects of Ionizing radiation. Vienna: IAEA; 1978; 1: 231-249.
11. Boice J. D., Land, C. E., Shore, R. E. Risk of breast cancer following low-dose radiation exposure. Radiology. 1979; 131: 589-597.
12. Boice J. D., Monson, R. B. Breast cancer following repeated fluoroscopic examinations of the chest. J. Natl. Cancer Inst.. 1977; 59: 823-832.
13. Bookstein, F. L. Distortion correction. Toga, A. W., editor. Three Dimensional Imaging. USA: Raven Press, Ltd.; 1990: 235-249.
14. Bosman, I. D. The Human Visual System. Image Processing Techniques. USA: Technical Editing and Reproduction Ltd.; 1982(119): 2.1-2.22. (AGARD Lectures Series).
15. Breipohl, A. M. Probabilistic systems analysis; An introduction to probabilistic models, decisions, and applications of random processes. New York: John Wiley & Sons; 1970.
16. Brigham, E. O. The Fast Fourier Transform. USA: Prentice- Hall, Inc.; 1974.
17. Brown, J. M. Linearity versus nonlinearity of dose response for radiation carcinogenesis. Health Phys.. 1976; 31: 31-231.
18. Brown, J. M. The shape of the dose-response curve for radiation carcinogenesis: Extrapolation to low doses. Radiat. Res.. 1977; 71: 34-51.

19. Budinger, T. F., Gullberg, G. T., Huesman, R. H. Emission Computed Tomography. Herman, G. T., editor. Image Reconstruction from Projections. Implementation and Applications. Germany: Springer-Verlag Berlin-Heidelberg; 1979: 147-242. (Topics in Applied Physics; v. 32).
20. Castleman, K. R. Digital Image Processing. Englewood Cliffs, N.J.: Prentice-Hall, Inc.; 1979.
21. Childers, D. G., Durling, A. Digital Filtering and Signal Processing. St. Paul, Minn.: West Publishing; 1975.
22. Cho, z. H., Chan, J. K. A comparative study of 3-D image reconstruction algorithms with reference to number of projections and noise filtering. IEEE Trans. Nucl. Sci.. 1975; NS-22(February): 344-358.
23. Chu, T. H., Lee, P. C. Projection deconvolution algorithm for image reconstruction from incomplete spectrum data. Appl. Opt.. 1988; 27(18): 3800-3805.
24. Clarke, A. B. Probability and random processes: A first course with applications. New York: John Wiley & Sons; 1985.
25. Cole, P. Major aspects of the epidemiology of breast cancer. Cancer. 1980; 46: 865-867.
26. Committee on the Biological Effects of Ionizing Radiation. The effects on populations of exposure to low levels of ionizing radiation. Washington, DC: National Academy of Sciences; 1980.
27. Consul, P. C. Generalized Poisson distributions: Properties and applications. New York: M. Dekker; 1989.
28. Cornsweet, T. N. Visual perception. New York: Academic Press; 1970.
29. Cramer, H. Random variables and probability distributions. Cambridge, Engl.: University Press; 1962.
30. Dahlquist, G., Bjorck, A. Numerical Methods. Englewood Cliffs, New Jersey: Prentice-Hall, Inc.; 1974; ISBN: 0-13-627315-7.
31. Dougherty, E., Giardina, C. R. Matrix structured image processing. USA: Prentice-Hall, Inc.; 1987; ISBN: 0-13-565623-0.
32. Dreike, P., Boyd, D. P. Convolution reconstruction of fan-beam projections. Comput. Graph. Image Process.. 1976; 5: 459-469.
33. Ekstrom, M. P., editor. Digital image processing techniques. USA: Academic Press, Inc.; 1984.
34. Evans, A. L. The Evaluation of Medical Images. Great Britain: Adam Hilger Ltd.; 1981. (Lenihan, J. M. A. Medical Physics Handbooks; v. 10).
35. Faulkner, K., Moores, B. M. The noise power spectrum of CT images. Phys. Med. Biol.. 1987; 32(7): 1047-1049.
36. Feig, S. A. Radiation risk from mammography: Is it clinically significant? Am J Roentgenol. 1984; 143: 469-475.
37. Feig, S. A., Ehrlich, S. M. Estimation of radiation risk from screening mammography: Recent trends and comparison with expected benefits. Radiology. 1990; 174(3): 638-647.
38. Frieden, B. R. Probability, Statistical Optics, and Data Testing. A Problem Solving Approach. USA: Springer-Verlag Berlin-Heidelberg; 1983; ISBN: 3-540-11769-5.

39. Frieden, B. R. Restoring with maximum likelihood and maximum entropy. *J. Opt. Soc. Am.*. 1972; 62: 511-518.
40. GE Medical Systems. CT 9800 Quick HiLight detector. . 1987.
41. GE Medical Systems. CT 9800 Quick Computed Tomography System. . 1988.
42. Geckinli, D. Y., Nezh, C. Discrete Fourier Transformation and its Applications to Power Spectra Estimation. USA: Elsevier; 1983. (Studies in Electrical and Electronic Engineering).
43. Gilbert, P. Iterative methods for the three-dimensional reconstruction of an object from projections . *J. Theor. Biol.*. 1972; 36: 105-117.
44. Gisvold, J. J., Reese, D. F., Karsell, P. R. Computed tomographic mammography (CTM). *Am J Roentgenol.* 1979; 133(December): 1143-1149.
45. Gonzalez, R. C., Wintz Paul. Digital Image Processing. USA: Addison- Wesley Publishing Company; 1983.
46. Gordon, R. A tutorial on ART (Algebraic Reconstruction Techniques). *IEEE Trans. Nucl. Sci.*. 1974; NS-21: 78-93.
47. Gordon, R., Bender, R., Herman, G. T. Algebraic reconstruction techniques (ART) for three-dimensional electron microscopy and x- ray photography. *J. Theor. Biol.*. 1970; 29: 471-481.
48. Gordon, R., Bender, R. New three- dimensional Algebraic Reconstruction Techniques (ART). Proc. 29-th Annual Meeting Electron Microscopy Society of America. 9-13 August, 1972-73: Boston.
49. Gordon, R., Herman, G. T. Reconstruction of pictures from their projections. *Comm.A.C.M.*. 1971; 14(12): 759-768.
50. Gordon, R., Herman, G. T. Three dimensional reconstruction from projections: A review of algorithms. *Int. Rev. Cytol.*. 1974a; 38: 111-151.
51. Gordon, R. Industrial applications of computed tomography and NMR imaging: an OSA topical meeting. *Appl. Opt.*. 1985; 24(23): 3948-3949.
52. Gordon, R., Rangayyan, R. M. Radiographic feature enhancement, information content, and dose reduction in mammography and cardiac angiography. Proc. 5th Annual Conf. Frontiers of Engineering and Computing in Health Care, IEEE-EMBS. ; 1983: 161-165.
53. Gore, J. C., Leeman, S. The reconstruction of objects from incomplete projections. *Phys. Med. Biol.*. 1980; 25: 129-136.
54. Greening, J. R., editor. Medical Physics; 25th June-7th July, 1979; Varenna, Italy. Amsterdam, New York: Elsevier North-Holland; 1981. Proceedings of the International School of Physics "Enrico Fermi" course 76).
55. Grunbaum, F. A. A study of Fourier space methods for limited-angle image reconstruction. *Numerical Funct. Anal. Optim.*. 1980(2): 31-42.
56. Gullberg, G. T. The reconstruction of fan-beam data by filtering the back-projection. *Comput. Graph. Image Process.*. 1979; 10: 30-47.
57. Hageman, L. A., Young, D. M. Applied Iterative Methods. USA: Academic Press; 1981; ISBN: 0-12-313340-8.

58. Haight, F. A. Handbook of the Poisson distribution. New York: John Wiley & Sons; 1967.
59. Hall, E. J. Radiobiology for the Radiologist. Philadelphia, PE: Harper and Row, Publishers, Inc.; 1978.
60. Hall, E. L. Computer Image Processing and Recognition. USA: Academic Press, Inc.; 1979; ISBN: 0-12-318850-4.
61. Hamming, R. W. Digital Filters. USA: Prentice- Hall, Inc.; 1977.
62. Hanson, K. M. CT reconstruction from limited projection angles. Proc. Soc. Photo-Opt. Instrum. Eng.. 1982(374): 166-173.
63. Heffernan, P. B., Robb, R. A. Image reconstruction from incomplete projection data: Iterative Reconstruction-Reprojection Techniques. IEEE Trans. Biomed. Engin.. 1983; BME-30(12): 838-841.
64. Hendee, W. R. Medical Radiation Physics. USA: Year Book Medical Publishers, Inc.; 1970; ISBN: 0-8151-4240-4.
65. Herman, G. T. Two direct methods for reconstructing pictures from their projections: A comparative study. Comput. Graph. Image Process.. 1972(1): 123-144.
66. Herman, G. T., Lakshminarayanan, A. V., Naparstek, A. Convolution reconstruction techniques for divergent beams. Comput. Biol. Med.. 1976a; 6: 259-271.
67. Herman, G. T., Lent, A., Rowland, S. W. ART: Mathematics and applications (a report on the mathematical foundations and on the applicability to real data of the algebraic reconstruction techniques.). J. Theor. Biol.. 1973; 42(1): 1-32.
68. Herman, G. T., Naparstek, A. A Radon inversion integral for diverging x-rays. Proceedings of the Third International Joint Conference on Pattern Recognition; November 8-11, 1976; Colorado, CA.
69. Herman, G. T., Rowland, S. Resolution in ART: an experimental investigation of the resolving power of an algebraic picture reconstruction technique. J. Theor. Biol.. 1971; 33: 213-223.
70. Herman, G. T. Corrections for beam hardening in Computed Tomography. Phys. Med. Biol.. 1979; 24(1): 81-106.
71. Herman, G. T. Image Reconstruction from Projections. The Fundamentals of Computerized Tomography. USA: Academic Press, Inc.; 1980; ISBN: 0-12-342050-4.
72. Herman, G. T. Three methods for reconstructing objects from x-rays: A comparative study. Comput. Graph. Image Process.. 1973a(2): 151-178.
73. Hershel, R. C. Unified approach to restoring degraded images in the presence of noise. Optical Sciences Center, Univ. of Arizona, Tucson; 1971; Tech. Rep. No. 71.
74. Hobbie, R. K. Intermediate Physics for Medicine and Biology. USA: John Wiley & Sons; 1988.
75. Horn, B. K. P. Fan-beam reconstruction methods. Proc. IEEE. 1979; 67(12): 1616-1623.
76. Howe, G. R. Epidemiology of radiogenic breast cancer. Boice J. D., Fraumeni, J. F., editors. Radiation Carcinogenesis: Epidemiology and Biological Significance. New York: Raven; 1984: 119-129.

77. Hu, H., Gullberg Grant T. Convolutional reconstruction algorithm for fan beam concave and convex circular detectors. *IEEE Trans. Med. Imaging.* 1988; 7(3): 233-238.
78. Huda, W., Bissessur. Effective dose equivalents, H_E , in diagnostic radiology. *Med. Phys.* 1990; 17(6): 998-1003.
79. Hull, T. E., Dobell, A. R. Mixed congruential random number generators for binary machines . *J. Assoc. Comput. Mach.* 1964; 11(1): 31-40.
80. Inouye, T. Image reconstruction with limited-view angle projections. *Digest of the International Workshop on Physics and Engineering in Medical Imaging.* Washington, D.C.: Optical Society of America; 1982: 165-168.
81. Inouye, T. Image reconstruction with limited angle projection data. *IEEE Trans. Nucl. Sci.* 1979; NS-26(2): 2666-2669.
82. Johns, H. E. *The Physics of Radiology.* USA: Charles C Thomas; 1983.
83. Johnson, N. L., Kotz, S. *Discrete distributions.* Boston: Houghton Mifflin; 1969.
84. Kereiakes, J. G. *Handbook of radiation doses in nuclear medicine and diagnostic x-ray.* Boca Raton, Fla: CRC Press; 1980.
85. Kijewski, M. F., Judy, P. F. Comments on the noise power spectrum of CT images. Reply. *Phys. Med. Biol.* 1987; 32(8): 1049-1051.
86. Kijewski, M. F., Judy, P. F. The noise power spectrum of CT images. *Phys. Med. Biol.* 1987; 32(5): 565-575.
87. Kirkpatrick, S., Gelatt, C. D., Vecchi, M. P. Optimization by Simulated Annealing. *Science.* 1983; 220(4598): 671-680.
88. Land, C. E., Normann, J. E. Latent periods of radiogenic cancers occurring among Japanese A-bomb survivors. *Late Biological Effects of Ionizing radiation.* Vienna: IAEA; 1978; 1: 29-47.
89. Land, C. E. Estimating cancer risks from low doses of ionizing radiation. *Science.* 1980a; 209(September): 1197-1203.
90. Land, C. E. Low-dose radiation-a cause of breast cancer? *Cancer.* 1980; 46: 868-873.
91. Land, C. E., Boice, J. D., Shore, R. E. Breast cancer risk from low-dose exposures to ionizing radiation: Results of parallel analysis of three exposed populations of women. *J. Natl. Cancer Inst.* 1980b; 65: 353-376.
92. Land, C. E., McGregor, D. H. Temporal distributions of risk after exposure. *Proceedings of the Third International Symposium on Detection and Prevention of Cancer, Part J: Prevention, 1, Etiology.* New York; 1977: 831-843.
93. Larson, H. J., Shubert, B. O. *Probabilistic models in Engineering Sciences.* New York: John Wiley & Sons; 1979.
94. Lewitt, R. M. Processing of incomplete measurement data in computed tomography. *Med. Phys.* 1979; 6(5): 412-417.
95. Li, X., Ferdousi, M., Chen, M. Image matching with multiple templates. *IEEE Computer Society Conference on Computer Vision and Pattern Recognition;* June 22-26; Miami Beach, Florida. Washington , DC, USA: IEEE Computer Society Press; 1986: 610-613.

96. Mackenzie, I. Breast cancer following multiple fluoroscopies. *Br. J. Cancer*. 1965; 19: 1-8.
97. MacLaren, M. D., Marsaglia, G. Uniform random number generators. *J. Assoc. Comput. Mach.*. 1965; 12(1): 83-89.
98. Macovski, A., Alvarez, R. E., Chan, L. Energy dependent reconstruction in x-ray computerized tomography. *Comput. Biol. Med.*. 1976; 6: 325-336.
99. Mannos, J. L., Sakrison, D. J. The effects of a visual fidelity criterion on the encoding of images. *IEEE Trans. Inf. Theory*. 1974; IT-20(July): 525-536.
100. Mathai, A. M., Pederzoli, G. Characterizations of the normal probability law. New York: John Wiley & Sons; 1977.
101. Mazur, A. Image Correlation Technique for recovering deformation fields from images . Winnipeg, MB, Canada: The University of Manitoba; 1992b.
102. Mazur, A., Gordon, R. Image Correlation Technique for recovering deformation fields from images . submitted. 1992c.
103. Mazur, E. J., Gordon, R. Interpolative Algebraic Reconstruction Techniques without beam partitioning (IART) for computed tomography. submitted. 1992a.
104. Mazur, E. J., Gordon Richard. New ways of using the Fourier spectrum in computed tomography. submitted. 1992.
105. McGregor, D. H., Land, C. E., Choi, D. Breast cancer incidence among atomic bomb survivors, Hiroshima and Nagasaki, 1950-69. *J. Natl. Cancer Inst.*. 1977; 59: 799-811.
106. Medoff, B. P. Image reconstruction from limited data: Theory and applications in computerized tomography. Stark, H., editor. *Image Recovery: Theory and Applications*. New York: Academic Press; 1987.
107. Medoff, B. P., Brody, W. R., Nassi, M. Iterative convolution backprojection algorithms for image reconstruction from limited data. *J. Opt. Soc. Am.*. 1983; 73(November): 1493-1500.
108. Naparstek, A. Short-scan fan-beam algorithms for CT. *IEEE Trans. Nucl. Sci.*. 1980; NS-27(3): 1112-1120.
109. Nassi, M., Brody, W. R., Medoff, B. P. Iterative reconstruction-reprojection: an algorithm for limited data cardiac computed tomography. *IEEE Trans. Biomed. Engin.*. 1982; BME-29: 333-341.
110. Northcott, M. J., Dainty, J. C., Ayers, G. R. Algorithms for image reconstruction from photon limited data using the triple correlation. *J. Opt. Soc. Am.*. 1988; 5(7): 986-992.
111. Nussbaumer, H. J. *Fast Fourier transform and Convolution Algorithms*. Berlin; New York: Springer- Verlag Berlin- Heidelberg; 1981.
112. Ogawa, K., Nakajima, M. A reconstruction algorithm from truncated projections. *IEEE Trans. Med. Imaging*. 1984; MI-3(1): 34-40.
113. Ollinger, J. M., Karp, J. S. An evaluation of three algorithms for reconstructing images from data with missing projections. *IEEE Trans. Nucl. Sci.*. 1988; 35(1): 629-634.
114. Ollinger, J. M. Iterative reconstruction-reprojection and the expectation-maximization algorithm. *IEEE Trans. Med. Imaging*. 1990; 9(1): 94-98.

115. Oppenheim, A. V., Schafer, R. W. Digital Signal Processing. Englewood Cliffs, N. J.: Prentice-Hall, Inc.; 1975.
116. Oppenheim, B. E. Reconstruction tomography from incomplete projections. Ter-Pogossian, M. M., Editor. Reconstruction Tomography in Diagnostic Radiology and Nuclear Medicine. Baltimore: University Park Press; 1977: 155-183.
117. Oskoui, P., Syark, H. A comparative study of three reconstruction methods for a limited-view computer tomography problem. IEEE Trans. Med. Imaging. 1989; 8(1): 43-49.
118. Oskoui-Fard, P., Stark, H. Tomographic image reconstruction using the theory of convex projections. IEEE Trans. Med. Imaging. 1988; 7(1): 45-58.
119. Papoulis, A. Probability, random variables, and stochastic processes. New York: McGraw-Hill; 1984.
120. Patel, J. K., Read, C. B. Handbook of the normal distribution. New York: M. Dekker; 1982.
121. Pavlidis, T. Algorithms for Graphics and Image Processing. USA: Computer Science Press; 1982.
122. Pazner, Micha; Kirby, K. Chris; Thies, N. MAPII map processor. A geographic system for the Macintosh. New York: John Wiley & Sons; 1989.
123. Peng, H., Stark, H. Direct Fourier reconstruction in fan-beam tomography. IEEE Trans. Med. Imaging. 1987; 6(3): 209-219.
124. Peng, H., Stark, H. One-step image reconstruction from incomplete data in computer tomography. IEEE Trans. Med. Imaging. 1989; 8(1): 16-31.
125. Peres, A. Tomographic reconstruction from limited angular data. J. Comput. Assisted Tomog.. 1979(3): 800-803.
126. Pratt, W. K. Digital Image Processing. USA: John Wiley & Sons; 1978; ISBN: 0-471-01888-0.
127. Programmer's Extender. Ann Arbor, Michigan: Invention Software; 1986.
128. Ramirez, R. W. The FFT, Fundamentals and Concepts. USA: Prentice- Hall, Inc.; 1985.
129. Recommendations of the International Commission on Radiological Protection (ICRP). ICRP Publication no. 26. Elmsford, NY: Pergamon Press; 1977.
130. Reeds, A., Shepp, L. A. Limited angle reconstruction in tomography via squashing. IEEE Trans. Med. Imaging. 1987; MI-6(2): 89-97.
131. Report of the National Institutes of Health Ad Hoc Working Group to develop radioepidemiological tables. NIH Publication no. 85-2748. Rockville, Md: U.S. Department of Health and Human Services; 1985.
132. Rosenfeld, A., Kak, A. C. Digital Picture Processing. USA: Academic Press, Inc.; 1982; ISBN: 0-12-597301-2.
133. Rothschild, V. Probability distributions. New York: John Wiley & Sons; 1986.
134. Rowland, S. W. Computer Implementation of Image Reconstruction Formulas. Herman, G. T., editor. Image Reconstruction from Projections. Implementation and Applications. Germany: Springer- Verlag Berlin- Heidelberg; 1979: 9-78. (Topics in Applied Physics; v. 32).

135. Sankar, P. V., Nalcioğlu, O., Sklansky, J. Undersampling errors in region-of-interest tomography. *IEEE Trans. Med. Imaging*. 1982; MI-1: 168-173.
136. Sata, T., Norton, S. J., Linzer, M. Tomographic image reconstruction from limited projections using iterative revisions in image and transform spaces. *Appl. Opt.*. 1981; 20(3): 395-399.
137. Sato, T., Norton, S. J., Linzer, M. Tomographic image reconstruction from limited number of projections using iterative revisions in image and transform spaces. *Appl. Opt.*. 1981(20): 395-399.
138. Sezan, I., Stark, H. Tomographic image reconstruction from incomplete view data by convex projections and direct Fourier inversion. *IEEE Trans. Med. Imaging*. 1984; MI-3(2): 91-98.
139. Shore, R. E., Hempelmann, L. H., Kowaluk, E. Breast neoplasms in women treated with x-rays for acute post-partum mastitis. *J. Natl. Cancer Inst.*. 1977; 59: 813-822.
140. Skubic, S. E., Fatouros, P. Absorbed breast dose: Dependence on radiographic modality and technique, and breast thickness. *Radiology*. 1986; 161: 263-270.
141. Sutherland, J. V. Estimation of the cancer risk associated with radiation exposure. Hendee, W. R., editor. *Health Effects of Low Level Radiation*. Norwalk, CT: Appleton-Century-Crofts; 1984: 93-118.
142. Suzuki, S., Yamaguchi, S. Comparison between an image-reconstruction method of filtering backprojection and the filtered backprojection method. *Appl. Opt.*. 1988; 27(14): 2867-2870.
143. Tam, K. C., Perez-Mendez, V. Limited-angle three dimensional reconstruction using Fourier transform iterations and Radon transform iterations. *Opt. Engin.*. 1981(20): 586-589.
144. Tam, K. A., Perez-Mendez, V. Limits to image reconstruction from restricted angular input. *IEEE Trans. Nucl. Sci.*. 1981a; NS-28(1): 179-181.
145. Tam, K. A., Perez-Mendez, V. Tomographical imaging with limited angle input. *J. Opt. Soc. Am.*. 1981b; 71: 582-592.
146. Think Technologies, I. *Lightspeed Pascal. User's Guide and Reference Material*. Lexington, MA: Think Technologies, Inc.; 1986.
147. Thomas, J. B. *An Introduction to Applied Probability and Random Processes*. USA: John Wiley & Sons, Inc.; 1971; ISBN: 73-127670.
148. Thompson, J. W. A. *Applied Probability*. USA: Holt, Rinehart and Winston, Inc.; 1969; ISBN: 03-079555-9.
149. Tokunaga, M. N., Assano, M. Malignant breast neoplasms among atomic bomb survivors, Hiroshima and Nagasaki, 1950-1974. *J. Natl. Cancer Inst.*. 1979; 62: 1347-1359.
150. Tsokos, C. P. *Probability Distributions: An Introduction to Probability Theory with Applications*. USA: Duxbury Press; 1972; ISBN: 0-87872-011-1.
151. Tuy, H. K. An algorithm for incomplete range of views reconstruction. *Tech. Dig. Topical Meet. Signal Recovery, Synthesis with incomplete Inform. Partial Constraints.* ; Jan. 1983: FA1-1 and FA1-4.
152. Wadsworth, G. P., Bryan, J. G. *Introduction to Probability and Random Variables*. USA: The Mapple Press Company; 1960.

153. Wagner, W. Reconstruction from restricted region scan data - New means to reduce patient dose. IEEE Trans. Nucl. Sci.. 1979; NS-26: 2866-2869.
154. Weaver, H. J. Applications of discrete and continuous Fourier analysis. USA: John Willey & Sons; 1983; ISBN: 0-471-87115-X.
155. Webster, E. W. On the question of cancer induction by small x-ray doses. Am J Roentgenol. 1981; 137: 647-666.
156. Wood, S. L., Macovski, A. Reconstructions with limited data using estimation theory. Computer Aided Tomography and Ultrasonics in Medicine. Amsterdam: North-Holland; 1979: 219-233.

APPENDIX

SOURCE CODE

This source code contains Think Pascal code of units and procedures that were used in a program developed for the purpose of this thesis work. The program was built in the Think Pascal language, using the Programmer's Extender [Programmer's, 1986].

```

{*****}
{purpose: Computes a reconstruction image using IART algorithm for a
parallel geometry beam}
{}
{author: Elzbieta J. Mazur}
{}
{address: Department of Electrical and Computer Engineering, The
University of Manitoba, Winnipeg, MB, R3T 2N2}
{}
{description of parameters: }
{angle - direction of a projection under consideration}
{initialvalue - value chosen to fill in the reconstruction matrix
before starting the iteration process}
{itercount - iteration counter}
{projection - the input projection data}
{projnumber - number of projections in the input set}
{projrange - half of the length of a projection}
{pseudoprojection - computed projection of intermediate image}
{rechange - half of the length of a reconstruction matrix}
{startangle - direction of the first projection}
{stepangle - distance between consecutive projection directions}
{t1, t2} - two detectors affected by a pixel}
{*****}

```

```

unit IARTReconstr;
interface
  procedure IART;
implementation
  procedure createprojectionmatrix;
  external;
  procedure createreconstrmatrix;
  external;
  procedure controlwindow;
  external;
  function proj (i, j: integer): projectionptr;
  external;

```

```

function rec (i, j: integer): reconstrptr;
external;
type
  reconstrptr = ^real;
  projectionrecord = record
    projection: real;{longint}
    pseudoprojection: real;
  end;
  projectionptr = ^projectionrecord;
var
  recpointer: reconstrptr;
  projarrayptr: projectionptr;
  temptr2: reconstrptr;
  temptr1: projectionptr;
  temprec, tempproj: longint;
  Edistance: real;
procedure IART;
  const
    dialogidl = 16084;
  var
    i, j, k, t1, t2, x, y: integer;
    delta, bprojline, c, s, a, tm1, tm2, criterion, initialvalue,
difference, controll, t3: real;
    projdiscrepancy, iterationdiscr, sum, bp, bpl, tt,
meanObjectIntensity, meanObjectIntensity1, entropy, variance: real;
    dp: dialogptr;
    textfile1, textfile2, textfile3, textfile4: text;
    name, mystring: str255;
    frefnumber, itemtype, itcount, iterationlimit, itemnum, itercount,
previtem1, previtem2, stop: integer;
    handl6, handl7, handl8, handl11, handl111: handle;
    distrect: rect;
    default: boolean;
  procedure savereconstruction; {saves the reconstruction in an output
file}
    var

```

```

x, y: integer;
v: real;
begin
seek(textfile1, 0);
for x := rechange downto -rechange + 1 do
begin
for y := -rechange + 1 to rechange do
begin
tempptr2 := rec(x, y);
write(textfile1, round(tempptr2^), ' ');
end;{y}
writeln(textfile1);
end;{x}
end;{savereconstruction}
begin
showtext;
setprojparam; {reads parameters of an input projection file}
createreconstmatrix; {allocates memory for a reconstruction matrix}
createprojectionmatrix; {allocates memory for an input projection
set}
itercount := 0;
controlwindow; {reads the number of iterations and the option of
filling in the reconstruction matrix before starting the iteration
process}
if default = true then
for i := rechange downto -rechange + 1 do {filling up the rec. matrix
with the initial value}
for j := -rechange + 1 to rechange do
begin
tempptr2 := rec(i, j);
tempptr2^ := initialvalue;
end{for i,j}
else
begin
name := oldfilename('old reconstruction');
open(textfile1, name);

```

```

    for i := rechange downto -rechange + 1 do {filling up the rec.
matrix with the values of a chosen file}
    for j := -rechange + 1 to rechange do
    begin
        read(textfile1, t3);
        tempptr2 := rec(i, j);
        tempptr2^ := t3;
    end;{for i, j}
    close(textfile1);
end;{if default }
name := oldfilename('projection data');
open(textfile1, name);
for i := 1 to projnumber do {reads in the input set of projections}
begin
    for j := -projrange + 1 to projrange do
    begin
        read(textfile1, t3);
        sum := sum + t3;
        tempptr1 := proj(i, j);
        tempptr1^.projection := t3;
        tempptr1^.pseudoprojection := 0;
    end;{j}
    readln(textfile1);
end;{i}
close(textfile1);
name := newfilename('backprojection map');
open(textfile1, name);
repeat
    angle := startangle;
    for k := 1 to projnumber do
    begin
        c := cos(angle);
        s := sin(angle);
        for x := rechange downto -rechange + 1 do
            for y := -rechange + 1 to rechange do
                begin

```

```

bprojline := y * c + x * s;
if (bprojline > -projrange + 1) and (bprojline < projrange) then
begin
t1 := trunc(bprojline);
if bprojline >= 0 then
t2 := t1 + 1
else
begin
t2 := t1;
t1 := t2 - 1;
end;
{ pseudoprojection calculation}
temppt1 := proj(k, t1);
a := temppt1^.pseudoprojection;
temppt1^.pseudoprojection := a + (1 - abs(bprojline - t1)) *
rec(x, y)^;
temppt1 := proj(k, t2);
a := temppt1^.pseudoprojection;
temppt1^.pseudoprojection := a + (1 - abs(bprojline - t2)) *
rec(x, y)^;
end;{if and}
end;{y,x}
for j := -projrange + 1 to projrange do
begin
temppt1 := proj(k, j);
if temppt1^.pseudoprojection > 0 then
{calculation the (projection/pseudoprojection[q]) ratio}
temppt1^.pseudoprojection := temppt1^.projection /
temppt1^.pseudoprojection;
end;{j}
{ f[q+1] = f[q]* projection/pseudoprojection[q] }
for x := rechange downto -rechange + 1 do
for y := -rechange + 1 to rechange do
begin
bprojline := y * c + x * s;      {line for back projection}
if (bprojline > -projrange + 1) and (bprojline < projrange) then

```

```

begin
  t1 := trunc(bprojline);
  if (bprojline >= 0) then
    t2 := t1 + 1
  else
    begin
      t2 := t1;
      t1 := t2 - 1;
    end;
  tml := proj(k, t1)^.pseudoprojection;
  tm2 := proj(k, t2)^.pseudoprojection;
  tempptr2 := rec(x, y);
  tempptr2^ := ((1 - abs(t1 - bprojline)) * tml + (1 - abs(t2 -
bprojline)) * tm2) * tempptr2^;
  end;{if}
  tempptr2 := rec(x, y);
  end;{y,x}
  angle := angle + stepangle;
  for j := -projrangle + 1 to projrange do      {zeroing
pseudoprojection matrix before the next iteration}
    begin
      tempptr1 := proj(k, j);
      tempptr1^.pseudoprojection := 0;
    end;{j}
  end;{k}
  itercount := itercount + 1;
until iterationlimit = itercount;
savereconstruction;
dispose(projarrayptr);
dispose(recpointer);
disposdialog(dp);
CloseResFile(frefnumber);
close(textfile1);
end;{IART}
end.{unit}

```

```

{*****}
{purpose: Computes a reconstruction image using IART algorithm for a fan
beam}
{}
{author: Elzbieta J. Mazur}
{}
{address: Department of Electrical and Computer Engineering, The
University of Manitoba, Winnipeg, MB, R3T 2N2}
{}
{description of parameters: }
{angle - direction of a projection under consideration}
{initialvalue - value chosen to fill in the reconstruction matrix
before starting the iteration process}
{itercount - iteration counter}
{odDist - distance between a detector array and the center of an object
matrix}
{pixShadow - length of a pixel shadow}
{pointDist - pixel distance from the x - ray source}
{projection - the input projection data}
{projnumber - number of projections in the input set}
{projrange - half of the length of a projection}
{pseudoprojection - computed projection of intermediate image}
{reorange - half of the length of a reconstruction matrix}
{sdDist - distance between x - ray source and a detector array}
{soDist - distance between x - ray source and the center of an object
matrix}
{startangle - direction of the first projection}
{stepangle - distance between consecutive projection directions}
{t1, t2} - the extreme detectors (left, right) of the set of detectors
affected by a pixel}
{x1, y1 - pixel coordinates in a rotated system}
{*****}

```

```
Unit IARTReconstrDiv;
```

```
Interface
```

```
Procedure divIART;
```

Implementation

```

Procedure setDivprojparam (Var soDist, odDist, sdDist: real);
external;

Procedure createprojectionmatrix1;
external;

Procedure createreconstrmatrix1;
external;

Function proj1 (i, j: integer): projectionptr;
external;

Function reconst1 (i, j: integer): reconstrptr;
external;

Procedure controlwindow1;
external;

Type
  reconstrptr = ^real;
  projectionrecord = Record
    projection: longint;
    pseudoprojection: real;
  End;
  projectionptr = ^projectionrecord;

Var
  recpointer: reconstrptr;
  projarrayptr: projectionptr;
  tempptr2: reconstrptr;
  tempptr1: projectionptr;
  temprec, tempproj: longint;
  Edistance: real;

Procedure divIART;

Const
  dialogid1 = 16084;

Var
  i, j, k, t1, t2, x, y: integer;
  delta, c, s, a, tm1, tm2, criterion, initialvalue, difference,
  controll: real;

```

```

    projdiscrepancy, iterationdiscr, sum, bp, bp1, tt,
meanObjectIntensity, meanObjectIntensity1, entropy, variance, x1, y1:
real;
    gamma, pointDist, soDist, odDist, sdDist, pixShadow, pixDist, ldet,
rdet: real;
    dp: dialogptr;
    textfile1, textfile2, textfile3, textfile4: text;
    name, mystring: str255;
    frefnumber, itemtype, itcount, iterationlimit, itemnum, itercount,
previtem1, previtem2, stop: integer;
    handl6, handl7, handl8, handl11, handl111: handle;
    distrect: rect;
    default: boolean;
    Procedure savereconstruction1; {saves the reconstruction in an
output file}
    Var
        x, y: integer;
        v: real;
    Begin
        seek(textfile1, 0);
        For x := -rechange + 1 To rechange Do
            Begin
                For y := -rechange + 1 To rechange Do
                    Begin
                        v := recl(x, y)^;
                        If (v > 0.00000001) And (v < 1) Then
                            v := 1;
                        write(textfile1, round(v), ' ');
                    End;{y}
                    writeln(textfile1);
                End;{x}
            End;{savereconstruction1}
        Begin
            setDivprojparam(soDist, odDist, sdDist); {reads the scanning system
geometry}
            createreconstrmatrix1; {allcates memory for a reconstruction matrix}

```

```

    createprojectionmatrix1; {allcates memory for an input set of
projections}
    itercount := 0;
    controlwindow1; {reads the number of iterations and the option of
filling in the reconstruction matrix before starting the iteration
process}
    If default = true Then
    For i := -rechange + 1 To rechange Do {filling in the
reconstruction. matrix with the initialvalue}
    For j := -rechange + 1 To rechange Do
    Begin
    tempptr2 := recl(i, j);
    tempptr2^ := initialvalue;
    End{for i,j}
    Else
    Begin
    name := oldfilename('old reconstruction');
    open(textfile1, name);
    For i := -rechange + 1 To rechange Do {filling in the
reconstruction. matrix with the} {values of a chosen file}
    For j := -rechange + 1 To rechange Do
    Begin
    read(textfile1, t3);
    tempptr2 := recl(i, j);
    tempptr2^ := t3;
    End;{for i,j}
    close(textfile1);
    End;{if default }
    name := oldfilename('projection data');
    open(textfile1, name);
    For i := 1 To projnumber Do {reads in the input set of
projections }
    Begin
    For j := -projrange + 1 To projrange Do
    Begin
    read(textfile1, t3);

```

```

temppt1 := proj1(i, j);
temppt1^.projection := t3;
temppt1^.pseudoprojection := 0;
End;{j}
readln(textfile1);
End;{i}
close(textfile1);
name := newfilename('backprojection matrix');
open(textfile1, name);
Repeat
  angle := startangle;
  For k := 1 To projnumber Do
  Begin
    c := cos(angle);
    s := sin(angle);
    For x := -rechange + 1 To rechange Do
      For y := -rechange + 1 To rechange Do
        Begin
          x1 := x * c + y * s;
          y1 := y * c - x * s;
          gamma := arctan(x1 / (soDist - y1));
          pointDist := (soDist - y1) / cos(gamma);
          pixShadow := sdDist / (2 * pointDist);
          pixDist := sdDist * gamma;
          ldet := pixDist - pixShadow;
          rdet := pixDist + pixShadow;
          t1 := trunc(ldet);
          If ldet < 0 Then
            t1 := t1 - 1;
          t2 := trunc(rdet);
          If rdet < 0 Then
            t2 := t2 - 1;
          if (t1 >= -projrange - 1) and (t2 < projrange) then
            begin
{ pseudoprojection calculation}
          temppt1 := proj1(k, t1);

```

```

    a := tempptr1^.pseudoprojection;
    tempptr1^.pseudoprojection := a + ((1 - abs(ldet - t1)) / (2
* pixshadow)) * recl(x, y)^;
    tempptr1 := proj1(k, t2);
    a := tempptr1^.pseudoprojection;
    tempptr1^.pseudoprojection := a + (abs(rdet - t2) / (2 *
pixshadow)) * recl(x, y)^;
    For i := (t1 + 1) To (t2 - 1) Do
    Begin
        tempptr1 := proj1(k, i);
        a := tempptr1^.pseudoprojection;
        tempptr1^.pseudoprojection := a + (1 / (2 * pixshadow)) *
recl(x, y)^;
    End;
    End; {if}
    End; {y,x}
    For j := -projrange + 1 To projrange Do
    Begin
        tempptr1 := proj1(k, j);
        If tempptr1^.pseudoprojection > 0 Then
        {calculation the (projection/pseudoprojection[q]) ratio}
            tempptr1^.pseudoprojection := tempptr1^.projection /
tempptr1^.pseudoprojection;
        End; {j}
    { f[q+1] = f[q]* projection/pseudoprojection[q] }
    For x := -rechange + 1 To rechange Do
    For y := -rechange + 1 To rechange Do
    Begin
        x1 := x * c + y * s;      {in rotated system}
        y1 := y * c - x * s;
        gamma := arctan(x1 / (soDist - y1));
        pointDist := (soDist - y1) / cos(gamma);
        pixShadow := sdDist / (2 * pointDist);
        pixDist := sdDist * gamma;
        ldet := pixDist - pixShadow;
        rdet := pixDist + pixShadow;
    End;
    End;
    End;

```

```

t1 := trunc(ldet);
If ldet < 0 Then
  t1 := t1 - 1;
t2 := trunc(rdet);
If rdet < 0 Then
  t2 := t2 - 1;
If (t1 >= -projrange - 1) And (t2 < projrange) Then
Begin
  tm1 := proj1(k, t1)^.pseudoprojection;
  tm2 := proj1(k, t2)^.pseudoprojection;
  tempptr2 := recl(x, y);
  tt := ((1 - abs(ldet - t1)) / (2 * pixshadow)) * tm1 +
(abs(rdet - t2) / (2 * pixshadow)) * tm2;
  For i := (t1 + 1) To (t2 - 1) Do
  Begin
    tempptr1 := proj1(k, i);
    a := tempptr1^.pseudoprojection;
    tt := tt + (1 / (2 * pixshadow)) * a;
  End;
  tempptr2^ := tt * tempptr2^;
  tempptr2 := recl(x, y);
  variance := variance + sqr(tempptr2^ - meanObjectIntensity);
  tt := tempptr2^ / meanObjectIntensity;
  If tt > 0 Then
    entropy := entropy + tt * ln(tt);
  End; {if}
End; {y,x}
angle := angle + stepangle;
For j := -projrange + 1 To projrange Do {zeroing
pseudoprojection matrix before the next iteration}
  Begin
    tempptr1 := proj1(k, j);
    tempptr1^.pseudoprojection := 0;
  End; {j}
End; {k}
itercount := itercount + 1;

```

```
Until iterationlimit = itercount;  
  savereconstruction1;  
  dispose(projarrayptr);  
  dispose(recpointer);  
  disposdialog(dp);  
  CloseResFile(frefnumber);  
  close(textfile1);  
End; {IART}  
End. {unit}
```

```

{*****}
{purpose: computes set of projections for a parallel beam geometry}
{}
{author: Elzbieta J. Mazur}
{}
{address: Department of Electrical and Computer Engineering, The
University of Manitoba, Winnipeg, MB, R3T 2N2}
{}
{description of parameters: }
{projlength - length of a single projections in the input set}
{projnumber - number of projections in the input set}
{rechange - half of the length of a reconstruction matrix}
{startangle - direction of the first projection}
{stepangle - distance between consecutive projection directions}
{*****}

```

```

procedure MapProjection;
  type
    reconstrptr = ^real;
  var
    recpointer, temptr2: reconstrptr;
    textfile1, textfile2: text;
    j, i, projectionrange, x, y, temp1, temp2: integer;
    temp, deltaangle, bprojline, a, s, c, density: real;
    name, PROMPT: str255;
    time1, time2: longint;
  begin
    showtext;
    setprojparam; {reads the description of of a set of projections to
compute}
    vectorptr(prjptr, projnumber, projlength); {allocates memory for a
projection set}
    createreconstrmatrix; {allocates memory for an object matrix}
    name := oldfilename('DENSITY MATRIX FROM MAP');
    open(textfile1, name);
    for i := rechange downto -rechange + 1 do {reads in an object matrix}

```

```

begin
  for j := -reorange + 1 to reorange do
    begin
      read(textfile1, density);
      tempptr2 := rec(i, j);
      tempptr2^ := density;
    end; {for i, j}
  end;
close(textfile1);
name := newfilename('projection file');
open(textfile2, name);
for j := 1 to projnumber do {zeroing projections matrix}
  for i := -proorange + 1 to proorange do
    begin
      temprealpointer := arrvector(j, i + proorange);
      temprealpointer^ := 0.0;
    end; {j, i}
  for x := reorange downto -reorange + 1 do {computes the projection
set}
    for y := -reorange + 1 to reorange do
      begin
        angle := startangle;
        for j := 1 to projnumber do
          begin
            c := cos(angle);
            s := sin(angle);
            bprojline := y * c + x * s;
            temp1 := trunc(bprojline);
            if bprojline >= 0 then
              temp2 := temp1 + 1
            else
              begin
                temp2 := temp1;
                temp1 := temp2 - 1;
              end;
            temprealpointer := arrvector(j, temp1 + proorange);

```

```

    a := temprealpointer^;
    temprealpointer^ := a + (1 - abs(bprojline - temp1)) * rec(x,
y)^;

    temprealpointer := arrvector(j, temp2 + projrange);
    a := temprealpointer^;
    temprealpointer^ := a + (1 - abs(bprojline - temp2)) * rec(x,
y)^;

    angle := angle + stepangle;
    end;{j}
end;{y,x}

for j := 1 to projnumber do {writes in the projection set into an
output file}
    begin
        for i := -projrange + 1 to projrange do
            write(textfile2, ' ', arrvector(j, i + projrange)^);
        end;{j}
        writeln('taking projections time = ', (time2 - time1) / 60 : 5 : 2,
'sec');
        close(textfile2);
    end;{mapprojection}

```

```

{*****}
{purpose: computes noisy sinogram}
{}
{author: Elzbieta J. Mazur}
{}
{address: Department of Electrical and Computer Engineering, The
University of Manitoba, Winnipeg, MB, R3T 2N2}
{}
{description of parameters: }
{p - number of photons emitted by an x-ray source}
{projlength - length of a single projections in the input set}
{projnumber - number of projections in the input set}
{rechange - half of the length of a reconstruction matrix}
{startangle - direction of the first projection}
{stepangle - distance between consecutive projection directions}
{*****}

```

```

procedure NoisyAtProj;
var
  l2n, i, j, Ndet, l, loc, ml, m: integer;
  k: longint;
  Nperc, loc1, det, ufl, v, p, pp, a, v1, v2, w: real;
  c: array[1..2] of real;
  name: str255;
  textfile: text;
{computes a normally distributed random number v with a given mean am and
standard deviation s }
{procedure is based on the central limit theorem}
  procedure gauss (var ix: longint; am: real; procedure randu (ix:
longint; var iy: longint; var yfl: real); var v: real; var i: integer;
a, y: real;
  begin
    a := 0;
    for i := 1 to 12 do
      begin
        randu(ix, iy, y);

```

```

ix := iy;
a := a + y;
end;
v := (a - 6) * sqrt(am) + am;
end; { gauss}
{computes uniformly distributed random real numbers yfl between 0 and 1
and random integers iy between 0 and 2**31}
{for the first entry ix must contain any odd integer with nine or less
digits}
{procedure is based on the power residue method}
procedure randu (ix: longint; var iy: longint; var yfl: real);
begin
iy := ix * 65539;
if iy < 0 then
begin
iy := iy + 2147483647 + 1;
yfl := iy;
end
else
yfl := iy;
yfl := yfl * 0.4656613 * 0.000000001;
end; {randu}
begin
showtext;
writeln('number of photons emitted by a source = ');
readln(p); {reads number of photons emitted by an x-ray source}
Param(projnumber, projlength, l2n); {reads the description of an
input sinogram}
vectorptr(prjptr, projnumber, projlength); {allocates memory for a
sinogram file}
name := oldfilename('PROJECTION FILE');
open(textfile, name);
for i := 1 to projnumber do {reads in sinogram file}
for j := 1 to projlength do
begin
temprealpointer := arrvector(i, j);

```

```

    read(textfile, v);
    temprealpointer^ := exp(-v);
end; {for i, j}
close(textfile);
ix := 5;
pp := p * projnumber;
for i := 1 to projnumber do
  for j := 1 to projlength do
    begin
      temprealpointer := arrvector(i, j);
      det := temprealpointer^ * p;
      repeat
        repeat {computes a sample of the reference detector counts during
the actual measurement}
          gauss(ix, p, randu, v);
          until v > 0;
          a := v;
          for m := 1 to 2 do
            begin
              repeat {computes samples of counts of the reference det. and the
det. under investigation }
{during the calibration measurement}
                gauss(ix, pp, randu, v);
                until v > 0;
                c[m] := v;
            end; {m}
            repeat {computes a sample of the det. under investigation counts
during the actual measurement}
              gauss(ix, det, randu, v);
              until v > 0;
              v1 := -ln((v / a) / (c[1] / c[2]));
              v2 := -ln((v / a) / (c[2] / c[1]));
              if v1 > v2 then
                w := v1
              else
                w := v2;

```

```
    until w > 0;
    temprealpointer^ := w;
end; {i,j}
name := newfilename('noisy sinogram');
open(textfile, name);
for i := 1 to projnumber do
  begin
    for j := 1 to projlength do
      write(textfile, arrvector(i, j)^);
      writeln(textfile);
    end;{for i,j}
  close(textfile);
end; {NoisyAtProj}end;
end.
```

```

{*****}
{purpose: image enhancement through using a directional filter}
{}
{author: Elzbieta J. Mazur}
{}
{address: Department of Electrical and Computer Engineering, The
University of Manitoba, Winnipeg, MB, R3T 2N2}
{}
{description of parameters: }
{c (phi), s (phi) - functions of an angle phi that an edge forms with a
coordinate axis}
{h( ) - directional filter function}
{n - size of an image matrix}
{v( ) - function calculated for 00, 450, 900, and 1350}
{*****}

{Procedure uses directional filter to enhance the picture. }
{At each pixel an effort is made to estimate the direction of an edge,
if any, }
{and the filter avoids averaging points across the edge. For description
see Section 3.4.}
procedure dirFilter;
var
  n, l2n, i, j, k, phi, l, m: integer;
  vi, min, sum, t: real;
  ptr1, ptr2: deconvptr;
  realsize, timel, time2: longint;
  textfile: text;
  name: str255;
  angle: array[1..4] of integer;
  tempprojptr: deconvptr;
function c (phi: integer): integer;
begin
  if (phi = 0) or (phi = 45) then
    c := 1
  else if phi = 90 then

```

```

    c := 0
  else
    c := -1;
end; {c}
function s (phi: integer): integer;
begin
  if (phi = 0) then
    s := 0
  else
    s := 1;
end; {s}
function h (i, j, phi: integer; function c (phi: integer): integer;
function s (phi: integer): integer): real; {filter function}
  var
    cc, ss: integer;
  begin
    cc := c(phi);
    ss := s(phi);
    if (i = 0) and (j = 0) then
      h := 0.5
    else if (i = cc) and (j = ss) or (i = -cc) and (j = -ss) then
      h := 0.25
    else
      h := 0;
    end; {h}
  function v (phi, i, j, n: integer; realsize: longint; ptr1: deconvptr;
function c (phi: integer): integer; function s (phi: integer): integer;
function elm (i, j, n: integer; realsize: longint; ptr1: deconvptr):
deconvptr): real;
  begin
    v := sqr(elm(i, j, n, realsize, ptr1)^ - elm(i - s(phi), j + c(phi),
n, realsize, ptr1)^) + sqr(elm(i, j, n, realsize, ptr1)^ - elm(i +
s(phi), j - c(phi), n, realsize, ptr1)^);
  end; {v}
begin
  showtext;

```

```

SetParam(n, l2n); {reads in the size of an image matrix}
MatrixMem(ptr1, realsize, n); {allocates memory for an image matrix}
MatrixMem(ptr2, realsize, n); {allocates memory for an enhanced image
matrix}

name := oldfilename('object matrix');
open(textfile, name);
for i := 1 to n do    {reads in image file}
begin
  for j := 1 to n do
begin
  read(textfile, t);
  tempprojptr := elm(i, j, n, realsize, ptr1);
  tempprojptr^ := t;
  tempprojptr := elm(i, j, n, realsize, ptr2);
  tempprojptr^ := 0;
end; {j}
  readln(textfile);
end; {j}
close(textfile);
angle[1] := 45;
angle[2] := 90;
angle[3] := 135;
for i := 2 to n - 1 do
  for j := 2 to n - 1 do
begin
  phi := 0;
  min := v(0, i, j, n, realsize, ptr1, c, s, elm);
  for k := 1 to 3 do
begin
  vi := v(angle[k], i, j, n, realsize, ptr1, c, s, elm);
  if vi < min then
begin
  phi := angle[k];
  min := vi;
end;
end; {k}

```

```

sum := 0;
for l := -1 to 1 do {applies filter function}
  for m := -1 to 1 do
    sum := sum + h(l, m, phi, c, s) * elm(i - m, j + 1, n, realsize,
ptr1)^;
    tempprojptr := elm(i, j, n, realsize, ptr2);
    tempprojptr^ := sum;
  end; {j}
for i := 1 to n do {filling in the border columns in the filtered
image matrix}
  begin
    tempprojptr := elm(i, 1, n, realsize, ptr2);
    tempprojptr^ := elm(i, 2, n, realsize, ptr2)^;
    tempprojptr := elm(i, n, n, realsize, ptr2);
    tempprojptr^ := elm(i, n - 1, n, realsize, ptr2)^;
  end; {i}
for i := 1 to n do {filling in the border rowss in the filtered image
matrix}
  begin
    tempprojptr := elm(1, i, n, realsize, ptr2);
    tempprojptr^ := elm(2, i, n, realsize, ptr2)^;
    tempprojptr := elm(n, i, n, realsize, ptr2);
    tempprojptr^ := elm(n - 1, i, n, realsize, ptr2)^;
  end; {i}
name := newfilename('filtered object matrix');
open(textfile, name);
for i := 1 to n do
  begin
    for j := 1 to n do
      begin
        t := elm(i, j, n, realsize, ptr2)^;
        write(textfile, round(t), ' ');
      end; {j}
    writeln(textfile);
  end; {i}
close(textfile);

```

```
dispose(ptr1);  
dispose(ptr2);  
end; { dirFilter}
```

```

{*****}
{purpose: computes set of projections for a fan beam geometry}
{}
{author: Elzbieta J. Mazur}
{}
{address: Department of Electrical and Computer Engineering, The
University of Manitoba, Winnipeg, MB, R3T 2N2}
{}
{description of parameters: }
{angle - direction of a projection under consideration}
{initialvalue - value chosen to fill in the reconstruction matrix
before starting the iteration process}
{itercount - iteration counter}
{odDist - distance between a detector array and the center of an object
matrix}
{pixShadow - length of a pixel shadow}
{pointDist - pixel distance from the x - ray source}
{projection - the input projection data}
{projnumber - number of projections in the input set}
{projrange - half of the length of a projection}
{pseudoprojection - computed projection of intermediate image}
{reorange - half of the length of a reconstruction matrix}
{sdDist - distance between x - ray source and a detector array}
{soDist - distance between x - ray source and the center of an object
matrix}
{startangle - direction of the first projection}
{stepangle - distance between consecutive projection directions}
{t1, t2} - the extreme detectors (left, right) of the set of detectors
affected by a pixel}
{x1, y1 - pixel coordinates in a rotated system}
{*****}
procedure MapDivProjection;
var
  textfile1, textfile2: text;
  j, i, projectionrange, x, y, temp1, temp2, density: integer;

```

```

temp, deltaangle, a, s, c, x1, y1, gamma, pointDist, soDist, odDist,
sdDist, pixShadow, pixDist, ldet, rdet: real;
name, PROMPT: str255;
time1, time2: longint;
begin
showtext;
setDivprojparam(soDist, odDist, sdDist); {reads in the description of
a projection set to compute}
vectorptr2(prjptr, projnumber, projlength); {allocates memory for a
projection set}
name := oldfilename('DENSITY MATRIX FROM MAP');
open(textfile1, name);
name := newfilename('projection file');
open(textfile2, name);
for j := 1 to projnumber do {zeroing projection matrix}
for i := -projrange + 1 to projrange do
begin
temprealpointer := arrvector2(j, i + projrange);
temprealpointer^ := 0.0;
end;{j,i}
seek(textfile1, 0);
for x := -reorange + 1 to reorange do {computes the projections}
begin
for y := -reorange + 1 to reorange do
begin
read(textfile1, density);
if density <> 0 then
begin
angle := startangle;
for j := 1 to projnumber do
begin
c := cos(angle);
s := sin(angle);
x1 := x * c + y * s;
y1 := y * c - x * s;
gamma := arctan(x1 / (soDist - y1));

```

```

pointDist := (soDist - y1) / cos(gamma);
pixshadow := sdDist / (2 * pointDist);
pixDist := sdDist * gamma;
ldet := pixDist - pixShadow;
rdet := pixDist + pixShadow;
temp1 := trunc(ldet);
if ldet < 0 then
temp1 := temp1 - 1;
temp2 := trunc(rdet);
if rdet < 0 then
temp2 := temp2 - 1;
temprealpointer := arrvector2(j, temp1 + projrange);
a := temprealpointer^;
temprealpointer^ := a + ((1 - abs(ldet - temp1)) / (2 *
pixshadow)) * density;
temprealpointer := arrvector2(j, temp2 + projrange);
a := temprealpointer^;
temprealpointer^ := a + (abs(rdet - temp2) / (2 * pixshadow)) *
density;
for i := (temp1 + 1) to (temp2 - 1) do
begin
temprealpointer := arrvector2(j, i + projrange);
a := temprealpointer^;
temprealpointer^ := a + (1 / (2 * pixshadow)) * density;
end;
angle := angle + stepangle;
end; {j}
end;
end; {y}
readln(textfile1);
end; {x}
for j := 1 to projnumber do
begin
for i := -projrange + 1 to projrange do
write(textfile2, ' ', arrvector2(j, i + projrange)^);
writeln(textfile2);

```

```
end; {j}  
close(textfile1);  
close(textfile2);  
end;
```

```

{*****}
{purpose: applies window fuction to noisy sinogram}
{}
{author: Elzbieta J. Mazur}
{}
{address: Department of Electrical and Compuer Engineering, The
University of Manitoba, Winnipeg, MB, R3T 2N2}
{}
{description of parameters: }
{f( ) - window function}
{projlength - length of a single projections in the sinogram}
{projnumber - number of projections in the sinogram}
{*****}

```

```

unit SinFilter;
interface
  procedure LPFsin;
implementation
  procedure LPFsin;
  type
    sinptr = ^real;
  var
    i, j, nn, n3, l2n, k, c, np1, an, m, r, t: integer;
    t1, t2, fil, a, b: real;
    textfile: text;
    name: str255;
    arrayptr1: complexptr;
    time1, time2: longint;
    sptr, temrecpointer: sinptr;
  function filter (i: integer): real; {definition of window function}
  var
    frequency, s: real;
begin
  frequency := (i - 1) / projlength;
  if frequency <= 0.5 then
    filter := 0.8 + 0.2 * cos(pi * frequency / 0.5)

```

```

else
  filter := 0;
end; {filter}
begin
  showtext;
  sinParam(projnumber, projlength, l2n); {reads the description of an
input sinogram}
  nn := projlength div 2;
  n3 := nn + 1;
  ll2n := l2n - 1;
  arrmemptr1(arrayptr1, cplxsize, n3); {allocates auxiliary memory for
temporary results}
  createreSinogramarray; {allocates memory for a sinogram matrix}
  name := oldfilename('noisy sinogr');
  open(textfile, name);
  for k := 1 to projnumber do
    begin
      for i := 1 to nn do {rewrites projection real sequence into complex
sequence}
{before taking Fourier transform}
        begin
          r := 2 * i - 1;
          t := 2 * i;
          read(textfile, t1, t2);
          temrecpointer := rr(k, r);
          temrecpointer^ := t1;
          temrecpointer := rr(k, t);
          temrecpointer^ := t2;
          tempptr := arrayy1(i, cplxsize, arrayptr1);
          tempptr^.re := t1;
          tempptr^.im := t2;
        end;
      c := 1;
      dfftreall1(nn, ll2n, c, cplxsize, arrayptr1);
      npl := nn + 1;
      c := -1;
    end;
  end;
end;

```

```

for i := 1 to npl do {applies window function}
begin
  fil := filter(i);
  tempptr := arrayyl(i, cplxsize, arrayptr1);
  a := -tempptr^.im * fil;
  tempptr^.im := a;
  b := tempptr^.re * fil;
  tempptr^.re := b;
end;{i}
dfftreal1(nn, ll2n, c, cplxsize, arrayptr1);
for i := 1 to npl do
begin
  tempptr := arrayyl(i, cplxsize, arrayptr1);
  a := -tempptr^.im;
  tempptr^.im := a;
end;{i}
an := nn;
for i := 1 to nn do
begin
  tempptr := arrayyl(i, cplxsize, arrayptr1);
  a := (tempptr^.im / an);
  tempptr^.im := a;
  b := (tempptr^.re / an);
  tempptr^.re := b;
end;{i}
for m := 1 to nn do {rewrites filtered projection complex sequence
back into real sequence}
begin
  r := 2 * m - 1;
  t := 2 * m;
  temrecpointer := rr(k, r);
  if temrecpointer^ = 0 then
  begin
  end
else
  temrecpointer^ := arrayyl(m, cplxsize, arrayptr1)^.re;

```

```

    temrecpointer := rr(k, t);
    if temrecpointer^ = 0 then
        begin
            end
        else
            temrecpointer^ := arrayy1(m, cplxsize, arrayptr1)^.im;
        end; {m}
    end; {k}
{projection array filled up}
    close(textfile);
    name := newfilename('filtered sinogr');
    open(textfile, name);
    for i := 1 to projnumber do {writes in the filtered sinogram into the
output file}
        begin
            for k := 1 to projlength do
                begin
                    temrecpointer := rr(i, k);
                    if temrecpointer^ < 0 then
                        temrecpointer^ := 0;
                    write(textfile, temrecpointer^);
                end;
            writeln(textfile);
        end; {i}
    close(textfile);
    dispose(arrayptr1);
    dispose(sptr);
end; {LPFsin}
end. {SinFilter}

```

```

{*****}
{purpose: evaluates the reconstruction quality using different
similarity measures}
{}
{author: Elzbieta J. Mazur}
{}
{address: Department of Electrical and Computer Engineering, The
University of Manitoba, Winnipeg, MB, R3T 2N2}
{}
{description of parameters: }
{n - size of a square object/reconstruction matrix (n x n)}
{ep1 - correlation coefficient}
{ep2 - Euclidean distance}
{ep3 - average absolute difference}
{ep4 - largest difference}

```

```

{*****}

```

```

unit evaluation;
interface
  procedure evaluationMeasures;
implementation
  procedure evaluationMeasures;
  var
    n, l2n, i, j: integer;
    t, t1, t2, t3, ep1, ep2, ep3, ep4, b, c, sum, meanR, meanI: real;
    textfile: text;
    name: str255;
    ObjPointer, tempptr: complexptr;
begin
  showtext;
  SetParam(n, l2n); {reads the description of an image matrix}
  createFourierObjectMatrix(ObjPointer, reconstroffset, n); {allocates
memory for reference }
{and reconstruction matrix}
  name := oldfilename('reference matrix');

```

```

open(textfile, name);
sum := 0;
for i := 1 to n do {reads in a reference object file}
  for j := 1 to n do
    begin
      read(textfile, t);
      sum := sum + t;
      tempptr := MatrixElem(i, j, n, reconstroffset, ObjPointer);
      tempptr^.re := t;
    end; {j,i}
meanR := sum / (n * n);
close(textfile);
name := oldfilename('image matrix');
open(textfile, name);
sum := 0;
for i := 1 to n do {reads in a reconstruction file}
  for j := 1 to n do
    begin
      read(textfile, t);
      sum := sum + t;
      tempptr := MatrixElem(i, j, n, reconstroffset, ObjPointer);
      tempptr^.im := t;
    end; {j,i}
meanI := sum / (n * n);
close(textfile);
sum := 0;
b := 0;
c := 0;
ep2 := 0;
ep3 := 0;
ep4 := 0;
for i := 1 to n do
  for j := 1 to n do
    begin
      t1 := (MatrixElem(i, j, n, reconstroffset, ObjPointer)^.re -
meanR);

```

```

t2 := (MatrixElem(i, j, n, reconstroffset, ObjPointer)^.im -
meanI);
sum := sum + t1 * t2;
b := b + t1 * t1;
c := c + t2 * t2;
ep2 := ep2 + sqr(MatrixElem(i, j, n, reconstroffset,
ObjPointer)^.re - MatrixElem(i, j, n, reconstroffset, ObjPointer)^.im);
t3 := abs(MatrixElem(i, j, n, reconstroffset, ObjPointer)^.re -
MatrixElem(i, j, n, reconstroffset, ObjPointer)^.im);
ep3 := ep3 + t3;
if t3 > ep4 then
ep4 := t3;
end; {j,i}
ep1 := sum / (sqrt(b * c) + 0.00000001);
ep2 := sqrt(ep2 / (n * n));
ep3 := ep3 / (n * n);
time2 := tickcount;
name := newfilename('evaluation');
open(textfile, name);
writeln(textfile, 'correlation coefficient = ', ep1 : 13 : 9);
writeln(textfile, 'Euclidean distance = ', ep2 : 13 : 9);
writeln(textfile, 'average absolute difference = ', ep3 : 9 : 3);
writeln(textfile, 'largest difference = ', ep4 : 9 : 3);
close(textfile);
dispose(ObjPointer);
end; {evaluationMeasures}
end.

```

```

{*****}
{purpose: computes Fourier spectrum of an object}
{}
{author: Elzbieta J. Mazur}
{}
{address: Department of Electrical and Computer Engineering, The
University of Manitoba, Winnipeg, MB, R3T 2N2}
{}
{description of parameters: }
{n - size of a square object matrix (n x n)}
{spectrum - Fourier spectrum of an object}
{*****}

```

```

procedure FSpectrum;
  var
    n, l2n, m, k: integer;
    textfile: text;
    name: str255;
    spectrum: real;
    ObjPointer, arrayptr1: complexptr;
    time1, time2: longint;
  begin
    showtext;
    SetParam(n, l2n); {reads information on object matrix}
    arrmemptr1(arrayptr1, cplxsize, n); {allocates auxiliary memory for
FFT purpose}
    createFourierObjectMatrix(ObjPointer, reconstroffset, n); {allocates
memoryfor object array in Fourier domain}
    name := oldfilename('object matrix');
    open(textfile, name);
    F2D(textfile, n, l2n, cplxsize, reconstroffset, arrayptr1,
ObjPointer); {computes 2D Fourier transform}
    close(textfile);
    name := newfilename('Fourier spectrum of object');
    open(textfile, name);
    for k := 1 to n do {computes Fourier transform of an object}

```

```
begin
  for m := 1 to n do
    begin
      spectrum := sqrt(sqr(MatrixElem(k, m, n, reconstroffset,
ObjPointer)^.re) + sqr(MatrixElem(k, m, n, reconstroffset,
ObjPointer)^.im)); {Fourier spectrum of the object}
      write(textfile, ' ', round(spectrum));
    end;
    writeln(textfile);
  end;
  close(textfile);
  dispose(arrayptr1);
  dispose(ObjPointer);
end; {FSpectrum}
```

```

{*****}
{purpose: computes Fourier phase of an object}
{}
{author: Elzbieta J. Mazur}
{}
{address: Department of Electrical and Computer Engineering, The
University of Manitoba, Winnipeg, MB, R3T 2N2}
{}
{description of parameters: }
{n - size of a square object matrix (n x n)}
{phase - Fourier phase of an object}
{*****}

```

```

procedure FPhase;
  var
    n, l2n, m, k: integer;
    textfile: text;
    name: str255;
    phase: real;
    ObjPointer, arrayptr1: complexptr;
    time1, time2: longint;
  begin
    showtext;
    SetParam(n, l2n); {reads the description of an object matrix}
    arrmemptr1(arrayptr1, cplxsize, n); {allocates auxiliary memory for
    FFT purpose}
    createFourierObjectMatrix(ObjPointer, reconstroffset, n); {allocates
    memory for object array in Fourier domain}
    name := oldfilename('object matrix');
    open(textfile, name);
    F2D(textfile, n, l2n, cplxsize, reconstroffset, arrayptr1,
    ObjPointer); {computes 2D Fourier transform}
    close(textfile);
    name := newfilename('fourier phase object');
    open(textfile, name);
    for k := 1 to n do

```

```
begin
  for m := 1 to n do
    begin
      phase := arctan(MatrixElem(k, m, n, reconstroffset,
ObjPointer)^.im / (MatrixElem(k, m, n, reconstroffset, ObjPointer)^.re +
0.0000001)); {Fourier phase of the object}
      if (MatrixElem(k, m, n, reconstroffset, ObjPointer)^.im >= 0) and
(MatrixElem(k, m, n, reconstroffset, ObjPointer)^.re < 0) then
        phase := phase + pi;
      if (MatrixElem(k, m, n, reconstroffset, ObjPointer)^.im < 0) and
(MatrixElem(k, m, n, reconstroffset, ObjPointer)^.re < 0) then
        phase := phase + pi;
      write(textfile, ' ', round(phase * 1000));
    end;
    writeln(textfile);
  end;
  close(textfile);
  dispose(arrayptr1);
  dispose(ObjPointer);
end; {FPhase}
```